Doctoral Dissertation
Doctoral Program in Materials Science and Technology (36th Cycle)

Understanding the post-processing behaviour of additively manufactured A20X alloy: The new high strength Al alloy in the market

By

Jayant Barode

******

Supervisor(s):
Prof. Diego Manfredi, Supervisor
Prof. Federica Bondioli, Co-Supervisor

Doctoral Examination Committee:
Prof. Marina Cabrini, Università degli Studi di Bergamo
Prof. Alberto Castellero, Università degli Studi di Torino

Politecnico di Torino
2023

Declaration

I hereby declare that, the contents and organization of this dissertation constitute my own original work and does not compromise in any way the rights of third parties, including those relating to the security of personal data.

Jayant Barode

2023

* This dissertation is presented in partial fulfillment of the requirements for **Ph.D. degree** in the Graduate School of Politecnico di Torino (ScuDo).

I would like to dedicate this thesis to my wife and both of our parents.

Acknowledgment

I would like to begin by conveying my appreciation to Prof. Mariangela Lombardi and Prof. Paolo Fino for accepting my candidacy for the doctoral thesis at Politecnico di Torino, as well as for their generous financial support throughout my research endeavours. Furthermore, my sincere gratitude goes to Prof. Diego Manfredi and Prof. Federica Bondioli for graciously accepting me as their official doctoral student. I am particularly thankful for their understanding and support, as they granted me permission to visit India during the early stages of my doctoral studies due to family reasons. I extend my heartfelt thanks to Prof. Alberta Aversa, a senior colleague who served as my acting supervisor. The fruition of this thesis owes much to her unwavering support. I am grateful for her invaluable suggestions that guided me throughout my research endeavours and for granting me the freedom to explore and experiment with any proposed hypotheses.

Credit is owed to Prof. Emilio Bassini for his collaboration and expertise in hot isostatic pressing techniques. Gratitude is extended to Mr. Dario Pezzini for his invaluable assistance in conducting numerous tensile tests. I would also express my appreciation to Dr. Ashok Vayyala for his collaboration on the electron microscopy facility at the Ernst Ruska-Centre for Microscopy and Spectroscopy with Electrons (ER-C-2), Forschungszentrum Jülich GmbH, Germany. I extend my gratitude to Mr. Giovanni and Mr. Matteo, senior technicians at the Integrated Additive Manufacturing Facility, for their invaluable assistance amidst their busy schedules. A special acknowledgment goes to my office mates, Enrico Virgillito, Francesco Viola, and Luigi Rotella, for serving as

Italian translators and providing support in overcoming language communication barriers during crucial administrative activities for immigrants. I extend my appreciation to every member of the research group (Gamma team) for their contributions. The Friday lunches, regular coffee breaks, and casual discussions have played a crucial role in maintaining a healthy work-life balance.

Lastly, I wish to express my gratitude to my wife, our families, and all friends whose unwavering support has been instrumental in guiding me along my scientific journey.

Abstract

Laser Powder Bed Fusion (LPBF) stands as an advanced metal additive manufacturing process, enabling the creation of components with intricate shapes through the localized melting of successive layers of powders using a computer-controlled laser beam. In recent years, LPBF has garnered considerable attention, not only for its inherent benefits in providing high design flexibility but also for the opportunities/challenges it presents from a materials perspective. The spectrum of printable alloys is constrained due to its unconventional processing conditions. Among the limited alloys that exhibit good printability, there is growing interest in a newly developed high-strength aluminium alloy (A20X) for additive manufacturing. The alloy was developed and patented by Aeromet International Ltd, UK.

In the present thesis, the commercial high strength A20X alloy was processed by LPBF, and their post-processing behaviour was investigated. Firstly, the printability of the A20X alloy was investigated. The alloy was easy to process and possess a wide processing window with high relative densities. Being a precipitation hardening alloy, various post-processing conditions were investigated as they have remarkable effect on the mechanical behaviour of the printed parts.

The post-processing heat treatment investigated were: Artificial aging (T6 and T7), natural aging (T4) and hot isostatic pressing (HIPing).

To understand the post-processing behaviour of A20X alloy, a conventional long-T6 heat treatment was employed, and its microstructural evolution and mechanical behaviour was investigated. Post to the analysis, a new heat treatment (short-T6) was proposed and compared with the long-T6. The short-T6 heat treatment offers superior ductility as compared to long-T6 along with a slight improvement in strength. It was discovered that the alloy also responds well to the T4 condition and achieved its peak hardness in around 20 days at room

temperature (28 °C). The alloy in its T4 state possess a combination of good-strength and high-ductility. An insight into the structure-property relationship was obtained by evaluating various strengthening mechanism and their contribution to the overall yield strength of the alloy. The thesis also has a dedicated chapter on understanding the strain hardening behaviour and failure mechanism of various post-processing conditions. Finally, the effect of HIP (most commonly employed techniques for AM parts) was studied and compared with the short-T6 condition.

Contents

1. Introduction to additive manufacturing 1

1.1 Additive Manufacturing vs. Conventional Manufacturing......................1

1.2 Metal additive manufacturing processes: 3

1.3 Laser powder bed fusion (LPBF) 5

1.3.1 Machine parts and how it works: 5

1.3.2 LPBF processing parameters: 6

1.3.3 Microstructure of the melt pool 11

1.3.4 Metallurgical defects in LPBF parts 12

1.3.4 Defects characterization and analysis: 17

1.3.5 Strategies to mitigate defects: 20

2. Processing of high-strength Al alloys by LPBF 24

2.1 Introduction to high strength Al alloys:...24

2.2 Processing challenges by LPBF: 27

2.2.1 Oxidation: 27

2.2.2 Poor flowability 28

2.2.3 High laser reflectivity: 29

2.2.4 High thermal conductivity: 30

2.2.5 Cracking..30

2.3 Role of ceramic addition to improve printability: 33

2.3.1 Improved absorptivity:..33

2.3.2 Lower thermal conductivity:...34

2.3.3 Columnar to equiaxed grained microstructure:..............................34

2.4 Literature review on A20X (Al-Cu-Mg-Ag-TiB_2)..............................35

2.4.1 Development of Al-Cu-Mg-(Ag) alloy:...35

2.4.2 Role of alloying elements: 37

2.4.3 Addition of TiB_2 to Al-Cu-Mg-Ag alloy: 38

3. Motivation and Methodology 40

3.1 Motivation 40

3.2 Methodology...41

3.2.1 Powder flowability:...41

3.2.2 3D printing:...41

3.2.3 Post-processing treatments: 42

3.2.4 Characterization tools: 43

4. Printability of the A20X alloy by LPBF: Process optimization, as-built microstructure, and mechanical properties 47

4.1 Introduction 47

4.2 Methodology...47

4.3 A20X powder characterization...48

4.3.1 Powder flowability..48

4.3.2 Powder phase analysis and microstructure 50

4.4 Printability of powder..52

4.5 As-built microstructure..54

4.5.1 TiB_2 cluster size: Effect of laser power and scanning speed 54

4.6 Mechanical property and fracture behaviour:.......................................55

4.7 Conclusion:..57

5. Long T6 vs Short T6 post-processing behaviour: Role of multiple-steps and single-step in a solution treatment 58

5.1 Introduction 58

5.2 Methodology...59

5.3 Micro-hardness and microstructural evolution 60

5.4 On the grain boundary cracking during aging 71

5.5 Microstructural evolution during MS-ST 72

5.6 A comparison of multiple-step (MS-ST) and single-step (SS-ST) solution treatments 76

5.7 Tensile behaviour 80

5.8 Conclusions 82

6. Comparison of natural and artificial aging behaviour of A20X alloy 84

6.1 Introduction 84

6.2 Methodology 85

6.2 Results 85

6.2.1 Micro-hardness response 85

6.2.2 Thermal analysis: 86

6.2.3 Phase analysis 87

6.2.4 Microstructure: 88

6.2.5 Tensile behaviour: 92

6.3 Discussion 93

6.3.1 Age hardening behaviour 93

6.3.2 Strengthening mechanisms: 94

6.4 Conclusion: 102

7. Strain hardening and fracture behaviour of post-processed LPBF-A20X alloy 103

7.1 Introduction 103

7.2 Strain hardening behaviour 104

7.3 Failure mechanism 108

7.4 Conclusion 113

8. Effect of hot isostatic pressing on the mechanical behaviour 114

8.1 Introduction 114

8.2: Part-1 115

8.2.1 Methodology 115

8.2.2 Results 116

8.2.3 Discussion 122

8.2.4 Part-1: Conclusion 124

8.3 Part-2 125

8.3.1 Methodology 125

8.3.2 Results: 125

8.3.3 Discussion 130

8.3.4 Part-2 Conclusion 131

8.4 Chapter summary: 131

9. Summary 132

9.1 LPBF processibility of A20X alloy: 132

9.2 Microstructural evolution of long-T6 and the role of short-T6: 133

9.3 Comparison of T4 and short-T6 heat treatment: Strengthening mechanisms 134

9.4 Strain hardening and fracture behaviour of T4, Short-T6 and Long-T6 135

9.5 Effect of hot isostatic press (HIP) on the mechanical behaviour: 135

9.5.1 Summary of part 1: 136

9.5.2 Summary of part 2: 136

10. References 137

List of Figures

Fig 1.1: Comparison between conventional and additive manufacturing processes [4] 2

Fig 1.2: Classification of metal additive manufacturing process 4

Fig 1.3: Displaying the parts of LPBF systems [15] 5

Fig 1.4: Schematic of (a) main processing parameters in an LPBF process [27] and (b) various scan strategies [22] 8

Fig 1.5: A schematic of ray tracing model displaying multiple laser reflection in a powder bed [49]. 10

Fig 1.6: (a) Effect of temperature gradient G and growth rate R on the morphology and size of solidification microstructure [9], (b) Illustration depicting the microstructural evolution of AlSi10Mg during LPBF: (a) Initiation of the primary solid phase (α-Al) occurs at the interface between the solid and liquid phases, characterized by a higher temperature gradient. (b) Subsequent growth of primary α-Al grains takes place towards the centre of the melt pool, where elevated temperatures lead to solidification along the preferential <001> direction. (c) During the cooling phase, the material exhibits a composition featuring columnar α-Al grains interspersed with fine eutectic Si particles [56]. 12

Fig 1.7: Defects observed in LPBF processing: (a) gas induced porosity [64], (b) lack of fusion defects [64], and keyhole porosity [65] 13

Fig 1.8: Equilibrium vapour pressure of metals at various temperatures [68] 13

Fig 1.9: Hot cracking in an IN718 processed by laser additive manufacturing (a) Liquation cracking by (b) Solidification cracking [73] 15

Fig 1.10: Layer delamination and cracking in M2 tool steel [69]. 15

Fig 1.11: SEM micrograph of single scan tracks displaying balling phenomena at different scan speed values [83] 16

Fig 1.12: Powder spattering seen through high-speed images of side (Left) and top (Right) views as a function of laser power and scan speed: (a) and (b) 50 W and 0.1 m/s; (c) and (d) 100 W and 0.5 m/s and (e) and (f) 200 W and 1 m/s. *Inset is a schematic of the melt pool shape, which determines the laser plume direction* [85]. 17

Fig 1.13: (a) Density measurement by Archimedes method, and (b) Printed sample cross-sectioning along vertical and parallel direction for optical microscopy [90] 19

Fig 1.14: (A-D) Workflow of the X-ray computed tomography (A) fundamental depiction of a tomographic setup, encompassing the X-ray source, detector, and the specimen. Projection images are generated by incrementally rotating the specimen through angles denoted as θ. (B) 2D sample projections captured at varying angles, (C) 2D projections are digitally reconstructed (D) 3D rendered volume and 2D cross-sectional slices. (E) Porosity visualization from a 3D constructed data and (F) CT slice image showing porosities [94,95]. 19

Fig 1.15: (a) A schematic of a HIP process [122], (b) cross sectional slice image: left (before HIP), right (after HIP), and below their corresponding 3D view displaying closure of lack of fusion pores after HIP except a small number near the surface [117] 23

Fig 2.1: (A) Marangoni convection in the melt pool, (B) Oxide disruption during solidification and (C) Oxide network revealed after etched with NaOH an LPBF-6061 alloy [143]. 28

Fig 2.2: SEM micrograph of atomized powder particles (a) Al–12Si and (b) Ti–6Al–4V 29

Fig 2.3: The minimum laser power required for melting various metals using a pulsed Nd:YAG laser, *inset: absorptivity of common metals over spectrum of wavelengths* [153]. 29

Fig 2.4: (a) Crack susceptibility of high strength Al alloys by Temperature vs. solid fraction curve showing maximum steepness; (**b**) maximum steepness in for various alloys [167]. (c) Solidification cracking mechanism [168], T_l and T_s are liquidus temperature and solidus temperature, respectively. v_s is liquidus isotherm velocity. (d) EBSD-IPF map of the LPBF-2024 alloy showing solidification cracks and (e) a higher magnification of the cracked region [169]. 32

Fig 2.5: Reduction of laser reflectivity in AlSi10Mg on addition of various ceramic particles: (a) Nano-TiB_2 [185] (b) TiN [186] and (c) TiB_2+TiC [178]....34

Fig 2.6: Columnar to equiaxed transition of microstructure in various LPBF-Al alloys by the addition of (a) TiC [178], (b) TiB_2 [196], (c) TiN [182] and (d) TiC+TiH_2 [194]..35

Fig 3.1: (a) EOS M270 machine, (b) build plate after printing, and (c) schematic of a tensile specimen with ASTM E8 dimensions obtained after EDM cutting. 41

Fig 3.2: (a) HIP Quintus QIH 15 L machine and (b) Uniform Rapid Cooling module with Molybdenum furnace..42

Fig 4.1: FESEM micrographs of A20X powder (a) low and (b) high magnification of powder morphology; Powder cross-section at (c) low and (d) high magnifications...51

Fig 4.2: XRD pattern of the A20X powder..51

Fig 4.3: (a) Porosity vs. VED, (b), (c) and (d) porosity vs. scan speed for each laser power -hatching distance combination. The green arrow indicates the optimized set of building parameters..53

Fig 4.4: LPBF processed as-built A20X alloy at 195 W with various scanning speed (mm/s) (a) 500, (b) 600, (c) 700, (d) 800, (e) 900, and (f) 1000. 53

Fig 4.5: SEM-BSE micrograph of AB-A20X alloy (a) high brightness, (b) low brightness, and (c) Al_2Cu network of cell boundaries..54

Fig 4.6: TiB_2 cluster size as a function of (a) laser power and (b) scanning speed 55

Fig 4.7: (a) A typical tensile curve of an as-built A20X sample, (b) SEM micrograph of fracture surface displaying dimples and (c) SEM-SE micrograph (left) with (d) its corresponding BSE micrograph (right)....................................56

Fig 5.1: A representation illustrating the different heat treatment processes conducted on the as-built A20X alloy. 60

Fig 5.2: Micro-hardness evolution of A20X alloy during MS-ST and artificial aging..61

Fig 5.3: SEM-BSE micrographs of A20X samples without metallographic etching in the (a) AB, (b) MS-ST, (c) PA and (d) OA states *(Yellow arrows depict grain boundary cracks)*..62

Fig 5.4: SEM-BSE micrograph of (a) Ab, (b) MS-ST, (c) PA and (d) OA condition showing θ-Al_2Cu (bright) and TiB_2 (grey) phase in Al matrix (black) .63

Fig 5.5: EBSD micrographs showing evolution of grain structure in various conditions (a) AB, (b) MS-ST (c) PA and (d) OA..64

Fig 5.6: (a) Identification of phases through XRD measurements in the AB, MS-ST, PA, and OA states. Individual peak profiles for (b) Al_2Cu {110} and (c) Al {111}. (d) Determination of θ-Al_2Cu and TiB_2 phase quantities via Rietveld refinement. (e) Estimation of dislocation density using the W-H plot. 65

Fig 5.7: (a) DSC plots of AB, MS-ST, PA and OA states and (b) deconvolution of the broad exothermic peak of MS-ST state. 67

Fig 5.8: High resolution HAADF-STEM micrograph and corresponding EDS mapping of a grain boundary triple junction in the PA state. 69

Fig 5.9: High resolution HAADF-STEM micrograph and corresponding EDS mapping of a grain boundary triple junction in the OA state *(Note the elemental colour identities are different than in Fig 5.8).* 70

Fig 5.10: Particle size distribution of the needle type precipitates Ω/θ’ in (a) PA and (b) OA state. 70

Fig 5.11: High resolution HAADF-STEM micrographs showing the PFZs in PA (a-b) and OA (c-d) state near micro-TiB_2 particles and near grain boundaries. 72

Fig 5.12: SEM-BSE micrographs under high (a-e) and low (a’-e’) brightness showing microstructural evolution at various interrupted steps during solution treatment. (a and a’) AB, (b and b’) ST-A, (c and c’) ST-B, (d and d’) ST-C and (e and e’) ST-D and (f and f’) MS-ST. (*TiB_2 particles as grey and θ-Al_2Cu as white)*. A schematic view of the corresponding microstructure (on the right-hand side) is shown for each interrupted step. 74

Fig 5.13: Evolution of various features of θ-Al_2Cu precipitate as a function of interrupted solution steps showing (a) area equivalent average-radius and circularity and (b) number density and inter-precipitate spacing. 75

Fig 5.14: SEM-BSE micrograph under high and low brightness of A20X alloy solution treated at 530 °C for (a and d) 1h, (b and e) 6h, and (c and f) 12 h. The micro-hardness values are also mentioned in the rectangular box for each condition. 77

Fig 5.15: (a) Area-equivalent average radius and area fraction of θ-Al_2Cu precipitates in short-T6 and long-T6; SEM-BSE micrographs under low brightness (b) short-T6 and (c) long-T6 *(TiB_2 particles as grey and θ-Al_2Cu as white)*; HAADF-STEM micrographs of short-T6 indicating PFZs, (d) near micro-TiB_2 particles, (e) near grain boundaries and (f) matrix precipitates length distribution. 79

Fig 5.16: SEM-BSE micrographs of (a) short-T6 and (b) long-T6 *(Yellow arrows depict grain boundary cracks)*..79

Fig 5.17: Tensile stress-strain curves of A20X alloy in the AB, PA (long-T6) and short-T6 conditions 81

Fig 6.1: Micro-hardness evolution as a function of natural and artificial aging time 86

Fig 6.2: Heat flow behaviour of NA for various number of days and AA for 4 h in (a) low-temperature and (b) high-temperature range.....................................87

Fig 6.3: XRD patterns of T4 and short-T6 samples showing (a) whole line profile, (b) θ-Al_2Cu {110} and (c) Al {111}. 88

Fig 6.4: EBSD micrographs of A20X samples post-processed with T4 (a, c, and e) and short-T6 (b, d and f). Showing (a and b) IPF map, (c and d) phase map, and (e and f) grain size distribution 89

Fig 6.5: SEM-BSE micrographs of (a) T4 and (b) short-T6 specimen...........90

Fig 6.6: T4 (a-b) HAADF-STEM micrographs and (c-f) EDS maps of the (a) region 91

Fig 6.7: Short-T6 (a-b) HAADF-STEM micrographs and (c-f) EDS maps of the (a) region...92

Fig 6.8: Representative engineering stress-strain curves of LPBF-A20X alloy for various conditions 93

Fig 7.1: Tensile behaviour of the AB and various post-processed conditions (a) engineering stress-strain, and (b) true stress-strain curves............................105

Fig 7.2: The strain hardening rate as a function of reduced flow stress for (a) post-processed conditions and (b) as-built condition. 106

Fig 7.3: True stress-strain (σ vs. ε) and K-M (Θ vs. ε) plots showing the uniform elongation at their intersection in all the post-processed conditions. 106

Fig 7.4: SEM-SE micrographs of the fractured surface at low magnification (a, d and g), at high magnification (b, e and h) and their corresponding BSE micrographs (c, f and i) of T4 (a-c), short-T6 (d-f) and long-T6 (g-i). *(Blue and red arrows showing TiB_2 and θ-Al_2Cu particles, respectively)* 110

Fig 7.5: SEM micrographs of the fractured surface and EDS spot analysis on various particles in (a) T4, (b) short-T6 and (c) long-T6....................................111

Fig 7.6: SEM-BSE micrographs of the regions perpendicular to the fractured surface in various post-processed conditions: (a-b) T4; (b-c) short-T6 and (c-d) long-T6. *(blue and yellow arrow showing micro-voids at the TiB_2 particles/agglomerates and cracks, respectively)* 112

Fig 8.1: Optical micrography of the (a) AB, (b) SS-ST, (c) Short-T6 (d) HIP-1 (e) HIP-2, and (f) HIP-2A *(Red arrows showing porosities)* 117

Fig 8.2: XRD patterns of various conditions (a) full line profile and (b) individual peak profiles of Al_2Cu {110} 118

Fig 8.3: DSC curves of the various conditions of HIPed and non-HIPed A20X alloy 119

Fig 8.4: EBSD-IPF micrographs and their corresponding grain size distribution in (a) Short-T6 and (b) HIP-2A 120

Fig 8.5: SEM micrographs at low (BSE) and high magnification (in-lens SE) of (a-b) short-T6 and (c-d) HIP-2A 121

Fig 8.6: Representative tensile stress-strain curves of T6 and HIP-2A conditions 122

Fig 8.7: Optical micrographs of the (a) AB, (b) HIP-1S and (c) HIP-1SA conditions 126

Fig 8. 8**:** XRD patterns of various conditions (a) whole line profile and (b) individual peak profiles of θ-Al_2Cu {110} 127

Fig 8.9: DSC curves of the various HIPed conditions 128

Fig 8.10: SEM-BSE micrographs of HIPed conditions (a) HIP-1S and (b) HIP-1SA 128

Fig 8.11: Representative tensile stress-strain curves of T6-L and HIP-1SA conditions 129

List of Tables

Table 2.1: Temper designation for the heat treatment 25

Table 2.2: Classification of Al alloys...26

Table 3.1: The main artificially and naturally aged conditions of various heat treatments that are utilized and mentioned in the thesis. 43

Table 4.1: Various processing parameters utilized for the optimization of the processing window. 48

Table 4.2: Categorizing of powder flowability by various flowing characteristics [247,248]...49

Table 4.3: A20X powder characteristics...50

Table 5.1: Various post-processing heat treatments performed on A20X alloy. 59

Table 5.2: A summary of microstructural characteristics and mechanical properties of LPBF-A20X alloy in AB, PA (long-T6) and short-T6 conditions...81

Table 6.1: Characteristics of tensile curves in various conditions.................93

Table 6.2: Summary of the strengthening factors in various conditions.......101

Table 6.3: Summarizing different parameters with their physical meaning utilized in various strengthening mechanism [242,329,338,341,353,354]. 101

Table 7.1: Characteristics of the strain hardening behaviour of various post-processing conditions...106

Table 8.1: Nomenclature of the various heat treatments and their processing conditions...115

Table 8.2: Porosity content of various conditions of HIPed and non-HIPed A20X alloy...117

Table 8.3: Micro-hardness and tensile curves characteristics for the T6 and HIP-2A conditions 122

Table 8.4: Nomenclature of the various heat treatments and their processing conditions...125

Table 8.5: Porosity content of various HIPed and non-HIPed conditions 126

Table 8.6: Characteristics of tensile curves for the aged conditions of HIPed and non-HIPed 130

Chapter 1

Introduction to additive manufacturing

The process of joining materials usually in a layer-by-layer fashion to make 3D objects from a computer-aided design (CAD) or other digital model file is termed as Additive Manufacturing (AM) [1,2]. However, there are other common terms used for AM processes such as 3D printing, rapid prototyping, additive layer manufacturing or freeform fabrication [2].

AM originated as a technology primarily used for rapid prototyping using polymer-based powders with 3D printers. However, it has evolved to encompass the production of intricate complex shapes of metals, alloys, ceramics, metal matrix composites, functionally graded materials. AM has experienced a continuous and rapid development to meet the demands from various sectors such as automotive, aerospace, biomedical, semiconductors, fashion etc. [3].

1.1 Additive Manufacturing vs. Conventional Manufacturing

AM and Conventional Manufacturing are two distinct approaches to create parts and products, as illustrated in **Fig 1.1**. Each has its own set of advantages and disadvantages. Here, I will provide you with a comparison of these two methods.

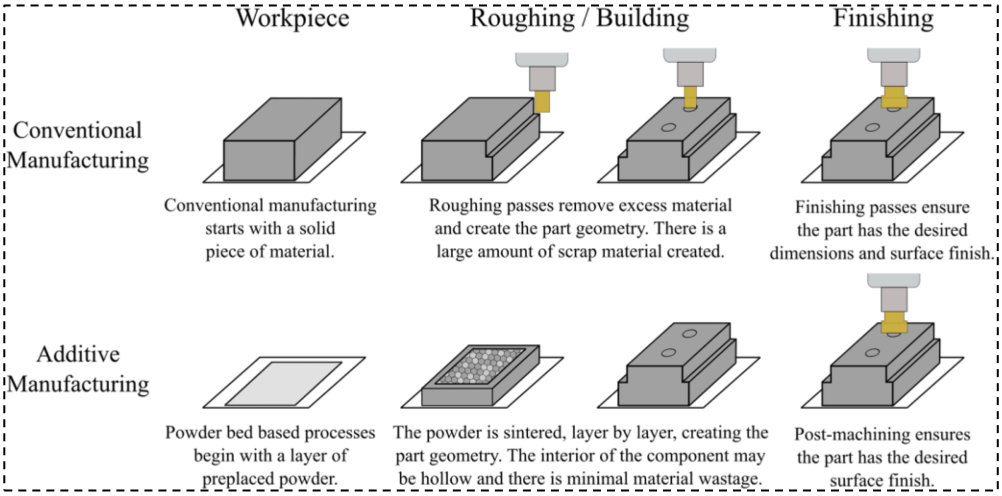

Fig 1.1: Comparison between conventional and additive manufacturing processes [4]

Advantages of AM processes:

1. Design flexibility: Conventional manufacturing processes are often constrained by the need for molds, dies, and tooling, limiting their design flexibility. Furthermore, to achieve complex shapes. they may require multiple steps, increasing the chances of errors. AM on the contrary, allows the production of complex geometries and the integration of multiple components into a single part, which is difficult or sometimes impossible with conventional manufacturing methods [5].

2. Rapid prototyping: Setting up and retooling conventional manufacturing processes can result in longer lead times for product development [6]. AM enables quick and cost-effective prototyping, reducing early development time and costs [7].

3. Reduced material waste: Conventional manufacturing processes generate more material waste compared to AM. It is an inherently more sustainable process as it generates minimal waste compared to subtractive manufacturing [8].

4. Customization: AM allows for easy customization and personalization of products, which is increasingly important in various industries [2].

5. Low tooling costs: There is no need for expensive molds or dies, which is a significant advantage for low-volume production [6].

Current challenges for AM processes:

1. Limited material selection: AM processes are limited by the range of materials available for 3D printing, which may not meet the requirements of all applications [9].

2. Surface finish: AM parts often have a rough surface finish, which may require additional post-processing steps [6].

3. Manufacturing speed: Building complex parts layer by layer can be time-consuming compared to the conventional manufacturing with an established set-up [5].

4. Cost per part: For high-volume production, AM can be more expensive than conventional manufacturing due to longer build times and material costs [10].

5. Quality assurance: Ensuring consistent quality and material properties can be challenging in AM, leading to potential reliability issues [11].

1.2 Metal additive manufacturing processes:

AM processes are typically classified into 5 different categories based on the energy source, feeding material, the method of feeding, and the type of bonding between layers [12]. These are (i) powder bed fusion (PBF), (ii) direct energy deposition (DED), (iii) sheet lamination (SL), (iv) material extrusion and (v) binder jetting/ material jetting, as shown in **Fig 1.2**.

At present, the majority of metal AM parts are produced using powder-based AM technologies. Powder bed fusion (PBF) and powder-feed directed energy deposition (DED) being the two most frequently used AM processes for metal components. As PBF and DED together account for 70 % of the metal AM market in 2019 [13].

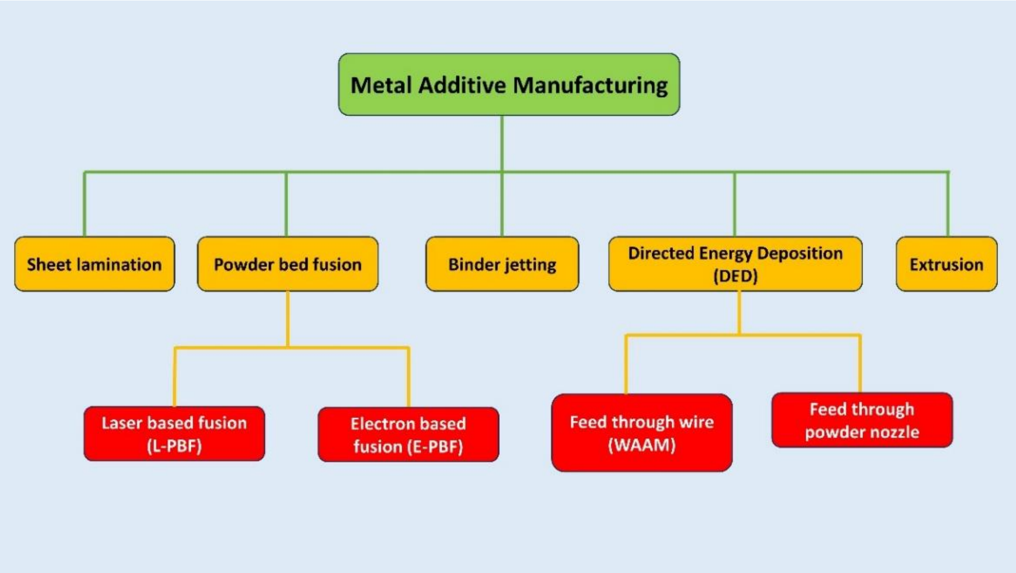

Fig 1.2: Classification of metal additive manufacturing process

Directed energy deposition:

DED create part by melting the feeding material as it is deposited. Both powder-feed and wire-feed DED methods are frequently used for metal AM. Powder-feed DED, also popularly known as laser engineered net shaping (LENS) or laser metal deposition (LMD), is a process that uses a continuous flow of metal powder fed through a nozzle to either create a new part or modify/repair an existing component [12].

Powder bed fusion:

PBF methods are categorized based on the energy source used to melt powder material i.e., laser powder bed fusion (LPBF) and electron beam powder bed fusion (E-PBF). LPBF, is alternatively known as selective laser melting (SLM) and direct metal laser sintering (DMLS) [2,14].

The next section is focused on LPBF systems and processing as in the current study LPBF system has been utilized for printing.

1.3 Laser powder bed fusion (LPBF)

1.3.1 Machine parts and how it works:

A typical LPBF machine is schematically represented in **Fig 1.3**. The build chamber consists of an energy source i.e., laser. The laser could be either of a gas-state (for example carbon dioxide (CO_2)) or a solid-state like Nd:YAG laser. The chamber also has a build platform which is usually pre-heated up to around 200 °C, a powder container, a powder spreader/recoater blade. The build chamber is also protected with a flow of inert gas (Ar, N_2) during processing to prevent oxidation.

The process starts by depositing a thin layer (typically between 20 and 100 µm in thickness) of spherical powder particles (typically from $D_{10} \geq 15$ µm to $D_{90} \leq 100$ µm in diameter) on top of a build plate using a recoating blade or a roller. Subsequently, a high-energy laser beam travels across the powder bed surface at a controlled speed, selectively fusing loose powder particles into a solidified layer according to a specific scanning strategy. Afterwards, the build plate moves downwards equal to the pre-defined layer thickness and the powder chamber moves upwards. The recoater blade spreads the fresh layer of the powder onto the build platform. Again, the laser scans and fuses the powder. Numerous successive layers are stacked on top of each other through a repeated action according to the pre-designed shape to form a 3D object.

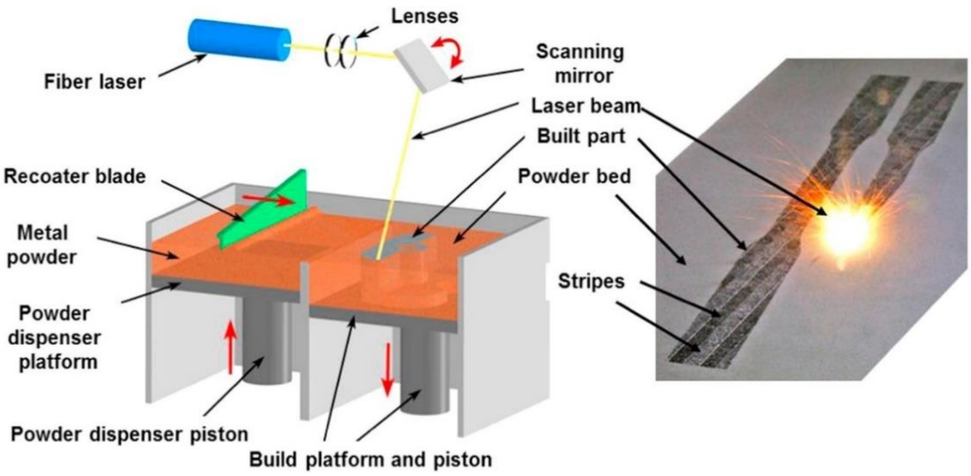

Fig 1.3: Displaying the parts of LPBF systems [15]

1.3.2 LPBF processing parameters:

With a high degree of freedom, there are multiple factors which affect the microstructure and quality of the built part. They can be classified as (i) Laser process parameter, (ii) Powder morphology and size (iii) Substrate material and temperature and (iv) Chamber environment. Additionally, material properties such as chemical composition, laser absorption, thermal conductivity, surface tension and viscosity of the melt.

1.3.2.1 Effect of laser parameter:

There are multiple laser parameters such as laser power, scan speed, hatching distance, layer thickness etc., that have a direct influence on the built quality and microstructure of the material. A schematic is presented highlighting various parameters in **Fig 1.4a**.

(i) Laser type: In general, the interaction between lasers and materials results in the generation of heat. The choice of laser wavelength can vary depending on the specific material being used for printing, as different wavelengths exhibit distinct behaviours when interacting with the material. For example, a shorter wavelength (Yb-fibre laser = 1060-1100 nm) is preferred over longer wavelength (CO_2 laser = 10.6 μm) [16] due to their higher laser absorption in the case of metals [17].

(ii) Laser power: The laser power plays a crucial role in determining the energy applied to melt the powder layer and to establish a effective melt pool. Lowering the laser power could lead to inadequate powder melting or a reduction in the depth of laser penetration, preventing complete fusion of successive layers. Conversely, excessive laser power may cause vaporization, trapping gas bubbles and resulting in porosity in the recently melted powder layers [18].

(iii) Scan speed: It is the speed of the laser spot and plays a crucial role in the LPBF process. It directly impacts the amount of heat available to create the melt pool, ensuring a consistent weld bead [19]. Moreover, the scan speed influences the microstructure, residual stress and porosities of the component by controlling the solidification rate of the metal and laser energy for powder layer penetration [20].

(iv) Scan strategies: Scan strategies refer to the specific way in which a cross-section is scanned. **Fig 1.4b** illustrates the most common scanning patterns employed in LPBF. These scanning patterns can be employed within a single layer and/or across multiple layers. For a single-layer scan, the scanning strategy varies by different scanning directions, sequence, vector rotation angle, vector length, time, and hatch space. Scanning strategy is an important parameter to reduce temperature gradients, distortions, residual stress, porosity [21–23].

(v) Laser beam diameter: The effective laser beam diameter refers to the size of the focused laser beam on the powder bed, typically measured in micrometres (μm). When the laser beam is focused on the powder, it creates a spot that melts the powder, resulting in a larger weld pool than the actual beam spot. This is because the heat conducted to the surrounding particles causes them to melt into the weld pool [3]. Furthermore, the heat conducted to the previous layers also affects them, leading to the formation of a heat affected zone (HAZ) in both the surrounding particles and previous layers. In essence, the diameter of the melted area is what we refer to as the effective laser beam. A smaller effective beam diameter allows for higher precision in printing but may slow down the overall printing process.

(vi) Hatch spacing: It is the distance between two laser tracks (hatches) **(Fig 1.4a)**. Increasing or decreasing the specified value of the hatch spacing between the tracks can lead to particles to either remelt or unmelt, respectively [2].

(vii) Layer thickness: The thickness of the powder layer applied during recoating is determined by the distance covered by the lowered platform after each laser scan [24]**.** This layer thickness is adjusted differently for each alloy, considering factors such as the metal/powder properties, including melting point, thermal conductivity, and reflectivity.

(viii) Laser beam shape: The profile of the laser beam mainly used is of a gaussian shape, but other shapes can also be utilized. Beam shaping affects the energy distribution and melting characteristics, and thus it has considerable effect on microstructure of the printed parts [25,26]. For example, a transverse elliptical beams shape promotes equiaxed grains, while longitudinal elliptical beams favour columnar grains [25].

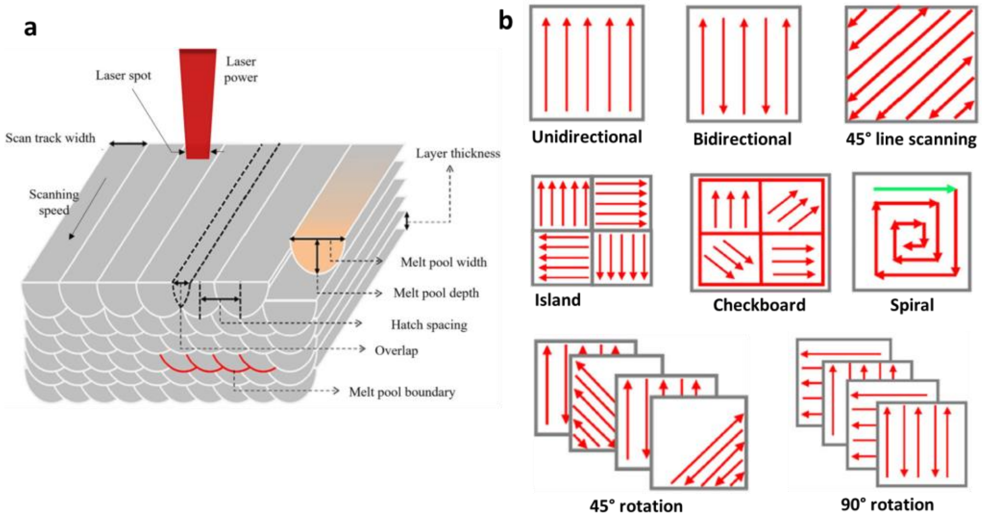

Fig 1.4: Schematic of (a) main processing parameters in an LPBF process [27] and (b) various scan strategies [22]

(ix) Beam offset: To correct the dimensional error caused by the effective laser beam, the actual laser beam is offset by half of its width from the contour to the core. This offset is determined using a calibration block from the boundary edge. Accurate calculations are essential to ensure effective melting and maintain the correct dimensions from the original CAD data [3].

(x) Overlap: Overlap refers to the area affected by repeated melting caused by the laser beam. When a track is melted, the heat generated re-melts a portion of another previously solidified track. This overlap depends on the laser beam diameter and weld pool size. The molten metal flow leads to heat convection, melting surrounding particles, resulting in a larger weld pool than the beam diameter. This process encourages inter-layer binding and reduces porosity. Despite some of the studies finding overlap not significantly affecting mechanical properties, and sufficient energy ensures favourable melting conditions [28,29].

(xi) Volumetric Energy Density (VED): VED is determined by the laser power (P) divided by the product of scan speed (v), hatching distance (h), and layer thickness (t). It represents the energy delivered per unit volume of the powder deposited in the bed.

$$\mathrm{E}_{\mathrm{VED}} = \frac{\mathrm{P}}{\mathrm{vht}} \left[\frac{J}{mm^3}\right] \qquad 1.1$$

This parameter significantly influences various aspects of the 3D printed parts, including their quality, dimensional accuracy, density, and strength [30]. A low energy density results in an inadequate melting of the powders, while a high energy density can lead to vaporization of the powder [31]. Insufficient melting may cause poor fusion between layers, resulting in distortions and layer delamination [32]. However, Prashanth et al. pointed out that, the laser power parameter in the VED, is the most influential parameters on process optimization [33]. VED can be used as a parameter to find process optimization window, but a more refined equation has to be defined that considers other important parameters such as scan strategy, laser spot diameter, its shape and offset, overlay, hatching offset and so on [33,34].

(xii) Chamber atmosphere: Maintaining an inert atmosphere in the build chamber is important in metal AM processes. Metallic particles are susceptible to degradation, and molten metal can be affected by gaseous attacks like oxygen and carbon dioxide, resulting in porosity and inferior part properties. Therefore, parts are typically fabricated in an inert environment to ensure high-quality production [35].

1.3.2.3 Effect of build platform material and temperature:

Ideally, the build platform material should closely match the powder material in terms of chemical composition to avoid the formation of brittle intermetallic compounds or mutual insolubility, which could lead to part detachment during manufacturing [36,37]. Additionally, preheating the build platform to an elevated temperature serves to reduce distortion and residual stresses caused by the abrupt thermal shock experienced by the first layer [38,39]. Moreover, this preheating is known to promote the formation of equiaxed grains, which are more strain-tolerant [40].

1.3.2.4 Effect of powder morphology and size:

The morphology and size of the feedstock powders play a crucial role in LPBF process as they influence powder flowability, laser energy absorption, and the thermal conductivity of the powder bed.

A higher packing density of the powder bed is desirable to reduce the porosities, internal stresses, shape distortion, and surface roughness in the as-built part [6,41,42]. The packing density is influenced significantly by the particle morphology, size, and distribution [42,43]. A wider distribution of particle size can lead to a higher powder bed packing density as the gaps between larger particles can be filled in with smaller particles [44]. A spherical particle morphology enhances powder flowability, leading to a higher packing density in the powder bed [42]. Consequently, gas-atomized powders with spherical shapes are commonly used as feedstock in additive manufacturing processes. On the contrary, non-spherical particle shapes hinders the powder flowability due to mechanical interlocking with each other. Such an obstruction causes non-uniform packing density and can result in defects like porosity and partial melting [42,45].

Apart from the thermal properties of the powder material, the thermal conductivity of a loose powder particles is also influenced by the packing density of the powder bed [46,47]. The higher is the packing density, the higher is the thermal conductivity [46,48]. Finally, the powder layer absorbs the incident laser beam through multiple reflections within the gaps among the particles [49–51], as shown in **Fig 1.5**. As a result, the laser energy absorption by the powder bed is substantially higher compared to a flat surface of solid metal with the same composition [51–53]. Additionally, there is a correlation between laser absorption and particle size distribution [54].

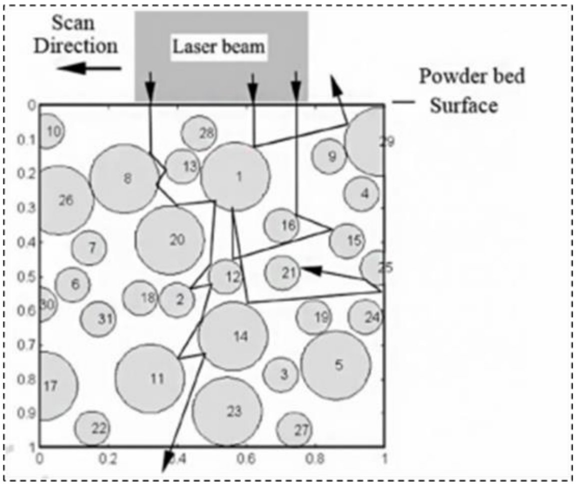

Fig 1.5: A schematic of ray tracing model displaying multiple laser reflection in a powder bed [49].

The optimization of all these processing parameters is desired for the printed parts to achieve the required mechanical properties, surface finish, and dimensional accuracy. Manufacturers and researchers are continuously working on refining these parameters to push the boundaries of what can be achieved with LPBF technology.

1.3.3 Microstructure of the melt pool

The microstructure developed following the solidification of the melt pool is influenced by the thermal gradient (G) and growth rate (R) [9], as illustrated in **Fig 1.6a**. A solidification map depicts G and R in their combined forms of GR and G/R. The G/R ratio dictates the solidification mode, whereas the product GR determines the scale of the solidification microstructure [55]. As G/R values decrease, the solidification microstructures can take on various forms, such as planar, cellular, columnar dendritic, or equiaxed dendritic. Increasing cooling rate GR is associated with a reduction in the dimensions of all four solidification microstructures. During LPBF, the material within the melt track is subjected to the G values in the range of 10^3-10^8 Km^{-1}, and to high R values in the range 0.1-30 ms^{-1} [9]. In conditions of non-equilibrium solidification, materials processed through LPBF typically display cellular or columnar-dendritic microstructures [9]. A schematic of the microstructure development for LPBF-AlSi10Mg is shown in **Fig 1.6b** [56]. The microstructure initiates growth from the border of the melt pool, characterized by a maximum G/R ratio and high temperature gradient, progressing towards the centre of the melt pool. At the melt pool centre, the temperature gradient is lower, and growth occurs along the direction of the maximum temperature gradient, perpendicular to the solidifying surface of the melt pool. The formation of elongated grains with a {100} texture along the building direction is attributed to the preferential [100] growth direction of the α-Al phase in the liquid [56]. This microstructure results in anisotropic behaviour and properties.

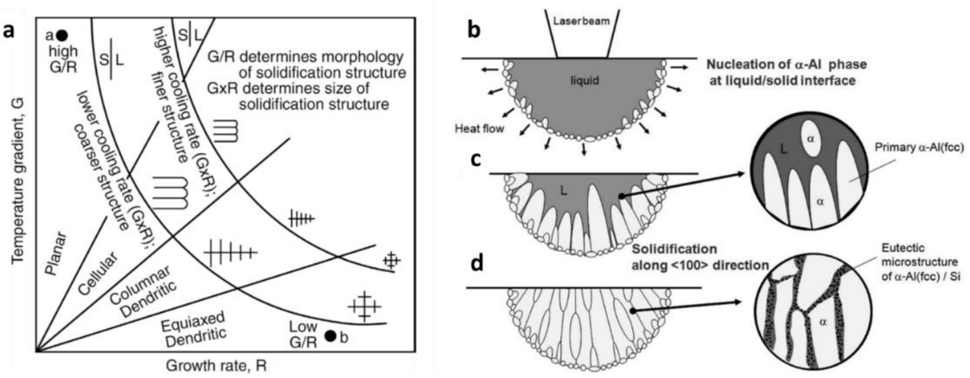

Fig 1.6: (a) Effect of temperature gradient G and growth rate R on the morphology and size of solidification microstructure [9], (b) Illustration depicting the microstructural evolution of AlSi10Mg during LPBF: (a) Initiation of the primary solid phase (α-Al) occurs at the interface between the solid and liquid phases, characterized by a higher temperature gradient. (b) Subsequent growth of primary α-Al grains takes place towards the centre of the melt pool, where elevated temperatures lead to solidification along the preferential <001> direction. (c) During the cooling phase, the material exhibits a composition featuring columnar α-Al grains interspersed with fine eutectic Si particles [56].

1.3.4 Metallurgical defects in LPBF parts:

Defects such as porosity, cracks, residual stresses, and surface irregularities are often produced in an LPBF part. These defects adversely affect the properties and performances of these materials because they reduce the part density and act as stress risers.

1.3.4.1 Porosity:

(i) Gas induced porosity: Gas porosities are formed due to gas entrapment. They are either inherited from a (i) gas-atomized powder during powder production [9,57] or (ii) from the presence of moisture on the powder surface [58]. Gas-entrapped pores are characterized by their spherical shape. These defects are typically on the order of 5 to 20 μm **(Fig 1.7a)** [59].

(ii) Lack of fusion (LOF): The formation of the LOF defects is due to the insufficient or partial melting of the deposited layer on the previous one [9,60]. LOF defects are identified as an irregular, elongated shapes with a size ranging from 50 μm to several millimetres **(Fig 1.7b)** [57]. Increasing the linear energy density and/or reducing the hatching distance have demonstrated to reduce the presence of such defects.

(iii) Keyhole pores: When LPBF processes are operated at very high energy density melting may arise in a keyhole mode [61,62]. Without careful control of keyhole melting mode, keyholes can become unstable and repeatedly form and collapse, leaving voids inside the deposit that consist of entrapped vapor [63]. Keyhole pores vary in shape and range in size from 10 to 50 µm **(Fig 1.7c)** [61].

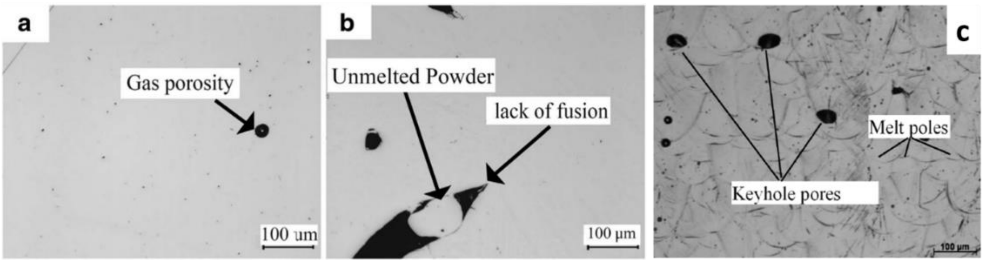

Fig 1.7: Defects observed in LPBF processing: (a) gas induced porosity [64], (b) lack of fusion defects [64], and keyhole porosity [65]

*(iv) Loss of elements (LOE)***:** Higher laser power during LPBF processing triggers the vaporization of specific alloying elements such as Zn, Mg possessing lower melting points. This phenomenon occurs due to their higher equilibrium vapor pressure compared to the matrix element [22,66]. The equilibrium vapor pressures of different alloying elements in relation to temperature are illustrated in **Fig 1.8**. This selective evaporation of volatile elements during laser melting can induce chemical composition alteration and has a detrimental impact on the mechanical properties and solidification process of the alloy. Consequently, it leads to an unstable scan track and the creation of porosity of spherical shape [62,67].

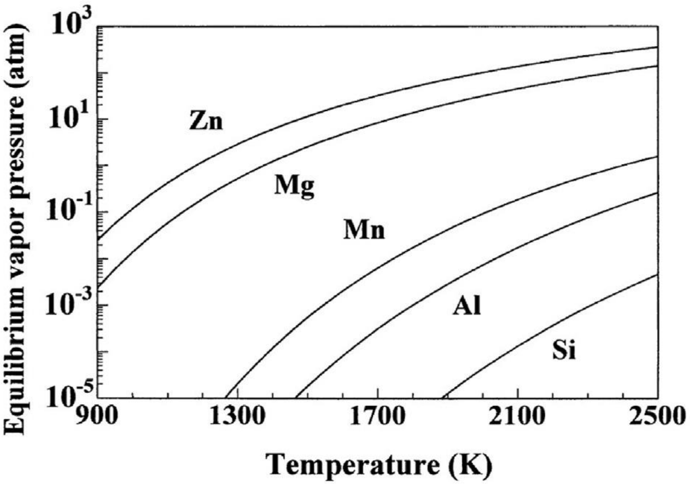

Fig 1.8: Equilibrium vapour pressure of metals at various temperatures [68]

1.3.3.2 Cracks:

In an LPBF process, metal powders undergo rapid melting and rapid solidification under a highly localized laser energy input. The cooling rate of the molten pool reaches 10^8 K/s [9,39], which creates a great temperature gradient and correspondingly a large residual thermal stress causing crack initiation and propagation in the printed part [9,69,70].

There are three main types of cracks observed in the AM parts: (i) Liquation cracking (ii) Solidification cracking, and (iii) Delamination.

(i) Liquation cracking:

Liquation cracking is observed in the mushy zone or partially melted zone (PMZ) of the build [71]. In PMZ rapid heating below the liquidus temperature of the alloy causes melting of certain low melting phases located at the grain-boundaries. **Fig 1.9a** shows the liquation cracking observed in an IN718 alloy due to the presence of low melting lave phases. As the PMZ undergoes cooling, it suffers a tensile force due to the solidification shrinkage and thermal contraction. Under this force, the liquid films around those grain boundary phases tend to act as cracking sites [71,72]. Additionally, alloys exhibiting wide mushy zone, large solidification shrinkage and large thermal contraction are the most susceptible to liquation cracking [72].

(ii) Solidification cracking:

The solidifying deposit tends to contract due to both solidification shrinkage, thermal contraction and coarse columnar grains. However, the substrate or the previously deposited layers are cooler than those of the depositing layer. Thus, the contraction of the depositing layer is more than that of the lower layer and the contraction of the solidifying layer is thus hindered by the substrate or the previously deposited layer. That results in the generation of a tensile stress at the solidifying layer. If the magnitude of this tensile stress exceeds the strength of the solidifying metal, cracking may be observed along grain boundaries of columnar grains **(Fig 1.9b)** [9,72].

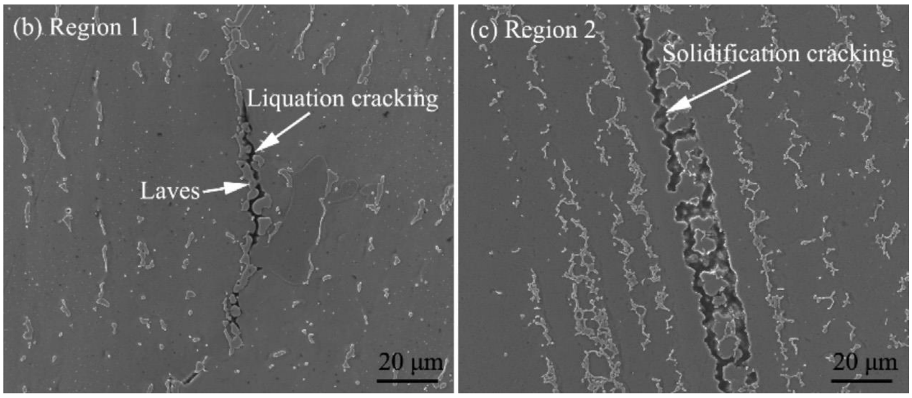

Fig 1.9: Hot cracking in an IN718 processed by laser additive manufacturing (a) Liquation cracking by (b) Solidification cracking [73]

(iii) Delamination:

Delamination is a macroscopic crack that occurs parallel to the build plate [9], as shown in **Fig 1.10**. It is the separation of adjacent layers, especially near the edges of the part. The susceptibility to delamination has been associated with the ratio of residual stress to the yield strength [38,69]. Although, other processing defect such as lack of fusion has been also reported to cause delamination [74].

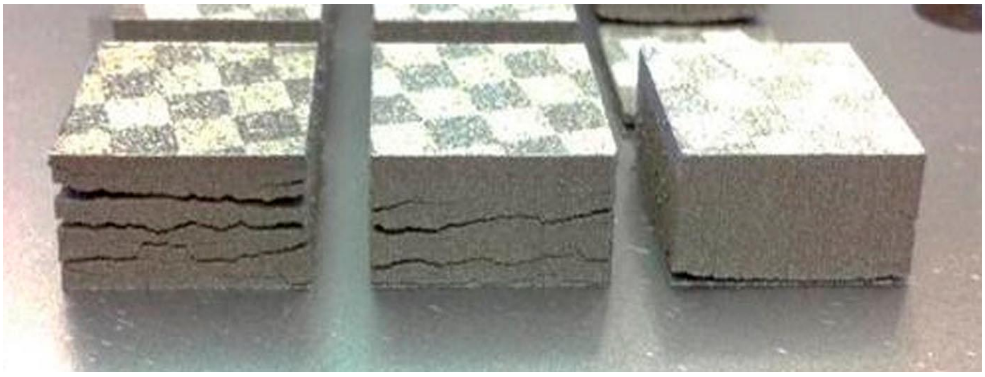

Fig 1.10: Layer delamination and cracking in M2 tool steel [69].

1.3.3.3 Residual stresses and distortion:

Residual stresses are common in metal AM parts due to (i) large thermal gradients caused by localized heating and cooling (ii) thermal expansion and contraction of material due to repeated thermal cycles and (iii) strain compatibility [9,75]. Complex geometries and overlapping passes also lead to the non-uniform accumulation of residual stresses [76,77]. The presence of residual stresses can result in the deformation of components, deviations from intended geometrical specifications, and the separation of deposited layers (delamination). Furthermore, these stresses can lead to a decline in the mechanical properties of the manufactured parts [78,79].

Gaining a quantitative comprehension of the progression of thermal stresses during LPBF process is imperative to both understand and subsequently address or mitigate the mentioned concerns. Various methodologies have been employed to quantify residual stress in AM parts [2,7,38]. The magnitude of residual stress and the strategies for its mitigation are influenced by the specific manufacturing process being employed.

1.3.3.4 Surface irregularities:

(i) Balling:

In some cases the solidified material can rise above the plane of powder distribution and melting [31]. This phenomenon is a result of surface tension effects linked to the geometry of the molten pool. At high laser scanning speeds, the molten pool stretches, potentially breaking into smaller segments due to Raleigh instability [6,80]. This occurrence is commonly termed the "*balling phenomenon*" [81]. It contributes to the roughness and porosity of the finished component [9]. Utilizing high laser power and lower scanning speeds generates substantial heat input, ensuring a sufficient remelting of the previous layers subsequently reducing the balling phenomenon **(Fig 1.11)** [82].

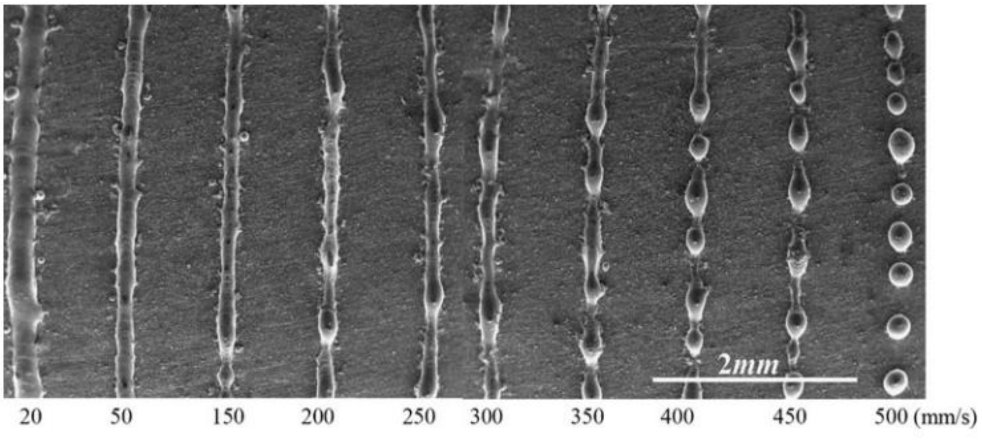

Fig 1.11: SEM micrograph of single scan tracks displaying balling phenomena at different scan speed values [83]

(ii) Spattering:

When the laser beam interacts with the powder particles, the energy absorbed can cause some particles to rapidly heat up and potentially vaporize or melt. This can lead to a sudden increase in internal pressure within the powder bed. If this pressure exceeds the cohesive forces holding the particles together, some particles as well as molten material can be propelled outward from the bed resulting in spatter formation [9,31,84]. Spattering direction is varied based on the laser power and scanning speed employed [85], as shown in **Fig 1.12**. These ejected particles can then land on the surrounding surfaces, including previously solidified layers, resulting in potential defects and surface irregularities. Since laser beam parameters are mainly responsible for the generation of spatters, it has been suggested to decrease the laser power density or to use laser beam shaping such as top-hat beam profile [86]. Other parameters such as gas flow, dynamics of the melt pool and powder material also affects the spattering [87–89].

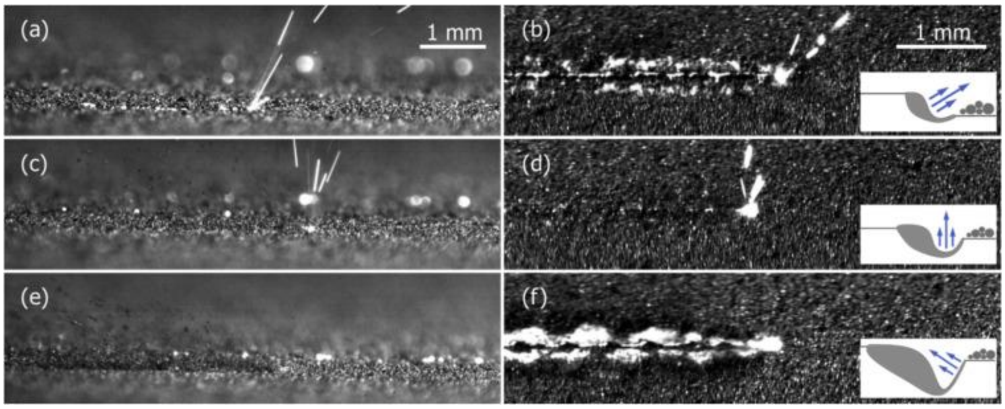

Fig 1.12: Powder spattering seen through high-speed images of side (Left) and top (Right) views as a function of laser power and scan speed: (a) and (b) 50 W and 0.1 m/s; (c) and (d) 100 W and 0.5 m/s and (e) and (f) 200 W and 1 m/s. *Inset is a schematic of the melt pool shape, which determines the laser plume direction* [85].

1.3.4 Defects characterization and analysis:

1.3.4.1 Porosity and crack detection:

Measuring porosity of LPBF parts is essential, and there exists a diverse range of techniques for this purpose. Among these, the *Archimedes method* is widely favoured within the additive manufacturing community. Another popular approach involves dissecting the sample, utilizing *optical microscopy*, and employing image analysis techniques. Emerging technique involves utilizing laboratory *X-ray tomography*, which uses 3D data to perform a similar image analysis as seen in 2D optical microscopy. However, the 3D data goes beyond and includes intricate 3D distribution details and information about pore structure. Among these techniques, only X-ray tomography enables the identification and quantification of both open and closed porosity i.e., to be able to differentiate between internal pores that are connected to the surface pores thorough narrow channels.

(i) Archimedes method

This method is extensively employed, offering notable speed and cost-efficiency despite its inherent limitations. It relies on a precise scale and involves measuring the mass of the component in both air and a fluid, usually water, although acetone is occasionally utilized as well **(Fig 1.13a)**. The ensuing equation is applied for this purpose:

$$\rho_p = \frac{m_a}{m_a - m_{fl}} \rho_{fl} \qquad 1.2$$

where m_a is the mass in air, m_{fl} is the mass in fluid, ρ_p is the density of the part, ρ_{fl} is the

density of the fluid. The relative density can be obtained by subtracting from the theoretical density. The method's drawbacks encompass assumptions regarding the material's reference density, which result in challenges when measuring minute porosity levels. Furthermore, the fluid can infiltrate open cavities, causing density readings to appear artificially elevated ("false high"). Additionally, there's the potential for air bubbles to adhere to uneven surfaces, potentially influencing mass measurements within the fluid [90].

(ii) Cross-sectioning and Optical microscopy:

This is widely utilized method due to its relatively uncomplicated nature in assessing porosity. The practice of sectioning, refining through polishing, and applying etching techniques to components is already extensively utilized for microstructural analysis **(Fig 1.13b)**, which naturally extends to porosity assessment. Nevertheless, the precision of quantitative evaluation might depend on the chosen magnification and the specific procedures employed for image analysis, such as optimizing threshold algorithm used in micrograph analysis [91]. The cost and time investments are also often underestimated as the entire process is labour-intensive.

A drawback of this approach is that the microstructural area of interest doesn't accurately represent the entire fabricated component. Nevertheless, micrographic analysis excels in identifying pores of various sizes, shapes, and locations, which other methods like the Archimedes' principle cannot achieve. This advantage facilitates accurate assessments during material qualification, as its correlation with processing parameters enables opportunities for parameter optimization [92]. It was further emphasised by Aboulkhair et al. [39] that the limitation of the cross-sectioning and microscopy method becomes more pronounced in samples with low pore fractions.

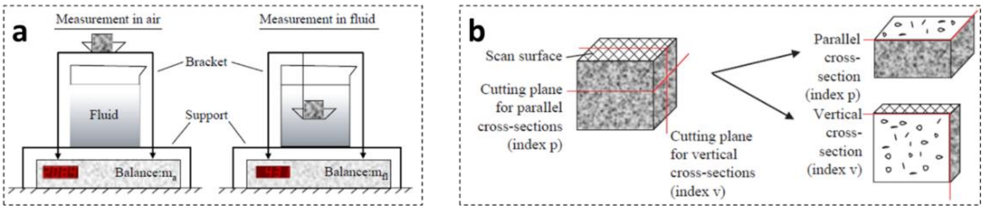

Fig 1.13: (a) Density measurement by Archimedes method, and (b) Printed sample cross-sectioning along vertical and parallel direction for optical microscopy [90]

(iii) X-ray computed tomography:

X-ray computed tomography (X-CT) is a powerful technique, but not as widely used as other methods. Its advantages are its ability to visualize 3D distributions of pores, pore morphologies, and also quantification using prescribed image analysis [93,94]. While the limitations being high cost and maximum size of the sample. The key benefit of X-CT is the ability to easily identify pores or cracks in any part of the sample.

In an X-CT scan, a sequence of X-ray projection images is captured while an object is rotated between an X-ray source and a detector **(Fig 1.14A-D)**. These projection images, taken from different angles, are then employed to reconstruct a three-dimensional depiction of the object. This reconstruction is based on the material's or phase's linear absorption coefficient, and it employs a back-projection algorithm. The resulting 3D representation consists of a collection of cross-sectional slices, where each pixel corresponds to the X-ray density of the corresponding part of the object. Brighter pixels indicate denser regions while pore spaces appear darker. The 3D porosity visualization of the part is shown in **Fig 1.14D** and **Fig 1.14E**.

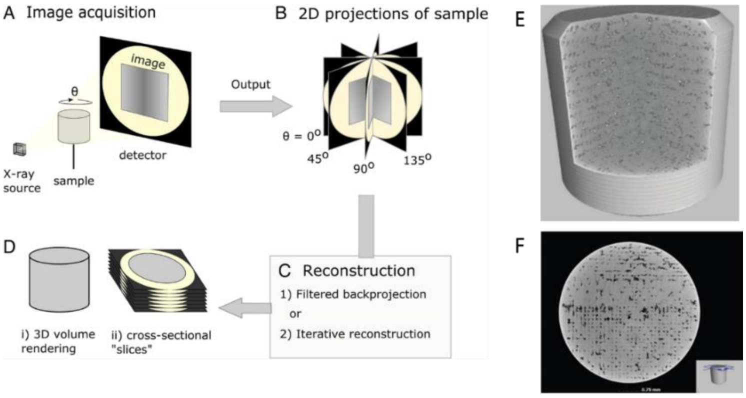

Fig 1.14: (A-D) Workflow of the X-ray computed tomography (A) fundamental depiction of a tomographic setup, encompassing the X-ray source, detector, and the specimen. Projection images are generated by incrementally rotating the specimen through angles denoted as θ. (B) 2D sample projections captured at varying angles, (C) 2D projections are digitally reconstructed (D) 3D rendered volume and 2D cross-sectional slices. (E) Porosity visualization from a 3D constructed data and (F) CT slice image showing porosities [94,95].

1.3.4.2 Residual stress measurement

The effective control of residual stress and qualification of the manufacturing process

for various applications depend on accurate measurement of the residual stresses. Evaluation of residual stress is done by means of measuring strain employing a variety of methods and using the measured strain to calculate stress based on variations of Hooke’s laws.

There are number of methods mentioned in the literature to measure residual stress of an LPBF part. They can be classified as destructive and non-destructive. Methods such as micro-hardness, hole drilling method , contour method, curvature method, and digital image correlation [96–100] are categorized as destructive methods. These methods require measuring residual stress by inducing stress relaxation followed by strain or deflection measurements [101]. Non-destructive methods include *neutron* and *X-ray diffraction*. Both diffraction methods basically make use of the inter-atomic *d*-spacing. The *d*-spacing is then calculated from employing Bragg’s law of constructive interference according to:

$$n\lambda = 2d \sin\theta \qquad 1.3$$

where *n* and λ represent the diffraction order and wavelength of the neutron/x-ray radiation, respectively, and d is the lattice spacing. Due to the high penetration power of neutrons, neutron diffraction can measure volumetric residual stress in thick specimens. Unfortunately, neutron diffraction is expensive, time consuming and facilities are very limited. Thus, XRD becomes a more feasible option, except that X-rays have less penetrating power than neutrons. A detailed overview of each method has been well described by Yadroitsev et al. [2].

1.3.5 Strategies to mitigate defects:

Defect suppression is challenging. Presently, the main strategy to suppress defect formation in LPBF is to implement optimal adjustment of process parameters that can eliminate the formation of porosities, cracks, surface irregularities and residual stresses. It is important to note that, there is no standard LPBF processing parameter applicable to the various processing materials as they interact differently with laser. Thus, specific strategies have to be employed for specific defects.

1.3.5.1 In-process parameters optimization:

The effect of process parameters, such as laser power, layer thickness, scanning speed, and hatch distance has been described to mitigate defects.

(i) Laser power and scanning speed: Fine-tuning laser parameters such as power and scan speed can significantly influence the melt pool dynamics and heat distribution. Optimizing these parameters can help control solidification and reduce defects.

A combination of high laser power and low scan speed is generally able to reduce the lack of fusion defects in most of the alloys [102,103]. Whereas a combination of low power and high scan speed can help achieve faster solidification and reduce thermal gradients, mitigating defects like surface roughness and keyhole porosity [104,105].

(ii) Scanning Strategies: Employing optimized scanning paths, like bidirectional scanning or island scanning or 67° rotation between layers, can enhance energy distribution, minimize thermal gradients, and mitigate defects like balling and lack of fusion residual stress [106,107].

(iii) Hatching distance / Overlapping: Adjusting the overlap between adjacent scan lines can impact energy distribution and reduce defects such as keyhole porosities and lack of fusion [108].

(iv) Substrate preheating: Applying a preheating step before the main melting process can reduce thermal gradients and enhance powder fusion, thereby minimizing cracks and pores [98,109].

1.3.5.2 Post processing:

(i) Heat treatment:

Residual stresses are by default present in LPBF parts. It is a common practice to perform post-processing stress-relief heat treatments to relieve stresses. Typically, this heat treatment is carried out prior to separating parts from the base plate to prevent any potential distortion during the detachment process [43,110]. Stress relief encompasses a process known as “recovery”, wherein atomic diffusion becomes more pronounced at higher temperatures. In this phenomenon, atoms situated in areas of elevated stress can migrate towards zones of lower stress, ultimately leading to the alleviation of internal strain energy. Stress relief procedures necessitate the application of temperatures sufficiently elevated to enable atomic movement, while concurrently maintaining brief durations to curb the occurrence of grain growth – a phenomenon typically linked to strength reduction [31]. It has been observed that around 70-90% of residual stress can be relieved with an appropriate heat treatment [111–113]. Despite the widespread use of stress-relief heat treatments, the process does not necessarily remove residual stress completely. Salmi et al. [114] revealed that, the presence of high tensile stresses on stress-relieved LPBF AlSi10Mg alloy, . In certain cases, occurring of recrystallization was also noticed during annealing [96,115]. It was theorised that thermal residual stress acts as the driving force for observed recrystallization phenomena [31,96]. Recrystallization could be desirable to promote equiaxed grains from columnar microstructure [31].

(ii) Hot isostatic pressing (HIP):

HIP can be used to close internal pores and cracks in metal LPBF parts [116,117]. Internal pores are closed pores, that are surrounded by material in the centre of the sample. During the HIP process, a high-isostatic-pressure is applied onto the build part using gas (typically Ar). The pressure usually ranges from 100-200 MPa, although it depends on the yield strength of the material. The temperature is such, that it is below the solidus but higher enough to allow plastic flow by the mobility of atoms/vacancy to heal the porosity [118,119]. A typical schematic of HIP set-up is shown in **Fig 1.15a** and XCT images of parts post-processed by HIP in **Fig 1.15b**. Initially, a pore diminishes in size due to plastic flow, followed by diffusional mechanisms. Four primary mechanisms are responsible for pore elimination through HIP: plastic flow, power-law creep, Coble (grain boundary) creep, and Nabarro–Herring (lattice) creep. To summarize, all these mechanisms ultimately result in a densified component. However, the pace at which pores are eradicated varies based on the chosen mechanism [118,119].

HIP is less efficient in the closure of open pores which are present near the surface [31]. Thus, sometimes could be paired with mechanical surface treatments such as shot peeing [114,120,121]. Shot peening is the process of impacting the surface with high-speed by balls of metals, ceramic or glass beads, to plastically deform the impacted surface. Shot peeing was shown to be effective in the closure of near surface pores.

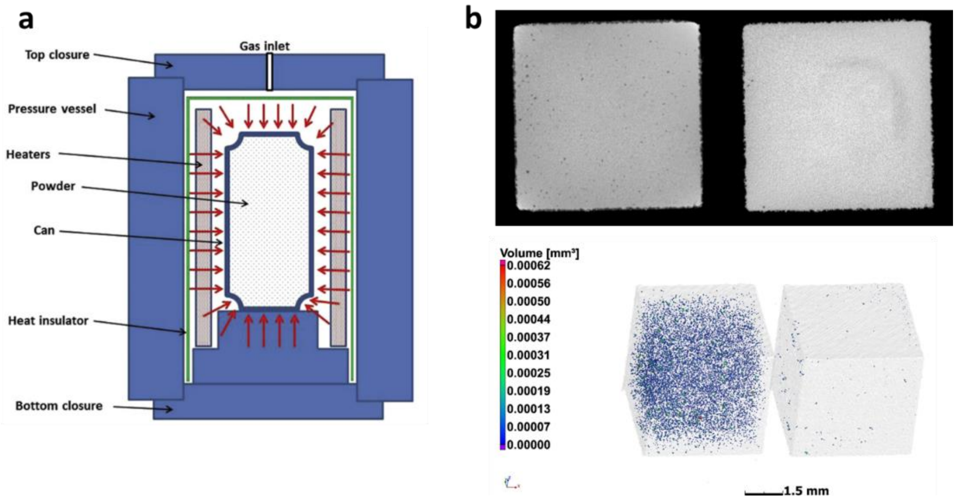

Fig 1.15: (a) A schematic of a HIP process [122], (b) cross sectional slice image: left (before HIP), right (after HIP), and below their corresponding 3D view displaying closure of lack of fusion pores after HIP except a small number near the surface [117]

Chapter-2

Processing of high-strength Al alloys by LPBF

2.1 Introduction to high strength Al alloys:

High-strength Al alloys are extensively employed in creating structural elements for the aerospace and automotive sectors due to their remarkable strength-to-weight and stiffness-to-weight ratios, coupled with favourable machinability traits [123,124]. The intricate shapes often linked with aerospace parts present challenges in traditional manufacturing methods. Additionally, the LPBF technique has the capability to construct such intricate components by part consolidation, leading to reduced individual parts in an aircraft or automotive assemblies [125]. This reduction subsequently lowers material costs, waste, and the risk of part failures, while enhancing part performance [126,127]. Therefore, LPBF processes are especially well-suited for this domain.

The high-strength Al alloys that achieve their strength by heat treatment or in temper conditions are 2xxx (Al-Cu), 6xxx (Al-Mg-Si) and 7xxx (Al-Zn-Mg) series [123,126,128]. [129]. Designations of various temper conditions is presented in **Table 2.1**. Classification of Al alloys based on the type of alloying elements is presented in **Table 2.2**.

Table 2.1: Temper designation for the heat treatment

Temper	**Designation**
T1	Subjected to natural aging after being cooled from a high temperature shaping process
T2	Cooled from a high temperature shaping process, cold worked, and naturally aged
T3	Solution heat treated, cold worked, and then naturally aged
T4	Solution heat treated followed by naturally aged
T5	Cooled from a high temperature shaping process, followed by artificial aging
T6	Solution heat treated and then artificially aged till peak aged
T7	Solution heat treated, followed by artificially aged till overaged
T8	Solution heat treated, cold worked, and then artificially aged
T9	Solution heat treated, artificially aged, and then cold worked
T10	Cooled from an high temperature shaping process, artificially aged, and then cold worked

Table 2.2: Classification of Al alloys

Type	**Alloy system**	**Strengthening phases**	**Properties**	**Application**
1xxx	Al	-	Low strength, good corrosion resistance, conductivity, and weldability	Food packaging trays, decorated foil for drinks and foods [130]
2xxx	Al-Cu	θ’-Al_2Cu Ω-Al_2Cu S’-Al_2CuMg	High strength, good heat resistance, poor weldability and corrosion resistance	Automobile wheels, aircraft parts, laboratory instrument [131]
3xxx	Al-Mn	-	Good weldability, and machinability and formability	Anti-rust, pressure vessels, heat-exchangers and, beverage cans [132,133]
4xxx	Al-Si	-	Good corrosion and wear resistance, good weldability	As filler material [134]
5xxx	Al-Mg	-	Excellent corrosion resistance, medium to high wear resistance, good weldability	Suitable for marine application, aircraft hydraulic tubes, various sheet metal works and armor plate [135,136]
6xxx	Al-Mg-Si	β' - Mg_2Si	Medium strength, good corrosion resistance, good machinability and weldability	Railroad cars, truck components, pipelines, storage tanks and space vehicle [137,138]
7xxx	Al-Mg-Zn	η’ - $MgZn_2$	High strength, good fatigue and corrosion resistance, poor weldability	Aircraft wings, automobile gear components, cycle parts [132,139]
8xxx	Al-Fe/Al-Li/Al-Sn	-	-	Depending on the elemens

2.2 Processing challenges by LPBF:

LPBF processing of high strength Al alloys possess several unique challenges. These challenges primarily stem from the properties of the powder material, encompassing factors like the stability of the oxide layer, inadequate flow behaviour, remarkable reflectivity, hot cracking sensitivity and elevated thermal conductivity.

2.2.1 Oxidation:

The inherent properties of Al alloys lead to the formation of a stable and adherent surface oxide layer, predominantly constituted by the ubiquitous sesquioxide (Al_2O_3), which covers the entire Al surface. This oxide thermodynamic stability and passivating properties hinder the successful production of dense high quality parts [126,129]. In LPBF process, oxide inclusion can mainly come from two sources: (i) from the partial oxidation of the powder feedstock and (ii) due to the gas entrapment by the surface turbulent of the melt pool [63]. Oxides can form even in an inert atmosphere with the oxygen content in the build chamber of 0.1-0.2% [140]. The formation of Al_2O_3 during LPBF of Al alloys impedes the fusion of powder particles, diminishes the metallurgical bonding between solidified layers and scanning paths, exacerbates the balling phenomenon, and diminishes the part densification [86]. The presence of oxide inclusions frequently initiates cracks, leading to decreased fatigue resistance and mechanical properties of the components [141,142].

The oxidation mechanism and oxide film morphology of an LPBF AA6061 as shown in **Fig 2.1** was revealed by Louvis et al. [143]. The authors suggested that oxide films form to surround the molten pool covering all the sides **(Fig 2.1A)**. The upper-surface oxide films undergo evaporation, giving rise to fumes that disperse from the molten pool beneath the laser beam. Conversely, the oxide films on the lower side of the molten pool experience fragmentation due to the stirring effects caused by Marangoni flow **(Fig 2.1B)**. These phenomena create an oxide network that was observed after deep corrosion of the sample in NaOH solution **(Fig 2.1C)**. The presence of oxide films reduces the wettability of the melt with the previous layer or substrate. The areas where adjacent tracks overlap give rise to enclosed or partially enclosed pores, within which certain melted or un-melted powder particles become entrapped. Fragmented oxide particles, may act as a microcracks and are detrimental to the mechanical properties of the printed part [144].

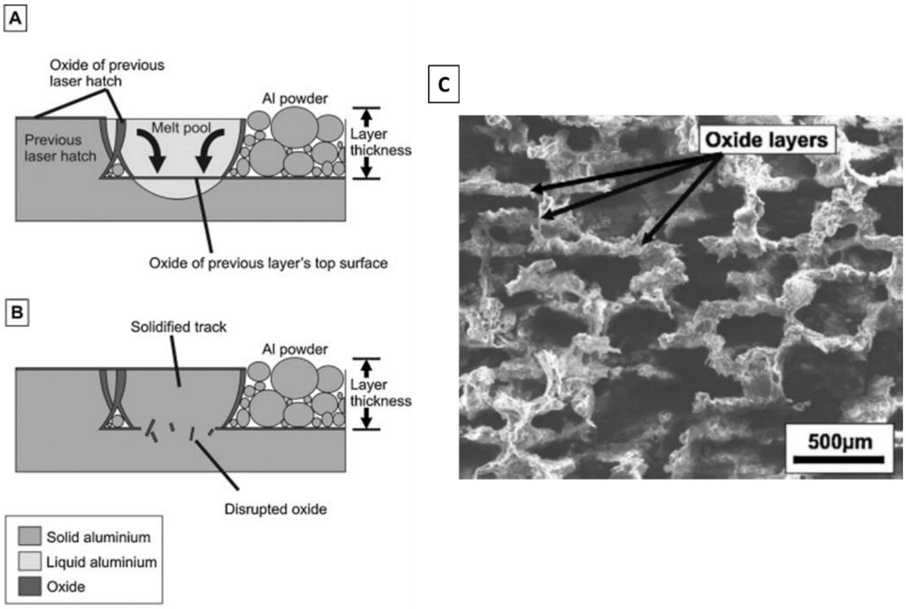

Fig 2.1: (A) Marangoni convection in the melt pool, (B) Oxide disruption during solidification and (C) Oxide network revealed after etched with NaOH an LPBF-6061 alloy [143].

To reduce the oxidation of Al alloy in LPBF process, the partial pressure of the oxygen should be sufficiently low. For this purpose, oxygen analysers should be helpful to monitor the level of oxygen in a building chamber [145]. Kempen et al. [146] were able to achieve almost 100% density by introducing argon during processing. Furthermore, to reduce oxidation, Al alloy powder feedstock must be dried before loading into the LPBF machine [58]. Li et al. performed powder drying at 100 °C for 60 min immediately before processing and were able to enhance the density of the part [147].

2.2.2 Poor flowability

Al powders generally have poor flowability which can hinder the deposition of a thin layer of powder that is essential in LPBF process [144,148].

The inadequate flow of Al powder is linked to two attributes: (i) its non-spherical shape and (ii) its low density. When Al undergoes atomization, the emergence of oxide islands on the powder surface serves as anchor points, restraining the surface tension forces that are striving to shape the molten particle into a sphere [149]. Consequently, Al powders often adopts a non-spherical structure, even when atomized within a protective atmosphere. **Fig 2.2** presents a comparison between the morphology of Al–12Si and Ti–6Al–4V powders. The visual representation in this figure distinctly illustrates that the shape of Al powder is less spherical when compared to Ti–6Al–4V powder [144]. This non-spherical characteristic of Al powder significantly influences its flowability properties. The low density of Al particles also contributes to their poor flowability, due to dominating interparticle cohesion by the Van der Waals forces over powder particle weight [150].

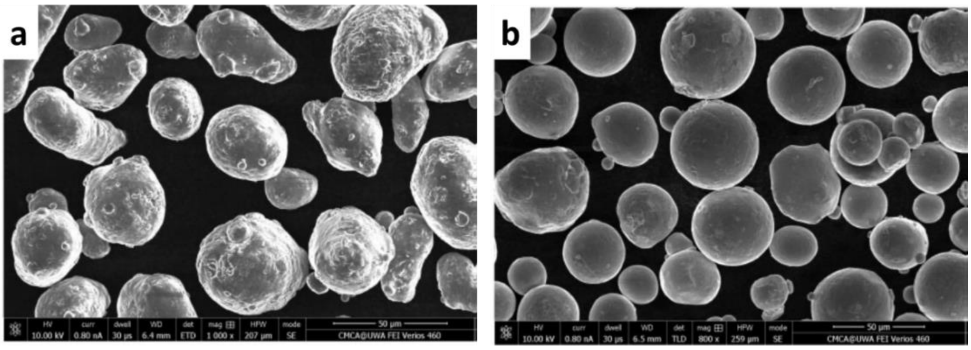

Fig 2.2: SEM micrograph of atomized powder particles (a) Al–12Si and (b) Ti–6Al–4V

2.2.3 High laser reflectivity:

Aluminium and its alloys are highly reflective to the infrared laser **(Fig 2.3)**, having a typical wavelength of 1060 µm. Al flat surfaces absorb only 7% of the incident laser energy [151]. However, the actual Al powder absorption is higher due to multiple absorption and reflection events in the powder bed [152], see **Fig 1.5**.

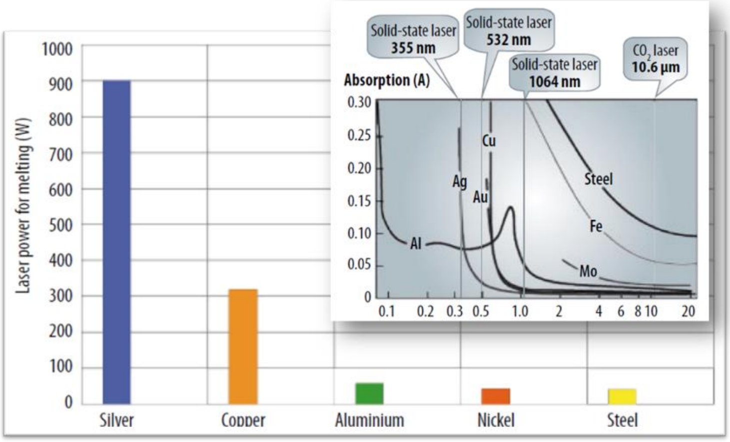

Fig 2.3: The minimum laser power required for melting various metals using a pulsed Nd:YAG laser, *inset: absorptivity of common metals over spectrum of wavelengths* [153].

Such a low absorptivity of the laser energy causes insufficient melting of the powder particles resulting in lack of fusion defects and poor surface quality [70].

To overcome these issues, Al alloys are usually processed with high laser power[154,155]. Furthermore, there is a substantial difference in absorptivity between the already deposited layer and the adjacent powder. Consequently, the utilization of overlapping scan tracks is prone to generate temperature gradients, potentially culminating in balling phenomenon [144].

Interestingly, Si has a very high absorptivity of around 70%, and this could be one of the factors for the success of Al-Si based alloys [151]. Developing new Al alloys for improved laser absorptivity is ongoing research. One of the strategies reported is by loading or coating of high absorptivity materials/phases on the Al powder surface, such as Co [156], Ni [157], carbon nanomaterials [158] etc.

2.2.4 High thermal conductivity:

Al alloys, have a high thermal conductivity [144,159] (~ 113 W/mK) [132].

Because of this reason they tend to rapidly dissipate the heat away from the melt pool. As a result, the molten metal can quickly solidify and cool, leading to insufficient fusion between successive layers or insufficient bonding between the deposited material and the existing build. The consequence of this are as follows [144]:

(i) A higher amount of laser energy is necessary compared to materials having lower thermal conductivity.

(ii) There was larger difference between the thermal conductivities of the solid and powder, potentially leading to density variations.

(iii) The width of the molten path expands considerably compared to metals with low conductivity due to outward heat conduction, causing the adjacent powder to melt.

This can result in poor mechanical properties and reduced part integrity.

2.2.5 Cracking

The most severe issue faced in LPBF processing of high strength Al alloys is related to their high tendency to cracking [70,126], see **Fig 2.4**. The presence of pores and the thermal stress encountered during solidification additionally promote the formation and propagation of cracks [160]. In the L-PBF process for Al alloys, the occurrence of cracking can be classified into two types: liquation cracking and solidification cracking [161]. Such a cracking tendency was also a characteristic of high strength alloy of different material processed by LPBF (see Chapter-1).

(i) Liquation cracking:

The liquation cracking phenomenon, which was previously described in Chapter-1, often occurs in high strength Al alloys due to the localized melting of certain phases having a lower melting temperature with respect to the matrix. Low melting phases are usually located at the grain boundaries as particles or as a high degree of solute segregation which tends to melt and acts as a site for decohesion [162]. For example, Kumar et al. found that Cu tends to segregate strongly at the grain boundaries in AA2024 alloy processed by LPBF and promotes liquation cracking [163]. The tendency of liquation cracking is associated to the high concentration of alloying elements and high thermal conductivity, thus high strength Al alloys are the potential candidates to experience such cracking. Liquation cracking can be mitigated by minimizing the dissipated energy density on the powder bed or substrate [126].

(ii) Solidification cracking:

Solidification cracking occurs in the last stage of solidification, when an inadequate liquid flow exists to bridge the gaps between the interdendritic regions. [70,126]. Numerous solidification cracks were overserved by in the LPBF high strength Al alloys due to their wide solidification range ($\Delta T = T_{Liquidus} - T_{Solidus}$), exposure of rapid cooling [164]. The formation of solidification cracks in the matrix is typically influenced by three primary factors: (i) solidification shrinkage, (ii) thermal stress, and (iii) the generation of a substantial quantity of coarse columnar grains.

Solidification shrinkage is an inherent property of Al alloys that is tied to their solidification temperature range. Different Al alloys exhibit distinct solidification temperature ranges. For instance, AlSi10Mg has a solidification range of 36°C, whereas AA2024, AA2195, and AA7075 have ranges of 120°C [163], 144°C, and 175°C [165], respectively. A broad solidification range leads to the formation of elongated intergranular liquid channels, depicted in **Fig 2.4c**. If the solidifying time of the melt pool is not enough or the liquid fluidity is poor, solidification cracks can occur easily. This indicates the potential for controlling the solidification process by adjusting the alloy's chemical composition, thus mitigating the solidification shrinkage effect [166].

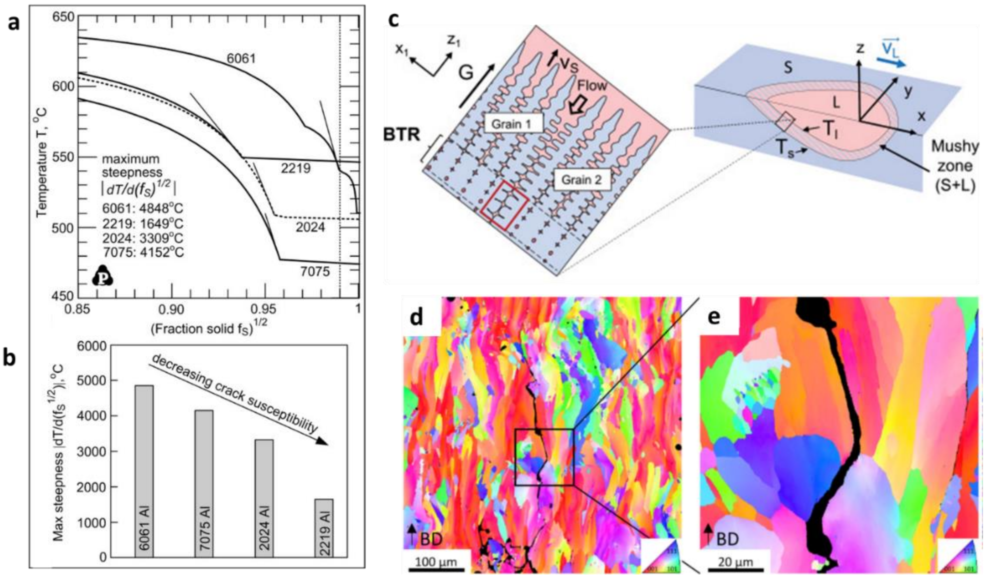

Fig 2.4: (a) Crack susceptibility of high strength Al alloys by Temperature vs. solid fraction curve showing maximum steepness; (**b**) maximum steepness in for various alloys [167]. (c) Solidification cracking mechanism [168], T_l and T_s are liquidus temperature and solidus temperature, respectively. v_s is liquidus isotherm velocity. (d) EBSD-IPF map of the LPBF-2024 alloy showing solidification cracks and (e) a higher magnification of the cracked region [169].

Due to the complex thermal history i.e., repeated rapid heating, cooling and remelting/solidification of a deposited layer in the LPBF process, *high residual stresses* are generated [170]. High residual stress support the formation of cracks and eventually lead to failure of the part [171]. Strategies such as preheating the substrate or by using substrate with low thermal conductivity can be helpful to reduce the thermal stress [172]. The extensive development of *coarse columnar grains* in the LPBF process stands as a paramount contributor to the solidification cracking. These columnar grains grows epitaxially along the thermal gradient, which in turn leads to the creation of lengthy viscous liquid channels [173], see **Fig 2.4c**.

During the final stages of solidification (solid fraction, f_s=0.7- 0.98), the mobility of the viscous liquid is further limited by the inter-dendritic arms [174]. Under the combined action of rapid drop in temperature and solidification shrinkage, the solidification cracking occurs when the tensile stress generated in the adjacent columnar grains exceeds the ultimate tensile strength at a point [175][70][176]. Soysal et al. [167] characterize the cracking susceptibility of common high strength Al alloys by the steepness of the solidification temperature (T) vs solidified fraction (f_s) curve i.e. dT/d$(f_s)^{1/2}$. Higher the steepness indicates higher susceptibility to cracking, see **Fig 2.4a** and **Fig 2.4b**. This indicates that, the solidification cracking is arising due to the insufficient liquid backfill **(Fig 2.4c**). Among the studied Al alloys, 6061 possess highest susceptibility to cracking, followed by 7075 and 2024 alloy. These cracks could extend in the length of 10-100 um [177] as shown in **Fig 2.4d** and **Fig 2.4e**.

Microstructures with the fine and equiaxed grains are more strain tolerant and have shown to significantly reduce the solidification cracking tendency. [173][40][174].

2.3 Role of ceramic addition to improve printability:

2.3.1 Improved absorptivity:

In the previous section it was mentioned that Al alloys have low infrared laser absorption, resulting in various defects such as lack of fusion, poor geometrical accuracy, high surface roughness and low mechanical properties of the part. In order to reduce this effect, it is a promising approach to incorporate materials such as ceramics having high laser absorption rate into Al based powder or onto the powder surface [169,178–189].

For example, Li et al., incorporated nano-TiB_2 particles (11.6 wt.%) in an AlSi10Mg alloy by an in-situ process [185]. The laser absorption of the composite was improved by 50% compared to the AlSi10Mg alloy and the LPBF processibility improved **(Fig 2.5a)**. This resulted in a crack-free and fully dense build parts. A similar effect was noticed using nano-TiN particles on an Al alloy powder surface [182,184], see **Fig 2.5b**. Gao et al. [184] mixed nano-TiN powder particles (2.5 wt.%) with AlSi10Mg alloy, which reduced the laser reflectivity of AlSi10Mg alloy from 62% to 25%.

The influence of type of ceramic reinforcement (SiC/ TiB_2) on AlSi10Mg was investigated by Gu et al. [187]. The laser absorptivity improved to 59% and 44% for both SiC/AlSi10Mg and TiB_2/AlSi10Mg, respectively.

There are also few studies on the usage of multiple ceramic reinforcement into Al alloy powder [178,188]. Cheng et al. for example, incorporated 1.5 wt% of both TiC and TiB_2 by ball milling on AlSi10Mg to reduce the laser reflectivity of the composite powder and obtained 52% reduction [178] **(Fig 2.5c)**. This was due to the low reflectivity of both TiB_2 (13.9%) and TiC (10.2%) particles. It was observed that, the laser absorptivity increase is also due to surface modification by ceramic reinforcement that creates more surface roughness and causes multiple reflection [183].

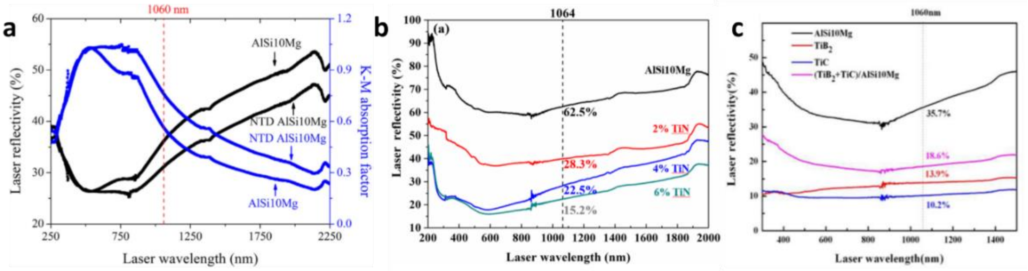

Fig 2.5: Reduction of laser reflectivity in AlSi10Mg on addition of various ceramic particles: (a) Nano-TiB_2 [185] (b) TiN [186] and (c) TiB_2+TiC [178].

2.3.2 Lower thermal conductivity:

The elevated thermal conductivity of Al results in a substantial temperature gradient, ultimately reducing the melt pool's lifespan and giving rise to defects like balling or cracks during processing. Therefore, LPBF of Al alloys demands significantly higher laser power. However, incorporating ceramic reinforcements such as TiB_2 and TiC particles, which possess considerably lower thermal conductivity than Al alloys, serves to impede the heat flux [179,180,189]. Consequently, the heat is retained within the melt pool, causing a reduction in the temperature gradient. This, in turn, promotes the formation of equiaxed grains and fosters isotropic properties in the LPBF components.

2.3.3 Columnar to equiaxed grained microstructure:

Large columnar grains lead to anisotropic mechanical properties of the high strength Al LPBF parts. One of the earliest studies that reported on the transition of such columnar grains into fine and equiaxed grains (equal in length, width and height) on metal 3D printing was reported by Martin et al. [173]. They functionalized the powder surface of high strength Al alloys (AA7075 and AA6061 series) with nucleating agents such as TiB_2, WC, ZrH_2. Nucleating agents for specific alloy were chosen based on the minimum lattice mismatching, as they offer lower barrier to the nucleation. This strategy was successful to obtain crack-free and fine-equiaxed grained LPBF high strength Al alloy parts. Furthermore, this microstructure is also effective in eliminating orientation anisotropy, that is considered as defects for materials demanding bulk isotropic properties [70,173]. Other ceramic nucleating agents for high strength Al alloys includes LaB_6 [190], CaB_6 [169], TiN [182],TiC [191], SiC [192], Al_20_3 [193] also multiple nucleating agents such as TiC-TiH_2 [194], TiC-TiB_2 [178]. **Fig 2.6** display columnar to equiaxed transition in various Al alloys by the addition of ceramic particles.

Among various ceramic reinforcement TiB_2 is among the promising one to Al alloy due to its (i) High hardness, (ii) Non-reactivity with molten Al (iii) High laser absorption (λ = 1064 nm), (iv) effective grain refiner and (v) Low thermal conductivity [195].

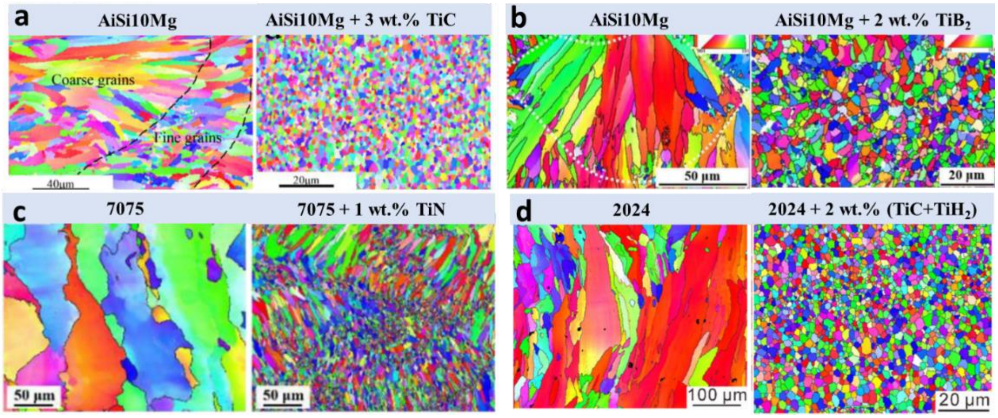

Fig 2.6: Columnar to equiaxed transition of microstructure in various LPBF-Al alloys by the addition of (a) TiC [178], (b) TiB_2 [196], (c) TiN [182] and (d) $TiC+TiH_2$ [194]

2.4 Literature review on A20X (Al-Cu-Mg-Ag-TiB_2)

2.4.1 Development of Al-Cu-Mg-(Ag) alloy:

Al-Cu-Mg-Ag alloys were developed in the early 1960s by Prof. Ian Polmear and his research group [197–199]. These alloys were designed to meet the large industrial interest in extending the strength and creep properties of the conventional 2xxx (Al-Cu-Mg) series Al alloys.

In 1985 Arumalla et al. demonstrated that a small addition of Ag around 0.4 wt.% to the Al-4Cu-0.3Mg alloy lead to a superior creep behaviour at 125 °C in an underaged condition [200]. Since then, a detailed investigation on Al-Cu-Mg-Ag alloys has begun. In 1988, I.J. Polmear and M.J Couper [201], designed a new alloy composition as Al-6.3Cu-0.45Mg-0.4Ag-0.3Mn-0.2Zr which showed a high yield strength at room temperature and an improved creep resistance in the range of 150 to 220 °C. The alloy treated with T6 heat treatment demonstrated a yield strength of around 520 MPa at room temperature. This strength value is superior to the one of other commercial alloys such as 2219-T6 and 2618-T6 that have a yield strength around 290 MPa and 390 MPa, respectively. The superior mechanical properties of this alloy have been attributed to the fine, uniform, and stable plate-type precipitation of Al_2Cu on the Al {111} planes during aging. This precipitate was designated as **Ω**. This alloy was also considered to be weldable and less susceptible to stress corrosion cracking as compared to 2xxx and 7xxx high strength alloys. Particular emphasis has been given to the Al-Cu-Mg-Ag alloys with high Cu:Mg ratios as they demonstrated higher mechanical properties even at elevated temperature [202,203]. With such superior properties, alloys based on the Al-Cu-Mg-Ag system are very attractive for applications where light weight, high strength and creep resistance are major concerns, such as in aircraft.

The presence of the Ω phase is now understood to be responsible for the enhanced strength observed in the Al-Cu-Mg-Ag alloy. However, several crystal structures have been suggested to this phase [204,205]. The misleading interpretation is due to the fact that, the structure and chemical composition of Ω phase is similar to the equilibrium θ-Al_2Cu phase. However, it was finally concluded that, it has a face-centred orthorhombic structure (Fmmm, a = 0.496 nm, b= 0.859 nm and c=0.848 nm) [206]. The Ω phase also holds the following orientation relationship with the α-Al matrix: $\{111\}_\alpha//\{001\}_\Omega$, $[10\bar{1}]_\alpha//[010]_\Omega$, $[1\bar{2}1]_\alpha//[100]_\Omega$ [206,207].

There were also several mechanisms proposed on the nucleation and growth mechanisms of the Ω phase [202,207–213]. The mechanism which is currently accepted was well established by the study of Reich et al. [214] using a 3D atom probe tomography (3D APT) during the precipitation process. In the early stages of aging (5 s at 180 °C), only Ag-Mg co-clusters form. This indicates that there is a stronger interaction force between Ag-Mg atoms than Cu-Mg atoms. The same was also observed by Ringer et al. [215]. As the aging continues, Cu atoms incorporate into the Ag-Mg co-clusters to form plate-type morphology on $\{111\}_\alpha$ planes. Subsequently, the $\{111\}_\alpha$ plates transform into Ω-Al_2Cu precipitates with a Cu concentration reaching 33 at.%. The Ag and Mg atoms migrate out of the Ω precipitates and accumulate at the Ω/α interface as a monolayer. Being precipitated on the primary glide planes of Al i.e., {111} planes, they offer much higher resistance to dislocation motion. Additionally, the Ω plates exhibit excellent coarsening resistance up to 200 °C [201,213,216]. Such a high coarsening resistance is due to the lack of ledges in the strong vacancy field normal to the broad side of the plate [216].

2.4.2 Role of alloying elements:

Cu: Addition of Cu to Al alloys enhances the strength through two distinct mechanisms: solid solution strengthening and precipitation hardening, however, it reduces the ductility. Based on the phase diagram of Al-Cu binary alloy [217], the maximum concentration of Cu that can be dissolve in an Al matrix is 5.7 wt.% at 495 °C. At lower temperature, the solubility of Cu decreases as defined by the solvus curve. By the process of heat treatment i.e., solution treatment followed by aging, Cu can be precipitated out as small particles in the form of Al_2Cu. The precipitation sequence is as follows [211]:

$$\text{SSSS} \rightarrow \text{Cu-Cu (GP zone)} \rightarrow \theta'' \rightarrow \theta' \rightarrow \theta\text{-}Al_2Cu \qquad 2.1$$

Cu could also be consumed in the formation of Ω-Al_2Cu in an Al-Cu-Mg-Ag quaternary alloy [212]. The choice of heat treatment cycles involving solutioning and aging steps needs to be carefully customized based on the desired properties.

Mg: In ternary Al-Cu-Mg alloys, with high Cu:Mg ratio, Mg binds with vacancy to promote high number density of GP zones and θ'' precipitates which enhance the strength of the alloy. Even a 0.5 wt.% Mg can alter the aging behaviour of the Al-Cu alloy and enhance the peak strength [139]. In an Al-Cu-Mg-Ag alloy, Mg forms Ag-Mg co-clusters in the early stages of aging which act as precursors to the phase Ω [206,208,218,219].

Ag: In Al alloys, Ag binds with Mg effectively, in fact it is known to trap the Mg [220–223], forming Ag-Mg co-clusters for the precipitation of Ω phase. After the precipitation of Ω phase, the Ag-Mg segregate at the Ω/Al interface and reduce the strain associated with the interplanar spacing of the two phases. This stabilizes the interface and keep them well bonded [214,224]. Ag does not incorporate into the chemical composition of Ω but enhances the precipitation kinetics of the Ω phase [223,225].

Si and Fe (Minor elements): Si and Fe are presents in a very small amount (<0.1 wt.%). They can be considered as an impurity or unwanted elements in Al-Cu-Mg-Ag alloy system. Si addition has shown to reduce the number density of Ω phases. Silicon interacts with Mg and limits the Mg availability for the Ag-Mg pre-precipitate clusters formation on {111} plane [226,227]. A Mg/Si ratio >2 is suggested for Ω nucleation.

Fe has a detrimental effect on Al alloys and the concentration is usually kept low. However, it helps in the smooth ejection of the cast parts in the die-casting process [228]. However, at higher concentrations it could interact with Si to form intermetallic compounds such as $FeSiAl_5$ and $FeSiAl_8$ [229] and with Cu by forming Cu_2FeAl_7 [139].

2.4.3 Addition of TiB_2 to Al-Cu-Mg-Ag alloy:

The addition of TiB_2 as a reinforcement to the Al-Cu-Mg-Ag alloy was performed by Aeromet International Ltd. by an in-situ process [230–232].

The in-situ production of TiB_2, as described by Indriyati [232], involves the reaction between potassium-based salt mixtures K_2TiF_6 and KBF_4, and liquid Al. The quantity of salts is added to meet the stoichiometry of TiB_2. Both these salts react with liquid Al to form intermediate compounds such as Al_3Ti and AlB_2. These compounds further react to release Ti and B ions into molten Al. The reactions during in-situ production of a master Al-Ti-B alloy are as follows:

$$3\,K_2TiF_6 + 13\,Al \rightarrow 3\,TiAl_3 + 3\,KAlF_4 + K_3AlF_6 \qquad 2.2$$

$$2\,KBF_4 + 3Al \rightarrow AlB_2 + 2\,KAlF_4 \qquad 2.3$$

$$AlB_2 + TiAl_3 \rightarrow TiB_2 + 4Al \qquad 2.4$$

Although, the presence of small amount of free-Ti could also lead to the formation of $TiAl_3$ particles, additional to TiB_2 [233]. The developed alloy is known as A20X [234,235]. The A20X alloy was able to tackle well the defects arising in casting and additive manufacturing of high strength Al-Cu alloys such as shrinkage porosity, micro-segregation and solidification cracking. The A20X is able to reduced such defects due to the combination of TiB_2 and $TiAl_3$ particles which alter the solidification behaviour and feeding mechanism of the alloy [231]. Additionally, both TiB_2 and $TiAl_3$ particles act as grain refiners in Al alloys [233,236,237]. Although, TiB_2 and $TiAl_3$ particles are beneficial for the strength of the alloy, they could also be crack initiator by acting as a stress concentrator during deformation and thereby affect the alloy ductility.

The composition of the alloy was standardized by Aerospace Materials Specifications (AMS) for casting and designated as AMS4471 and AMS4482 for investment casting and sand casting respectively [238,239]. By looking at the potential success of A20X alloy in the AM process, the company has recently commercialized their gas atomized A20X powders [234,235]. The A20X alloy has been registered at the Aluminium Association as AA205 and designated as AMS7033 by SAE international [240]. According to the manufacturer, the AM processed alloy demonstrated high yield strength up to 440 MPa, an ultimate tensile strength of around 500 MPa and elongation to failure of 10-13 % in a heat treated condition [235], the alloy competes with other high strength Al alloys of 2xxx and 7xxx series.

Chapter 3

Motivation and Methodology

3.1 Motivation

The present thesis finds its motivation from the lack of knowledge in the literature related to the post-processing behaviour of the high strength A20X alloy processed by laser powder bed fusion.

The A20X (Al-Cu-Mg-Ag-Ti-B) alloy is a structural alloy which mainly finds application in the aerospace industry. This alloy gains its strength thanks to the precipitation of strengthening phases. Thus, the mechanical properties of the printed parts are strongly influenced by the post-processing heat treatments.

The thesis attempts to the investigate the following research gaps:

- Is the conventional post-processing heat treatment developed for castings also applicable for the LPBF parts? **(Chapter 5)**
- Is there any post-processing treatment that could be more suitable for LPBF parts? **(Chapter 5)**
- Does the A20X alloy respond to natural aging? If yes, what kind of microstructure and mechanical properties can be achieved? **(Chapter 6)**
- What are the A20X major strengthening mechanisms in the different post-processing conditions? **(Chapter 6)**
- How the material deforms under tensile loading and how it fails? **(Chapter 7)**
- HIP is among the most common post-processing treatment employed for LPBF parts. What is its effect on the LPBF A20X alloy? **(Chapter 8)**

It is believed that a better understanding of the post-processing behaviour of this alloy could further enhance its applicability in the competitive and rapidly growing AM market.

3.2 Methodology

3.2.1 Powder flowability:

The flowability of the powder was carried out by Carney and Hall method according to the ASTM standard [241].

3.2.2 3D printing:

Parallelepipeds samples (12x10x10 mm^3) and tensile specimen with sub-size plate-type dimensions according to the ASTM E8 standard (with higher thickness than required) were printed by EOS M270 dual mode system in an argon atmosphere **(Fig 3.1)**. The platform was pre-heated to 100 °C. A rotated scanning strategy 67° was employed across the successive layers. After printing, the samples were removed from the base plate by electrical discharge machining (EDM) and the tensile specimen with the required thickness was also extracted.

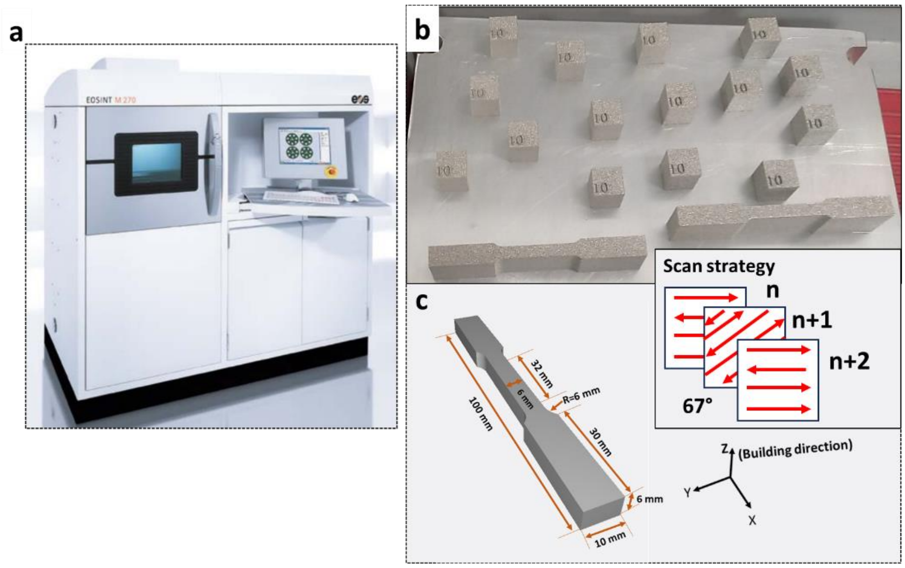

Fig 3.1: (a) EOS M270 machine, (b) build plate after printing, and (c) schematic of a tensile specimen with ASTM E8 dimensions obtained after EDM cutting.

3.2.3 Post-processing treatments:

3.2.3.1 Heat treatment:

The post-processing heat treatments were comprised of solution treatments followed by either artificial aging or natural aging. The solution treatments were performed in a horizontal tubular furnace (Nabertherm RHTC 80 -710/15) under an argon atmosphere. The artificial aging treatments were performed in an oven (Memmert) for different aging time whereas natural aging was done for various number of days (up to 100) at room temperature. The nomenclatures of peak aged conditions are presented in **Table 3.1**.

3.2.3.1 Hot Isostatic Pressing:

The Hot Isostatic Pressing of the sample was performed within a Quintus QIH 15 L equipped with a Molybdenum furnace **(Fig 3.2a)**. It was equipped with a Uniform Rapid Cooling (URC) module **(Fig 3.2b)**. The HIP process was performed under a pressure of 100 MPa at 530 °C and 540 °C followed by either rapid cooling by URC module or natural cooling. The HIPed samples were then artificially aged at 190 °C or 150 °C, as presented in a **Table 3.1**.

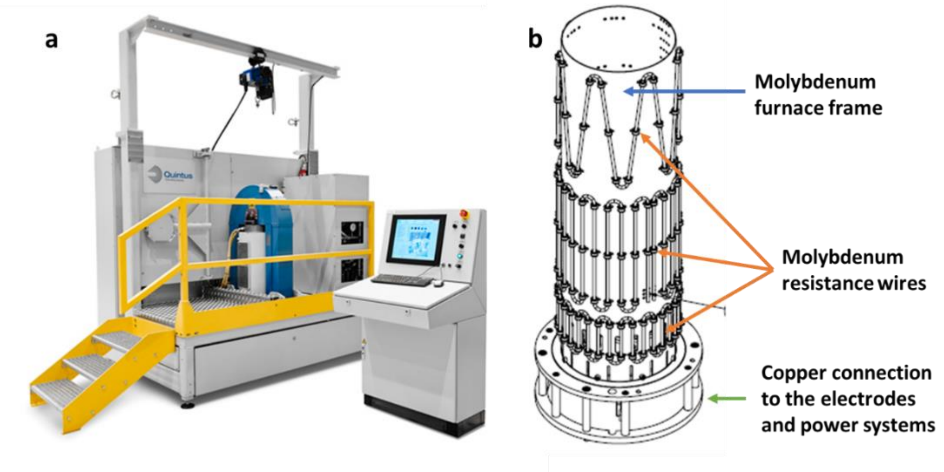

Fig 3.2: (a) HIP Quintus QIH 15 L machine and (b) Uniform Rapid Cooling module with Molybdenum furnace

Table 3.1: The main artificially and naturally aged conditions of various heat treatments that are utilized and mentioned in the thesis.

Heat treatment	HIP	Solutioning	Aging	Ref.
Conventional-T7	-	495 °C for 5 h + 505 °C for 6 h + 525 °C for 11 h + 538 °C for 24 h	170 °C for 8h	[242]
Modified-T7	-	505 °C for 2 h + 530 °C for 4 h	190 °C for 4-6h	[243]
Long-T7	-	495 °C for 4 h + 505 °C for 6 h + 530 °C for 12 h	190 °C for 10h	Present
Long-T6	-	495 °C for 4 h + 505 °C for 6 h + 530 °C for 12 h	190 °C for 6h	Present
Short-T6	-	530 °C for 1 h	190 °C for 4-6h	Present
T4	-	530 °C for 1 h	≈ 28 °C for 20 d	Present
T6-L	-	530 °C for 1 h	150 °C for 4h	Present
HIP-1SA	530 °C for 1 h + 100 MPa	530 °C for 1 h	150 °C for 4h	Present
HIP-2A	540 °C for 1 h + 100 MPa	-	190 °C for 4h	Present

3.2.4 Characterization tools:

3.2.4.1 Morphological and microstructural:

Metallographic sample preparations were performed by polishing according to the standard metallographic procedure.

Optical microscopy:

Initial microstructural characterization was performed in a Leica DMI 5000 M.

Scanning electron microscopy:

Metallographic sample preparations were performed by polishing according to the standard metallographic procedure and by etching with Keller's reagent for 5 seconds. Microstructural characterizations were performed using an optical microscope (Leica DMI 5000 M), a Phenom XL table-top Scanning Electron Microscope (SEM) and a TESCAN S900 Field Emission Scanning Electron Microscope (FESEM) equipped with Secondary Electron (SE), Back Scattered Electron (BSE) detectors and an Energy Dispersive Spectroscopy (EDS). Electron backscattered diffraction (EBSD) was performed using 20 kV and 10 nA with a step size of 0.2 μm.

Transmission electron microscopy:

Microstructural features that were too small to be resolved by SEM were characterized by transmission electron microscopy (TEM). TEM imaging was carried out at our colleagues at the Ernst Ruska-Centre for Microscopy and Spectroscopy with Electrons (ER-C-2), Forschungszentrum Jülich, Germany. The characterizations were conducted on an extremely thin lamella with a thickness close to 100 nm. These lamellae were prepared from bulk samples using a Helios NanoLab 460 F1 dual-beam focused ion beam scanning electron microscope (FIB-SEM) equipped with a Ga^+ ion source. A detailed, step-by-step procedure for creating these damage-free lamellae can be found in a separate reference [244].

High-angle annular dark-field (HAADF) scanning transmission electron microscopy (STEM) imaging, along with corresponding energy-dispersive X-ray spectroscopy (EDX) chemical mapping, was carried out using an FEI Titan G2 80-200 ChemiSTEM microscope, operating at 200 kV. This microscope was equipped with a high-brightness field-emission gun, a probe Cs corrector, and a super-X energy-dispersive X-ray spectroscopy system [245]. The convergence semi-angle employed for STEM imaging was approximately 25 mrad, and the collection semi-angle ranged from 80 to 200 mrad.

3.2.4.2 Image analysis

The microstructural features observed by various characterization techniques such as optical, SEM and TEM were quantified using an ImageJ 1.53k software.

3.2.4.3 Phase and structural analysis

Phase analysis of the A20X powder, as-built, and various post-processed samples were conducted using X-ray Diffraction (XRD) with a Panalytical X’Pert PRO PW 3040/60 X-ray diffractometer operated at 40 kV and 40 mA. This diffractometer employed monochromatic Cu-Kα radiation with a wavelength of 1.54 Å. The data were collected with a step size of 0.013° and a duration of 25 seconds per step. For individual peak profiles, a step size of 0.007° and a duration of 30 seconds per step were employed.

Quantification of phases was achieved through the Rietveld refinement method, utilizing Panalytical X'Pert Highscore Plus software. The refined parameters encompassed the phase scale factor, specimen displacement, unit cell parameters, peak broadening factors (U, V, and W), peak shape factor, and preferred orientation coefficient. To account for instrumental broadening, a reference pattern from a LaB_6 standard sample was employed. Additionally, dislocation density calculations were carried out using XRD line profile analysis, using the Williamson-Hall (W-H) plot method [246,247].

3.2.4.4 Thermal:

Differential scanning calorimetry (DSC) data was generated utilizing the NETZSCH DSC 214 Polyma instrument. The DSC specimens were weighed at approximately 10-15 mg each and were subjected to the following heating process under nitrogen (N_2) atmosphere: (i) temperature ramping-up from 27 °C to 550 °C at a rate of 10, 20 K/min, (ii) holding at 550 °C for 5 min and (iii) temperature ramping-down from 550 °C to 27 °C at a rate of 10, 20 K/min.

3.2.4.5 Mechanical:

Micro-hardness:

Micro-hardness values were obtained with a micro-Vickers Leica VMHT indenter using 100 g load and 15 seconds of dwell time. 10 indentations (measurements) were made per sample with a separation of 2 mm between adjacent indentations.

Tensile test:

The bulk mechanical behaviour was characterized by tensile tests by Zwick-Roell ProLine Z0505 with 8x10^{-3} s^{-1} as strain rate. The sample dimensions of a sub-size plate-type specimen was utilized based on an ASTM E8 standard.

Chapter 4

Printability of the A20X alloy by LPBF: Process optimization, as-built microstructure, and mechanical properties

4.1 Introduction

In this chapter, the printability of the A20X powder by LPBF technique is demonstrated. The powders were at first characterized by various techniques to check their flowability and then their phase and microstructural analysis was carried out. An optimized process window was obtained based on the combination of lowest porosity values and with high build-up rate. In the later part, the microstructure, tensile property, and fracture analysis of the as-built parts are presented.

4.2 Methodology

Parallelepiped samples of size 10x10x12 samples were printed in an EOS M270 machine. The **Table 4.1** presents various parameters utilized for optimizing the processing parameters.

Table 4.1: Various processing parameters utilized for the optimization of the processing window.

Parameter	Value range
Laser power (P)	170, 180 and 195 (W)
Scanning speed (v)	500, 600, 700, 800, 900 and 1000 (mm/s)
Hatching distance (h)	0.13, 0.15 and 0.17 (mm)
Layer thickness (t)	30 µm (fixed)
VED	37-100 J/mm^3

4.3 A20X powder characterization

4.3.1 Powder flowability

The properties of the powders exert a substantial impact on the quality of the parts processed by LPBF. Factors such as particle shape, particle size, and flowability are prime examples of these influential characteristics. In most of the powder-based AM techniques, the common practices to estimate powder flow are by Carney and Hall funnel method, Hausner’s ratio, Carr’s compressibility index, and angle of repose [248–250].

Carney and Hall funnel methods are considered as standards to characterize powders for AM processes by ASTM International [241]. They both have the same test functionalities, as they measure the time taken for a 50 g of powder to completely flow through a funnel. The funnel diameter for Carney and Hall are 5 mm and 2.5 mm, respectively. The funnel’s slope is 60° [251]. There are two approaches to measure the flow rate: static flow and dynamic flow. In the static flow method, the powder flow is halted, and the time is recorded from when the powder initially begins to flow through the orifice until it completely passes through. In contrast, the dynamic flow method involves a continuous powder pour into the flowmeter without obstructing the orifice, and the time is measured in the same way as in the static flow method [252]. For cohesive powders that do not flow through Hall funnel it is suggested to use Carney funnel [253].

Hausner's ratio (HR) and Carr's compressibility index (CI) are numerical values that rely on the apparent and tap densities of the powders [248]. Accurate determination of the apparent and tap densities can be achieved by adhering to the

ASTM standards [254]. Tap density is calculated as the ratio of mass of the powder to the volume it occupies after being tapped for a specified duration. This tap density reflects the random dense packing of the powder.

$$\text{Hausner Ratio: } \rho_a/\rho_t \qquad 4.1$$

$$\text{Carr Index: } \{(\rho_t - \rho_a)/\rho_t\}\text{ x100} \qquad 4.2$$

Where ρ_a and ρ_t are apparent and tap densities.

Another parameter to check the flowability of powders is angle of repose (AOR) [249]. One of the frequently employed definitions of the angle of repose is the maximum angle or slope at which a pile of powder material will naturally settle and maintain its shape on a flat surface. A steeper angle of repose often suggests poorer flowability, while a shallower angle indicates better flowability.

Various flow characteristics and indexes for powders are presented in **Table 4.2** and the flow characteristics of the A20X powder in

Table 4.3. Based on various flowability indexes, the A20X powder demonstrated the flowability in the range of excellent - good.

Table 4.2: Categorizing of powder flowability by various flowing characteristics [248,249]

Flowability	**Angle of repose, °**	**Hausner's ratio**	**Compressibility index**
Excellent	<30	1.00-1.11	<10
Good	31-35	1.12-1.18	11-15
Fair	36-40	1.19-1.25	16-20
Passable	41-45	1.26-1.34	21-25
Poor	46-55	1.35-1.45	26-31
Very poor	56-65	1.46-1.59	32-37
Very, very poor	>66	>1.60	>38

Table 4.3: A20X powder characteristics

Powder characteristics	Value
Apparent density	1.47 ± 0.01
Packing density	0.55 ± 0.00
Tap density	1.72 ± 0.01
Hall flow	84.7 s
Carney flow	12.6 s
Hausner's ratio	1.17 ± 0.01
Compressibility index	17.16 ± 0.66
AOR (Carney)	27.04°

4.3.2 Powder phase analysis and microstructure

FESEM micrographs of the A20X powder are shown in **Fig 4.1**. The powder particles are predominantly in spherical shape, with only a limited number of satellite particles observed on their surfaces (**Fig 4.1a**). The particle size distribution (PSD) exhibits a unimodal distribution **(Fig 4.1b)**, having the D_{10}, D_{50}, and D_{90} values of 21 μm, 30.6 μm, and 49.8 μm, respectively.

The micrographs (**Fig 4.1c** and **Fig 4.1d**) of the powder cross-section revealed a cellular microstructure. The cell boundaries are enriched with high Cu concentration, while the cells themselves are composed primarily of an α-Al matrix. Additionally, TiB_2 particles were observed to be present at the cell boundaries, at triple cell junctions and few large particles across the cells. These observations suggest that most of the TiB_2 particles served as heterogeneous nucleation sites for α-Al, promoting the formation of fine grains during solidification [255,256].

The phase analysis of the powder is shown in **Fig 4.2**. The phases identified are Al_2Cu, TiB_2, and Al. As there was no peak of Cu identified as a single phase, it was believed that the Cu-rich cell boundaries are of a eutectic product of α-Al + θ-Al_2Cu. This was due to the Cu enrichment of the liquid phase during rapid solidification. It is worth noting that the formation of the Al_2Cu phase occurs exclusively during the solidification process [257].

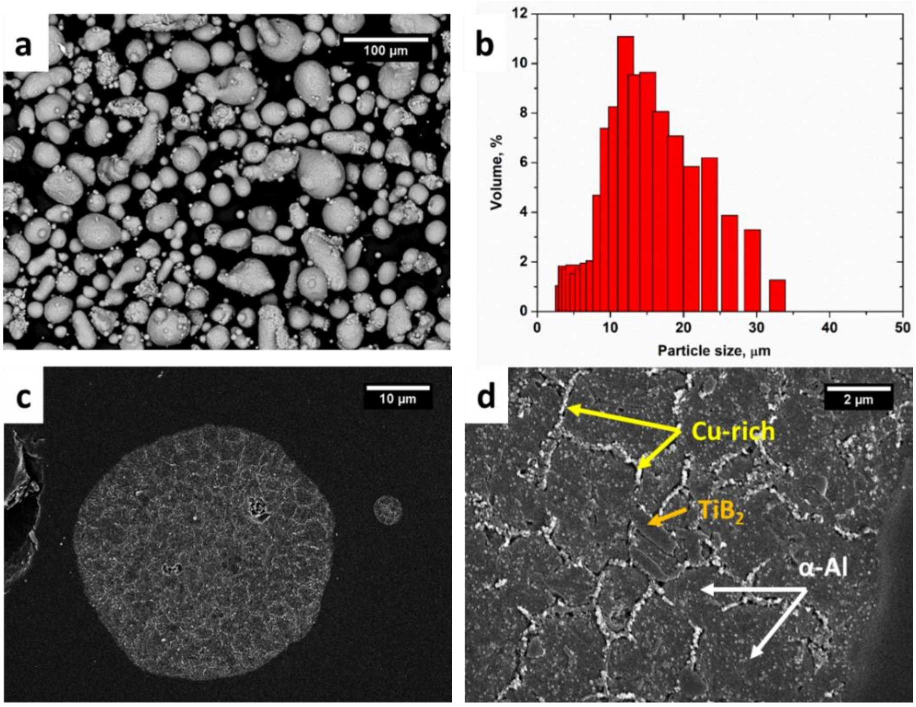

Fig 4.1: FESEM micrographs of A20X powder (a) low and (b) high magnification of powder morphology; Powder cross-section at (c) low and (d) high magnifications.

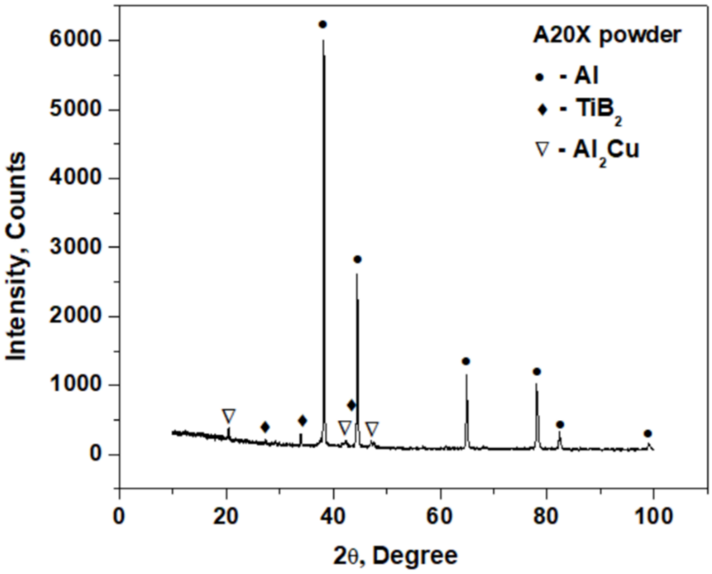

Fig 4.2: XRD pattern of the A20X powder

4.4 Printability of powder

The first issue to face when using a new powder in AM is its printability or processability which is generally estimated by evaluating the parameters process window that allows the production of dense and crack free parts. The porosity values of A20X samples built with different combinations of process parameters are plotted with their corresponding VED values in **Fig 4.3a**. This graph presents the overall effect of the building parameters on the LPBF consolidation. The plot follows the general trend observed in most AM materials i.e., the higher the VED, the lower is the porosity [258]. However, recent works suggested the non-suitability of the VED approach alone when it comes to the selection of the most suitable building parameters. Prashanth et al. suggested, in fact that some parameters, such as the laser power, have stronger repercussions on densification than others, thus, their effect has to be studied separately [33].

The effect of various building parameters on the porosity values of the A20X powder is shown in **Fig 4.3(b-d)**. It can be noticed that, in all the plots of laser power (P) vs. hatching distance (h_d), the porosity follows the general trend of higher the scanning speed, higher is the porosity. The **Fig 4.4** displays the series of SEM micrographs of A20X alloy processed with fixed laser power (195 W) with different scanning speed. At higher scanning speed, the porosities are arising mainly due to the lack of fusion of powder particles and an inadequate penetration of the molten fluid in the previously deposited layer [102,259].

The most suitable set of building parameters selected based on the above-mentioned considerations is: $P = 195$ W, $v = 800$ mm/s and $h_d = 0.13$ mm. This set of parameters was selected as it produces highly dense samples having a porosity value of 0.07±0.04%, maintaining a low VED value and a high build-up rate [260]. Low build-up rates are indeed undesired from a production point of view as they slow down the production process and increase the processing cost. On the other hand, high VEDs are also usually not desired as they create large melt pools and cause lower cooling rates, thus, producing coarser grain structures during solidification which reduces the yield strength of the material [261].

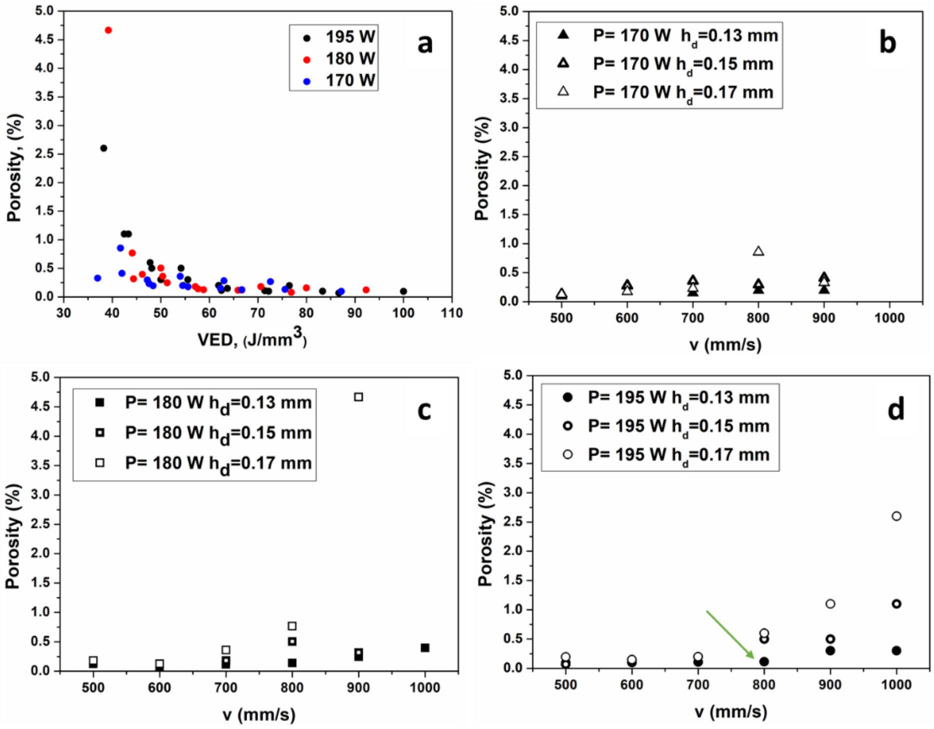

Fig 4.3: (a) Porosity vs. VED, (b), (c) and (d) porosity vs. scan speed for each laser power -hatching distance combination. The green arrow indicates the optimized set of building parameters.

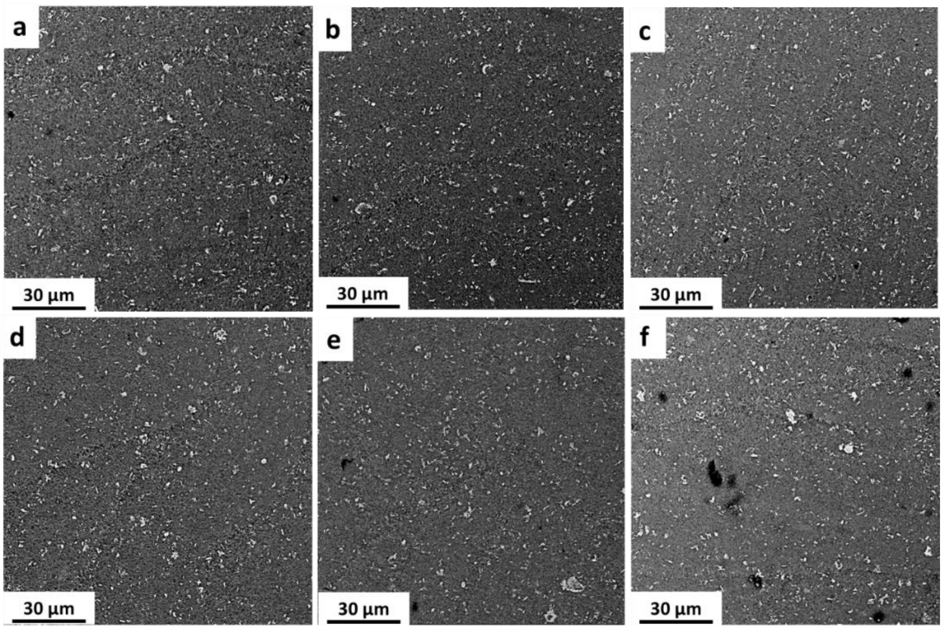

Fig 4.4: LPBF processed as-built A20X alloy at 195 W with various scanning speed (mm/s) (a) 500, (b) 600, (c) 700, (d) 800, (e) 900, and (f) 1000.

4.5 As-built microstructure

The **Fig 4.5a** presents the as-built microstructure of the A20X XZ cross-section of a sample printed with the optimized building parameters. The as-built microstructure has cellular structures with well-defined cell boundaries of θ-Al_2Cu phase and uniformly distributed elongated TiB_2 particles **(Fig 4.5b-c)**. Unlike the θ-Al_2Cu formation in A20X powder which happens solely during solidification, in LPBF as-built samples, the θ-phase could form in two different ways, first as a eutectic product during solidification along cell boundaries and second as a precipitate, by a solid-state process. Precipitation occurred due to multiple thermal cycles experienced by previously solidified layers which are supersaturated with Cu due to rapid solidification [262]. However, since most of the Cu atoms are rejected into liquid during solidification, the amount of supersaturated Cu within the Al matrix is reduced resulting in a very minute amount of precipitation.

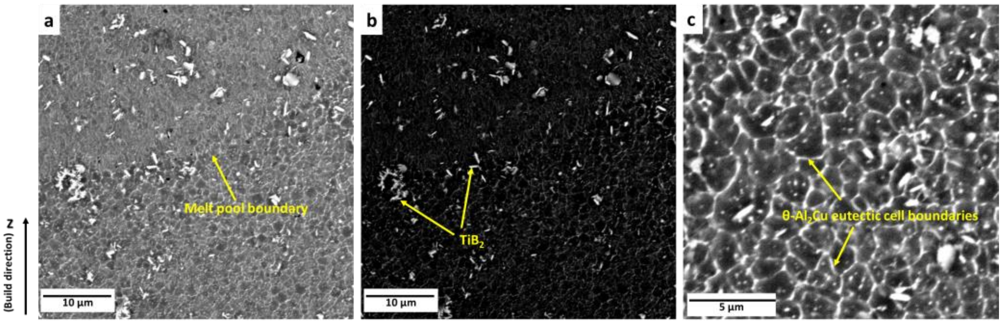

Fig 4.5: SEM-BSE micrograph of AB-A20X alloy (a) high brightness, (b) low brightness, and (c) Al_2Cu network of cell boundaries

4.5.1 TiB_2 cluster size: Effect of laser power and scanning speed

It has been usually observed in LPBF of metal matrix composites (MMCs), that the ceramic particles/cluster distribution varies as a function of laser power and scan speed [144,195,263]. The distribution of ceramic particles is influenced by the wettability of the particles with the melt, viscosity of the melt pool and Marangoni convection [263–266]. Based on these considerations, in the present work the selection of the most suitable process window for the A20X powder included also the study of the TiB_2 distribution. The analyses revealed a uniform dispersion of TiB_2 particles independent of processing parameters such as laser power **(Fig 4.6a)** and scanning speeds **(Fig 4.6b)** in the analysed range. The TiB_2 cluster size remained similar to the cluster size around 0.30 μm^2. The same observation was also made elsewhere in the LPBF processing of A20X alloy [267,268]. The uniform dispersion of TiB_2 particles could be due to their good wettability by Al melt, high chemical stability, high melting point (3230 °C) and intense enough Marangoni convection in the melt pool [195,267–269].

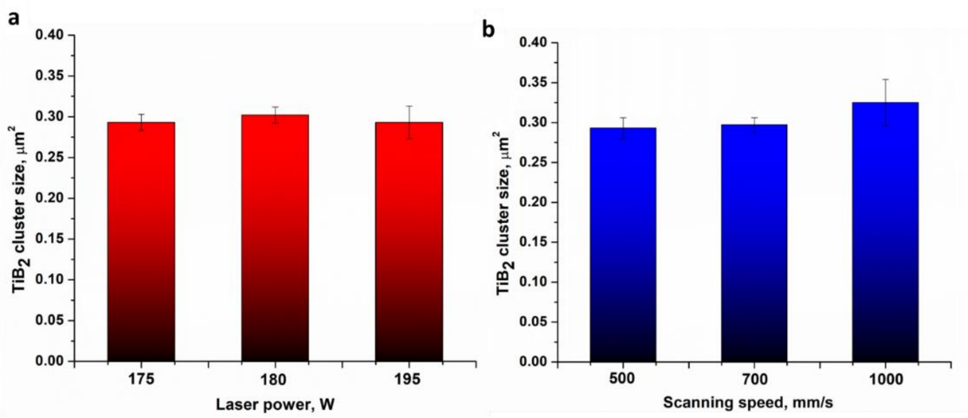

Fig 4.6: TiB_2 cluster size as a function of (a) laser power and (b) scanning speed

4.6 Mechanical property and fracture behaviour:

The tensile and fracture behaviour of the as-built A20X alloy in the optimized processing conditions is shown in **Fig 4.7**. As-built samples exhibit the typical stress-strain curve of an additive manufactured A20X alloy **(Fig 4.7a)**. The tensile curves displayed yield drop phenomena followed by an inhomogeneous deformation and then strain hardening along with serrated flow behaviour [270,271]. The yield drop phenomenon occurs in the initial stage of plasticity which marks the onset of lüders band formation causing localized deformation and a sudden drop in stress. Further deformation makes the lüders bands spread across the gauge section of the specimen by an inhomogeneous elongation [271]. However, as the deformation continues, a series of serrations are observed in the strain hardening regime, they are identified as type-B serrations. These observed serrations are due to repeatedly locking and unlocking of dislocations by solute atoms such as Mg and Cu. This phenomenon is known as Portevin-Le Chatelier (PLC) effect [272,273]. The curve characteristics such as yield strength (YS), ultimate tensile strength (UTS) and total elongation to failure (e %) are 304 ± 3 MPa, 378 ± 6 MPa, and 12.5 ± 1.6 % respectively.

The fractography of the as-built sample is presented in **Fig 4.7b.** A SEM-SE and its corresponding SEM-BSE micrograph is also presented in **Fig 4.7c** and **Fig 4.7d**, respectively. The specimens failed in a ductile manner characterized by fine and uniform dimples at the fractured surface **(Fig 4.7b).** Whereas regions with Al-TiB_2 interface failed in a brittle manner, leaving TiB_2 particles inside these micro-dimples (**Fig 4.7c** and **Fig 4.7d)**. In the as-built state, the TiB_2 particles were well bonded with the Al matrix giving rise to a higher percentage of elongation to failure [274].

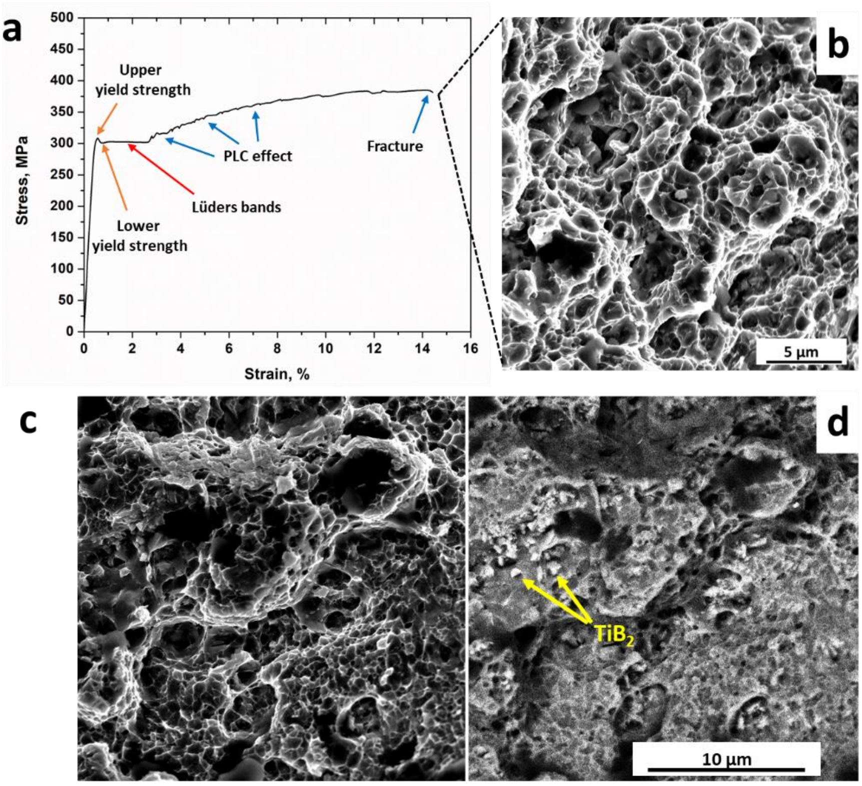

Fig 4.7: (a) A typical tensile curve of an as-built A20X sample, (b) SEM micrograph of fracture surface displaying dimples and (c) SEM-SE micrograph (left) with (d) its corresponding BSE micrograph (right).

4.7 Conclusion:

In this chapter, the powder properties, LPBF processability, microstructure and properties of A20X were investigated. The results can be summarised as follows:

i. The A20X powder was well processed by LPBF technique. The samples built with an optimized building parameters contains around 0.07±0.04% of porosity keeping the VED values low (62.5 J/mm^3).

ii. The microstructure of both powder and as-built sample was composed of fine cellular structures with α-Al cells and θ-Al_2Cu eutectic as cell boundaries. The TiB_2 particles are uniformly distributed, they are mainly located at the cell boundaries, at cell triple junctions but also within the cells.

iii. The distribution of TiB_2 particles in an as-built state was not much affected by laser power or scanning speed.

iv. The tensile behaviour demonstrated a good combination of strength-ductility. The average yield strength, ultimate tensile strength and elongation to failure are 304 MPa, 378 MPa and 12.5%, respectively.

v. The typical characteristic of a tensile curve includes upper and lower yield point, formation of lüders band and serrated flow of type B due to PLC effect.

vi. Fractography revealed that the specimen failure was in a ductile manner with micro-sized dimples at the fracture surface.

Chapter 5

Long T6 vs Short T6 post-processing behaviour: Role of multiple-steps and single-step in a solution treatment

5.1 Introduction

This chapter is a modified version of the published journal article "Barode, J., Vayyala, A., Virgillito, E., Aversa, A., Mayer, J., Fino, P., & Lombardi, M. (2023). Revisiting heat treatments for additive manufactured parts: A case study of A20X alloy. *Materials & Design*, *225*, 111566"

The A20X alloy manufacturer (Aeromet International Ltd.) suggested a post-processing heat treatment for the LPBF parts, called as long-T6 in the present thesis. The long-T6 was a modified version of the conventional-T7 heat treatment that was initially developed for the castings [242], see **Table 3.1**. The heat treatment comprised of a multiple-steps of solutioning followed by artificial aging at 190 °C for 4-6 h. The multiple-steps of solutioning treatment are as follows: 495 °C for 4 h + 505 °C for 6 h + 530 °C for 12 h. The multiple-steps of solution treatment allows (i) complete dissolution of θ-Al_2Cu, and (ii) prevents incipient melting of S-Al_2CuMg and Q-$Al_7Cu_3Mg_6$ phases [275–278].

The present chapter provides a detailed investigation on the microstructural evolution of the suggested heat treatment, namely, as-built, multiple-steps solution treatment, peak aged (long-T6) and over aged (long-T7). Post to the analysis, a new heat treatment (short-T6) was proposed that was more favourable and specific to the AM processing conditions. The proposed heat treatment (short-T6) was also investigated and shown an improved mechanical property, specifically in ductility as compared with the long-T6 heat treatment.

5.2 Methodology

The parallelepipeds samples (12x10x10 mm^3) and tensile specimens were printed by LPBF with an optimized set of parameters: Laser power = 195 W, scan speed = 800 mm/s, hatching distance = 0.13 mm, layer thickness = 30 µm, pre-heat to 100 °C and rotating scanning strategy of 67°.

The multiple-steps solution treatment (MS-ST) was carried out using a horizontal tubular furnace (Nabertherm RHTC 80-710/15) within an argon atmosphere. Subsequently, the solution treated sample was quenched by immersing it in a room temperature water. Interrupted solution treatments were conducted to monitor the changes in the microstructure. The specifics and naming conventions for these heat treatments are outlined in **Table 5.1**.

Table 5.1: Various post-processing heat treatments performed on A20X alloy.

Heat treatment	Temperature and Time
ST-A	300 °C for 4 h
ST-B	400 °C for 4 h
ST-C	495 °C for 4 h
ST-D	495 °C for 4 h + 505 °C for 6 h
MS-ST	495 °C for 4 h + 505 °C for 6 h + 530 °C for 12 h
SS-ST	530 °C for 1 h
Aging	190 °C for 2, 4, 6, 8 and 10 h

Subsequent aging processes were conducted by placing the material in an oven at 190 °C for different time durations, followed by natural air cooling. A visual representation of the heat treatment steps is illustrated in **Fig 5.1a** and a proposed heat treatment with single-step of solution treatment (SS-ST) in **Fig 5.1b**.

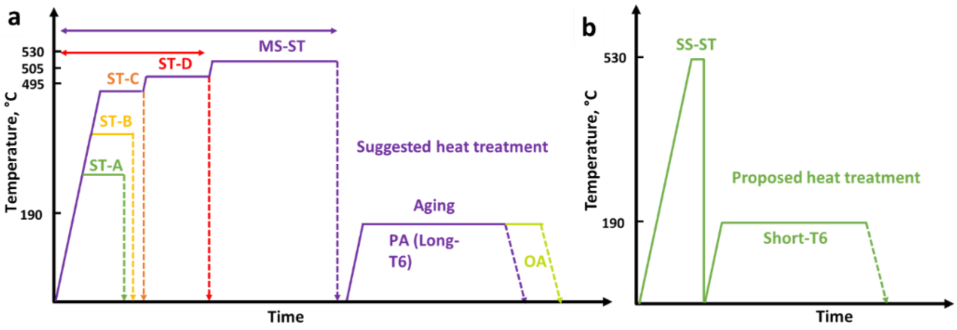

Fig 5.1: A representation illustrating the different heat treatment processes conducted on the as-built A20X alloy.

5.3 Micro-hardness and microstructural evolution

The histogram in **Fig 5.2** displays the micro-hardness evolution for both the AB and heat-treated samples. The hardness values experienced a reduction from the AB state (113 HV) to the MS-ST (103 HV) condition. While aging at 190 °C, the micro-hardness values followed a characteristic Gaussian distribution, with the highest hardness point (approximately 152 HV) reached after 6 hours, referred to as the peak-aged (PA) state. Further aging to 10 hours resulted in a reduction of hardness to 124 HV, which is termed as the over-aged (OA) state.

In order to gain a deeper insight into the prominent microstructural characteristics contributing to the peak hardness, a comprehensive microstructural analysis was conducted utilizing SEM-BSE **(Fig 5.3)**, SEM-BSE under low brightness **(Fig 5.4)**, and EBSD **(Fig 5.5)** for each of the four distinct stages: AB, MS-ST, PA (6 h at 190 °C) and OA (10 h at 190 °C).

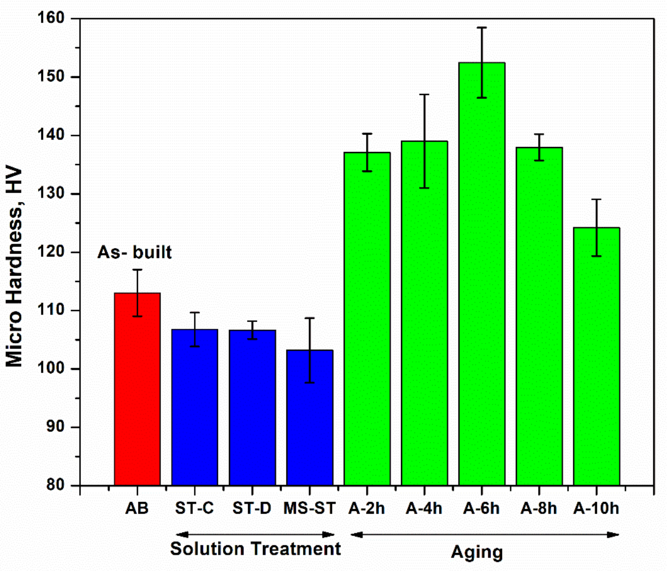

Fig 5.2: Micro-hardness evolution of A20X alloy during MS-ST and artificial aging

The microstructure of the AB specimen (**Fig 5.3a** and **Fig 5.4a**) exhibited the characteristic cellular structures commonly found in additively manufactured A20X alloy, as documented in previous studies [270,271,279] and explained in Chapter 1 and Chapter 4.

After the MS-ST, the eutectic network composed of θ-Al_2Cu disappeared, as depicted in **Fig 5.3b**. Micro-TiB_2 particles were predominantly found at the junctions of grain boundaries or along the grain boundaries. Additionally, a few θ-Al_2Cu precipitates were observed near the micro-TiB_2 particles, as shown in **Fig 5.4b**. Subsequent aging resulted in the formation of the θ-Al_2Cu phase, as the solubilized Cu precipitated out near the micro-TiB_2 particles and along the grain boundaries, as illustrated in **Fig 5.3c** and **Fig 5.4c**.

The formation of θ-Al_2Cu at the micro-TiB_2 particles can be attributed to the difference in the thermal expansion coefficient (α) between Al (26.5×10^{-6} K^{-1}) and TiB_2 (7.7×10^{-6} K^{-1} along c-axis and 4.1×10^{-6} K^{-1} along a-axis). Due to this dissimilarity, during the quenching process, dislocations become trapped near the TiB_2-Al interface [280–282]. As aging progresses, Cu atoms diffuse through these regions of high dislocation density via a pipe diffusion mechanism, facilitating the nucleation and growth of θ-Al_2Cu precipitates at the TiB_2 particles [280,281,283,284]. Excessive aging (OA) at 190 °C for 10 hours, significantly increased the size of θ-Al_2Cu precipitates, nearly enveloping the micro-TiB_2 particles, as shown in **Fig 5.3d** and **Fig 5.4d**. Thus, in the OA state, distinguishing between θ-Al_2Cu and micro-TiB_2 particles is challenging, even at reduced brightness.

Interestingly, some grain boundary cracks were also observed in the PA state (indicated by the yellow arrow in **Fig 5.3c**). These cracks were more frequent and severe in the OA state. Such cracks were not observed in the AB state, suggesting that their origin is likely related to the post-processing heat treatment.

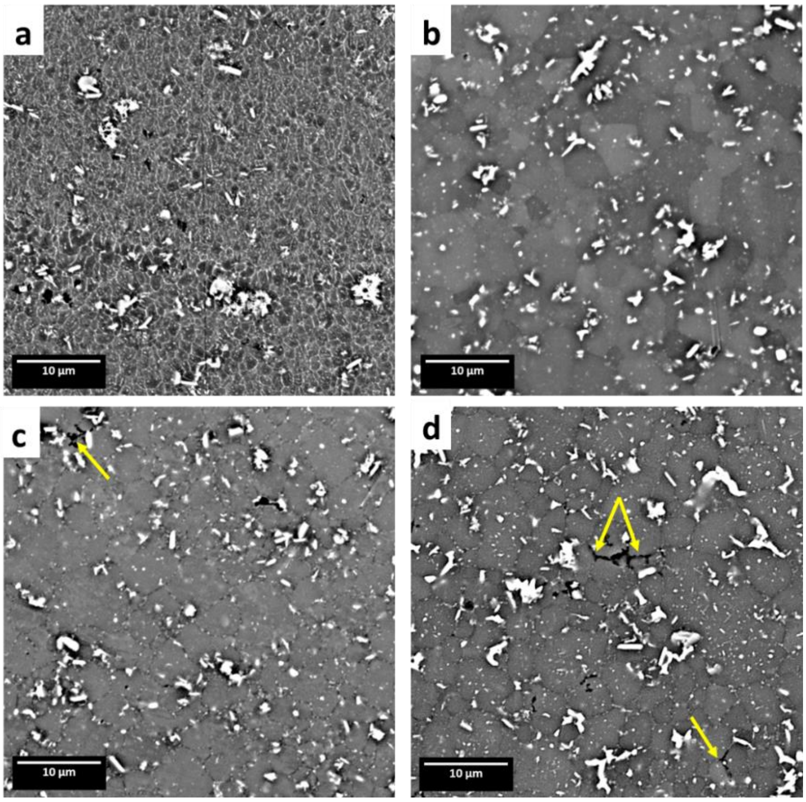

Fig 5.3: SEM-BSE micrographs of A20X samples without metallographic etching in the (a) AB, (b) MS-ST, (c) PA and (d) OA states *(Yellow arrows depict grain boundary cracks)*

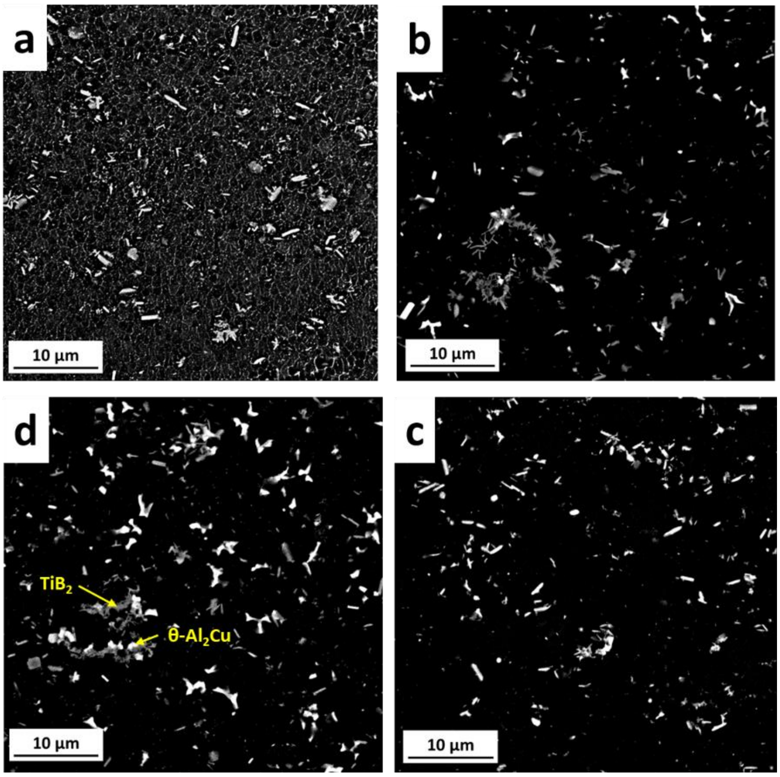

Fig 5.4: SEM-BSE micrograph of (a) Ab, (b) MS-ST, (c) PA and (d) OA condition showing θ-Al_2Cu (bright) and TiB_2 (grey) phase in Al matrix (black)

Fig 5.5 displays the EBSD-IPF maps for the four states under consideration. In the AB state, the grain size was estimated to be approximately 1.05 µm **(Fig 5.5a)**. Furthermore, it was observed that the cell size was equivalent to the grain size. The unindexed black interconnected patches surrounding the grains are likely to be an indicative of the eutectic θ-Al_2Cu phase. Following the MS-ST, the grain size reached 1.97 µm **(Fig 5.5b)**. It is worth noting that there was no significant increase in the grain size despite an extended duration in the solution treatment, which lasted nearly 24 h. This limited grain growth can be attributed to the Zenner pinning effect caused by the micro-TiB_2 particles located at the grain boundaries within the matrix [285]. The average grain size in both the PA and OA states was nearly similar to that in the MS-ST state, measuring approximately 2.16 µm **(Fig 5.5c)** and 1.93 µm **(Fig 5.5d)**, respectively.

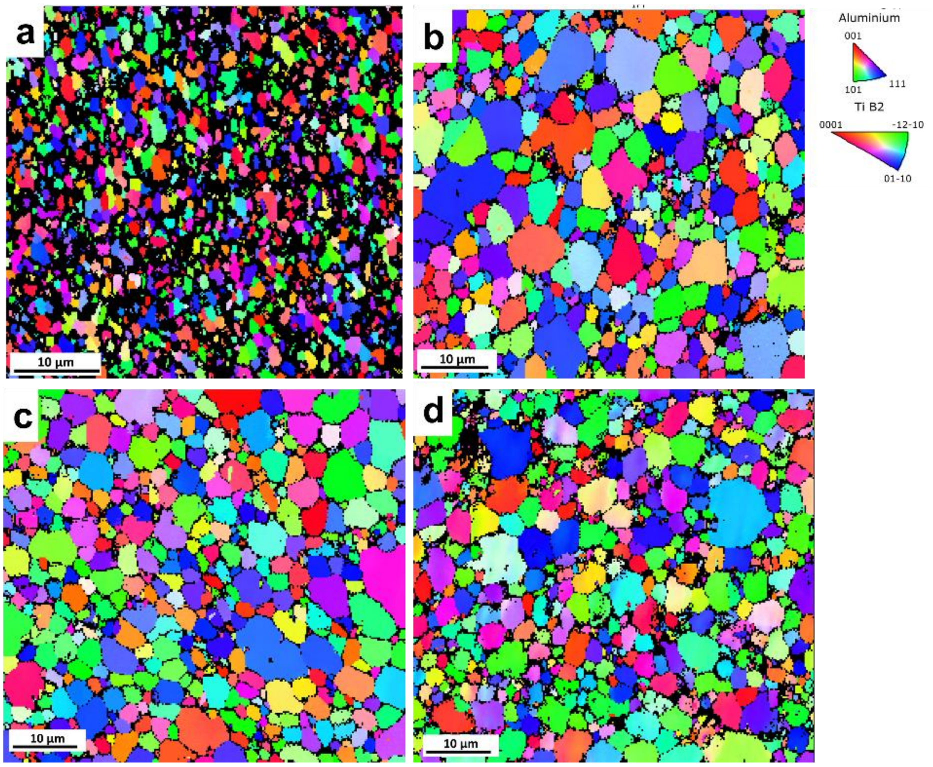

Fig 5.5: EBSD micrographs showing evolution of grain structure in various conditions (a) AB, (b) MS-ST (c) PA and (d) OA.

The phase analysis in various conditions was carried out by XRD as shown in **Fig 5.6**. Majorly three phases have been recognized: Al, TiB_2 and θ-Al_2Cu **(Fig 5.6a)**. The reference codes utilized for Al, θ-Al_2Cu and TiB_2 are 98-006-1729, 98-009-6862 and 98-001-3140 of ICDD respectively. Further, individual major peak of θ-Al_2Cu {110} and Al {111} phases are shown in **Fig 5.6b** and **Fig 5.6c**, respectively. The rise in the intensity of the θ-Al_2Cu peak observed during aging indicates the occurrence of θ-Al_2Cu precipitation and its subsequent growth.

A quantitative assessment of the phase transformation from the AB state to the OA state was conducted using the Rietveld method, and the results are illustrated in **Fig 5.6d**. In the AB state, the θ-Al_2Cu phase was quantified to be ~ 4 wt.%. However, the phase quantification for the MS-ST state was not carried out due to the very low peak-to-background ratio of the θ-Al_2Cu phase, which would introduce errors in the quantification during peak fitting. In the PA state, the θ-Al_2Cu phase content increased to ~ 2 wt.%, which further significantly rose to ~ 4 wt.% in the OA state. These quantifications are consistent with the observations made from SEM-BSE micrographs **(Fig 5.4)**. The phase quantification of TiB_2 remained relatively constant at around ~ 5 wt.% across all states.

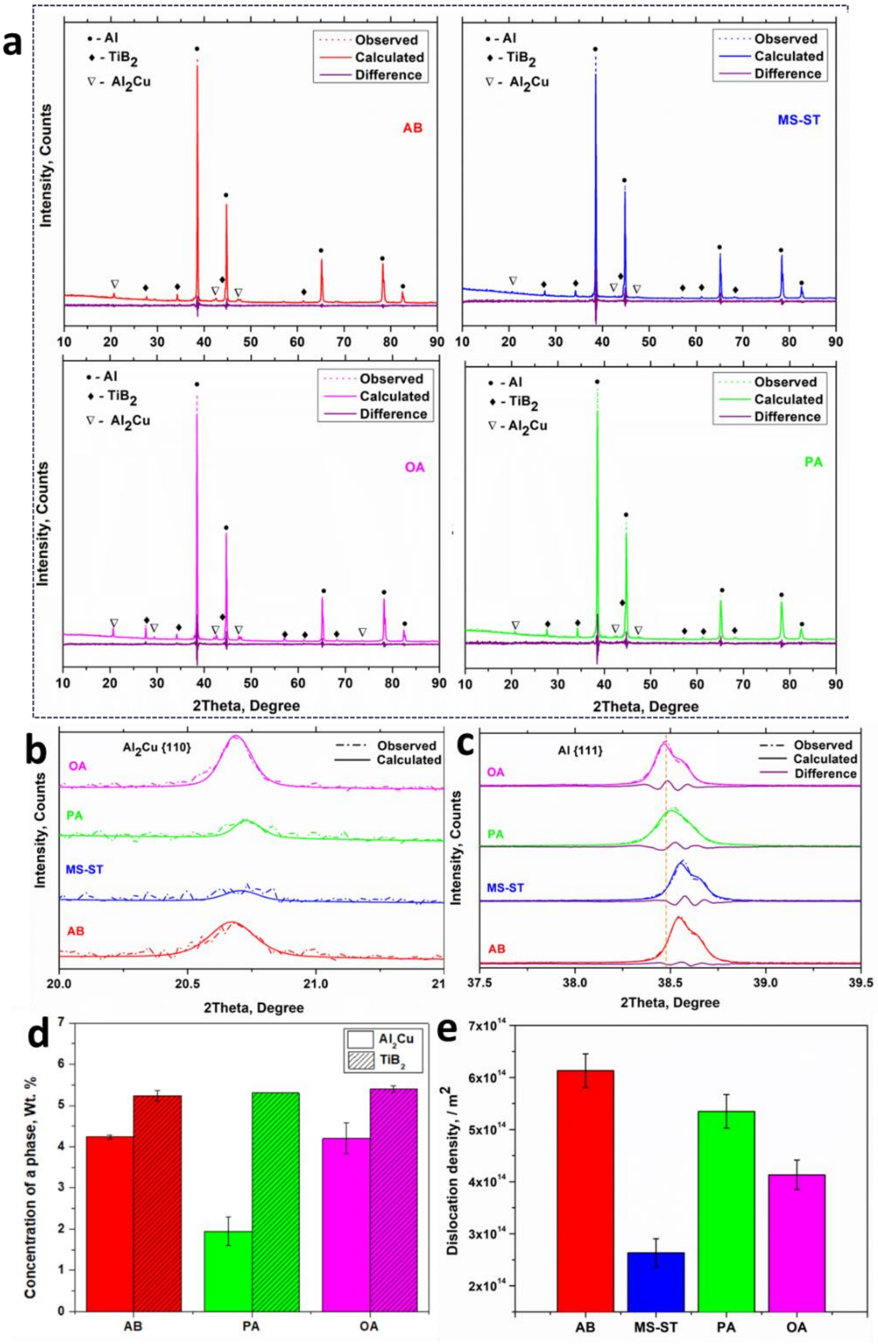

Fig 5.6: (a) Identification of phases through XRD measurements in the AB, MS-ST, PA, and OA states. Individual peak profiles for (b) Al_2Cu {110} and (c) Al {111}. (d) Determination of θ-Al_2Cu and TiB_2 phase quantities via Rietveld refinement. (e) Estimation of dislocation density using the W-H plot.

The individual peak profiles of Al {111} displayed a shift towards higher 2θ values following the MS-ST when compared to its reference position (indicated by the dotted line). This shift in the peak corresponds to a reduction in its lattice parameters due to the solid solution by Cu [286].

During aging, a broadening of the Al peak was also observed in **Fig 5.6c**. The average full-width at half maximum (FWHM) of the Al {111} peak in the AB, MS-ST, PA, and OA states were 0.106°, 0.088°, 0.096°, and 0.094° (2θ), respectively. The dislocation density within the Al matrix is associated with this peak broadening and was determined using a W-H plot, (**Fig 5.6e)**. The AB state exhibited a high dislocation density of 6.13 x $10^{14}/m^2$, which is a common characteristic of additively manufactured Al alloys [287]. The dislocation density decreased after MS-ST to 2.63 x $10^{14}/m^2$ but then increased significantly in the PA state (5.34 x 10^{14} $/m^2$) and OA (4.12 x 10^{14} $/m^2$) states.

To comprehend the source of such a high dislocation density observed during the aging process, DSC profiles were examined and analyzed the sequence of phase transitions (**Fig 5.7)**. In both the AB and MS-ST samples, three prominent peaks were identified **(Fig 5.7a)**. The first peak appeared as an endothermic event, attributed to the dissolution of Ag-Mg co-clustering [288]. The second peak was notably broad and exothermic, signifying the precipitation process. The third peak, also broad but endothermic, indicated the dissolution of all precipitates [289].

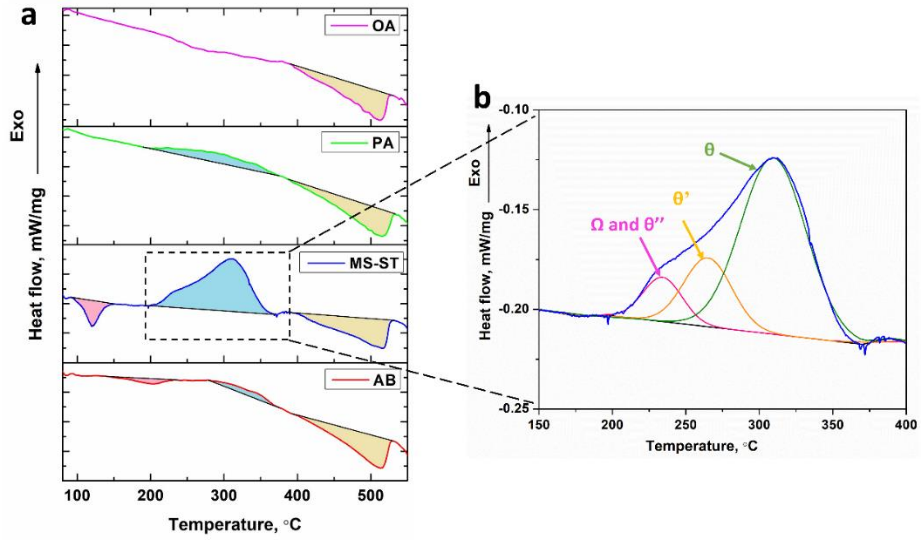

Fig 5.7: (a) DSC plots of AB, MS-ST, PA and OA states and (b) deconvolution of the broad exothermic peak of MS-ST state.

Comparing the DSC curves, it was evident that in the MS-ST state, the dissolution of Ag-Mg co-clusters occurred at significantly lower temperatures and exhibited a larger area under the peak compared to the AB state. This phenomenon is attributed to the dissolution of a higher volume fraction of smaller atomic clusters in the MS-ST state in comparison to the AB state [290]. In the case of the MS-ST sample, the exothermic peak displayed the largest area, signifying the highest amount of precipitation. However, the broadness of this peak indicates that the precipitation process was not a singular event but occurred over a range of temperatures. Upon deconvolution, we identified three sub-peaks, as illustrated in **Fig 5.7b**. These sub-peaks had peak temperatures of approximately 230°C, 260°C, and 310°C, corresponding to the precipitation of Ω & θ'', θ', and θ phases, respectively [288,289,291].

While the DSC results suggested the formation of multiple phases, the resolution provided by SEM was inadequate to distinguish these precipitates. Consequently, high-resolution STEM was employed for this purpose. STEM-EDS mapping of the PA and OA states are presented in **Fig 5.8** and **Fig 5.9**, respectively. In the PA state, fine and discontinuous precipitation along grain boundaries was observed **(Fig 5.8)**. These precipitates grew further upon continuous aging, as observed in the OA state **(Fig 5.9)**. These precipitates exhibited an enrichment in Cu and were accompanied by nanosized-TiB_2

particles. It was suspected that these precipitates were likely to be in an equilibrium state, specifically θ-Al_2Cu, and their formation might have been induced by the difference in coefficient of thermal expansion (CTE) between Al and TiB_2, as previously discussed. Additionally, we also noted the segregation of Mg at the grain boundaries.

Within the grains themselves, a substantial number of nanometric needle-shaped precipitates were observed **(Fig 5.8** and **Fig 5.9)**. These precipitates were measured approximately 52 nm in length in the PA state and 82 nm in an OA state (**Fig 5.10)**. They were enriched in Cu but were also partially segregated with Ag and Mg, as noted in **Fig 5.8**. These needle-shaped precipitates appeared to maintain a specific orientation relationship with the Al matrix. Based on the prior research, it is highly probable that these precipitates are of coherent Ω-Al_2Cu and semi-coherent θ'-Al_2Cu phases [243,279,292]. Both the Ω and θ' phases share the same chemical composition as of Al_2Cu and can arise from a supersaturated solid solution (SSSS) through two distinct and separate precipitation processes [211].

$$\text{SSSS} \rightarrow \text{G.P. Zone (Cu)} \rightarrow \theta'' \rightarrow \theta' \text{ on } \{001\}_\alpha \rightarrow \theta\text{-Al}_2\text{Cu} \quad 5.1$$

$$\text{SSSS} \rightarrow \text{G.P. Zone (Mg and Ag)} \rightarrow \Omega \text{ on } \{111\}_\alpha \rightarrow \theta\text{-Al}_2\text{Cu} \quad 5.2$$

However, the precipitation of the Ω phase is more favourable than that of the θ' phase in the Al-Cu-Ag-Mg alloys. This has been primarily attributed to the co-clustering of Ag-Mg atoms at the coherent $\{111\}_\alpha$ habit planes which effectively lowers the interfacial energy for nucleation of Ω [215,293,294].

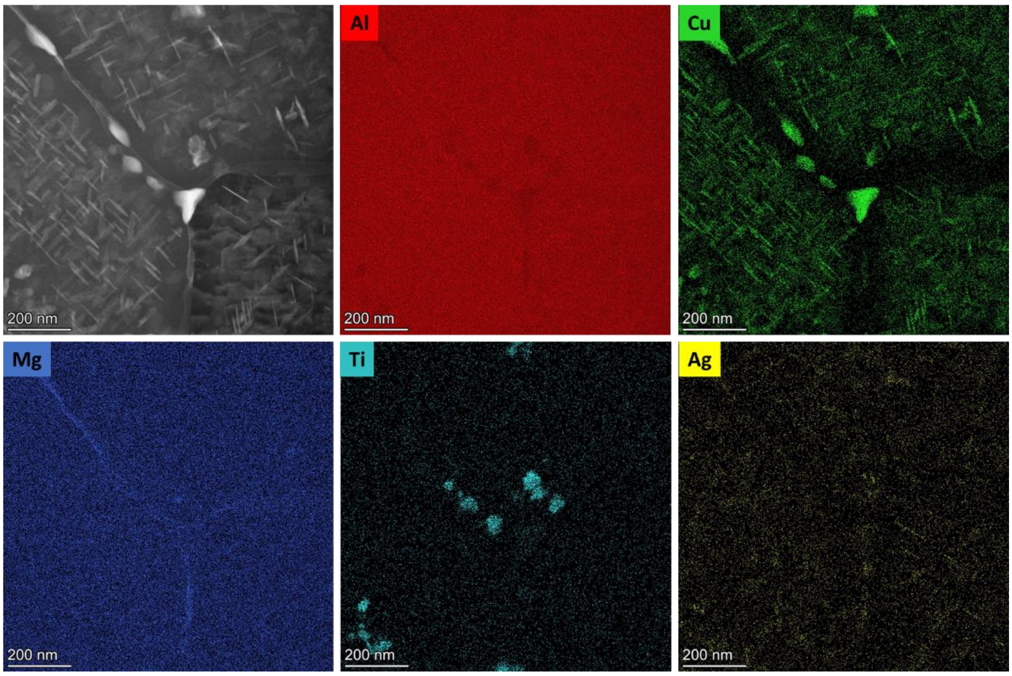

Fig 5.8: High resolution HAADF-STEM micrograph and corresponding EDS mapping of a grain boundary triple junction in the PA state.

The Ω and θ’ phases are recognized as the primary contributors to strengthening. However, Ω-plates exhibit significantly greater strength when subjected to elevated temperatures or extended aging periods, primarily due to their superior resistance to coarsening compared to θ’ [216,292,294–296].

Therefore, the presence of few large matrix precipitates (~ 420 nm in size), as observed in the OA state, is likely attributed to θ’ (refer to the inset in **Fig 5.10b**). Nonetheless, it is important to note that there exists a significant lattice misfit between the matrix precipitates (coherent Ω and semi-coherent θ’) and the Al matrix. This misfit leads to the development of micro-strains upon precipitation [297–300]. Consequently, a high density of Ω and θ’ precipitates resulted in a substantial micro-strain, which were directly correlated with the presence of high dislocation densities in the PA and OA states. Consequently, these precipitates were accountable for the observed peak broadening evident in the XRD patterns, as observed in **Fig 5.6b** and **Fig 5.6c**.

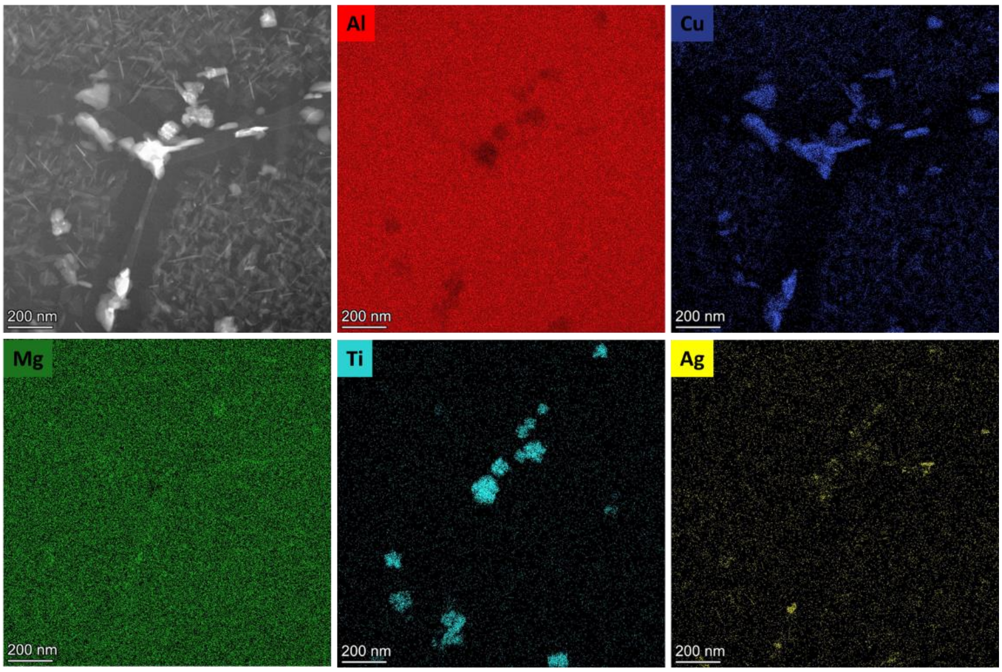

Fig 5.9: High resolution HAADF-STEM micrograph and corresponding EDS mapping of a grain boundary triple junction in the OA state *(Note the elemental colour identities are different than in Fig 5.8).*

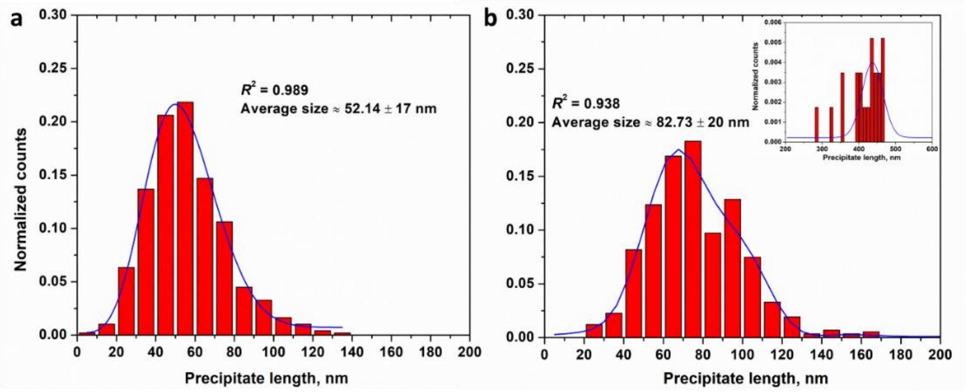

Fig 5.10: Particle size distribution of the needle type precipitates Ω/θ’ in (a) PA and (b) OA state.

Based on the current analysis of micro-hardness and microstructural evolution, the key factors contributing to the peak hardness achieved after 6 hours of aging **(Fig 5.2)** includes (i) the presence of numerous coherent **Ω** and semi-coherent θ’ nano-precipitates dispersed within the matrix, (ii) the optimal precipitation of θ-Al_2Cu (note that θ-Al_2Cu significantly coarsened in the OA state), and (iii) lower occurrence of grain boundary cracks compared to the OA state.

5.4 On the grain boundary cracking during aging

As aging progressed, microstructural analysis uncovered the occurrence of grain boundary cracking in both the PA and OA states. The presence of grain boundary cracking can be attributed to the combined effect of two factors. (i) The development of micro-strains (dislocations) due to the precipitation of coherent Ω-Al_2Cu and semi-coherent θ'-Al_2Cu nano-precipitates marked by the Al XRD peak broadening (**Fig 5.6e)**, and (ii) the increase in the width of precipitate-free zones (PFZs) near grain boundaries and micro-TiB_2 particles, as illustrated in **Fig 5.11**.

The process of precipitation and subsequent growth during aging leads to the formation of PFZs near specific microstructural features. From the PA state to the OA state, the width of PFZs near grain boundaries increased from 30 nm to 85 nm (as seen in **Fig 5.11b and Fig 5.11d)**, while the width of PFZs near micro-TiB_2 particles increased from 78 nm to 153 nm **(Fig 5.11a and Fig 5.11c)**. It is important to highlight that in both the PA and OA states, the width of PFZs near micro-TiB_2 particles was considerably larger than near grain boundaries. The widening of these PFZs is directly associated with the growth of precipitates at these specific locations.

The precipitates located along the grain boundaries near nano-TiB_2 particles did not exhibit a significant growth in size. In contrast, the θ-Al_2Cu precipitates near micro-TiB_2 particles experienced a substantial growth from the PA state to the OA state. This extensive growth resulted in the consumption of a larger quantity of solute atoms within the surrounding area, leading to a much wider PFZ. The precipitation of coherent Ω and semi-coherent θ' phases during aging can generate micro-strains, which subsequently contribute to the hardening of the grain interiors. The development of these micro-strains within the matrix is evident through the presence of high dislocation densities. This phenomenon leads to localized deformation near the grain boundaries, potentially inducing grain boundary cracking [301], a phenomenon commonly referred to as strain-age cracking. Strain-age cracking is typically observed during the post-weld heat treatment of superalloys [301–303]. Furthermore, this effect becomes particularly severe when PFZs exist near grain boundaries and at triple junctions [301]. The localized deformation occurring at the PFZs can initiate crack nucleation, which can easily propagate along these PFZs, ultimately resulting in grain boundary cracking [304,305].

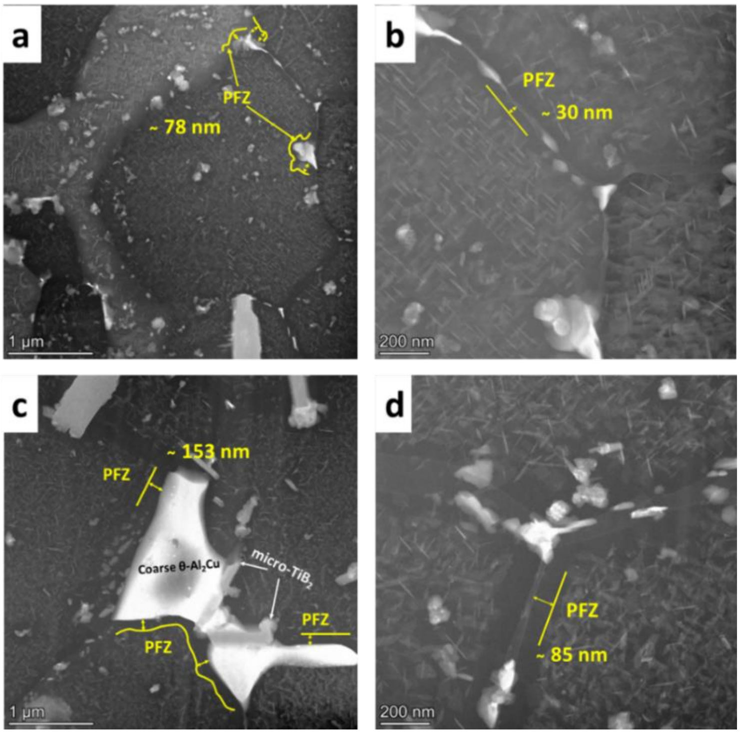

Fig 5.11: High resolution HAADF-STEM micrographs showing the PFZs in PA (a-b) and OA (c-d) state near micro-TiB_2 particles and near grain boundaries.

5.5 Microstructural evolution during MS-ST

During aging, the material experienced grain boundary cracks, a phenomenon that has been linked to the widening of PFZs caused by the substantial growth of θ-Al_2Cu at micro-TiB_2 particles. To comprehend whether the MS-ST plays a role in this specific aging behaviour, assessments of the microstructure at different stages of the solution treatment were conducted.

SEM micrographs were captured using the BSE mode with varying brightness levels, as illustrated in **Fig 5.12 (a-f and a'-f')**. These diverse image settings were employed to differentiate between the TiB_2 phase (appearing grey) and the θ-

Al_2Cu phase (appearing white) based on the atomic contrast. These micrographs were then utilized to quantify the microstructural characteristics of θ-Al_2Cu such as area-equivalent average radius (r), circularity (C), number density, and inter-precipitate spacing (λ), as presented in **Fig 5.13**.

Heat treatment of the AB sample (**Fig 5.12a** and **Fig 5.12a')** to the ST-A (300 °C for 4 hours) state (**Fig 5.12b** and **Fig 5.12b')** resulted in the disintegration of the cellular structure. The eutectic θ-Al_2Cu network breaks down into small spherical particles (r = 73 nm, C = 0.87). The ST-A microstructure characterized by a high number density of θ-Al_2Cu particles (0.21/μm^2) and a narrow inter-precipitate spacing (λ = 0.99 μm), see **Fig 5.13b**. These fine, fragmented particles have the potential to undergo spheroidization through the Rayleigh instability process, which occurs due to the diffusion of atomic species like Al and Cu from their edges towards the flat surfaces, driven by capillary forces [306,307].

Subsequently, heating to the ST-B state (400 °C for 4 hours), the spheroidized θ-Al_2Cu particles exhibited an increased size (r = 251 nm). They appeared to have migrated to the micro-TiB_2 particles, as observed in **Fig 5.12c** and **Fig 5.12c'**. Such a migration and growth of θ-Al_2Cu towards micro-TiB_2 particles can be attributed to the process of Ostwald ripening facilitated by the differences in the CTE of Al and TiB_2 [308]. This phenomenon of Ostwald ripening was quantitatively evident through a substantial increase in the average size of θ-Al_2Cu particles, growing from 73 nm to 251 nm **(Fig 5.13a)**, and a notable reduction in the average number density, decreasing from 0.21/μm^2 to 0.09/μm^2 **(Fig 5.13b)**. Subsequently, the migrated θ-Al_2Cu particles at micro-TiB_2 particles continued to coarsen during the ST-C heat treatment (495 °C for 4 hours) (**Fig 5.12d** and **Fig 5.12d')**, reaching their maximum average size of r = 310 nm (**Fig 5.13a**).

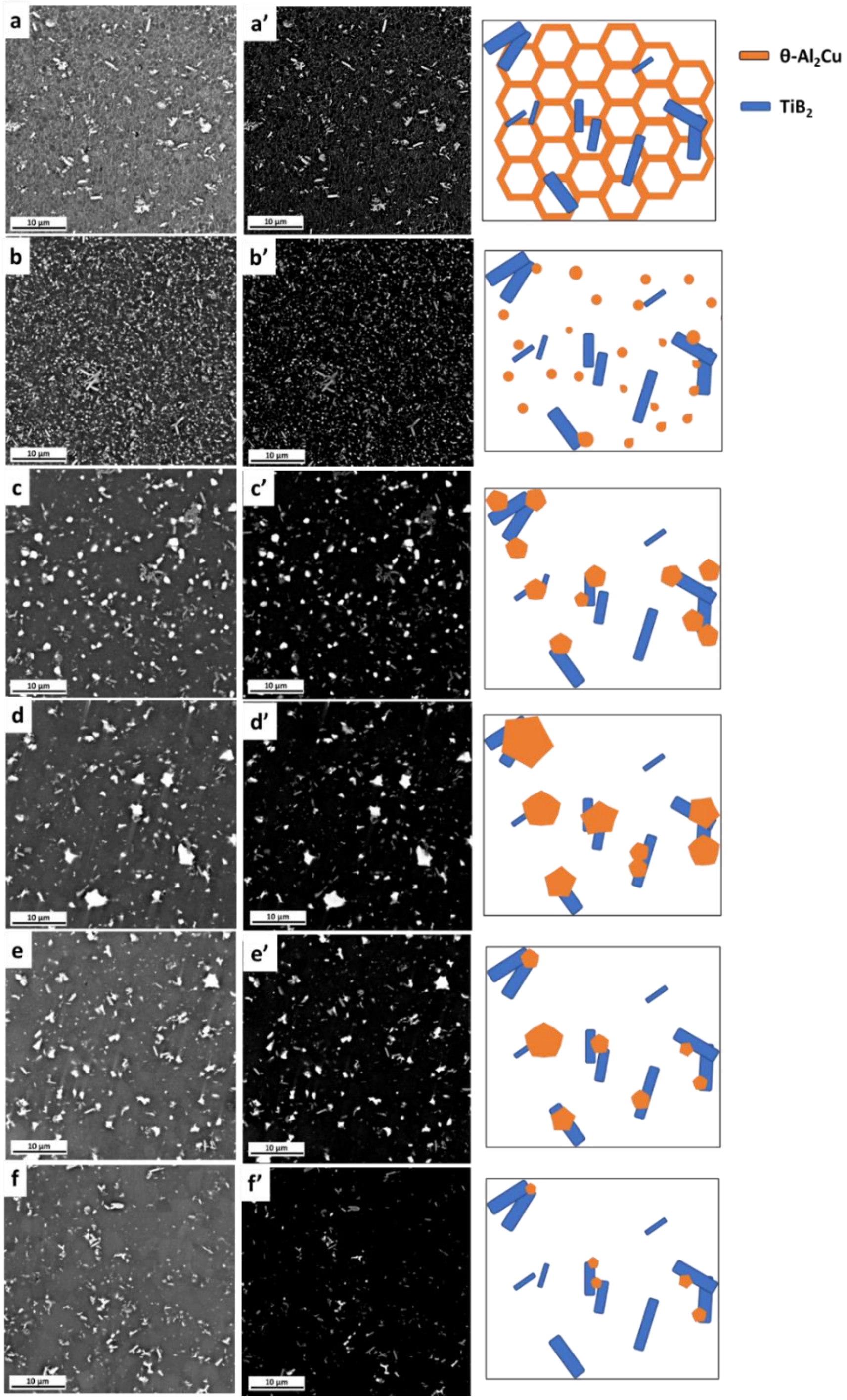

Fig 5.12: SEM-BSE micrographs under high (a-e) and low (a’-e’) brightness showing microstructural evolution at various interrupted steps during solution treatment. (a and a’) AB, (b and b’) ST-A, (c and c’) ST-B, (d and d’) ST-C and (e and e’) ST-D and (f and f’) MS-ST. (*TiB_2 particles as grey and θ-Al_2Cu as white)*. A schematic view of the corresponding microstructure (on the right-hand side) is shown for each interrupted step.

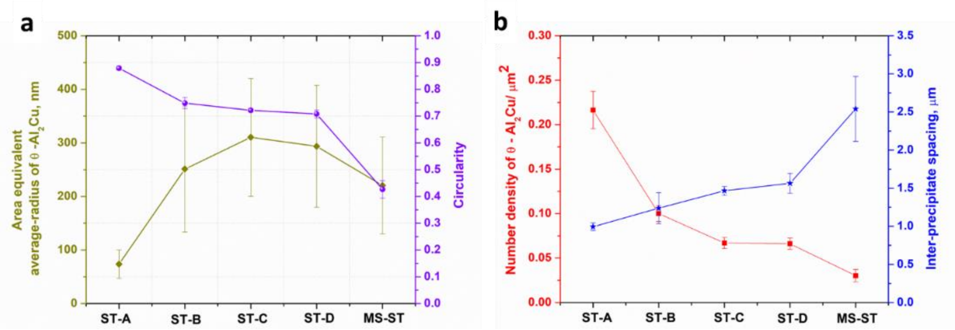

Fig 5.13: Evolution of various features of θ-Al$_2$Cu precipitate as a function of interrupted solution steps showing (a) area equivalent average-radius and circularity and (b) number density and inter-precipitate spacing.

After the ST-D heat treatment, involving exposure to 495 °C for 4 h followed by 505 °C for 6 h, the microstructure exhibited a combination of both fine and coarse θ-Al$_2$Cu precipitates. The observation indicates that certain θ-Al$_2$Cu precipitates were dissolved back into the matrix (**Fig 5.12e** and **Fig 5.12e')**. The temperature of 505 °C that was utilized in the ST-D heat treatment is known to initiate the dissolution of θ-Al$_2$Cu [278].

Finally, samples that underwent the extended MS-ST, involving heating 495 °C for 4 h + 505 °C for 6 h + 530 °C for 12 h, were characterised. MS-ST has been reported in the literature to completely dissolve the large blocky θ-Al$_2$Cu precipitates in castings of Al-Cu based alloys [309,310]. However, in the present observation, it was unable to completely dissolve the θ-Al$_2$Cu precipitates. Particularly those located near micro-TiB$_2$ particles, this can be seen in **Fig 5.12f** and **Fig 5.12f'**. Overall, due to the MS-ST treatment, there was a significant reduction in the average number density of θ-Al$_2$Cu precipitates, and the inter-precipitate spacing increased, reaching a value (λ = 2.5 μm) nearly equivalent to the average grain size achieved after the MS-ST.

The incomplete dissolution of the θ-Al$_2$Cu phase, even after an extended MS-ST, can be attributed to the shielding effect exerted by micro-TiB$_2$ particles. This shielding effect reduced the contact area between θ-Al$_2$Cu and the Al matrix which significantly restricted the dissolution rate [311]. A similar phenomenon has been described by Asghar et al. in the context of an AlSi12Ni alloy, where the 3D interconnectivity of rigid Ni-aluminides with eutectic Si hindered the spheroidization of Si [312]. More recently, Zamani et al. [309] demonstrated that the interconnectivity of TiB_2 and Al_2Cu impedes the diffusion of Cu atoms along the grain boundaries and at the Al_2Cu/α-Al interface. This phenomenon was modelled by reducing the effective diffusion coefficient of Cu in Al by 2-2.5 times than its typical value.

5.6 A comparison of multiple-step (MS-ST) and single-step (SS-ST) solution treatments

As explained earlier, given that the MS-ST microstructure acts as the starting point for aging, the existence of undissolved precipitates around the micro-TiB_2 particles might lead to adverse consequences during the subsequent aging process. In order to differentiate the impact of the MS-ST on the aging behaviour, single-step solution treatments (SS-ST) were carried out. The reason for considering a SS-ST is twofold:

(i) In the AB state, low-melting phases like S-Al_2CuMg and Q-$Al_7Cu_3Mg_6$ were not detected by any characterization technique. The extended MS-ST is typically performed in castings to prevent incipient melting, largely due to the existence of these phases. In the context of LPBF processes, the rapid cooling rates (~10^4-10^7 K/s) can inhibit the formation of these phases [278]. Therefore, it becomes feasible to employ a SS-ST, specifically at 530 °C, to dissolve the θ-Al_2Cu eutectic, as shown in **Fig 5.7a**. As 530 °C is the temperature of the last step of the MS-ST which was meant to dissolve θ-Al_2Cu.

(ii) It has become apparent that the MS-ST allows migration and coarsening of θ-Al_2Cu near the micro-TiB_2 particles, making it challenging to achieve complete dissolution even after holding at 530 °C for 12 hours, see **Fig 5.12**. Consequently, employing a SS-ST has the potential to prevent the migration and subsequent coarsening of θ-Al_2Cu precipitates near the micro-TiB_2 particles.

Solutioning time was optimized by comparing three durations at 530 °C: 1 h, 6 h and 12 h. All the three conditions could be able to dissolve θ-Al_2Cu effectively, see **Fig 5.14**. However, solution treatment performed for 1 h was considered as it provides higher hardness (**Fig 5.12)**.

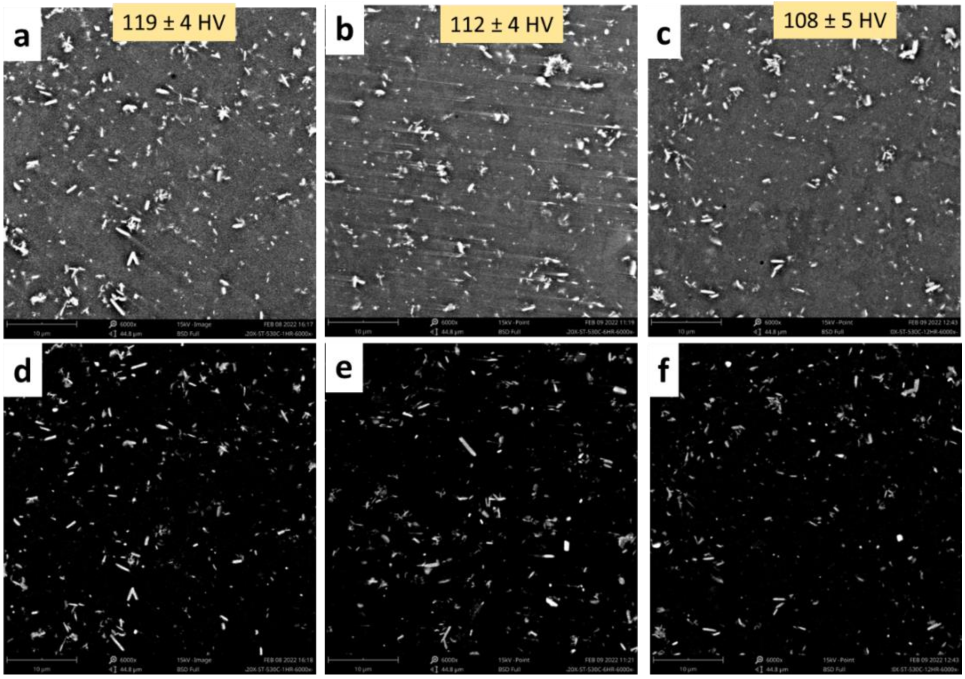

Fig 5.14: SEM-BSE micrograph under high and low brightness of A20X alloy solution treated at 530 °C for (a and d) 1h, (b and e) 6h, and (c and f) 12 h. The micro-hardness values are also mentioned in the rectangular box for each condition.

Following a SS-ST at 530 °C for 1 h, the specimen underwent aging at 190 °C for 6 hours, now called as short-T6. The results were compared with those of a specimen subjected to MS-ST, aged for 6 hours, denoted as the PA (long-T6). The microstructural comparisons were presented based on parameters such as the average size of θ-Al_2Cu, area fraction, and SEM-BSE micrographs (**Fig 5.15**). These microstructural features were summarized in **Table 5.2**.

In comparison to long-T6, the short-T6 exhibited notably smaller average sizes and reduced area fractions of θ-Al_2Cu phase **(Fig 5.15a)**. Furthermore, there was a minimal presence of θ-Al_2Cu precipitates in proximity to micro-TiB_2 particles in short-T6, as observed in **Fig 5.15b**, in contrast to long-T6 **(Fig 5.15c)**. This suggests that the majority of the θ-Al_2Cu eutectic was dissolved back into the α-Al matrix during SS-ST. The SS-ST further prevented the development of blocky Al_2Cu phases near micro-TiB_2 particles. This is in contrast quite evident with what was observed in the case of MS-ST **(Fig 5.12)**. This observation was also confirmed through the phase quantification by Rietveld refinement, indicated in **Table 5.2**. Short-T6 contains ~1 wt.% of Al_2Cu, whereas in long-T6 it was quantified as ~2 wt.%. The HAADF-STEM micrographs of the short-T6 specimen

(Fig 5.15d-e) revealed the presence of precipitates along grain boundaries and needle-shaped Ω and θ' precipitates within the grains. These microstructural features closely resembled those of the long-T6 state (**Fig 5.8**). The estimated dislocation density in short-T6, resulting from these matrix precipitates was in the same range as that measured in the long-T6 state ≈ $4.67 \times 10^{14}/\ m^2$. The average length of these matrix precipitates was ≈ 58 nm **(Fig 5.15f)**. However, their distribution exhibited a bimodal pattern suggesting the presence of some finer precipitates too.

Interestingly, the width of the PFZs near micro-TiB_2 particles (≈ 32 nm) and grain boundaries (≈ 43 nm) in the short-T6 was opposite to that observed in the long-T6 state. In the long-T6 state, the PFZ width was significantly greater near micro-TiB_2 particles compared to that near grain boundaries, see **Fig 5.11**. This decreased PFZs width near micro-TiB_2 particles has been ascribed to a more complete dissolution of θ-Al_2Cu in SS-ST. It is widely acknowledged that the presence of pre-existing precipitates accelerates the process of precipitation and exerts a significant influence on the aging behaviour [313–315]. The θ-Al_2Cu phase tends to coarsen preferentially at its pre-existing sites during aging, rather than forming an entirely new precipitate [314]. This rapid coarsening has detrimental effects on both the mechanical properties and corrosion resistance of the material, as it leads to an increase in PFZ width [315]. In the present study, it seems that the width of PFZs plays a pivotal role in the grain boundary cracking during aging. Multiple grain boundary cracks are indeed evident in the long-T6, whereas no such cracks were observed in the short-T6 (**Fig 5.16**). Consequently, the presence of pre-existing θ-Al_2Cu precipitates (incomplete dissolution) after the MS-ST alters the coarsening kinetics during aging and is thus undesirable to prevent the premature formation of PFZs.

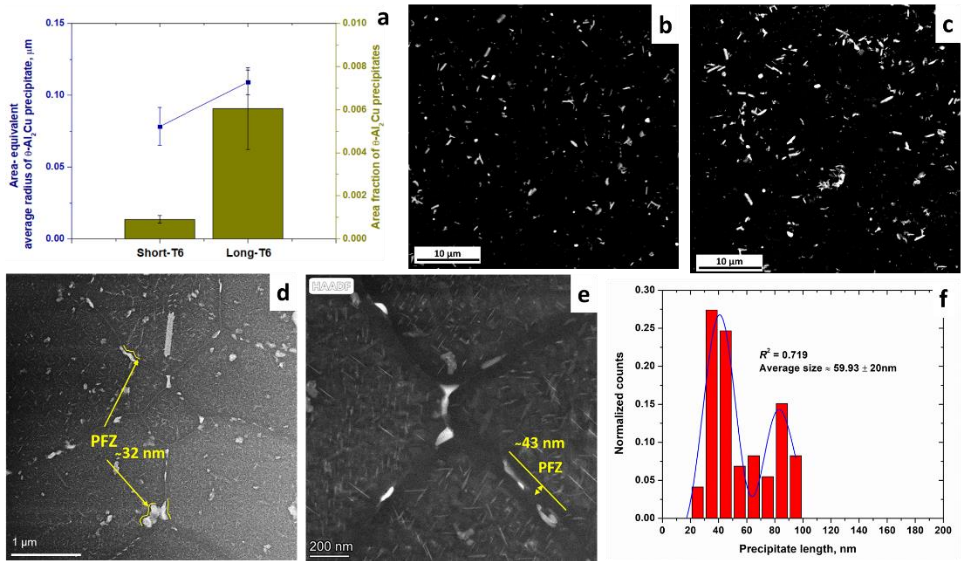

Fig 5.15: (a) Area-equivalent average radius and area fraction of θ-Al$_2$Cu precipitates in short-T6 and long-T6; SEM-BSE micrographs under low brightness (b) short-T6 and (c) long-T6 *(TiB$_2$ particles as grey and θ-Al$_2$Cu as white)*; HAADF-STEM micrographs of short-T6 indicating PFZs, (d) near micro-TiB$_2$ particles, (e) near grain boundaries and (f) matrix precipitates length distribution.

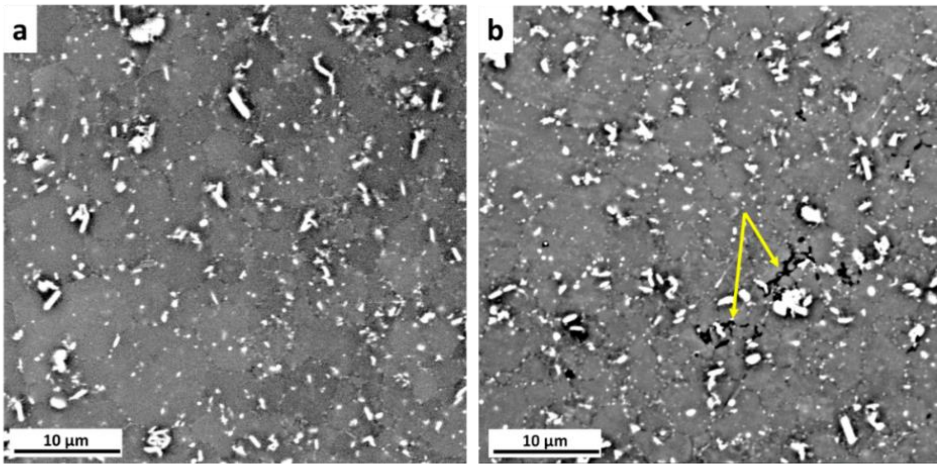

Fig 5.16: SEM-BSE micrographs of (a) short-T6 and (b) long-T6 *(Yellow arrows depict grain boundary cracks)*

5.7 Tensile behaviour

The mechanical behaviour of the A20X alloy post-processed with long-T6 and short-T6 is presented in **Fig 5.17**, along with the AB sample for a comparison. The microstructural attributes, along with curve characteristics such as yield strength (YS), ultimate tensile strength (UTS), and total elongation to fracture (e %), are detailed in **Table 5.2**.

Both long-T6 and short-T6 demonstrated an improved mechanical property i.e., considerable increase in the strength with no serrated flow (PLC effect) in the plastic regime with respect to the AB state **(Fig 5.17)**. This improvement can be attributed to the utilization of solute atoms such as Cu and Mg in the formation of matrix precipitates such as Ω and θ', as well as the precipitation of equilibrium θ-Al_2Cu phase during the aging. Moreover, there is a tendency for Mg to segregate at the grain boundaries, as seen in **Fig 5.8**.

When comparing short-T6 to long-T6, the tensile curve of short-T6 exhibited improvements in both strength and ductility. YS and UTS increased by 7.1% and 6.3%, respectively. Furthermore, the total elongation substantially increased by 45% (see **Table 5.2**). The reduced ductility observed in the long-T6 state can be attributed to the presence of grain boundary cracks and the creation of wide PFZs near micro-TiB_2 particles **(Fig 5.11)**. While grain boundary cracks have a more pronounced impact on ductility [304], PFZs exhibits lower strength than grain boundaries. Under the tensile loading, wide PFZs results in the formation of microcracks in these regions, which propagate more easily, leading to abrupt failure [316,317].

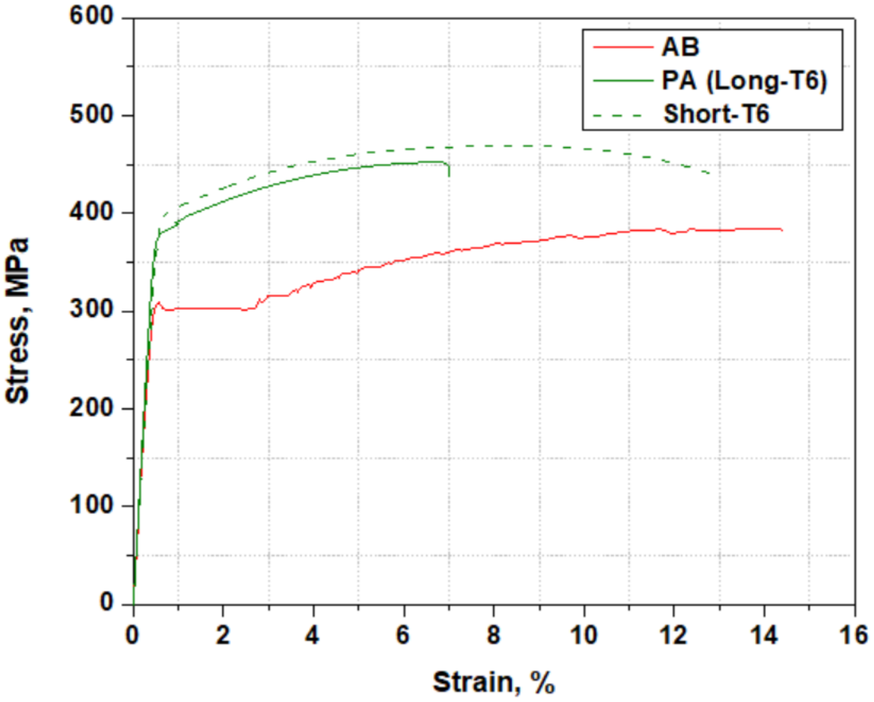

Fig 5.17: Tensile stress-strain curves of A20X alloy in the AB, PA (long-T6) and short-T6 conditions

Table 5.2: A summary of microstructural characteristics and mechanical properties of LPBF-A20X alloy in AB, PA (long-T6) and short-T6 conditions.

Sample	**Microstructural features**						**Mechanical properties**			
	Average grain size, µm	θ-Al_2Cu, wt.%	Length of nano-precipitates (Ω/θ’), nm	Dislocation density, x10^{14} /m^2	Width of PFZs, nm		Micro-hardness, HV	YS, MPa	UTS, MPa	e, %
					Near grain boundary	Near micro-TiB_2 particles				
AB	1.05 ± 0.4	~ 4	-	6.13 ±0.32	-	-	113 ± 4	304 ± 3	378 ± 6	12.5 ±1.6
MS-ST	1.97 ± 0.5	-	-	2.63 ±0.27	-	-	103 ± 5	-	-	-
PA (Long-T6)	2.17 ± 0.5	~ 2	54± 17	5.34 ±0.32	30 ± 6	85 ± 36	152 ± 6	370 ± 9	435 ± 13	7.3± 0.3
OA	1.93 ± 0.6	~ 4	82± 20 & 422± 63	4.14 ±0.28	78 ± 7	153 ± 58	124 ± 5	-	-	-
Short-T6	-	~ 1	58±25	4.67± 0.99	43 ± 8	32 ± 13	143 ± 2	396± 3	462 ± 4	10.6 ±1.8

5.8 Conclusions

In this chapter, the microstructural evolution of a long heat treatment (involving multiple-steps of solutioning) was firstly evaluated. Post to the analysis, a novel short heat treatment (short-T6) was proposed (involving single-step of solutioning) and compared with the peak condition of long heat treatment (long-T6). The principal findings of this investigation are as follows:

i. The cellular structure of the as-built (AB) state disappeared after the first step of solution treatment (MS-ST). The peak aged (PA) microstructure featured θ-Al_2Cu precipitates near micro- and nano-TiB_2 particles, primarily at the grain boundaries. The precipitation occurred in these locations due to the difference in thermal expansion coefficient between Al (matrix) and TiB_2 particles (ceramic). Excessive aging (OA) led to significant θ-Al_2Cu growth at micro-TiB_2 particle leading to engulfment.

ii. The low-temperature steps of the MS-ST disrupted the θ-Al_2Cu eutectic network into fine spheroidal particles that migrated towards micro-TiB_2, coarsening over time. The long MS-ST resulted in an incomplete θ-Al_2Cu dissolution, which was attributed to shielding effect of TiB_2 particles.

iii. PA and OA microstructures exhibited grain boundary cracks, more severe in the OA state. Grain boundary cracking originated from micro-strains caused by the precipitation of coherent-Ω and semi-coherent-θ’ phases in the grain interiors, coupled with widening of weak PFZs near grain boundaries and near micro-TiB_2 particles.

iv. PA (long-T6) exhibited 21% and 15% YS and UTS increases, respectively, compared to AB, but a 58% reduction in elongation to fracture. No PLC effect was observed in PA (long-T6).

v. Key microstructural factors contributing to PA hardness include: (i) presence of nano-sized coherent-Ω and semi-coherent-θ’ matrix precipitates (≈ 54 nm) (ii) optimal θ-Al_2Cu precipitation.

vi. The proposed single-step solution treatment (SS-ST) achieved a nearly complete θ-Al_2Cu dissolution. SS-ST-aged for 6 h microstructure (Short-

T6) showed a minimal θ-Al_2Cu precipitation near micro-TiB_2 particles. A narrower PFZs (≈ 32 nm) as compared to MS-ST-aged for 6h (long-T6) (≈ 85 nm), and no grain boundary cracks.

vii. Conversely, short-T6 displayed a 45% increase in elongation to fracture with respect to PA (long-T6), with 7.1% and 6.3% YS and UTS increases. Improved strength and ductility in short-T6 were attributed to the absence of grain boundary cracks.

According to the findings from this study, the suggested post-processing heat treatment for A20X alloy produced through LPBF presents superior mechanical characteristics when compared to the traditional long-T6 method. This alternative treatment is concise, straightforward, energy-efficient, and readily applicable in industrial settings.

Chapter 6

Comparison of natural and artificial aging behaviour of A20X alloy

6.1 Introduction

This chapter is a modified version of the journal article under review “Barode, Jayant and Vayyala, Ashok and Aversa, Alberta and Yang, Luyan and Mayer, Joachim and Fino, Paolo and Lombardi, Mariangela, *Natural and Artificial Aging Behaviour of Al-Cu-Ag-Mg-Tib2 (A205) Alloy Processed by Laser Powder Bed Fusion*”.

This chapter investigates another post-processing condition of LPBF-A20X alloy: single-step solution treatment followed by natural aging (NA) i.e., aging at room temperature. The results highlighted that the alloy shows a considerable response to the NA. The NA state was characterized by various techniques such as Vicker’s micro-hardness, DSC, XRD, SEM and TEM. The peak aged conditions of NA (T4) and artificially aged (Short-T6) were compared in terms of mechanical behaviour. In the end, structure-property correlation was established by estimating various strengthening mechanisms in the AB, T4 and short-T6 conditions.

6.2 Methodology

The A20X as-built parts manufactured by the optimized processing conditions were post-processed by two heat treatments:

(i) **NA**: Solution treatment at 530 °C for 1 h + water quenching + room temperature aging (28 °C).

(ii) **AA**: Solution treatment at 530°C for 1 h + water quenching + aging at 190 °C + air cooling.

Only the peak aged conditions of NA and AA were characterized further and compared. The peak aged conditions of NA and AA are termed as T4 and short-T6, respectively.

6.2 Results

6.2.1 Micro-hardness response

The micro-hardness evolution under natural aging and artificial aging specimens is presented in **Fig 6.1**. There was a rapid increase in the micro-hardness values of A20X specimens when artificially aged from the as-quenched state i.e., 0 h to 2 h. The A20X specimens reached their peak hardness value of 144 HV upon 4 h of artificial aging and retained the peak hardness up to 8 h. Aging longer than 8 h, only slightly decreased the hardness.

For the NA, the hardness developed more gradually. The A20X samples reached their peak hardness value after 20 days of natural aging (~138 HV). Then, the hardness value remained constant up to 100 days.

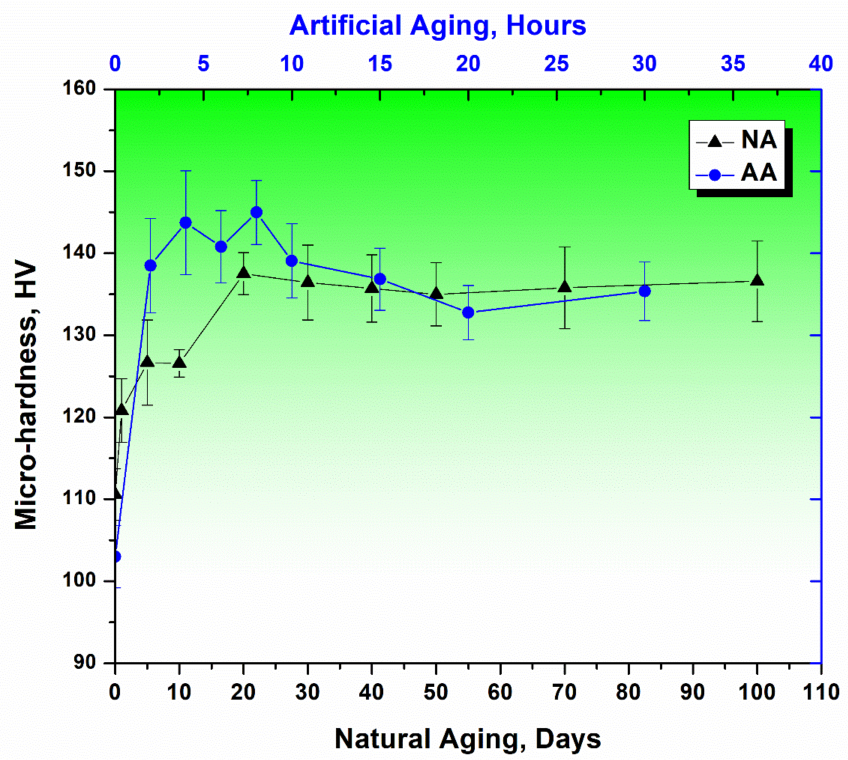

Fig 6.1: Micro-hardness evolution as a function of natural and artificial aging time

6.2.2 Thermal analysis:

DSC thermograms of NA and AA specimens are shown in **Fig 6.2**. The heat flow behaviours at low- and high-temperatures are presented in **Fig 6.2a** and **Fig 6.2b,** respectively. Only one endothermic peak was found in the 60-180 °C temperature range (**Fig 6.2a**). This peak has been associated with the dissolution of Ag-Mg co-clusters [318–321]. The area under the curve continued to increase as a function of NA time and the peak temperature slightly shifted towards higher temperatures. This indicates that Ag-Mg co-clusters were formed and have grown during NA. No endothermic peak was observed in the case of NA-0 days and AA-4h specimen (**Fig 6.2a**).

At higher temperatures **(Fig 6.2b)**, two more peaks were observed. First, is an exothermic peak, that corresponds to the precipitation of stoichiometric Al_2Cu in various forms, namely, Ω, θ' and θ as identified in Chapter 5 [320]. The second, is a broad endothermic peak that indicates the dissolution of all forms of Al_2Cu

precipitates. The dissolution occurred over a wide range of temperatures with its peak around 525 °C.

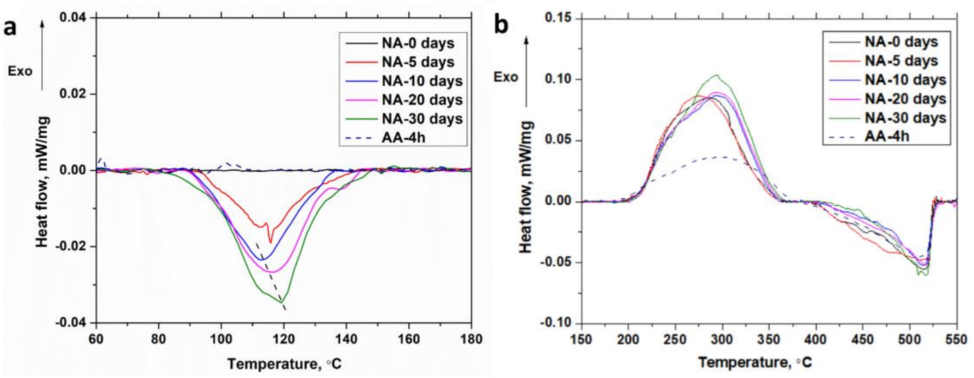

Fig 6.2: Heat flow behaviour of NA for various number of days and AA for 4 h in (a) low-temperature and (b) high-temperature range

6.2.3 Phase analysis

The peak aged conditions in both naturally aged and artificially aged specimens were considered for further characterizations and from now on, T4 indicates “naturally aged for 20 days” and short-T6 indicates “artificially aged for 4 h”.

The XRD patterns of T4 and short-T6 are shown in **Fig 6.3.** Their whole line profile in **Fig 6.3a**. Three phases were observed, namely, Al, θ-Al$_2$Cu and TiB$_2$. The individual peak profile of θ-Al$_2$Cu {110} and Al {111} planes are presented in **Fig 6.3b** and **Fig 6.3c**. It was demonstrated in Chapter 5 that single-step solutioning allowed a complete dissolution of eutectic θ-Al$_2$Cu [320]. The primary {110} peak of θ-Al$_2$Cu appears in the short-T6 specimen indicating that artificial aging causes a precipitation of this phase while it was absent in a T4 specimen suggesting a more complete dissolution (**Fig 6.3b)**. In addition, the short-T6 resulted in a broader Al {111} peak than the T4 one indicating a higher dislocation content. The estimated dislocation density values were calculated based on the W-H plot. The dislocation density in the short-T6 specimen (4.5×10^{14} /m^2) was almost twice to that of T4 specimen (2.1×10^{14} /m^2).

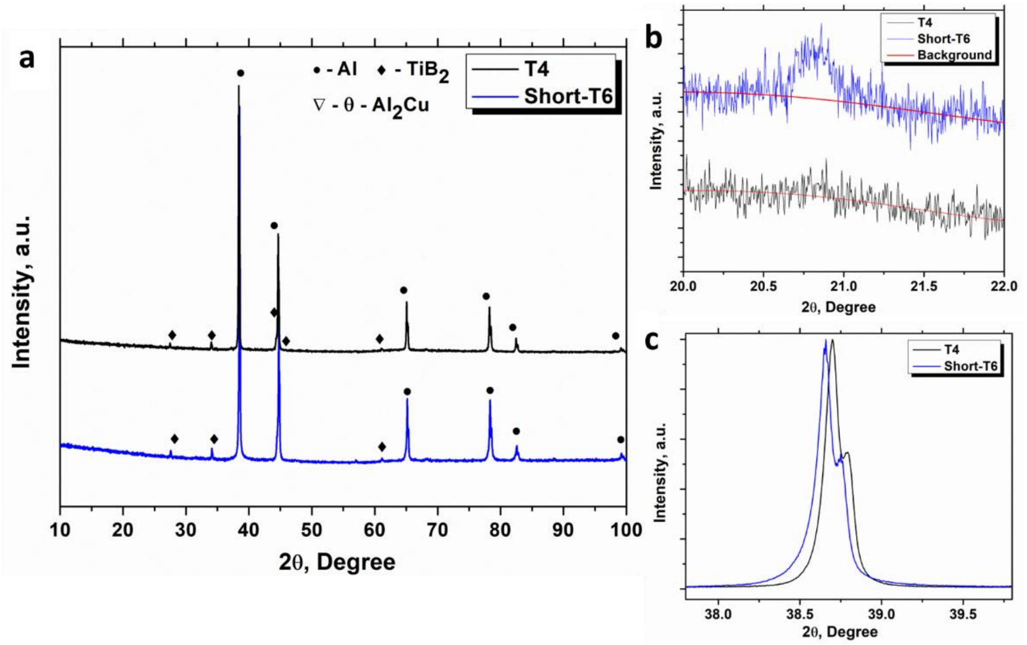

Fig 6.3: XRD patterns of T4 and short-T6 samples showing (a) whole line profile, (b) θ-Al_2Cu {110} and (c) Al {111}.

6.2.4 Microstructure:

The microstructural characterization of T4 and short-T6 samples was carried out by EBSD **(Fig 6.4)**, SEM **(Fig 6.5)** and HAAD-STEM **(Fig 6.6** and **Fig 6.7)**.

The EBSD data are reported as IPF maps (**Fig 6.4a** and **Fig 6.4b)**, phase maps **(Fig 6.4c and Fig 6.4d)** and grain size distributions **(Fig 6.4e and Fig 6.4f)**. Both post-processing conditions revealed a highly isotropic microstructure i.e., no presence of texture or directional grains. The average grain size in T4 and short-T6 specimens were 2.77 µm and 2.43 µm, respectively. The corresponding phase map distinguished the TiB_2 particles showing their distribution. These micrometric ceramic particles were usually observed at the grain triple junctions and grain boundaries (GBs) while some finer-TiB_2 particles were also located inside the grains. The average size of these TiB_2 particles was around ≈ 0.72 µm. Under the SEM-BSE mode **(Fig 6.5)**, the Al-matrix appeared grey while both TiB_2 particles and Al_2Cu phase were observed as bright. In the AA specimen, discontinuous precipitates were observed as white dots at the grain boundaries **(Fig 6.5b)**. Such grain boundary precipitates were not observed in the NA specimen (**Fig 6.5a)**. The solutes that remained within the Al lattice after solutioning did not precipitate out at grain boundaries during T4, and thus the average concentration of solutes inside the grains was obtained by performing the EDS spot analysis and resulted Cu (4.8 ± 0.20), Ag (0.99 ± 0.63) and Mg (0.25 ± 0.05) wt.%.

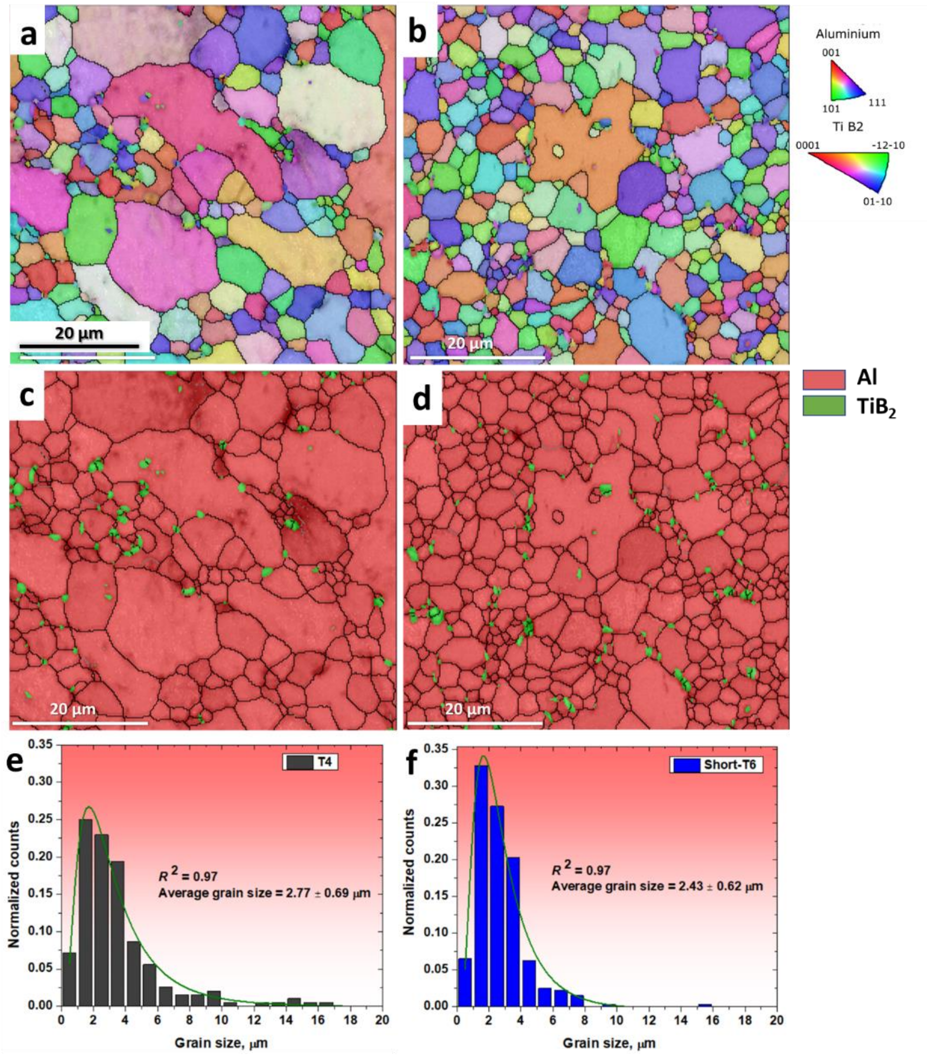

Fig 6.4: EBSD micrographs of A20X samples post-processed with T4 (a, c, and e) and short-T6 (b, d and f). Showing (a and b) IPF map, (c and d) phase map, and (e and f) grain size distribution

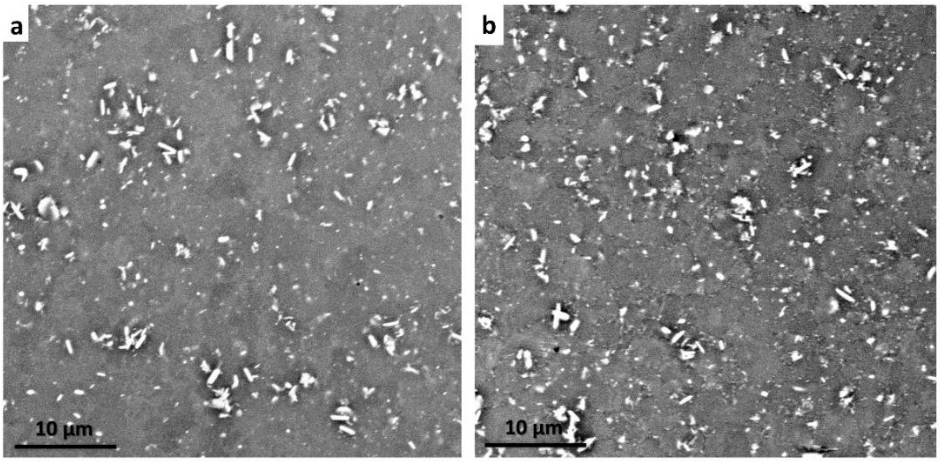

Fig 6.5: SEM-BSE micrographs of (a) T4 and (b) short-T6 specimen

Characterizations by a HAAD-STEM are displayed in **Fig 6.6** and **Fig 6.7**. **Fig 6.7a-b** confirmed the presence of grain boundary precipitates and precipitates at micro/nano-TiB_2 particles in a short-T6 specimen. These precipitates are likely to be of an equilibrium θ-Al_2Cu phase (irregular Cu rich phase). Such precipitation leads to the formation of precipitate free zones (PFZs) in their vicinity, as observed in **Fig 6.7b**. In addition, STEM micrographs also revealed the presence of high number density ($\approx 5.05 \times 10^{21}/m^3$) plate-type matrix precipitates having an average thickness (t_t) and diameter (d_t) of 1.7 nm and 53 nm, respectively **(Fig 6.7b)**. These plate-type precipitates correspond to the coherent-**Ω** and semi-coherent-θ' precipitates [322,323]. The morphological features of the precipitates in an artificial aged specimen were quantified by ImageJ 1.53 k software. Their volume fraction (f_v) and number density per unit volume (n) were calculated from the TEM micrographs by the Nei and Muddle method [324,325]:

$$n = \frac{N_1 + N_2}{A_{Obs} \times (T + d_t)} \tag{6.1}$$

$$N_2 = N_1 \times \frac{T + d_t}{\sqrt{A_{Obs}}} \tag{6.2}$$

$$f_v = n t_t \times \frac{(\pi d_t^{-2})}{4} \tag{6.3}$$

Where N_1 is the number of precipitates observed, N_2 is the number of precipitates not visible, due to weak contrast and overlapping of precipitates in the same region, A_{Obs} is the area of the observed region, T is the foil/lamella thickness, t_t and d_t are the average precipitate thickness and diameter, respectively.

In the T4 specimen, no plate-type Ω/θ’ precipitates were witnessed within the Al-matrix and even the grain boundaries were free from precipitates **(Fig 6.6a-b)**. Some of the irregular or spherical shaped Cu rich phases, possibly of θ-Al_2Cu were located inside the matrix and near nano-TiB_2 particles.

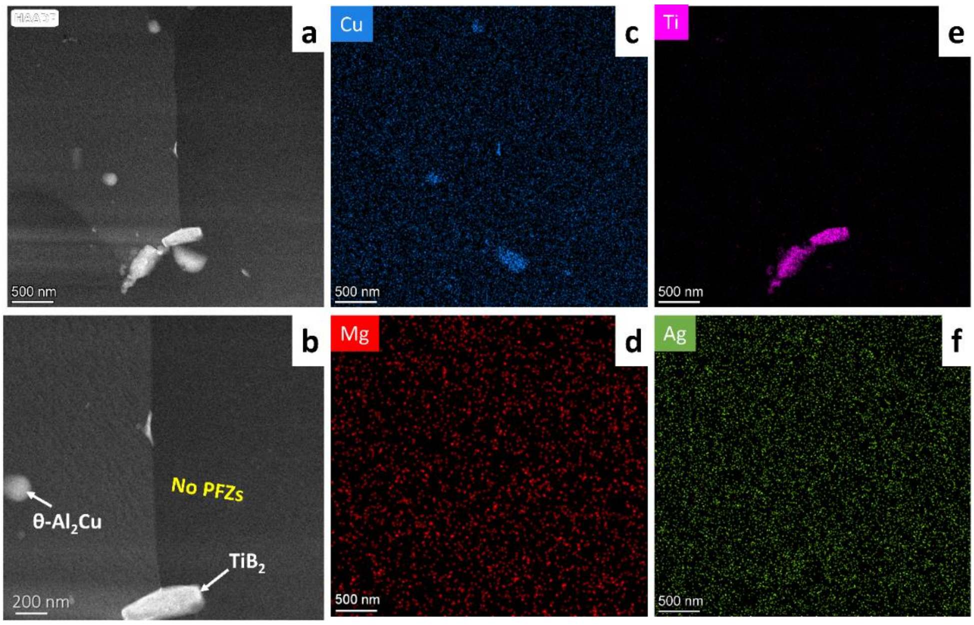

Fig 6.6: T4 (a-b) HAADF-STEM micrographs and (c-f) EDS maps of the (a) region

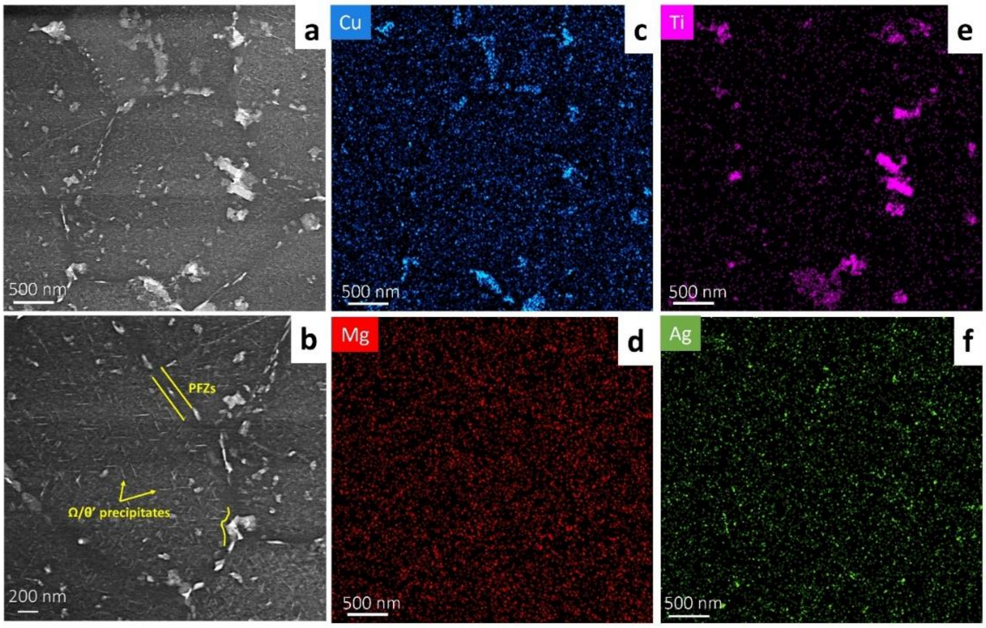

Fig 6.7: Short-T6 (a-b) HAADF-STEM micrographs and (c-f) EDS maps of the (a) region

6.2.5 Tensile behaviour:

The mechanical behaviour of T4 and short-T6 specimens under tensile loading is presented in terms of engineering stress-strain curves in **Fig 6.8**. The tensile behaviour of the as-built (AB) state was also considered for comparison. The curve characteristics such as yield strength (σ_y), ultimate tensile strength (σ_{UTS}) and elongation to fracture (ε_f %) are summarised in **Table 6.1**. It is to note that T4 specimens displayed an excellent elongation to fracture with respect to both short-T6 and AB states. Interestingly, T4 samples also have a σ_{UTS} comparable to short-T6 ($\Delta\sigma_{UTS} \approx 29$ MPa). However, the σ_y of T4 specimens was much lower (≈ 276 MPa) than the short-T6 one (≈ 464 MPa) but comparable to AB ($\Delta\sigma_y \approx 28$ MPa). Interestingly, no PLC effect was observed in both T4 and short-T6 states.

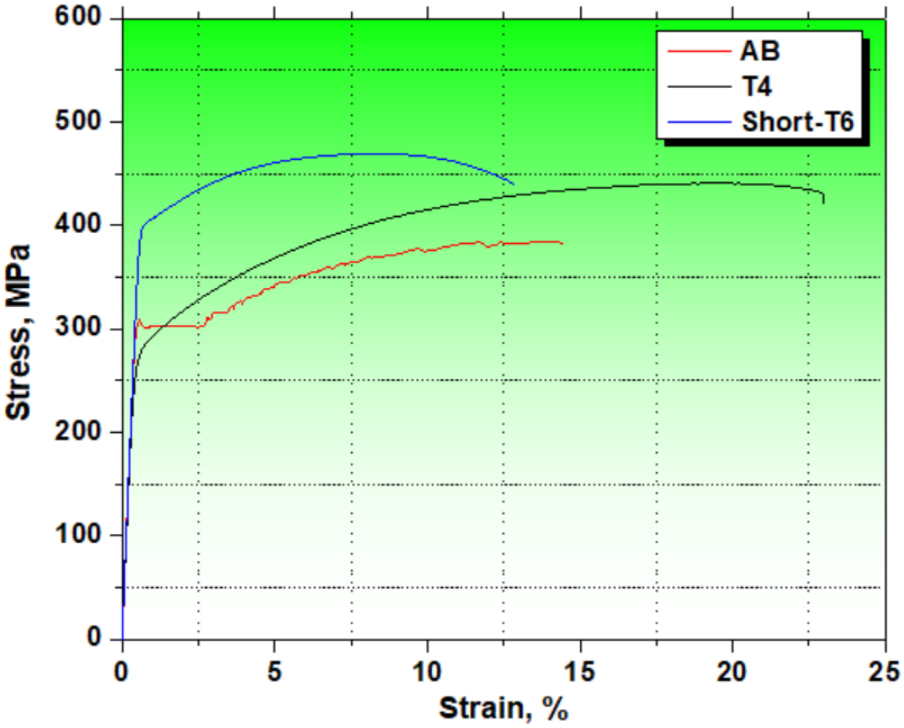

Fig 6.8: Representative engineering stress-strain curves of LPBF-A20X alloy for various conditions

Table 6.1: Characteristics of tensile curves in various conditions

Condition	Micro-hardness, HV	σ_y, MPa	σ_{UTS}, MPa	ε_f, %
T4	137 ± 2	276 ± 3	434 ± 4	20.4 ± 1.9
Short-T6	144 ± 6	397 ± 3	463 ± 5	11.6 ± 1.1
AB	113 ± 4	304 ± 3	378 ± 6	12.5 ± 1.6

6.3 Discussion

6.3.1 Age hardening behaviour

The LPBF-A20X alloy demonstrated a considerable amount of hardening during NA **(Fig 6.1)**. The increase in hardness from NA-0 days to NA-20 days was around 27 HV. The gradual increase in hardness has been attributed to the formation and growth of disordered Ag-Mg co-clusters [326–329]. The gradual increment in hardness with NA time was justified by DSC patterns **(Fig 6.2a)**. The increase in the peak area of Ag-Mg co-clusters dissolution with NA time indicates in fact that their volume fraction continuously increased during natural aging. Notwithstanding this continuous increase, we did not observe further increment of hardness after 20 days (**Fig 6.1**). This could be due to the growth of some co-clusters above a critical size above which they do not have further influence on hardness [330]. The formation of other known clusters in an Al-Cu-Mg alloy such as Cu-Mg and Cu-Cu was not observed in NA samples **(Fig 6.2a)**. The dissolution of Cu-Mg and Cu-Cu clusters occurs in the range of 200-230 °C [330,331] and 140-190 °C [332–334], respectively. These peaks were not detected by DSC in the present case. The absence of such clusters can be explained based on the results of Nagai et al. [335] and Ferragut et al. [221], who have studied the role of Ag on early cluster formation in an Al-Cu-Mg alloy. They observed that, a minor addition of Ag stabilizes the Mg-vacancy clusters during quenching or in the initial stages of aging by forming Ag-Mg-vacancy complexes. This was due to the stronger binding energy of Mg and Ag atoms with the vacancies than with the Cu atoms [328,329,336].

Unlike the NA condition, the hardening response of AA at 190 °C was quite steep **(Fig 6.1)**. Just after 2 h of aging there was a sudden increase in hardness up to around 138 HV and it reached its peak after 4 h (144 HV). The sudden rise of strength has been associated with the precipitation of plate-type coherent **Ω**-Al_2Cu and semi-coherent θ'-Al_2Cu, see **Fig 6.7b**. However, among them, **Ω** offers much higher strength than θ' due to its precipitation at the primary glide plane {111} of Al and also possesses superior coarsening resistance to growth [216,323,337,338]. Aging at 190 °C for more than 8 h caused a decrease in hardness. This might be due to the coarsening of the equilibrium θ-Al_2Cu phase near TiB_2 particles/at the grain boundaries and to the growth of θ' precipitates within the grains [320].

6.3.2 Strengthening mechanisms:

The A20X is a precipitation hardening alloy and it was confirmed that the alloy also gains its strength under natural aging. However, the responsible strengthening factors vary among different post processing conditions (AB, T4 and short-T6) due to their different microstructural features such as Ag-Mg co-clusters, Ω/θ' precipitates, solid solution (SS) and grain (GB) or cell boundaries.

Pre-existence of TiB_2 particles in the A20X powders further strengthens the material [243,320,339].

The estimation of the total yield strength (σ_{Total}) in AB, T4 and short-T6 conditions can be obtained by the sum of their individual strengthening increments [339]:

$$\sigma_{Total} = \Delta\sigma_{TiB_2} + \Delta\sigma_{Ag-Mg\,co-cluster} + \Delta\sigma_{\Omega/\theta'\,precipitates} + \Delta\sigma_{GB} + \Delta\sigma_{SS} + \sigma_0 \quad (6.4)$$

Where σ_0 is the lattice friction in pure Al (20 MPa) [339]. The contributions from all the strengthening mechanisms in various conditions and the constants utilized for calculations are presented in **Table 6.2** and **Table 6.3**, respectively.

6.3.2.1 Strengthening from TiB_2 particles:

The presence of a ceramic component in the matrix improves the yield strength of the material by multiple strengthening mechanism: (i) load-bearing strengthening, (ii) Orowan strengthening, (iii) modulus mismatch strengthening, and (iv) coefficient of thermal expansion (CTE) mismatch strengthening.

The volume fraction (V_P), average diameter (d_p) and inter-particle distance between the TiB_2 particles (λ) were obtained from the SEM-BSE micrographs. Being the same material (A20X), V_P, d_p and λ are considered the same for all the conditions namely AB, T4 and short-T6.

(i) *Load-bearing strengthening:*

TiB_2 particles enhance the strength of the material by directly transferring the load from the matrix to them [243,339]. The load-bearing strengthening contribution to the yield strength can be expressed as [340].

$$\Delta\sigma_{LB} = V_P \frac{1}{2} \sigma_m \quad (6.5)$$

Where V_P is the volume fraction of TiB_2 particles and σ_m is the yield strength of the matrix (σ_m= 289 MPa) [339]. The V_P was found to be around 1.3%. The increment in σ_y by the load-bearing strengthening was calculated to be 1.89 MPa.

(ii) *Orowan strengthening:*

During deformation, the hard TiB_2 particles cannot be cut-off by dislocations but instead they are by-passed by forming dislocation loops. This dislocation looping decreases the dislocations mean free path and the material experiences strengthening. The increase in yield strength by Orowan strengthening can be calculated as [243,339].

$$\Delta\sigma_{Orowan} = \frac{0.13G_m b}{\lambda}\ln\frac{d_p}{2b} \tag{6.6}$$

Where G_m is the shear modulus of the matrix (26.9 GPa), b is the burger vector (0.286 nm), d_p is the average particle diameter and λ is the inter-particle distance between the particles. The d_p and λ were calculated from SEM-BSE images and resulted as 0.72 μm and 3.26 μm, respectively. The Orowan strengthening was about 2.20 MPa.

(iii) *Modulus mismatch strengthening:*

An increment in the yield strength can be also due to the elastic modulus mismatch between the matrix and the particles [243]. It can be calculated as:

$$\Delta\sigma_{Modulus-TiB_2} = \sqrt{3}\alpha_{mt}G_m b\sqrt{\rho_{Moludus}} \tag{6.7}$$

$$\rho_{Modulus} = \frac{6V_p}{bd_p}\varepsilon_y \tag{6.8}$$

Where α_{mt} is a constant with a value of 0.5, it represents dislocation strengthening coefficient [243], $\rho_{Moludus}$ is the dislocation density arising due to the modulus mismatch, and ε_y is the yield strain of the composite. The contribution of modulus hardening to the yield strength resulted as 9.44 MPa.

(iv) *Coefficient of thermal expansion (CTE) mismatch strengthening:*

Additional dislocations are generated at the interface of Al-matrix and TiB_2 particles due to the difference in their coefficient of thermal expansion (CTE) and are responsible for the increment in strength of the material. The CTE of Al-matrix is 23.5×10^{-6} K^{-1} and for TiB_2 is 7.8×10^{-6} K^{-1} [243], thus the ΔCTE_{Al-TiB_2} = 16.8 x 10^{-6} K^{-1}. During processing or post processing steps involving temperature changes such as solidification in the case of AB or solution-quenching for T4 and short-T6 state, the estimation of a dislocation density and an increment of the strength can be calculated from the following equations [243,339]:

$$\Delta\sigma_{CTE} = \beta_{CTE} G_m b \sqrt{\rho_{CTE}} \tag{6.9}$$

$$\rho_{CTE} = \frac{12\, \Delta CTE\, \Delta T\, V_p}{b d_p\, (1 - V_p)} \tag{6.10}$$

Where β_{CTE} is a geometric constant of 1.25 [339], ρ_{CTE} is dislocation density arising due to CTE mismatch, ΔCTE is the thermal expansion coefficient difference between matrix and ceramic component and ΔT is the temperature difference. The value of ΔT is 635 K for the AB state i.e., from melting to room temperature and 505 K for T4 and short-T6 i.e., from solutioning temperature to room temperature. The dislocation generation and/or annihilation during artificial aging was neglected. The increment in the yield strength arising from the ΔCTE mismatch is around 26.78 MPa for AB state and 23.88 MPa for T4 and short-T6 conditions.

6.3.2.2 Strengthening from Ag-Mg co-clusters:

The presence of disordered clusters in the matrix increases the strength by two mechanisms: (i) modulus mismatch strengthening and (ii) coherent strengthening. The former is due to the difference in the elastic modulus between the matrix and atomic clusters or co-clusters, whereas the latter is due to the lattice mismatch. The strengthening contributions to the yield strength can be obtained from the following equation [330,339,341]:

$$\Delta\sigma_{Modulus-Clusters} = 1.4 {\alpha_{mc}}^{3/2}\, \Delta G^{3/2} f^{1/2}\, b \left(\frac{r}{b}\right)^{\frac{3\beta_{mc}}{2}-1} (2\pi\Gamma)^{-1/2} \tag{6.11}$$

$$\Delta\sigma_{CS-Clusters} = M \alpha_\varepsilon (G_m \varepsilon_c)^{3/2} \left(\frac{rf}{0.5 G_m b}\right)^{1/2} \tag{6.12}$$

Where α_{mc} and β_{mc} are constants that can be obtained from a dislocation-precipitate interaction model, their values are 0.096 and 0.76 respectively [330]. ΔG is the difference in the shear modulus of Al-matrix and Ag-Mg co-clusters (ΔG =2.6 GPa) [339]. Γ is the line tension of a dislocation in the matrix which is usually approximated as $\frac{1}{2} G_m b^2$ [330,341]. α_ε is a constant of 2.6 for FCC metals [342] and ε_c is the strain associated with the atomic cluster misfit with the matrix, which is around 1% for Ag-Mg co-clusters in the A20X alloy [339]. f and r are the volume fraction and average radius of the clusters. The volume fraction of Ag-Mg co-clusters in T4 has been approximated based on the Ag and Mg concentration inside the grains by EDS spot analysis and with an assumption that Ag and Mg form clusters in 1:1 atomic ratio. This assumption was based on multiple atom probe tomography (APT) studies on Al-Cu-Mg-Ag alloy [215,343,344]. The concentration of Mg was ≈ 0.25 wt.% which corresponds to the volume fraction of clusters as 0.0071. It has been reported that, Ag-Mg co-clusters were hard to be identified by TEM, this seems true also in the present investigation, see **Fig 6.6a**, and a more advanced techniques such as APT has been suggested [345,346]. However, in the present study, the average radius of the co-clusters in T4 was assumed as 1.8 nm (≈ 50 atoms). It was an average of the Ag-Mg co-cluster size (10-100 atoms) observed in an early stages of aging by various APT studies [347,348]. f in the AB state was taken as 0.0034 from the similar study on LPBF of A20X alloy with the same linear energy density (0.24 J/mm) [339]. In the short-T6 specimen, as the DSC did not show any sign of Ag-Mg co-clustering i.e., no endothermic peak in **Fig 6.2a**, it is reasonable to neglect the hardening from atomic clusters. The strengthening contribution obtained from $\Delta\sigma_{\mathrm{Modulus-Clusters}}$ in AB and T4 state were 1.41 MPa and 2.07 MPa, respectively and from $\Delta\sigma_{\mathrm{CS}}$ in AB and T4 state are 42.64 MPa and 64.05 MPa respectively.

6.3.2.3 Contribution from plate-type Ω/ θ' precipitates:

Interaction of dislocations with the precipitates can strengthen the material by either dislocation looping (Orowan strengthening) or by dislocation shearing (interfacial strengthening) mechanisms [296,324]. The character of a dislocation-precipitate interaction mechanism depends on its crystal structure, aspect ratio, volume fraction and number density.

There have been number of studies demonstrating that Ω plates were sheared by dislocations [349–351]. In contrast, θ' precipitates interacts by forming dislocation loops [352,353]. However, being precipitated on {111} Al plane, Ω plates provides more effective strengthening than {100} θ' plates [296,349]. For simplicity, it was assumed that all the plate-type precipitates (Ω and θ') in a short-T6 condition strengthen the material by dislocation shearing. No strengthening contribution from precipitates in T4 and AB conditions were considered. Nei and Muddle [324] have developed a model on dislocation shearing of plate-type precipitates that nucleated on {111} plane of Al, considering the effect of precipitate shape, orientation, and distribution on the increment in the yield strength of the alloy:

$$\Delta\sigma_{\Omega/\theta' \text{ precipitates}} = \frac{1.211\,\mathrm{M}d_t\gamma_i^{3/2}}{t_t^2}\sqrt{\frac{bf_v}{\Gamma}} \tag{6.13}$$

Where M=3.06 is the Taylor factor for polycrystalline materials, Γ is dislocation line tension, γ_i is the interfacial energy corresponding to the new interface (0.14 J/m^2) [296], f_v is the volume fraction of **Ω** precipitates, calculated from the TEM micrographs as 0.019 **(Eq. 6.1-6.3)**. t_t and d_t are average plate thickness and diameter with a value of 1.7 nm and 53 nm, respectively. The strengthening increment to the yield strength by the Ω/θ' precipitates was 254.90 MPa.

6.3.2.4 Grain boundary strengthening:

The strengthening contribution from the GBs can be calculated with the classical Hall-Petch relation [354].

$$\Delta\sigma_{GB} = kd^{-1/2} \tag{6.14}$$

Where k is the Hall-Petch coefficient, which represents the ability of the GBs to impede the dislocation motion. The value of k ranges from 0.04 MPa$\sqrt{m}$ for a fully recrystallized grain to 0.26 MPa$\sqrt{m}$ for a highly deformed ultra fine grain [354,355]. In the present study, two distinctive values of k have been considered: 0.17 MPa$\sqrt{m}$ for representing cellular microstructure of the AB state, the θ-Al_2Cu cell boundaries offers high obstacle to dislocation motion [339] and 0.14 MPa$\sqrt{m}$ representing matrix with a large number of high-angle grain boundaries (HAGBs) [354] for the case of T4 and short-T6 state. d is the average grain size of the alloy as 0.91 μm [320], 2.77 μm and 2.43 μm for AB, T4 and short-T6 conditions **(Fig 6.4e-f)**. The strength increments by grain boundary strengthening in an AB, T4 and short-T6 state are 169 MPa, 84 MPa and 90 MPa, respectively. Such a considerable strengthening increment to the yield strength was due to their finer grain sizes which is a typical characteristic of a LPBF process.

6.3.2.5 Solid solution strengthening:

The strengthening increment by solid solution can be calculated by the following equation [356].

$$\Delta\sigma_{SS} = \sum_{i=\text{element}} k_i \times c_{ss,i}^n \tag{6.15}$$

Where k_i is the strengthening contribution related to the solute-dislocation interaction [357]. For Cu and Mg, the k_{Cu} = 13.8 MPa/wt.% and k_{Mg} = 18.6 MPa/wt.%, respectively [339,356]. It was reported that Ag atoms have no strengthening effect in an Al alloys due to their negligible lattice misfit [358]. $c_{ss,i}^{n}$ is the concentration of solute i in the solid solution and n is a constant with a value of 1 [356]. The solid solution strengthening in the short-T6 state can be neglected, since Cu, Mg and Ag were all responsible for the precipitation of **Ω**, θ and θ' (Al_2Cu) and were either consumed by the precipitates during the process of nucleation and growth or constrained within the Al-precipitate interfaces [215,216,344,356]. In the T4 state, only solid solution strengthening from Cu atoms was considered, as it was assumed that all the Mg atoms bind to the Ag atoms to form Ag-Mg co-clusters. The concentration of Cu was around 4.8 wt.%. In the AB state, both Cu and Mg atoms contribute to the strengthening. The concentration of Cu and Mg were taken from the work of Jiang et al. [339], which have reported the solute concentration of A20X alloy in AB state processed by LPBF. The Cu and Mg concentration are 1.58 wt.% and 0.16 wt.%, respectively. The solid solution strengthening ($\Delta\sigma_{SS}$) in the AB and T4 state were 25 MPa and 66 MPa, respectively.

A summary of all the contributions from various strengthening factors in the AB, T4 and short-T6 states are presented in the **Table 6.2**. Strengthening due to the presence of TiB_2 particles was around ≈ 40 MPa in the AB and ≈37 MPa for both T4 and short-T6 conditions. Being processed by LPBF, the grain size strengthening significantly contributes to all the conditions, although the AB state has a cellular microstructure (eutectic θ-Al_2Cu cell boundaries) which offers much higher resistance to the dislocation motion than in T4 and short-T6 states (≈ 165 MPa). Strengthening in a T4 state was majorly due to coherent strengthening from disordered Ag-Mg co-clusters (≈ 64 MPa) and solid solution strengthening by Cu solutes (≈ 66 MPa), whereas in the short-T6 state, interfacial strengthening was dominated by the presence of high number density of plate-type Ω/θ' precipitates (≈ 254 MPa). The calculated yield strength in various processed and post-processed conditions were within the 5% deviations of the experimental values **(Table 6.2)** indicating a good match with the experimental.

Table 6.2: Summary of the strengthening factors in various conditions

Strengthening factors	AB, MPa	T4, MPa	Short-T6, MPa
σ_0	20	20	20
$\Delta\sigma_{GB}$	166	84	90
$\Delta\sigma_{SS}$	25	66	-
$\Delta\sigma_{TiB_2}$	40	37	37
$\Delta\sigma_{Ag-Mg\ co-cluster}$	44	66	-
$\Delta\sigma_{\Omega/\theta'\ precipitates}$	-	-	255
σ_{Total}	295	273	402
σ_y	304	276	397
$\sigma_y - \sigma_{Total}$	9	3	-5

Table 6.3: Summarizing different parameters with their physical meaning utilized in various strengthening mechanism [243,330,339,342,354,355].

Strengthening mechanism	Parameter	Value	Physical meaning
Al	G_m	26.9 GPa	Shear modulus
	M	3.06	Taylor factor for polycrystalline
	b	0.286 nm	Burger vector
	Γ	1.1 x 10^{-15} $MPam^2$	Dislocation line tension
	σ_0	20 MPa	Resistance to glide dislocation in the lattice
$\Delta\sigma_{GB}$	k	0.14 and 0.17 $MPa\sqrt{m}$	Obstacle to dislocation by grain boundary
$\Delta\sigma_{CTE}$	β_{CTE}	1.25	Geometric constant
$\Delta\sigma_{Modulus-TiB_2}$	α_{mt}	0.5	Dislocation strengthening coefficient
$\Delta\sigma_{Modulus-Clusters}$	α_{mc}	0.096	Constants from dislocation-precipitate interaction
	β_{mc}	0.76	
`$\Delta\sigma_{CS-Clusters}$	α_c	2.6 GPa	Constant for FCC metal
$\Delta\sigma_{\Omega/\theta'\ precipitates}$	γ_i	0.14	Specific interfacial energy between precipitate and matrix phase

6.4 Conclusion:

In the present study, we have demonstrated the response of A20X alloy processed by LPBF towards natural aging (NA) i.e., solution treatment followed by aging at room temperature, and compared it with an artificial aging (AA). The following conclusions can be drawn:

1. The LPBF A20X alloy achieved its peak hardness in around 20 days of NA at a temperature of ≈ 28 °C, whereas it took 4 h at 190 °C in the case of AA. The difference between the peak hardness values was ≈10 HV.

2. The tensile behaviour of naturally aged (T4) and artificially aged (short-T6) conditions were compared. The ultimate tensile strength of T4 was comparable to short-T6, with a difference of only 6.2 %. T4 caused a considerable improvement in the elongation to fracture with respect to short-T6 (43 %). However, the yield strength of T4 was 30 % lower than the short-T6 one.

3. The major strengthening contributions for the T4 were coherency strengthening by the Ag-Mg co-clusters and solid solution strengthening by Cu atoms, whereas strengthening by the dislocation shearing of Ω/θ’ plate-type precipitates was dominant in short-T6.

4. Grain boundary strengthening also contributed significantly to both T4 and short-T6.

To summarise, both post-processing heat treatments improved the mechanical property of the A20X alloy with respect to as-built state. The T4 gives good-strength and high-ductility whereas, the short-T6 provides high-strength and good ductility combination to the alloy, thus, one can get benefitted from both the heat treatments based on their intended application.

Chapter 7

Strain hardening and fracture behaviour of post-processed LPBF-A20X alloy

The chapter presents a preliminary study on understanding the deformation behaviour of the A20X alloy in its post-processing states. The post-processed conditions investigated are: T4 and T6. Two artificial aging were considered: short-T6 and long-T6. The T4 specimen demonstrated considerable strain hardening with respect to both the short-T6 and long-T6. Additionally, T4 had delayed necking and displayed much larger uniform elongation. Further, an attempt was made to understand the failure mechanism in all the post-processed conditions.

7.1 Introduction

The A20X alloy is specifically designed for structural applications, thus understanding its strain hardening behaviour is important for several reasons [359–368]:

(i) Strain hardening behaviour provides critical insights into how a material responds to mechanical deformation. In structural applications, components often experience various levels of stress, including cyclic loading and impact. An understanding of strain hardening helps engineers to select materials that can withstand these stresses and maintain their mechanical properties over time.

(ii) In predictive modelling, strain hardening data can be used in numerical simulations and finite element analysis to predict the behaviour of LPBF parts under different loading conditions. This helps engineers assess the structural integrity and performance of components before they are manufactured, saving time and resources in the development process.

Thus, understanding strain hardening behaviour is crucial for the successful design, fabrication, and performance assessment of LPBF parts in structural applications. It enables engineers to make informed decisions regarding material selection, design optimization, and process control to ensure the safety, reliability, and durability of these printed components.

7.2 Strain hardening behaviour

The mechanical behaviour of various post-processing conditions along with the as-built (AB) condition is presented in terms of engineering stress-strain curves **(Fig 7.1a)**. As it is better to utilize the true stress-strain curves for strain hardening investigation. The true stress-strain curves were extracted from the engineering stress-strain data by the following equation:

$$\varepsilon = \ln(1 + e) \tag{7.1}$$

$$\sigma = s(1 + e) \tag{7.2}$$

Where σ and ε are the true stress and true strain, respectively. e and s are the engineering stress and engineering strain, respectively. These equations are based on two assumptions: constant volume and uniform stress and strain over the gauge length of the specimen [369,370]. Thus, they are valid upto necking and no longer valid thereafter. As the state of the stress and strain becomes complex and non-uniform after necking. The true stress-strain curve is presented in **Fig 7.1b**. The strain hardening behaviour was understood from the standard Kocks-Mecking (K-M) plots, as demonstrated in **Fig 7.2**. The K-M plot shows the correlation between the strain hardening rate (Θ) vs. reduced flow stress [359,360]. The strain hardening rate is defined as $\Theta = d\sigma/d\varepsilon$. The reduced flow stress is calculated as $(\sigma - \sigma_y)$, where σ_y is the yield strength of the material. The K-M plots of the post-processed conditions are shown in **Fig 7.2a** and the AB condition in **Fig 7.2b**. Due to the serrated flow behaviour of the AB state, the strain hardening behaviour was not investigated.

In order to compare the strain hardening behaviour quantitatively, two parameters were extracted from the K-M plots as demonstrated elsewhere [359,360]. The two parameters were Θ_0 and β (**Fig 7.2a)**. Θ_0 is the initial strain hardening rate i.e., at the beginning of the plastic deformation and can be obtained by extrapolating the linear relation of plastic stage to the yield stress, as shown in **Fig 7.2a**. A high value of Θ_0 indicates quick strain hardening [360]. The second parameter, β is proportional to the rate of dynamic recovery i.e., the rate of dislocation annihilation/rearrangement surpasses the rate of dislocation storage [371]. A low value of β represents a low rate of dynamic recovery and was determined from the linear slope of the dotted lines ($\beta = -d\Theta/d(\sigma - \sigma_y)$) [360]. The values extracted from the K-M plots are presented in **Table 7.1**. The Θ_0 values for T4, short-T6 and long-T6 were 2.76 GPa, 2.36 GPa and 2.22 GPa, respectively. Whereas the β values were 9.26, 26.78 and 28.74, respectively. The uniform elongation was determined from the Considère's criterion [372]. The Considère's criterion signifies the onset of necking at the point where the strain-hardening rate (Θ or $d\sigma/d\varepsilon$) is equal to the true stress (σ). According to this criterion, the intersection of the two curves, Θ vs. ε and σ vs. ε occurs at the uniform elongation (ε_u) (see **Fig 7.3)**. The T4 specimens exhibited large uniform elongations (ε_u) of ≈17.96% whereas the short-T6 ($\varepsilon_u \approx$ 7.3%) and long-T6 ($\varepsilon_u \approx$ 6.2%) specimens had much lower uniform elongation i.e., early necking formation.

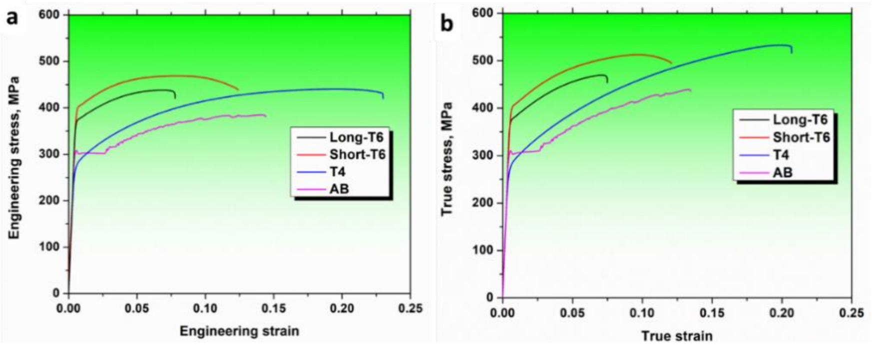

Fig 7.1: Tensile behaviour of the AB and various post-processed conditions (a) engineering stress-strain, and (b) true stress-strain curves.

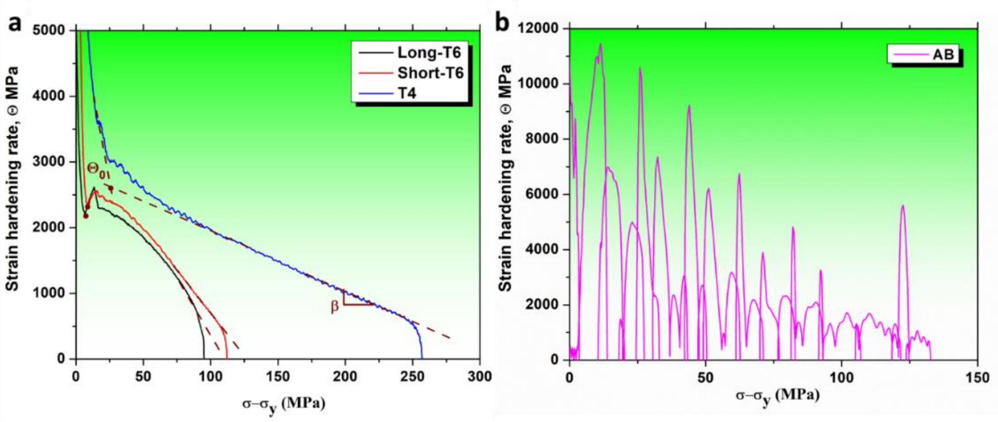

Fig 7.2: The strain hardening rate as a function of reduced flow stress for (a) post-processed conditions and (b) as-built condition.

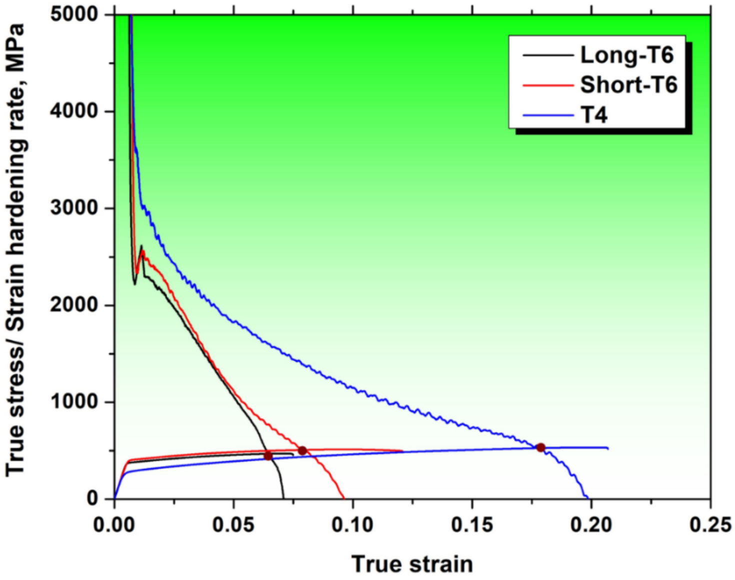

Fig 7.3: True stress-strain (σ vs. ε) and K-M (Θ vs. ε) plots showing the uniform elongation at their intersection in all the post-processed conditions.

Table 7.1: Characteristics of the strain hardening behaviour of various post-processing conditions.

Condition	K-M Plot		
	Θ_0, GPa	β	ε_u, %
T4	2.76 ± 0.12	9.26 ± 0.12	17.17 ± 0.61
Short-T6	2.36 ± 0.04	26.78 ± 1.45	7.32 ± 0.52
Long-T6	2.22 ± 0.02	28.74 ± 2.18	6.25 ± 0.14

The T4 specimens demonstrated superior ductility and a high uniform elongation than the T6 specimens. Such a behaviour could be well understood from the strain hardening behaviour. The K-M plots were similar for all the post-processed conditions **(Fig 7.2a)**. All curves were majorly characterized by two regions based on the evolution of Θ:

(i) initially a sudden linear drop in the early stages of plastic deformation i.e., after yielding.

(ii) a gradual linear decrease and thereafter a sudden drop to zero.

The discussion associated with such a strain hardening behaviour for T4 and T6 (short-T6 and long-T6) conditions are presented separately as below:

T4:

The higher value of Θ_0 (2.76 GPa) indicated that the T4 specimens hardened very quickly in the early stages of plastic deformation with respect to the T6 specimens (**Table 7.1**). Furthermore, the value of $\beta \approx 9.26$ was much lower than short-T6 ($\beta \approx 26.78$) and long-T6 ($\beta \approx 28.74$).

This quick hardening and low dynamic recovery have been associated to the (i) high concentration of solute Cu atoms (≈ 4.8 wt.%) within the Al matrix, and (ii) the presence of Ag-Mg co-clusters (volume fraction, $f = 0.0071$) **(see chapter 6)**. Both these microstructural features contributed to the strength and increased dislocation storage, which resulted in a higher Θ_0 [359,373,374]. The Cu solute atoms would slow down the mobility of the mobile dislocations and inhibit the dislocation annihilation by the action of solute drag [373–375]. Furthermore, Ag-Mg co-clusters have been reported to reduce the stacking fault energy of Al that restricts the dislocation motion to cross-slip [220,376]. Thus, with the mild dynamic recovery rate, the dislocation storage would continue to dominate throughout the deformation which significantly delays the necking formation or uniform elongation.

T6:

In the case of T6 i.e., short-T6 and long-T6, the lower value of Θ_0 and higher values of β **(Table 7.1)** has been associated to the (i) loss of Cu solid solution from the matrix, (ii) dissolution of Ag-Mg co-clusters, and (iii) precipitation of the shearable **Ω**-Al_2Cu precipitates.

During artificial aging to 190 °C for 4 h, most of the Cu solute atoms were consumed and confined within the Al_2Cu type of precipitates such as θ, θ' and **Ω**. The Mg and Ag atoms are known to form a monolayer at the broad interface of the **Ω** plates and Al during the early stages of artificial aging [216]. Furthermore, the **Ω** precipitates are shearable by dislocations [296,377] and thus, do not contribute to the dislocation storage. As the shearable precipitates hinders the dislocation slip without promoting the processes of dislocation storage [378]. Thus, the rate of dynamic recovery dominates in the artificially aged conditions and leads to an early formation of necking ($\varepsilon_u \approx 7.3$ % and 6.2% for short-T6 and long-T6, respectively) as compared to the T4 ($\varepsilon_u \approx 17.2$ %).

A small peak in the early stages of strain hardening i.e., increase in Θ was also observed only in the case of T6 specimens, see **Fig 7.2a**. This could be due to the interaction of mobile dislocations with the pre-existing high dislocation density in short-T6 ($\approx 4.5\text{x}10^{14}/\text{m}^2$) and long-T6 ($\approx 5.4\text{x}10^{14}/\text{m}^2$) (**Table 5.2**).

7.3 Failure mechanism

The fractured analysis was carried out by SEM-SE/BSE micrographs of all the post-processed conditions i.e., T4 **(Fig 7.4a-c)**, short-T6 **(Fig 7.4d-f)** and long-T6 **(Fig 7.4g-i)**. The A20X alloy in all the post-processing conditions displayed a mix of fine and medium sized circular dimples representing a ductile fracture behaviour **(Fig 7.4a-b, d-e and g-h)**. Observing the fracture surface at a higher magnification in a SEM-SE mode and their corresponding SEM-BSE micrographs **(Fig 7.4c, f and i)** revealed the presence of TiB_2 and θ-Al_2Cu particles seated inside the dimples, indicating that brittle fracture would have occurred at these micro-TiB_2/Al_2Cu and Al-matrix interfaces. Their identification was done by the EDS spot analysis, presented in **Fig 7.5**. The TiB_2 and θ-Al_2Cu particles are pointed out by blue and red arrows, respectively.

In the T4 condition, the θ-Al_2Cu particles are less, as most of the eutectic θ-Al_2Cu, that dissolved back into the matrix during solution treatment, did not precipitate during NA **(Fig 6.3b)**. Among the artificially aged conditions, the long-T6 **(Fig 7.4f)** has more θ-Al_2Cu particles (red arrows) than short-T6 **(Fig 7.4d)**. In the long-T6 samples, due to the presence of multiple-steps of solutioning, there were more incomplete dissolution of θ-Al_2Cu **(Fig 5.12)**, that further grows preferentially during artificial aging.

The fractography **(Fig 7.4)** doesn't give a clear picture on the failure initiation mechanism thus, the cross-sectional micrographs perpendicular to the fractured surface were analysed (**Fig 7.6)**. They revealed the presence of micro-voids at the TiB_2 particles/agglomerates (blue arrow) in all the post-processed conditions. Besides these, in the short-T6 and long-T6, there were also multiple cracks, marked as yellow arrows **(Fig 7.6d and Fig 7.6f)**. Moreover, the severity of such cracks is higher in the long-T6 **(Fig 7.6f)** than short-T6 **(Fig 7.6d)**. It is important to highlight that most of the cracks were located at the grain boundaries.

The formation of these grain boundary cracks could be explained by the following mechanism, during deformation, the matrix precipitates (Ω/θ') were either being sheared or by-passed by dislocations. At higher strain values, the matrix becomes hardened, and dislocations gets piled-up at the grain and sub-grain boundaries causing a highly localized strain. This would result in a nucleation of voids near the weak precipitate free zones (PFZs) that were present along the grain boundaries and at triple junctions leading to an intergranular fracture [317,379]. The long-T6 samples have the higher crack density **(Fig 7.6f)** and are characterised by wider PFZs (≈ 85 nm **(Chapter 5)**) than short-T6 ((≈30 nm **(Chapter 6)**) along the grain boundaries. It is widely accepted that, a wider PFZs are more vulnerable to cracking during deformation. The higher cracking density in the long-T6 specimens were further supported by the presence of pre-existing cracks prior to tensile tests **(Chapter 5)**.

No such grain boundary cracks were observed in the T4 specimen **(Fig 7.6e)** as there were neither grain boundary precipitates which promotes weak PFZs nor high strength Ω/θ'-Al_2Cu precipitates which hardens the Al-matrix relative to grain boundaries (**Fig 6.6a-b)**. Thus, in the T4 specimen, the failure initiation is solely at TiB_2 particles which were located at the grain boundaries and at grain triple junctions **(Fig 6.6b)**, which also lead to intergranular fracture at higher strains.

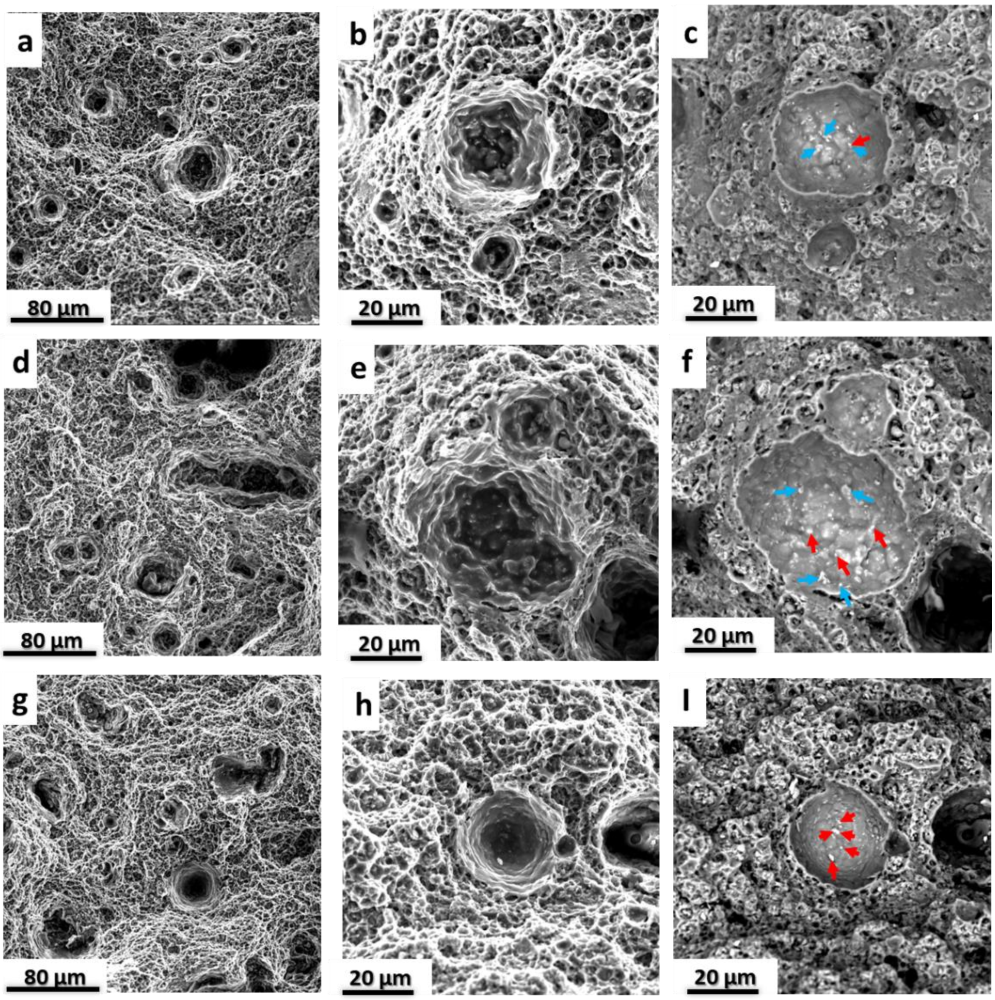

Fig 7.4: SEM-SE micrographs of the fractured surface at low magnification (a, d and g), at high magnification (b, e and h) and their corresponding BSE micrographs (c, f and i) of T4 (a-c), short-T6 (d-f) and long-T6 (g-i). *(Blue and red arrows showing TiB_2 and θ-Al_2Cu particles, respectively)*

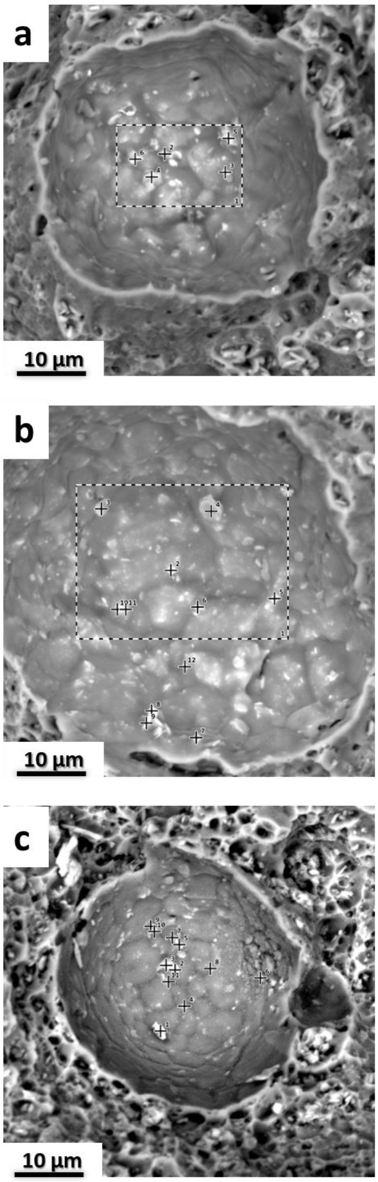

Location	Al, wt.%	Ti, wt.%	Cu, wt.%	Others, wt.%
Spot 2	57.20	24.80	15.65	2.35
Spot 3	82.29	4.91	12.80	-
Spot 4	57.89	28.87	9.26	3.98
Spot 5	57.11	37.76	5.13	-
Spot 6	68.28	8.41	20.75	2.56

Location	Al, wt.%	Ti, wt.%	Cu, wt.%	Others, wt.%
Spot 2	72.31	22.02	5.68	-
Spot 3	70.42	27.08	2.45	0.05
Spot 4	51.30	42.09	0.63	5.48
Spot 5	90.85	3.45	5.71	-
Spot 6	60.80	33.71	5.48	0.01
Spot 7	78.51	10.76	8.02	2.71
Spot 8	52.62	41.73	2.00	3.65
Spot 9	62.88	34.28	2.84	-
Spot 10	64.07	7.47	24.55	3.91
Spot 11	63.44	5.47	27.79	3.3
Spot 12	57.89	4.80	33.51	3.8

Location	Al, wt.%	Ti, wt.%	Cu, wt.%	Others, wt.%
Spot 1	63.59	4.08	32.33	-
Spot 2	59.34	3.81	36.47	0.38
Spot 3	65.12	-	34.88	
Spot 4	37.35	-	62.65	-
Spot 5	55.43	-	44.57	-
Spot 6	57.19	-	42.81	-
Spot 7	54.19	-	42.82	-
Spot 8	51.00	-	49.00	-
Spot 9	59.85	2.10	29.99	8.06
Spot 11	55.52	-	44.48	-

Fig 7.5: SEM micrographs of the fractured surface and EDS spot analysis on various particles in (a) T4, (b) short-T6 and (c) long-T6

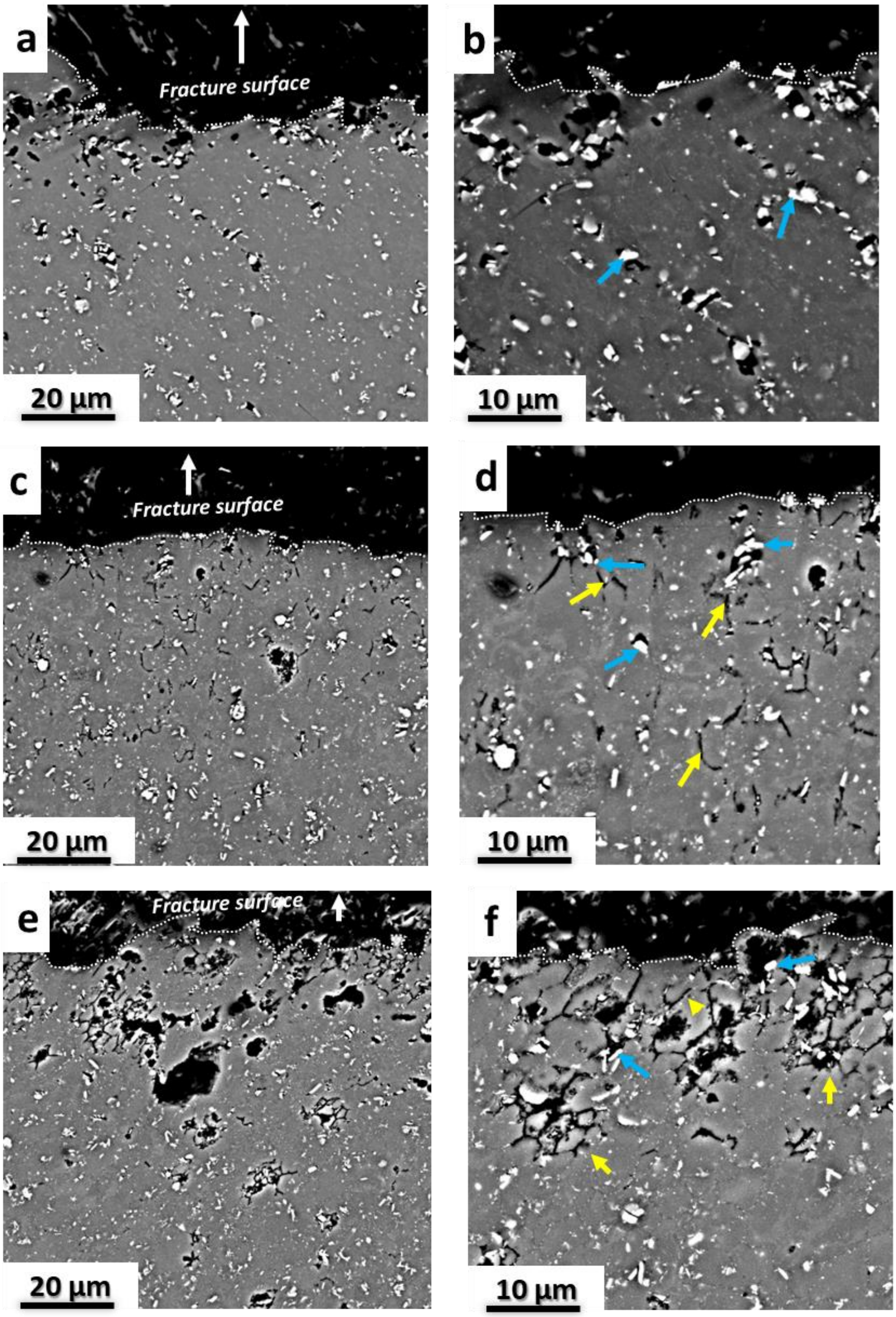

Fig 7.6: SEM-BSE micrographs of the regions perpendicular to the fractured surface in various post-processed conditions: (a-b) T4; (b-c) short-T6 and (c-d) long-T6. *(blue and yellow arrow showing micro-voids at the TiB_2 particles/agglomerates and cracks, respectively)*

7.4 Conclusion

Strain hardening and fracture behaviour of the A20X alloy post-processed with T4 and T6 (short-T6 and long-T6) was investigated. The outcomes are the following:

i. During plastic deformation, the T4 demonstrated superior strain hardening capability than short-T6 and long-T6. Also, the uniform elongation of T4 (ε_u = 17.7%) was higher than short-T6 (ε_u = 7.3%) and long-T6 (ε_u = 6.2%).

ii. The higher uniform elongation of the T4 specimens was due to the high amount of Cu solid solution and presence of Ag-Mg co-clusters. Both these microstructural features contributed to the dislocation storage.

iii. In the case of short-T6 and long-T6, the lower uniform elongation was associated to the loss of Cu solid solution, dissolution of Ag-Mg co-clusters and the precipitation of shearable Ω-Al_2Cu in the matrix. The shearable precipitate doesn't contribute to the dislocation storage.

iv. Fractography studies revealed the ductile failure with fine and uniform dimples at the surface whereas regions with Al-TiB_2 interface failed in a brittle manner in all the post-processed conditions.

v. The failure initiation mechanism was different in T4 with respect to short-T6 and long-T6. In T4, the failure initiates solely by the formation of micro-voids at the individual TiB_2 particles and at their agglomerates, whereas in both short-T6 and long-T6, it was by the combination of micro-void formation at TiB_2 particles and by grain boundary cracking due to presence of PFZs.

Chapter 8

Effect of hot isostatic pressing on the mechanical behaviour

8.1 Introduction

This chapter presents an attempt to understand the role of hot isostatic pressing (HIPing) on the microstructure and mechanical behaviour of the LPBF-A20X alloy. Although, the results are preliminary, and the work is ongoing.

The chapter is divided into two parts based on the post-processing conditions, as shown in a figure below. In Part-1, the HIP treatment was accompanied by solution treatment followed by quenching with the help of uniform rapid cooling (URC) module to simulate the cooling rate similar to the water quenching. The HIP treatment was then followed by artificial aging. In Part-2, the HIP treatment was considered as a stand-alone heat treatment and was then followed by furnace cooling. Because of this reason, a separate solution treatment was performed, and then artificially aged.

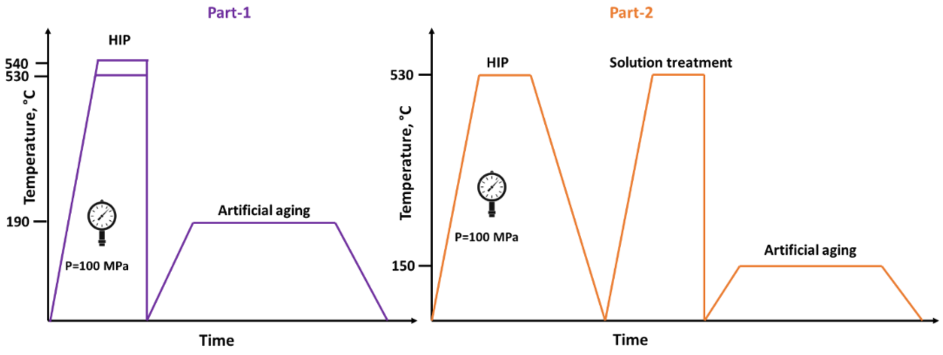

8.2: Part-1

8.2.1 Methodology

This study was carried out on the as-built (AB) samples printed using the set of parameters optimized based on the porosity content (see Chapter 4). The HIP was carried out under pressure of 100 MPa. Two HIPed solutioning temperatures were considered, 530 °C and 540 °C, the dwell time was 1 h.

After HIPing, the samples were rapidly cooled using the URC module and then artificially aged at 190 °C for 4 h. The artificially aged samples after HIPed were compared with the short-T6 ones. The nomenclature of the various conditions of HIPed and non-HIPed samples are presented in a **Table 8.1**.

Table 8.1: Nomenclature of the various heat treatments and their processing conditions

Heat treatment	Temperature, pressure, and time
ST-ST	530 °C for 1 h
Short-T6	530 °C for 1 h + 190 for 4 h
HIP-1	530 °C and 100 MPa for 1 h
HIP-2	540 °C and 100 MPa for 1 h
HIP-2A	540 °C and 100 MPa for 1 h + 190 C for 4 h

8.2.2 Results

8.2.2.1 Porosity analysis:

Fig 8.1 shows the optical micrographs of various conditions of HIPed and non-HIPed. Most of the porosities are fine in size and circular in shape (red arrows). Based on features, these are likely to be gas porosities. The porosity contents, evaluated by images analysis, are presented in **Table 8.2**. The average porosity content in the AB and solution treated (SS-ST) conditions were 0.070% and 0.074% respectively. After HIPing, the average porosity content slightly decreased i.e., HIP-1 and HIP-2 had around 0.028% and 0.051%, respectively. Although considering the standard deviation, the porosity content of all the post-processed conditions were similar.

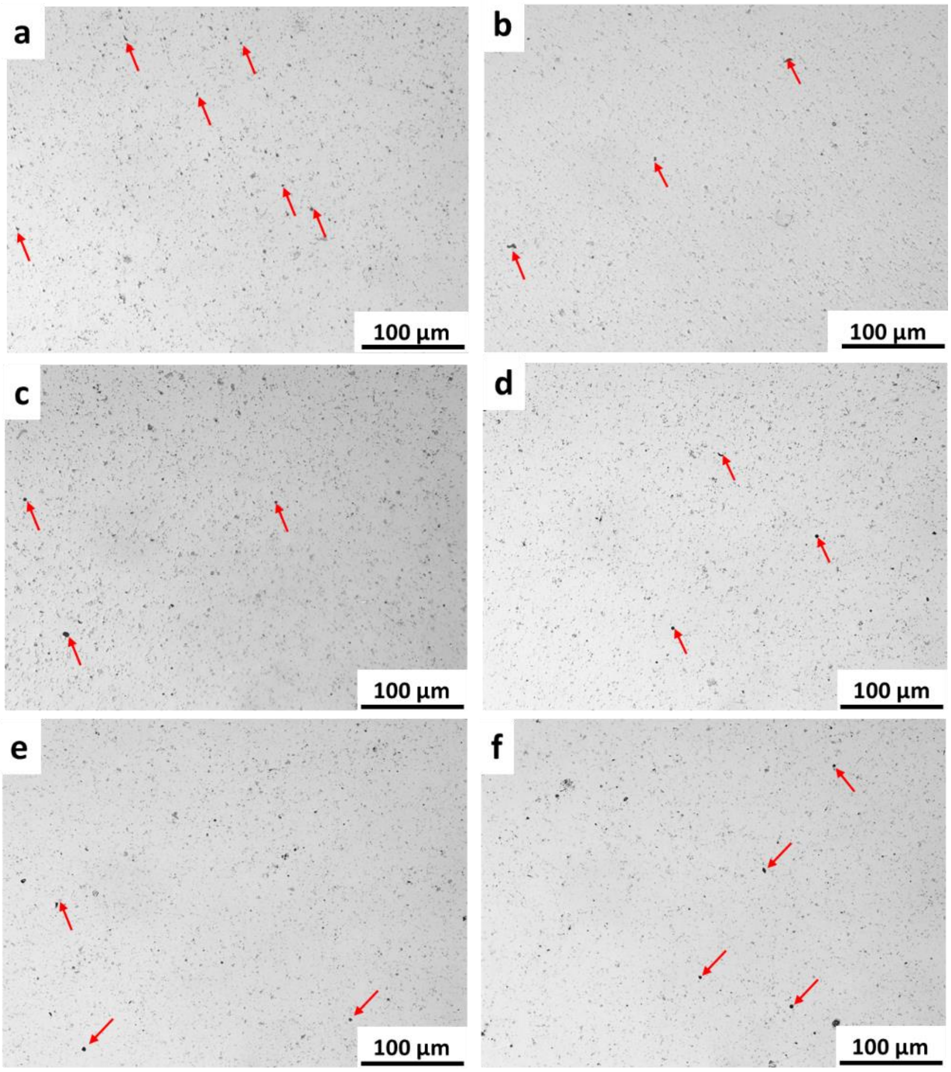

Fig 8.1: Optical micrography of the (a) AB, (b) SS-ST, (c) Short-T6 (d) HIP-1 (e) HIP-2, and (f) HIP-2A *(Red arrows showing porosities)*

Table 8.2: Porosity content of various conditions of HIPed and non-HIPed A20X alloy

Condition	**Porosity content, %**
AB	0.070 ± 0.040
SS-ST	0.074 ± 0.015
Short-T6	0.036 ± 0.052
HIP-1	0.028 ± 0.008
HIP-2	0.051 ± 0.037
HIP-2A	0.056 ± 0.001

8.2.2.2 Phase analysis:

Fig 8.2 display the XRD patterns of the HIPed and non-HIPed conditions. The whole line profile is presented in **Fig 8.2a** and the individual peak profile of θ-Al_2Cu {110} in **Fig 8.2b**. The phases identified were Al, TiB_2 and θ-Al_2Cu. Observing the individual peak profile of the θ-Al_2Cu {110} **(Fig 8.2b)**, an incomplete dissolution of the θ-Al_2Cu phase can be noticed in both HIP-1 and HIP-2. Whereas a more complete dissolution was observed in the SS-ST condition. For the aged conditions, the intensity of the θ-Al_2Cu peak was increased in the case of HIP-2A indicating that the θ-Al_2Cu phase has also increased, but the curve remained flat in the case of short-T6 **(Fig 8.2b)**.

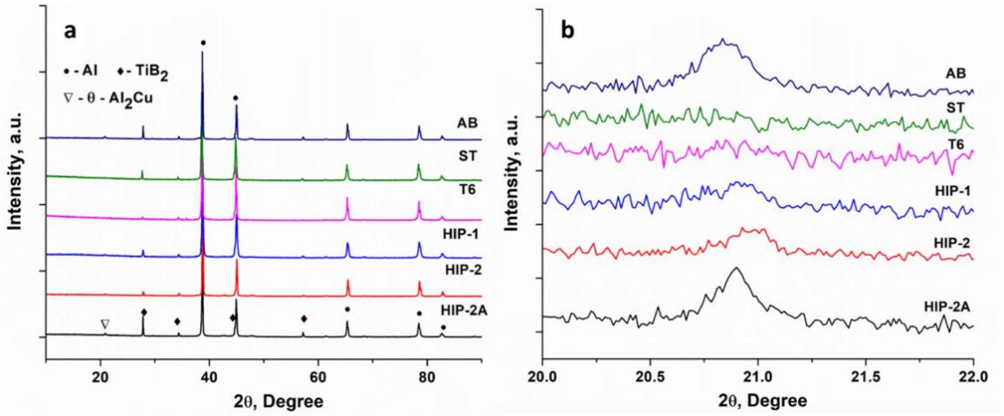

Fig 8.2: XRD patterns of various conditions (a) full line profile and (b) individual peak profiles of Al_2Cu {110}

8.2.2.2 Thermal analysis:

The DSC patterns of various post-processed conditions are presented in the **Fig 8.3**. Majorly 3 peaks were identified as follows (also mentioned in Chapter 5 and 6):

- Peak-1: A small endothermic peak occurred in the range of 80-140 °C and is associated with the dissolution of Ag-Mg co-clustering.
- Peak-2: A broad exothermic peak ranges from 190-350 °C. It is a peak representing precipitation of various types of Al_2Cu phase such as **Ω**, θ' and θ.

- Peak-3: A broad endothermic peak ranges from 400-530 °C representing the dissolution of all the forms Al_2Cu precipitates.

All the 3 peaks were present in the SS-ST, HIP-1and HIP-2 conditions. In the T6, only peak-2 and peak-3 were present. The presence of peak-2 indicates that the precipitation process was not complete. However, in the HIP-2A, only peak-3 was observed, indicates that the precipitation process was more complete after HIPing followed by aging.

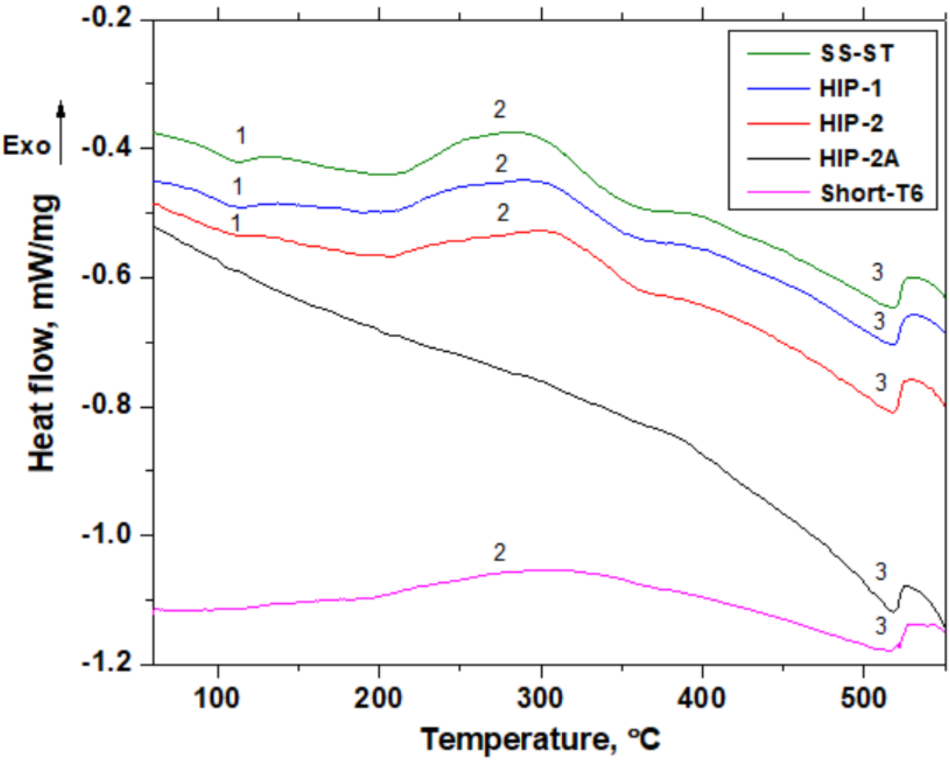

Fig 8.3: DSC curves of the various conditions of HIPed and non-HIPed A20X alloy

8.2.2.3 Microstructural characterization:

The microstructural characterization was performed by EBSD **(Fig 8.4)** and SEM-SE/BSE **(Fig 8.5)**. Only the aged conditions i.e., short-T6 and HIP-2A were evaluated for the microstructural characterization. The EBSD-IPF micrographs showed the presence of equiaxed grains in both conditions. Furthermore, there was no texture formation. The grain size distribution was also similar, averaging the grain size in short-T6 and HIP-2A as 2.78 µm and 2.90 µm, respectively **(Fig**

8.4a and **Fig 8.4b)**. **Fig 8.5a** and **Fig 8.5c** show the low-magnification SEM-BSE micrographs of short-T6 and HIP-2A, respectively, and a high-magnification in-lens SEM-SE micrographs in **Fig 8.5b** and **Fig 8.5d**, respectively. The dark grey background in the SEM-BSE micrographs is the Al matrix (**Fig 8.5a** and **Fig 8.5c**). Based on the atomic contrast and morphology, the identification of TiB_2 and Al_2Cu particles can be resolved. The light grey and elongated particles are of TiB_2 (Yellow arrow) whereas the white and spherical particles correspond to the θ-Al_2Cu (Orange arrow). The TiB_2 particles were found to present at the grain boundaries, grain triple junctions and, also within the grains. The Al_2Cu particles were majorly present within the grains and in some cases near TiB_2 particles. Higher magnification micrographs revealed the presence of very fine needle-type matrix precipitates in both short-T6 and HIP-2A conditions **(Fig 8.5c** and **Fig 8.5d)**. These precipitates are likely to be of Ω/θ'-Al_2Cu precipitates, as reported elsewhere in the artificial aged conditions of LPBF-A20X alloy [243,279,339]. Micrographs taken at a higher magnification also revealed the formation of precipitate free zones (PFZs) along the grain boundaries in both short-T6 and HIP-2A conditions, see **Fig 8.5c** and **Fig 8.5d**. The average width of the PFZs in the HIP-2A and short-T6 is ~ 90 nm and ~ 43 nm respectively.

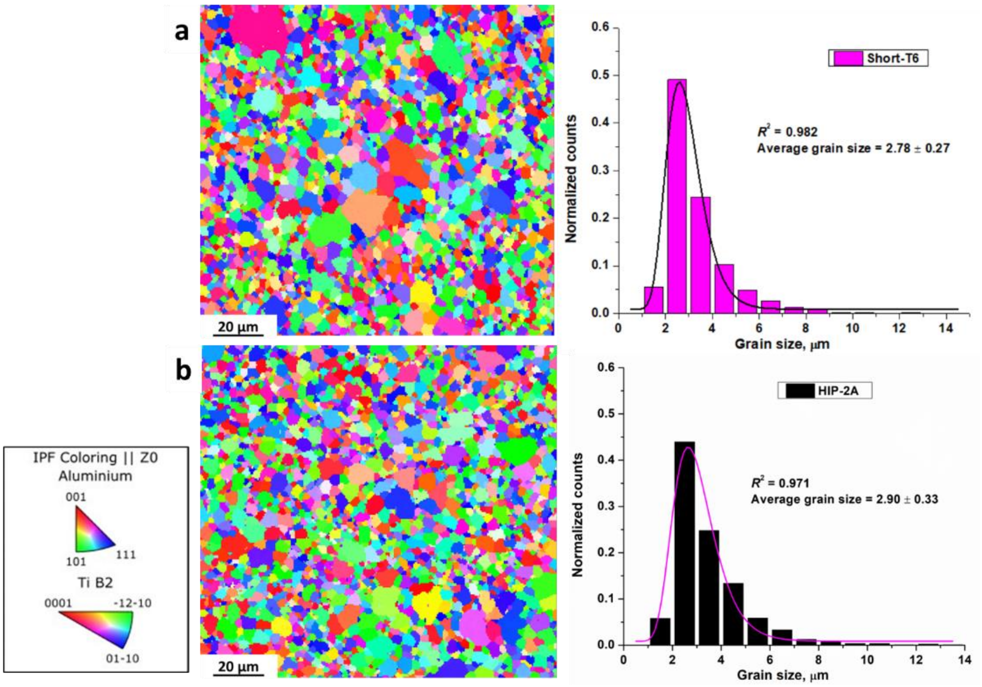

Fig 8.4: EBSD-IPF micrographs and their corresponding grain size distribution in (a) Short-T6 and (b) HIP-2A

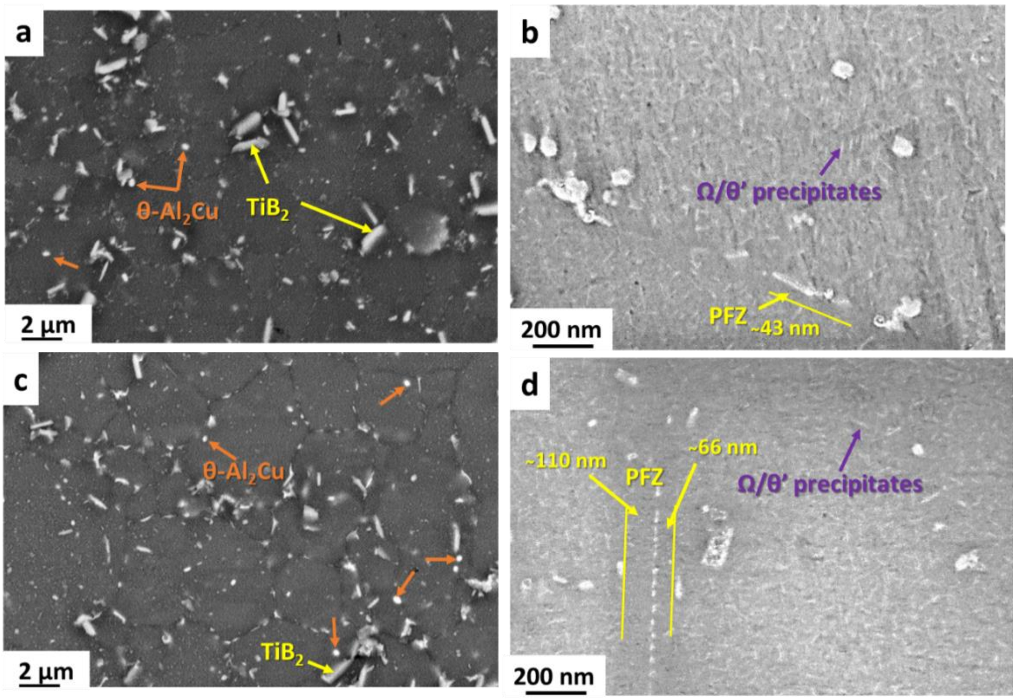

Fig 8.5: SEM micrographs at low (BSE) and high magnification (in-lens SE) of (a-b) short-T6 and (c-d) HIP-2A

8.2.2.4 Micro-hardness and tensile behaviour:

The mechanical behaviour of the aged conditions (short-T6 and HIP-2A) was evaluated by micro-hardness and tensile tests. The tensile curves are shown in a **Fig 8.6**. The characteristics of the tensile curves along with the micro-hardness values are presented in **Table 8.3**. The average micro-hardness values for the short-T6 and HIP-2A are 144 and 141 HV, respectively. The yield strength (Y.S.), ultimate tensile strength (U.T.S.) and elongation to fracture (e%) are 358 MPa, 448 MPa, 11.4% and 361 MPa, 436 MPa, 10.1% for short-T6 and HIP-2A, respectively. Interestingly, there was no significant difference in the tensile curve characteristics as well as in the micro-hardness values for the short-T6 and HIP-2A conditions.

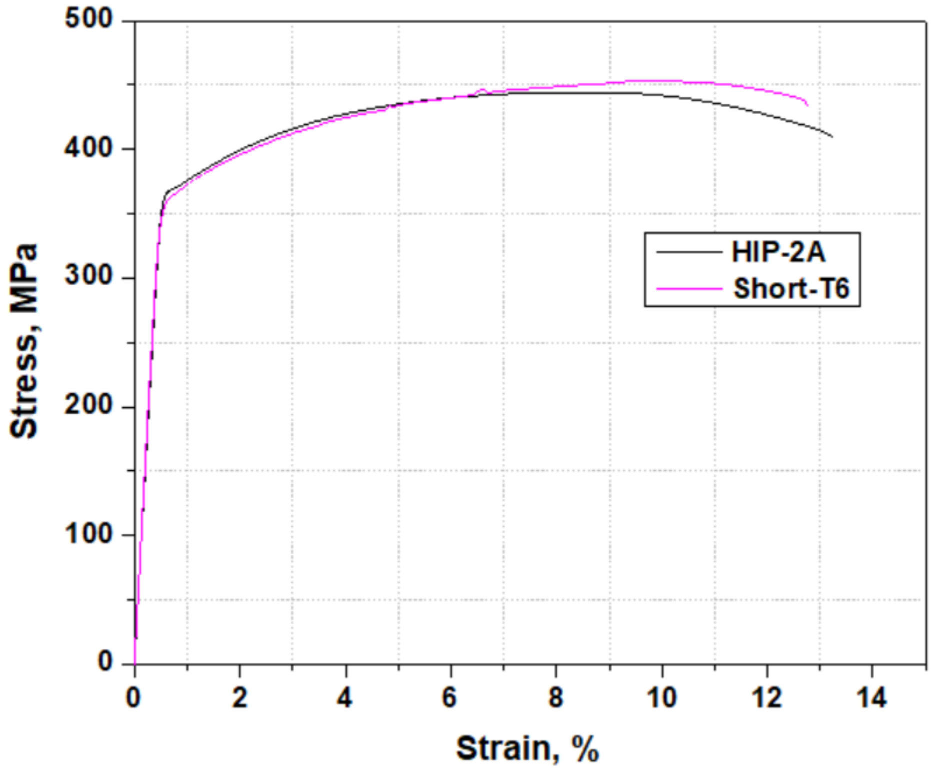

Fig 8.6: Representative tensile stress-strain curves of T6 and HIP-2A conditions

Table 8.3: Micro-hardness and tensile curves characteristics for the T6 and HIP-2A conditions

Conditions	Micro-hardness, HV	Y.S., MPa	U.T.S., MPa	e%
Short-T6	144 ± 3	358 ± 3	448 ± 5	11.4 ± 1
HIP-2A	141 ± 6	361 ± 4	436 ± 5	10.1 ± 2

8.2.3 Discussion

8.2.3.1 Incomplete dissolution of θ-Al_2Cu after HIP:

It was observed that the solution treatment at 530 °C for 1 h (SS-ST) could be able to dissolve the eutectic θ-Al_2Cu **(Fig 8.2b)**. Although, performing the same solution treatment under a pressure of 100 MPa i.e., HIP-1, there was an incomplete dissolution noticed **(Fig 8.2b)**. The incomplete dissolution of the eutectic θ-Al_2Cu phase could be associated to the effect of pressure on the eutectic melting temperature. According to the Clapeyron equation, the equilibrium temperature of the solid-liquid transition can be changed by the effect of pressure [380]. The equation is as follows:

$$P_2 - P_1 = \frac{L_f}{\Delta V} \ln \frac{T_2}{T_1} \qquad 8.1$$

Where $P_2 - P_1$ is the difference in the pressure (≈100 MPa), L_f is the latent heat of fusion associated to the phase transition (331 J/g [381]), ΔV is the change in the molar volume due to the phase transformation ($Al+Al_2Cu \rightarrow$ Liquid) it was calculated as $0.092x10^{-5}$ m^3/mol from the reference [382], and, T_2 and T_1 are the equilibrium temperature at P_2 and P_1 respectively. T_1 is 548 °C [382]. The new equilibrium eutectic temperature obtained was 553.19 °C, thus the increment (ΔT) was 5.19 °C. Considering the increment obtained from the calculation a new HIP temperature of 540 °C was employed (HIP-2). Surprisingly, the incomplete dissolution of Al_2Cu phase still exist, see **Fig 8.2b**.

There are some possibilities that a more complete dissolution was not possible by HIP-1 and HIP-2.

- The latent heat of fusion (L_f) of the eutectic reaction would be specific to the alloy and thus a more accurate value should be considered.
- Another possibility could be the heating rate of HIP. It might not be fast enough, such that the eutectic θ-Al_2Cu could have transformed into the bulk θ-Al_2Cu which would take longer time to dissolve.

Thus, a faster heating rate and a higher HIP temperature (>540 °C) could be checked for a more complete dissolution of the θ-Al_2Cu phase.

8.2.3.2 Mechanical behaviour:

The tensile curve characteristics (Y.S., U.T.S. and e%) of short-T6 and HIP-2A was very similar **(Fig 8.6)**. The similar mechanical behaviour has been associated with multiple factors that were similar in both the cases such as porosity content, grain size distribution, average grain size and the presence of needle-type matrix precipitates (major strengthening phases).

Although the amount of precipitation was more in the HIP-2A condition **(Fig 8.3)** and, also a wider PFZs along the grain boundaries than in the short-T6 condition **(Fig 8.5)**. However, from the present study it seems that the HIP treatment neither have a significant influence on the strength nor the ductility of the A20X alloy.

8.2.4 Part-1: Conclusion

In the present study, the role of hot isostatic pressing (HIP) was investigated. The mechanical behaviour of the aged condition of HIPed (HIP-2A) and non-HIPed (short-T6) was also compared. The outcomes are the following:

1. The average porosity content was slightly decreased after HIP, but they were within the standard deviation of non-HIPed conditions.

2. The HIP processing couldn’t be able to dissolve the eutectic Al_2Cu, but a non-HIP (solution treatment) could be able to dissolve successfully.

3. The tensile properties were similar for the HIP-2A and short-T6 conditions.

4. The similar tensile properties were associated to the similar porosity content, grain size distribution, average grain size and needle-type matrix precipitation.

8.3 Part-2

8.3.1 Methodology

In the present investigation, the HIP treatment was followed by solution treatment at 530 °C for 1 h and then artificially aged. The artificial aging was performed at 150 °C for 4 h. The nomenclature of various conditions of HIP and non-HIP samples are presented in a **Table 8.4**. The tensile properties of the aged conditions i.e., HIP and T6-L (non-HIP) are compared. However, the study is ongoing and data from few characterization techniques are yet to be extracted and analysed, especially for the T6-L condition.

Table 8.4: Nomenclature of the various heat treatments and their processing conditions

Heat treatment	Temperature, pressure, and time
T6-L	530 °C for 1h + 150 for 4 h
HIP-1S	530 °C and 100 MPa for 1 h + 530 °C for 1 h
HIP-1SA	530 °C and 100 MPa for 1 h + 530 °C for 1 h + 150 °C for 4 h

8.3.2 Results:

8.3.2.1 Porosity content:

Fig 8.7 shows the optical micrographs of various conditions. The porosities were finer and circular in shape, representing the gas-induced porosities. The porosity content of the HIP-1S and HIP-1SA are presented in a **Table 8.5**, along with the AB and ST conditions. The average porosity in HIP-1S and HIP-1SA was 0.023% and 0.038% respectively. The average porosity content in the AB and SS-ST were 0.070% and 0.074% respectively. After HIP, the average porosity content was slightly decreased but considering the standard deviation, the porosity content of all the post-processed conditions were similar.

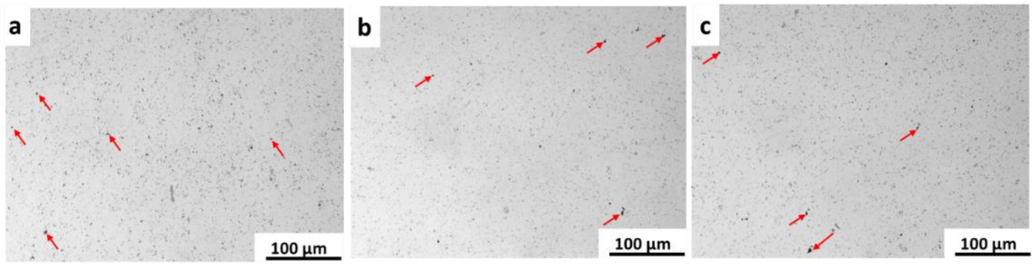

Fig 8.7: Optical micrographs of the (a) AB, (b) HIP-1S and (c) HIP-1SA conditions

Table 8.5: Porosity content of various HIPed and non-HIPed conditions

Condition	Porosity content, %
AB	0.070 ± 0.040
SS-ST	0.074 ± 0.015
T6-L	To do
HIP-1S	0.023 ± 0.006
HIP-1SA	0.038 ± 0.029

8.3.2.2 Phase analysis:

The **Fig 8.8** display the XRD patterns of various HIP conditions. The whole line profile is presented in the Error! Reference source not found.**Fig 8.8a** and the individual peak profile of θ-Al_2Cu {110} in **Fig 8.8b**. Three phases were identified from the whole line profile. They were of Al, Al_2Cu and TiB_2. A more complete dissolution of the eutectic θ-Al_2Cu was seen in the sample with a separate solution treatment after HIP i.e., HIP-1S, see **Fig 8.8b**. Indicating that the solution treatment without an externally applied pressure was beneficial for a more complete dissolution of θ-Al_2Cu. Post to the solution treatment (HIP-1S) followed by artificial aging at 150 °C for 4 h (HIP-1SA), a very small broad peak could be anticipated, suggesting some amount of θ-Al_2Cu precipitation has occurred **(Fig 8.8b)**.

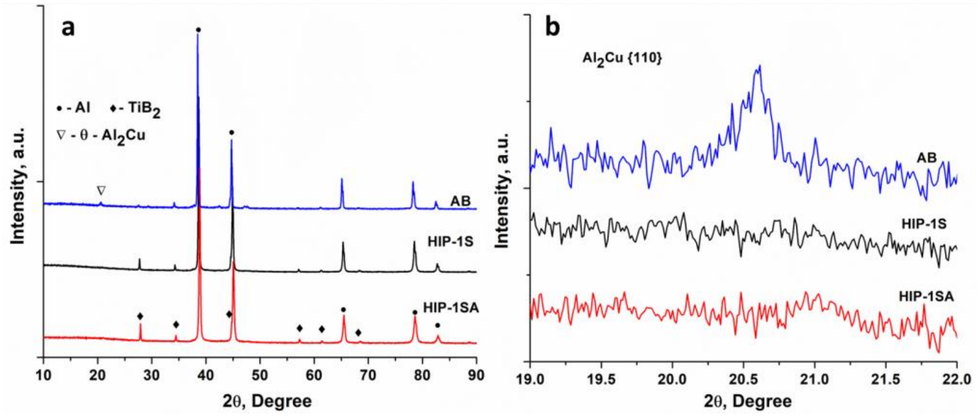

Fig 8. 8**:** XRD patterns of various conditions (a) whole line profile and (b) individual peak profiles of θ-Al_2Cu {110}

8.3.2.3 Thermal analysis:

The DSC patterns of the HIP-1S and HIP-1SA is presented in **Fig 8.9**. As observed in Part-1, three peaks were present. Peak-1 (80-140 °C): represents the dissolution of Ag-Mg co-clusters, peak-2 (190-350 °C): represents the precipitation of all forms of Al_2Cu and peak-3 (400-530 °C): correspond to the dissolution of all forms of Al_2Cu precipitates. In the case of HIP-1SA, instead of peak-1, a new peak appeared (peak-1') in the range of 170-230 °C. Peak-1' corresponds to the dissolution of Cu-Mg co-clusters [330,383]. This suggests that Cu-Mg co-clusters have formed during aging to 150 °C. Based on the part-1 DSC analyses, such Cu-Mg co-clusters were not present when the samples were aged to 190 °C **(Fig 8.3)**.

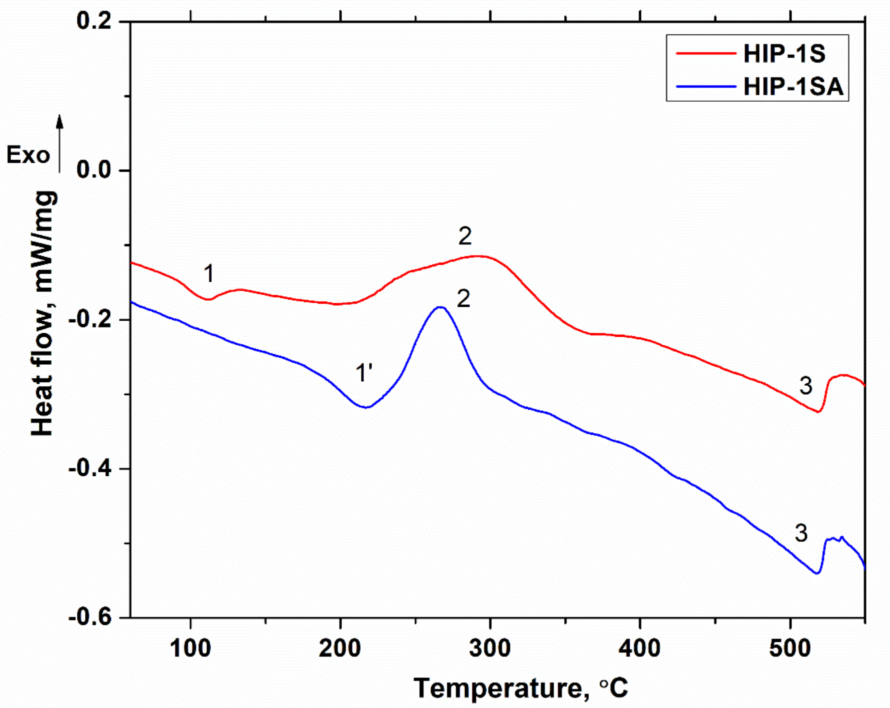

Fig 8.9: DSC curves of the various HIPed conditions

8.3.2.4 Microstructural behaviour:

The SEM-BSE micrograph **(Fig 8.10)** displaying the presence of TiB_2 particles and spheroidal Al_2Cu phases in a HIP-1S and HIP-1SA samples. The microstructure seems to be similar to the previous HIPed samples **(Fig 8.5c)**.

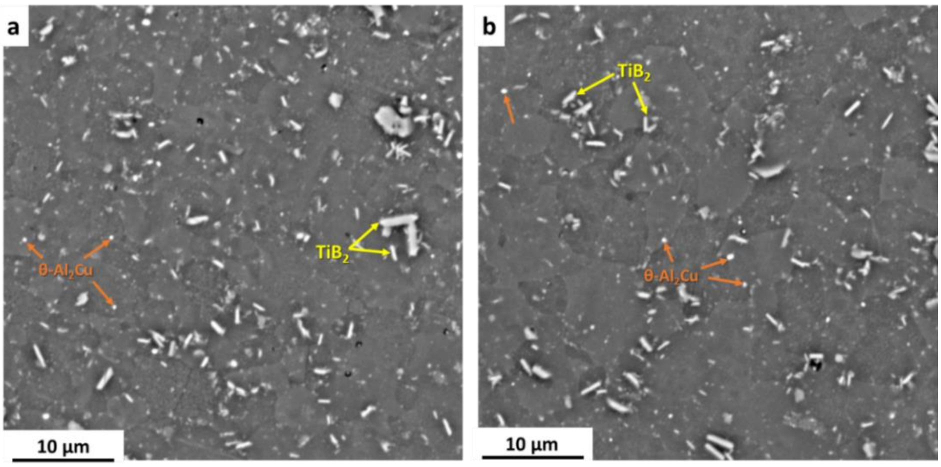

Fig 8.10: SEM-BSE micrographs of HIPed conditions (a) HIP-1S and (b) HIP-1SA

8.3.2.5 Tensile behaviour:

The mechanical behaviour of the HIP-1SA and T6-L was evaluated by the tensile tests. The curve characteristics are presented in a **Table 8.6**. The Y.S., U.T.S., and e% are 344 MPa, 464 MPa, 15.5% and 340 MPa, 463 MPa and 16.7% for T6-L and HIP-1SA, respectively. Both T6-L and HIP-1SA demonstrated a similar tensile behaviour. As compared to the HIP-2A and T6 that were aged at 190 °C, the Y.S. of the HIP-1SA and T6-L were lowered, although the UTS and e% were higher.

Furthermore, the tensile curves of HIP-1SA and T6-L showed serrated flow behaviour in the plastic regime after around 4.5% of strain (inset in **Fig 8.11**). Based on the characteristics of the serrations, they are identified as low-frequency type-A.

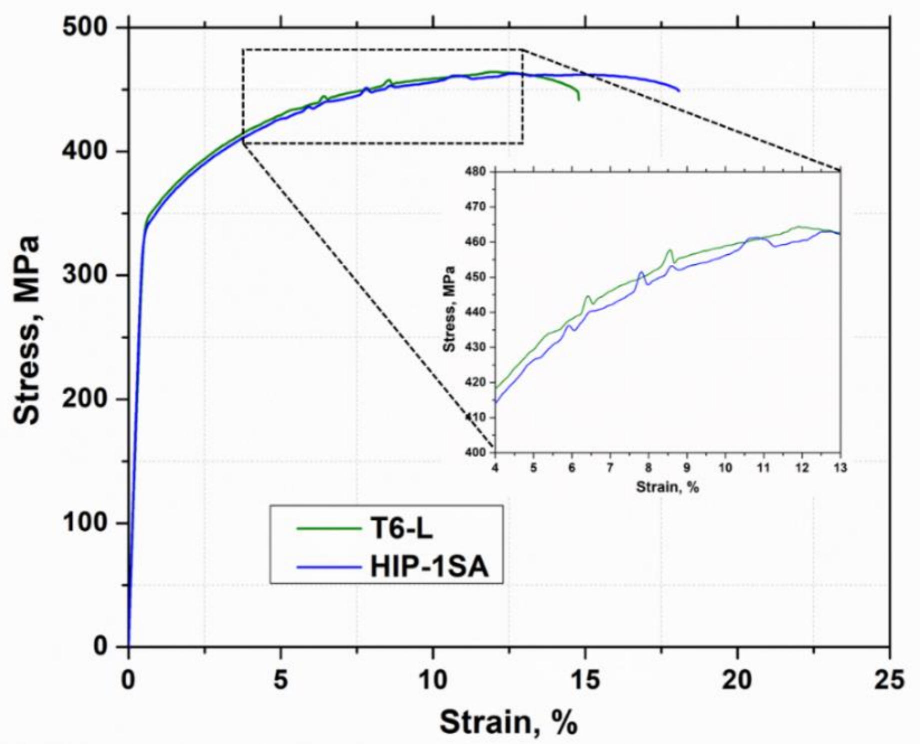

Fig 8.11: Representative tensile stress-strain curves of T6-L and HIP-1SA conditions

Table 8.6: Characteristics of tensile curves for the aged conditions of HIPed and non-HIPed

Conditions	**Y.S., MPa**	**U.T.S., MPa**	**e%**
T6-L	344 ± 2	464 ± 0.2	15.5 ± 1.1
HIP-1SA	340 ± 5	463 ± 0.7	16.7 ± 1.0

8.3.3 Discussion

8.3.3.1 On the serrated flow behaviour:

Both the aged conditions i.e., T6-L and HIP-2A demonstrated the serrated flow behaviour. The serrated flow behaviour in the A20X alloy has been associated with the presence of free-Mg atoms in the matrix [270,271]. In the case of HIP-1SA, the DSC patterns suggested that after aging at 150 °C for 4 h, there were Cu-Mg co-clusters. These Cu-Mg co-clusters have been reported to undergo dissolution upon deformation [384–387]. According to Bai et al. [384], the coherent Cu-Mg co-cluster can be sheared by dislocations during cyclic deformation. This repeated cutting of moving dislocations disrupts the association of Cu and Mg atoms and ultimately lead to the partial or complete dissolution of the co-clusters. The dissolution of Cu-Mg co-clusters involves the diffusion of Cu and Mg atoms from the interior of the co-cluster into the matrix. Xu et al. [387] also reported a similar phenomenon of strain-induced dissolution of Cu-Mg co-cluster during cold rolling of an Al2024 alloy. Thus, the process can free-up the Mg which is then responsible for the pinning and unpinning of dislocations as the deformation proceeds.

8.3.3.2 Mechanical behaviour:

The mechanical behaviour of the HIPed (HIP-1SA) and non-HIPed (T6-L) were similar **(Fig 8.11)**. The same conclusion was also found in the previous part of the chapter (Part-1). However, the present investigation is still on-going and further characterization of the HIP-1SA and T6-L conditions are required such as porosity content, heat flow behaviour and microstructural details.

8.3.4 Part-2 Conclusion

In the present study, the HIPed samples were first solution treated followed by artificial aging. The HIPed (HIP-1SA) and non-HIPed (T6) conditions were compared in terms of mechanical behaviour. The following are the conclusion:

1. The porosity content was slightly reduced after the HIP treatment as compared to the as-built condition. Although, the porosity values were all within the standard deviation.

2. A separate solution treatment step after the HIPing could be able to dissolve the eutectic θ-Al_2Cu more completely.

3. In the HIP-1SA condition, Cu-Mg co-clusters were formed. This could be associated to the low-temperature aging (150 °C).

4. The yield strength, ultimate tensile strength and elongation to fracture were similar for both the HIP-1SA and T6-L conditions.

5. Both HIP-1SA and T6-L demonstrated a serrated flow behaviour, which was associated to the dissolution of Cu-Mg co-cluster during the deformation.

8.4 Chapter summary:

The A20X alloy was well processed with a high relative density in its as-built condition. Performing a post-processing treatment of HIP does not significantly affect the porosity content. The mechanical behaviour of the HIPed and non-HIPed conditions were more or less similar in both the cases i.e. part-1 and part-2. The present study does give a good sign of the non-requirement of the expensive HIP post-processing treatment of the A20X alloy. However, for the critical applications demanding high safety and reliability standards, HIP could be used.

The fractography analysis is missing in the current chapter. This analysis would be vital to understand the failure mechanisms of HIPed with non-HIPed conditions and considered as the future work.

Chapter 9

Summary

In the present thesis, the commercial high strength A20X alloy was processed by laser powder bed fusion (LPBF) and its post-processing behaviour was investigated. The obtained results can be summarised as follows:

9.1 LPBF processibility of A20X alloy:

The A20X alloy powder was well processed by LPBF. With the optimized building parameters, it was possible to produce samples with around 0.07±0.04% of porosity keeping the VED values low (62.5 J/mm^3).

The microstructure of powder was similar to as-built (AB). The AB microstructure was composed of fine cellular structures with α-Al cells and θ-Al_2Cu eutectic as cell boundaries. XRD and EBSD data showed that it was also textured free. The TiB_2 particles were uniformly distributed, and their distribution was not much affected by the laser power or the scanning speed.

The tensile behaviour demonstrated a good combination of strength and ductility. The average yield strength (Y.S.), ultimate tensile strength (U.T.S.) and elongation to failure (e%) were 304 MPa, 378 MPa and 12.5%, respectively. Although, the tensile curves displayed Lüders band formation and serrated flow behaviour due to the PLC effect. Both the phenomena were associated with the presence of Mg atoms in a solid solution. The fractography revealed a ductile failure as the fractured surface was characterised by micro-sized dimples.

9.2 Microstructural evolution of long-T6 and the role of short-T6:

In this chapter, firstly, the microstructural evolution during a long-T6 post-processing heat treatment was investigated. The microstructure was studied at various stages of the heat treatment, including as-built (AB), after the multiple-steps solution treatment (MS-ST), in the peak-aged (PA), and over-aged (OA) states. The conclusions were as follows:

The cellular structure of the AB state disappeared after MS-ST. The PA microstructure comprised θ-Al_2Cu precipitates near TiB_2 particles and along the grain boundaries. In the OA state, these θ-Al_2Cu grew further, engulfing the TiB_2 particles. Additionally, grain boundary cracks appeared in both PA and OA states. However, the severity of such cracks was greater in the OA state. The origin of grain boundary cracks was associated with the synergistic effect of (i) hardening of the matrix by the precipitation of coherent and semi-coherent Ω and θ' precipitates and (ii) widening of the weak PFZs at TiB_2 particles and grain boundaries.

Secondly, the microstructural evolution during the various steps of the long multiple-steps of solution treatment was investigated. It was observed that, as the solution treatment proceeded in steps from low temperature to high temperature, the eutectic network of θ-Al_2Cu broke down into fine spheroidal particles that migrated and coarsened at the TiB_2 particles. The dissolution of θ-Al_2Cu present at the TiB_2 particles was difficult even after being kept at 530 °C for 12 h. This difficulty was attributed to the shielding effect of TiB_2 particles. During artificial aging, these θ-Al_2Cu particles preferentially grew and created wide PFZs at TiB_2 particles and grain boundaries. Such a condition gave rise to grain boundary cracking and had a negative impact on the ductility of the material.

To avoid such a situation, a single-step solution treatment (SS-ST) was proposed. SS-ST samples were then aged using the same artificial aging conditions as long-T6. The heat treatment was termed as short-T6. The short-T6 displayed a 45% increase in ductility with respect to the long-T6, with the yield strength (Y.S.) and ultimate tensile strength (U.T.S.) showing improvements of 7.1% and 6.3%, respectively. The improvement in the ductility of short-T6 was associated with the absence of grain boundary cracks.

9.3 Comparison of T4 and short-T6 heat treatment: Strengthening mechanisms

The A20X alloy responded well to natural aging after solution treatment i.e., T4 condition. The chapter compared the mechanical behaviour of the T4 and short-T6 (artificial aged) conditions. During natural aging, the alloy achieved its peak hardness in around 20 days at room temperature (≈ 28 °C), whereas it took 4 h at 190 °C in the case of artificial aging (short-T6). The difference between the peak hardness was ≈10 HV. The bulk mechanical behaviours of T4 and short-T6 were quite different. The Y.S. of T4 condition was around 30% lower than short-T6 while the U.T.S. of T4 was comparable to short-T6, with a difference of only 6.2 %. The elongation to fracture (e%) of T4 instead was around 43 % higher than short-T6.

The chapter also dealt with the estimation of increments in the yield strength by various strengthening mechanisms that contribute to the overall yield strength in the T4 and short-T6 conditions. Being processed by LPBF, the contribution from the grain boundary strengthening was significant in both T4 and short-T6. Other than grain boundary strengthening, the major strengthening contributions of T4 were the Ag-Mg co-clusters and solid solution strengthening by Cu atoms, whereas strengthening by the dislocation shearing of Ω/θ’ plate-type precipitates were dominant in the short-T6.

Both post-processing heat treatments improved the mechanical property of the A20X alloy with respect to the as-built state. The T4 gives good-strength and high-ductility whereas, the short-T6 provides high-strength and good-ductility combination to the alloy, thus, one can get benefitted from both the heat treatments based on the intended application.

9.4 Strain hardening and fracture behaviour of T4, Short-T6 and Long-T6

Strain hardening and fracture behaviour of the A20X alloy post-processed with T4 and T6 (short-T6 and long-T6) was investigated.

The T4 demonstrated superior strain hardening capability with high uniform elongation than short-T6 and long-T6. Also, the uniform elongation of T4 (ε_u = 17.7%) was higher than short-T6 (ε_u = 7.3%) and long-T6 (ε_u = 6.2%). The higher uniform elongation of the T4 specimens was due to the high amount of Cu solid solution and to the presence of Ag-Mg co-clusters. In the case of short-T6 and long-T6, the lower uniform elongation was associated to the loss of Cu solid solution, dissolution of Ag-Mg co-clusters and the precipitation of shearable Ω-Al_2Cu in the matrix.

Fractography studies revealed a ductile failure in all the post-processed conditions. However, the failure initiation mechanism differed in T4 compared to short-T6 and long-T6. In T4, the failure initiated solely through the formation of micro-voids at the individual TiB_2 particles and their agglomerates. On the other hand, in both short-T6 and long-T6, the initiation occurred through a combination of micro-void formation at TiB_2 particles and grain boundary cracking due to the presence of PFZs.

9.5 Effect of hot isostatic press (HIP) on the mechanical behaviour:

As HIP is one of the most common post-processing techniques performed on AM parts, in this chapter, the effect of HIP on the mechanical behaviour of LPBF A20X samples was investigated.

Two different processing conditions were studied:

Part-1: AB→HIP (Quench)→Artificial aged (190 °C) = HIP-2A

Part-2: AB→HIP (Furnace cooling)→Solutionized→ Artificial aged (150 °C) = HIP-1SA

9.5.1 Summary of part 1:

The HIP processing was unable to dissolve the eutectic θ-Al_2Cu, while the non-HIP solution treatment at the same temperature was successful in achieving a complete dissolution.

The tensile properties were similar for the HIP+2A and T6 conditions. The similarity in tensile properties was attributed to the similar porosity content, grain size distribution, average grain size, and needle-type matrix precipitation.

9.5.2 Summary of part 2:

The investigation related to Part-2 is still ongoing. However, few observations were made and briefly discussed.

In the HIP-1SA condition, Cu-Mg co-clusters were found. The mechanical behaviour of the T6 and HIP-1SA conditions was compared. The yield strength, ultimate tensile strength, and elongation to fracture were also similar for both conditions. Additionally, the tensile curves in the plastic regime were characterized by serrated flow behaviour. This behaviour was associated with the dissolution of Cu-Mg co-clusters during deformation and the freeing up of Mg atoms.

Both the studies suggested no significant effect of HIP on the mechanical behaviour of the A20X alloy. These results indicate that HIP can be useful only for safety-critical applications.

References

[1] A. Standard, Standard terminology for additive manufacturing technologies, ASTM Int. F2792-12a. (2012) 1–9.

[2] I. Yadroitsev, I. Yadroitsava, A. Du Plessis, E. MacDonald, Fundamentals of laser powder bed fusion of metals, Elsevier, 2021.

[3] D. Manfredi, F. Calignano, M. Krishnan, R. Canali, E. Paola, S. Biamino, D. Ugues, M. Pavese, P. Fino, Chapter Additive Manufacturing of Al Alloys and Aluminium Matrix Composites (AMCs), (2014).

[4] N. Tepylo, X. Huang, P.C. Patnaik, Laser-Based Additive Manufacturing Technologies for Aerospace Applications, 1900617 (2019) 1–35. https://doi.org/10.1002/adem.201900617.

[5] I. Gibson, D.W. Rosen, B. Stucker, Direct Digital Manufacturing BT - Additive Manufacturing Technologies: Rapid Prototyping to Direct Digital Manufacturing, in: I. Gibson, D.W. Rosen, B. Stucker (Eds.), Springer US, Boston, MA, 2010: pp. 378–399. https://doi.org/10.1007/978-1-4419-1120-9_14.

[6] J.P. Kruth, G. Levy, F. Klocke, T.H.C. Childs, Consolidation phenomena in laser and powder-bed based layered manufacturing, CIRP Ann. - Manuf. Technol. 56 (2007) 730–759. https://doi.org/10.1016/j.cirp.2007.10.004.

[7] J.-P. Kruth, M.-C. Leu, T. Nakagawa, Progress in additive manufacturing and rapid prototyping, Cirp Ann. 47 (1998) 525–540.

[8] A.J. Alsaffar, K. Raoufi, K.-Y. Kim, G.E. Okudan Kremer, K.R. Haapala, Simultaneous consideration of unit manufacturing processes and supply chain activities for reduction of product environmental and social impacts, J. Manuf. Sci. Eng. 138 (2016) 101009.

[9] T. DebRoy, H.L. Wei, J.S. Zuback, T. Mukherjee, J.W. Elmer, J.O. Milewski, A.M. Beese, A. Wilson-Heid, A. De, W. Zhang, Additive manufacturing of metallic components – Process, structure and properties, Prog. Mater. Sci. 92 (2018) 112–224. https://doi.org/10.1016/j.pmatsci.2017.10.001.

[10] T.T. Wohlers, T. Caffrey, Wohlers report 2015: 3D printing and additive manufacturing state of the industry annual worldwide progress report, Wohlers Associates, 2015.

[11] P. Wang, Y. Yang, N.S. Moghaddam, Process modeling in laser powder bed fusion towards defect detection and quality control via machine learning: The state-of-the-art and research challenges, J. Manuf. Process. 73 (2022) 961–984. https://doi.org/10.1016/j.jmapro.2021.11.037.

[12] M. Laleh, E. Sadeghi, R.I. Revilla, Q. Chao, N. Haghdadi, A.E. Hughes, W. Xu, I. De Graeve, M. Qian, I. Gibson, M.Y. Tan, Heat treatment for

metal additive manufacturing, Prog. Mater. Sci. 133 (2023) 101051. https://doi.org/10.1016/j.pmatsci.2022.101051.

[13] Aniwaa, Guide, Metal 3D printers in 2023: a comprehensive, (2023). https://www.aniwaa.com/buyers-guide/3d-printers/best-metal-3d-printer/.

[14] S.L. Sing, S. Huang, G.D. Goh, G.L. Goh, C.F. Tey, J.H.K. Tan, W.Y. Yeong, Emerging metallic systems for additive manufacturing: In-situ alloying and multi-metal processing in laser powder bed fusion, Prog. Mater. Sci. 119 (2021) 100795. https://doi.org/10.1016/j.pmatsci.2021.100795.

[15] L.E. Criales, Y.M. Arısoy, B. Lane, S. Moylan, A. Donmez, T. Özel, Laser powder bed fusion of nickel alloy 625: Experimental investigations of effects of process parameters on melt pool size and shape with spatter analysis, Int. J. Mach. Tools Manuf. 121 (2017) 22–36. https://doi.org/10.1016/j.ijmachtools.2017.03.004.

[16] Y. Wang, J. Bergström, C. Burman, Characterization of an iron-based laser sintered material, J. Mater. Process. Technol. 172 (2006) 77–87. https://doi.org/10.1016/j.jmatprotec.2005.09.004.

[17] M. Shellabear, O. Nyrhilä, DMLS – Development History and State of the Art, Lane 2004. (2004) 1–12.

[18] W. O'Neill, C.J. Sutcliffe, R. Morgan, A. Landsborough, K.K.B. Hon, Investigation on Multi-Layer Direct Metal Laser Sintering of 316L Stainless Steel Powder Beds, CIRP Ann. 48 (1999) 151–154. https://doi.org/https://doi.org/10.1016/S0007-8506(07)63153-9.

[19] A. Stwora, G. Skrabalak, Influence of selected parameters of Selective Laser Sintering process on properties of sintered materials, J. Achiev. Mater. Manuf. Eingineering. 61 (2013) 375–380.

[20] H. Pohl, A. Simchi, M. Issa, H.C. Dias, Thermal stresses in direct metal laser sintering, Proc. SFF Symp. (2001) 366–372. http://edge.rit.edu/edge/P10551/public/SFF/SFF 2001 Proceedings/2001 SFF Papers/41-Pohl.pdf.

[21] H. Jia, H. Sun, H. Wang, Y. Wu, H. Wang, Scanning strategy in selective laser melting (SLM): a review, Int. J. Adv. Manuf. Technol. 113 (2021) 2413–2435. https://doi.org/10.1007/s00170-021-06810-3.

[22] W. Abd-Elaziem, S. Elkatatny, A.E. Abd-Elaziem, M. Khedr, M.A. Abd El-Baky, M.A. Hassan, M. Abu-Okail, M. Mohammed, A. Järvenpää, T. Allam, A. Hamada, On the current research progress of metallic materials fabricated by laser powder bed fusion process: a review, J. Mater. Res. Technol. 20 (2022) 681–707. https://doi.org/10.1016/j.jmrt.2022.07.085.

[23] J.P. Kruth, M. Badrossamay, E. Yasa, J. Deckers, L. Thijs, J. Van Humbeeck, Part and material properties in selective laser melting of metals, 16th Int. Symp. Electromachining, ISEM 2010. (2010) 3–14.

[24] M.C. Leu, S. Pattnaik, G.E. Hilmas, Optimization of selective laser sintering process for fabrication of Zirconium Diboride parts, 21st Annu. Int. Solid Free. Fabr. Symp. - An Addit. Manuf. Conf. SFF 2010. (2010)

493–503.

[25] R. Shi, S.A. Khairallah, T.T. Roehling, T.W. Heo, J.T. McKeown, M.J. Matthews, Microstructural control in metal laser powder bed fusion additive manufacturing using laser beam shaping strategy, Acta Mater. 184 (2020) 284–305. https://doi.org/10.1016/j.actamat.2019.11.053.

[26] A. Okunkova, M. Volosova, P. Peretyagin, Y. Vladimirov, I. Zhirnov, A. V. Gusarov, Experimental approbation of selective laser melting of powders by the use of non-Gaussian power density distributions, Phys. Procedia. 56 (2014) 48–57. https://doi.org/10.1016/j.phpro.2014.08.095.

[27] Â. Cunha, A. Marques, M. Rodrigues, S. Flávio, F.S. Silva, M. Gasik, B. Trindade, Ó. Carvalho, Laser powder bed fusion of the steels used in the plastic injection mould industry : a review of the influence of processing parameters on the final properties, Springer London, 2022. https://doi.org/10.1007/s00170-022-09588-0.

[28] P. Hanzl, M. Zetek, T. Bakša, T. Kroupa, The influence of processing parameters on the mechanical properties of SLM parts, Procedia Eng. 100 (2015) 1405–1413. https://doi.org/10.1016/j.proeng.2015.01.510.

[29] K. Guan, Z. Wang, M. Gao, X. Li, X. Zeng, Effects of processing parameters on tensile properties of selective laser melted 304 stainless steel, Mater. Des. 50 (2013) 581–586. https://doi.org/10.1016/j.matdes.2013.03.056.

[30] John D williams, Carl R. Deckard, Advances in modelingthe effects of selectedparameters on theSLS process, Rapid Prototyp. J. 4 (1998) 90–100.

[31] W.J. Sames, F.A. List, S. Pannala, R.R. Dehoff, S.S. Babu, The metallurgy and processing science of metal additive manufacturing, Int. Mater. Rev. 61 (2016) 315–360. https://doi.org/10.1080/09506608.2015.1116649.

[32] M. Matsumoto, M. Shiomi, K. Osakada, F. Abe, Finite element analysis of single layer forming on metallic powder bed in rapid prototyping by selective laser processing, Int. J. Mach. Tools Manuf. 42 (2002) 61–67. https://doi.org/10.1016/S0890-6955(01)00093-1.

[33] K.G. Prashanth, S. Scudino, T. Maity, J. Das, J. Eckert, Is the energy density a reliable parameter for materials synthesis by selective laser melting?, Mater. Res. Lett. 5 (2017) 386–390. https://doi.org/10.1080/21663831.2017.1299808.

[34] M.A. Buhairi, F.M. Foudzi, F.I. Jamhari, A.B. Sulong, N.A.M. Radzuan, N. Muhamad, I.F. Mohamed, A.H. Azman, W.S.W. Harun, M.S.H. Al-Furjan, Review on volumetric energy density: influence on morphology and mechanical properties of Ti6Al4V manufactured via laser powder bed fusion, Prog. Addit. Manuf. 8 (2023) 265–283. https://doi.org/10.1007/s40964-022-00328-0.

[35] S.L. Campanelli, N. Contuzzi, A. Angelastro, A.D. Ludovico, Capabilities and performances of the selective laser melting process, New Trends Technol. Devices, Comput. Commun. Ind. Syst. 1 (2010) 233–252.

[36] G. Buffa, A. Costa, D. Palmeri, G. Pollara, A. Barcellona, L. Fratini, A new

control parameter to predict micro-warping-induced job failure in LPBF of TI6AL4V titanium alloy, Int. J. Adv. Manuf. Technol. 126 (2023) 1143–1157. https://doi.org/10.1007/s00170-023-11179-6.

[37] A.S. Shaikh, F. Schulz, K. Minet-Lallemand, E. Hryha, On the effect of building platform material on laser-powder bed fusion of a Ni-base superalloy HAYNES® 282®, Eur. J. Mater. 0 (2022) 1–19. https://doi.org/10.1080/26889277.2022.2132016.

[38] T. Mukherjee, W. Zhang, T. DebRoy, An improved prediction of residual stresses and distortion in additive manufacturing, Comput. Mater. Sci. 126 (2017) 360–372. https://doi.org/10.1016/j.commatsci.2016.10.003.

[39] N.T. Aboulkhair, M. Simonelli, L. Parry, I. Ashcroft, C. Tuck, R. Hague, Progress in Materials Science 3D printing of Aluminium alloys : Additive Manufacturing of Aluminium alloys using selective laser melting, Prog. Mater. Sci. 106 (2019) 100578. https://doi.org/10.1016/j.pmatsci.2019.100578.

[40] K. V. Yang, Y. Shi, F. Palm, X. Wu, P. Rometsch, Columnar to equiaxed transition in Al-Mg(-Sc)-Zr alloys produced by selective laser melting, Scr. Mater. 145 (2018) 113–117. https://doi.org/10.1016/j.scriptamat.2017.10.021.

[41] A.B. Spierings, N. Herres, G. Levy, Influence of the particle size distribution on surface quality and mechanical properties in AM steel parts, Rapid Prototyp. J. 17 (2011) 195–202. https://doi.org/10.1108/13552541111124770.

[42] H.J. Niu, I.T.H. Chang, Selective laser sintering of gas and water atomized high speed steel powders, Scr. Mater. 41 (1999) 25–30. https://doi.org/10.1016/S1359-6462(99)00089-5.

[43] D. Manfredi, F. Calignano, M. Krishnan, R. Canali, E.P. Ambrosio, E. Atzeni, From powders to dense metal parts: Characterization of a commercial alsimg alloy processed through direct metal laser sintering, Materials (Basel). 6 (2013) 856–869. https://doi.org/10.3390/ma6030856.

[44] M.S.J. Hashmi, Comprehensive materials processing, Newnes, 2014.

[45] H. Attar, K.G. Prashanth, L.C. Zhang, M. Calin, I. V. Okulov, S. Scudino, C. Yang, J. Eckert, Effect of powder particle shape on the properties of in situ Ti-TiB composite materials produced by selective laser melting, J. Mater. Sci. Technol. 31 (2015) 1001–1005. https://doi.org/10.1016/j.jmst.2015.08.007.

[46] M. Rombouts, L. Froyen, A. V. Gusarov, E.H. Bentefour, C. Glorieux, Photopyroelectric measurement of thermal conductivity of metallic powders, J. Appl. Phys. 97 (2005). https://doi.org/10.1063/1.1832740.

[47] A. V. Gusarov, T. Laoui, L. Froyen, V.I. Titov, Contact thermal conductivity of a powder bed in selective laser sintering, Int. J. Heat Mass Transf. 46 (2003) 1103–1109. https://doi.org/10.1016/S0017-9310(02)00370-8.

[48] M. Rombouts, L. Froyen, A. V. Gusarov, E.H. Bentefour, C. Glorieux,

Light extinction in metallic powder beds: Correlation with powder structure, J. Appl. Phys. 98 (2005) 1–9. https://doi.org/10.1063/1.1948509.

[49] X.C. Wang, T. Laoui, J. Bonse, J.P. Kruth, B. Lauwers, L. Froyen, Direct selective laser sintering of hard metal powders: Experimental study and simulation, Int. J. Adv. Manuf. Technol. 19 (2002) 351–357. https://doi.org/10.1007/s001700200024.

[50] A. Foroozmehr, M. Badrossamay, E. Foroozmehr, S. Golabi, Finite Element Simulation of Selective Laser Melting process considering Optical Penetration Depth of laser in powder bed, Mater. Des. 89 (2016) 255–263. https://doi.org/10.1016/j.matdes.2015.10.002.

[51] W.E. King, A.T. Anderson, R.M. Ferencz, N.E. Hodge, C. Kamath, S.A. Khairallah, A.M. Rubenchik, Laser powder bed fusion additive manufacturing of metals; physics, computational, and materials challenges, Appl. Phys. Rev. 2 (2015) 41304. http://dx.doi.org/10.1063/1.4937809http://aip.scitation.org/toc/are/2/4.

[52] A. V. Gusarov, I. Smurov, Modeling the interaction of laser radiation with powder bed at selective laser melting, Phys. Procedia. 5 (2010) 381–394. https://doi.org/10.1016/j.phpro.2010.08.065.

[53] S.C. Stacy, X. Zhang, M. Pantoya, B. Weeks, The effects of density on thermal conductivity and absorption coefficient for consolidated aluminum nanoparticles, Int. J. Heat Mass Transf. 73 (2014) 595–599. https://doi.org/10.1016/j.ijheatmasstransfer.2014.02.050.

[54] B. Zhang, C. Coddet, Selective Laser Melting of Iron Powder: Observation of Melting Mechanism and Densification Behavior Via Point-Track-Surface-Part Research, J. Manuf. Sci. Eng. Trans. ASME. 138 (2016) 1–9. https://doi.org/10.1115/1.4031366.

[55] W. Kurz, B. Giovanola, R. Trivedi, Theory of microstructural development during rapid solidification, Acta Metall. 34 (1986) 823–830. https://doi.org/https://doi.org/10.1016/0001-6160(86)90056-8.

[56] N. Takata, H. Kodaira, K. Sekizawa, A. Suzuki, M. Kobashi, Microstructure and mechanical properties of Al-10Si-0.4 Mg alloy fabricated by selective laser melting, J. Japan Inst. Light Met. 67 (2017) 582–588.

[57] M.C. Brennan, J.S. Keist, T.A. Palmer, Defects in Metal Additive Manufacturing Processes, J. Mater. Eng. Perform. 30 (2021) 4808–4818. https://doi.org/10.1007/s11665-021-05919-6.

[58] C. Weingarten, D. Buchbinder, N. Pirch, W. Meiners, K. Wissenbach, R. Poprawe, Formation and reduction of hydrogen porosity during selective laser melting of AlSi10Mg, J. Mater. Process. Technol. 221 (2015) 112–120. https://doi.org/10.1016/j.jmatprotec.2015.02.013.

[59] S.K. Everton, M. Hirsch, P.I. Stavroulakis, R.K. Leach, A.T. Clare, Review of in-situ process monitoring and in-situ metrology for metal additive manufacturing, Mater. Des. 95 (2016) 431–445. https://doi.org/10.1016/j.matdes.2016.01.099.

[60] T. Vilaro, C. Colin, J.D. Bartout, As-fabricated and heat-treated microstructures of the Ti-6Al-4V alloy processed by selective laser melting, Metall. Mater. Trans. A Phys. Metall. Mater. Sci. 42 (2011) 3190–3199. https://doi.org/10.1007/s11661-011-0731-y.

[61] C. Zhao, K. Fezzaa, R.W. Cunningham, H. Wen, F. De Carlo, L. Chen, A.D. Rollett, T. Sun, Real-time monitoring of laser powder bed fusion process using high-speed X-ray imaging and diffraction, Sci. Rep. 7 (2017) 1–11. https://doi.org/10.1038/s41598-017-03761-2.

[62] H. Gong, K. Rafi, H. Gu, T. Starr, B. Stucker, Analysis of defect generation in Ti-6Al-4V parts made using powder bed fusion additive manufacturing processes, Addit. Manuf. 1 (2014) 87–98. https://doi.org/10.1016/j.addma.2014.08.002.

[63] W.E. King, H.D. Barth, V.M. Castillo, G.F. Gallegos, J.W. Gibbs, D.E. Hahn, C. Kamath, A.M. Rubenchik, Observation of keyhole-mode laser melting in laser powder-bed fusion additive manufacturing, J. Mater. Process. Technol. 214 (2014) 2915–2925.

[64] P. Karimi, T. Raza, J. Andersson, L.E. Svensson, Influence of laser exposure time and point distance on 75-μm-thick layer of selective laser melted Alloy 718, Int. J. Adv. Manuf. Technol. 94 (2018) 2199–2207. https://doi.org/10.1007/s00170-017-1019-1.

[65] H. Hassanin, Y. Zweiri, L. Finet, K. Essa, C. Qiu, M. Attallah, Laser powder bed fusion of ti-6al-2sn-4zr-6mo alloy and properties prediction using deep learning approaches, Materials (Basel). 14 (2021). https://doi.org/10.3390/ma14082056.

[66] B. Zhang, Y. Li, Q. Bai, Defect Formation Mechanisms in Selective Laser Melting: A Review, Chinese J. Mech. Eng. (English Ed. 30 (2017) 515–527. https://doi.org/10.1007/s10033-017-0121-5.

[67] A. Haboudou, P. Peyre, A.B. Vannes, G. Peix, Reduction of porosity content generated during Nd: YAG laser welding of A356 and AA5083 aluminium alloys, Mater. Sci. Eng. A. 363 (2003) 40–52. https://doi.org/10.1016/S0921-5093(03)00637-3.

[68] H. Zhao, T. Debroy, Weld metal composition change during conduction mode laser welding of aluminum alloy 5182, Metall. Mater. Trans. B Process Metall. Mater. Process. Sci. 32 (2001) 163–172. https://doi.org/10.1007/s11663-001-0018-6.

[69] K. Kempen, L. Thijs, B. Vrancken, S. Buls, J. Van Humbeeck, J.P. Kruth, Producing crack-free, high density M2 HSS parts by Selective Laser Melting: Pre-heating the baseplate, 24th Int. SFF Symp. - An Addit. Manuf. Conf. SFF 2013. (2013) 131–139.

[70] H. Yang, J. Sha, D. Zhao, F. He, Z. Ma, C. He, C. Shi, N. Zhao, Defects control of aluminum alloys and their composites fabricated via laser powder bed fusion: A review, J. Mater. Process. Technol. 319 (2023) 118064. https://doi.org/10.1016/j.jmatprotec.2023.118064.

[71] L.N. Carter, M.M. Attallah, R.C. Reed, Laser Powder Bed Fabrication of

Nickel-Base Superalloys: Influence of Parameters; Characterisation, Quantification and Mitigation of Cracking, Superalloys 2012. (2012) 577–586. https://doi.org/10.1002/9781118516430.ch64.

[72] S. Kou, Welding metallurgy, John Wiley & Sons, 2020.

[73] Y. Chen, F. Lu, K. Zhang, P. Nie, S.R. Elmi Hosseini, K. Feng, Z. Li, Dendritic microstructure and hot cracking of laser additive manufactured Inconel 718 under improved base cooling, J. Alloys Compd. 670 (2016) 312–321. https://doi.org/10.1016/j.jallcom.2016.01.250.

[74] M. Yakout, I. Phillips, M.A. Elbestawi, Q. Fang, In-situ monitoring and detection of spatter agglomeration and delamination during laser-based powder bed fusion of Invar 36, Opt. Laser Technol. 136 (2021) 106741. https://doi.org/https://doi.org/10.1016/j.optlastec.2020.106741.

[75] I. Yadroitsev, A. Gusarov, I. Yadroitsava, I. Smurov, Single track formation in selective laser melting of metal powders, J. Mater. Process. Technol. 210 (2010) 1624–1631. https://doi.org/10.1016/j.jmatprotec.2010.05.010.

[76] D.D. Gu, W. Meiners, K. Wissenbach, R. Poprawe, Laser additive manufacturing of metallic components: Materials, processes and mechanisms, Int. Mater. Rev. 57 (2012) 133–164. https://doi.org/10.1179/1743280411Y.0000000014.

[77] B. Vrancken, L. Thijs, J.P. Kruth, J. Van Humbeeck, Heat treatment of Ti6Al4V produced by Selective Laser Melting: Microstructure and mechanical properties, J. Alloys Compd. 541 (2012) 177–185. https://doi.org/10.1016/j.jallcom.2012.07.022.

[78] P. Mercelis, J. Kruth, Residual stresses in selective laser sintering and selective laser melting, J. Penelit. Pendidik. Guru Sekol. Dasar. 6 (2016) 128. https://doi.org/https://doi.org/10.1108/13552540610707013.

[79] G.K. Lewis, E. Schlienger, 1-s2.0-S0261306999000783-main, (2000).

[80] A. Fathi, E. Toyserkani, A. Khajepour, M. Durali, Prediction of melt pool depth and dilution in laser powder deposition, J. Phys. D. Appl. Phys. 39 (2006) 2613–2623. https://doi.org/10.1088/0022-3727/39/12/022.

[81] D. Gu, Y. Shen, Balling phenomena in direct laser sintering of stainless steel powder: Metallurgical mechanisms and control methods, Mater. Des. 30 (2009) 2903–2910. https://doi.org/10.1016/j.matdes.2009.01.013.

[82] J.P. Kruth, L. Froyen, J. Van Vaerenbergh, P. Mercelis, M. Rombouts, B. Lauwers, Selective laser melting of iron-based powder, J. Mater. Process. Technol. 149 (2004) 616–622. https://doi.org/10.1016/j.jmatprotec.2003.11.051.

[83] R. Li, J. Liu, Y. Shi, L. Wang, W. Jiang, Balling behavior of stainless steel and nickel powder during selective laser melting process, Int. J. Adv. Manuf. Technol. 59 (2012) 1025–1035. https://doi.org/10.1007/s00170-011-3566-1.

[84] A.F.H. Kaplan, J. Powell, Spatter in laser welding, J. Laser Appl. 23 (2011). https://doi.org/10.2351/1.3597830.

[85] P. Bidare, I. Bitharas, R.M. Ward, M.M. Attallah, A.J. Moore, Fluid and particle dynamics in laser powder bed fusion, Acta Mater. 142 (2018) 107–120. https://doi.org/10.1016/j.actamat.2017.09.051.

[86] M. Simonelli, C. Tuck, N.T. Aboulkhair, I. Maskery, I. Ashcroft, R.D. Wildman, R. Hague, A Study on the Laser Spatter and the Oxidation Reactions During Selective Laser Melting of 316L Stainless Steel, Al-Si10-Mg, and Ti-6Al-4V, Metall. Mater. Trans. A Phys. Metall. Mater. Sci. 46 (2015) 3842–3851. https://doi.org/10.1007/s11661-015-2882-8.

[87] Q. Guo, C. Zhao, L.I. Escano, Z. Young, L. Xiong, K. Fezzaa, W. Everhart, B. Brown, T. Sun, L. Chen, Transient dynamics of powder spattering in laser powder bed fusion additive manufacturing process revealed by in-situ high-speed high-energy x-ray imaging, Acta Mater. 151 (2018) 169–180. https://doi.org/10.1016/j.actamat.2018.03.036.

[88] M.J. Matthews, G. Guss, S.A. Khairallah, A.M. Rubenchik, P.J. Depond, W.E. King, Denudation of metal powder layers in laser powder bed fusion processes, Acta Mater. 114 (2016) 33–42. https://doi.org/10.1016/j.actamat.2016.05.017.

[89] V. Gunenthiram, P. Peyre, M. Schneider, M. Dal, F. Coste, I. Koutiri, R. Fabbro, Experimental analysis of spatter generation and melt-pool behavior during the powder bed laser beam melting process, J. Mater. Process. Technol. 251 (2018) 376–386. https://doi.org/10.1016/j.jmatprotec.2017.08.012.

[90] A.B. Spierings, M. Schneider, R. Eggenberger, Comparison of density measurement techniques for additive manufactured metallic parts, Rapid Prototyp. J. 17 (2011) 380–386. https://doi.org/10.1108/13552541111156504.

[91] N. Saxena, R. Hofmann, F.O. Alpak, J. Dietderich, S. Hunter, R.J. Day-stirrat, Effect of image segmentation & voxel size on micro-CT computed effective transport & elastic properties, Mar. Pet. Geol. 86 (2017) 972–990. https://doi.org/10.1016/j.marpetgeo.2017.07.004.

[92] R. Cunningham, S.P. Narra, T. Ozturk, J. Beuth, A.D. Rollett, Evaluating the Effect of Processing Parameters on Porosity in Electron Beam Melted Ti-6Al-4V via Synchrotron X-ray Microtomography, 68 (2016) 765–771. https://doi.org/10.1007/s11837-015-1802-0.

[93] P. Anton du, G. Stephan, J. Waller, P. Sperling, N. Achilles, A. Beerlink, J. Métayer, M. Sinico, G. Probst, W. Dewulf, F. Bittner, H. Endres, M. Willner, Á. Drégelyi-kiss, T. Zikmund, J. Laznovsky, J. Kaiser, P. Pinter, S. Dietrich, E. Lopez, O. Fitzek, P. Konrad, Laboratory X-ray tomography for metal additive manufacturing : Round robin test, Addit. Manuf. 30 (2019) 100837. https://doi.org/10.1016/j.addma.2019.100837.

[94] A. Plessis, I. Yadroitsev, I. Yadroitsava, S.G. Le Roux, X-Ray Microcomputed Tomography in Additive Manufacturing : A Review of the Current Technology and Applications, 5 (2018) 227–247. https://doi.org/10.1089/3dp.2018.0060.

[95] J.D.B.O. Sullivan, J. Behnsen, T. Starborg, A.S. Macdonald, A.T. Phythian-adams, K.J. Else, S.M. Cruickshank, P.J. Withers, X-ray micro-computed tomography (μ CT): an emerging opportunity in parasite imaging, (2018).

[96] B. Song, S. Dong, Q. Liu, H. Liao, C. Coddet, Vacuum heat treatment of iron parts produced by selective laser melting : Microstructure , residual stress and tensile behavior, Mater. Des. 54 (2014) 727–733. https://doi.org/10.1016/j.matdes.2013.08.085.

[97] A.E. Giannakopoulos, S. Suresh, A new method for estimating residual stresses by instrumented sharp indentation, Acta Mater. 46 (1998) 5755–5767. https://doi.org/https://doi.org/10.1016/S1359-6454(98)00226-2.

[98] D. Buchbinder, W. Meiners, N. Pirch, K. Wissenbach, J. Schrage, D. Buchbinder, W. Meiners, N. Pirch, K. Wissenbach, components using selective laser melting Investigation on reducing distortion by preheating during manufacture of aluminum components using selective laser melting, 012004 (2015). https://doi.org/10.2351/1.4828755.

[99] J. Kruth, J. Deckers, E. Yasa, R. Wauthle, Assessing and comparing influencing factors of residual stresses in selective laser melting using a novel analysis method, 226 (2012) 980–991. https://doi.org/10.1177/0954405412437085.

[100] J.D. Lord, D. Penn, P. Whitehead, The Application of Digital Image Correlation for Measuring Residual Stress by Incremental Hole Drilling, (2008) 65–73. https://doi.org/10.4028/www.scientific.net/AMM.13-14.65.

[101] G.S. Schajer, Relaxation Methods for Measuring Residual Stresses : Techniques and Opportunities, (2010) 1117–1127. https://doi.org/10.1007/s11340-010-9386-7.

[102] K. Darvish, Z.W. Chen, T. Pasang, Reducing lack of fusion during selective laser melting of CoCrMo alloy: Effect of laser power on geometrical features of tracks, Mater. Des. 112 (2016) 357–366. https://doi.org/10.1016/j.matdes.2016.09.086.

[103] X. Chen, W. Mu, X. Xu, W. Liu, L. Huang, H. Li, Numerical analysis of double track formation for selective laser melting of 316L stainless steel, Appl. Phys. A Mater. Sci. Process. 127 (2021) 1–13. https://doi.org/10.1007/s00339-021-04728-x.

[104] W. Abd-Elaziem, S. Elkatatny, A.E. Abd-Elaziem, M. Khedr, M.A. Abd El-Baky, M.A. Hassan, M. Abu-Okail, M. Mohammed, A. Järvenpää, T. Allam, A. Hamada, On the current research progress of metallic materials fabricated by laser powder bed fusion process: a review, J. Mater. Res. Technol. 20 (2022) 681–707. https://doi.org/10.1016/j.jmrt.2022.07.085.

[105] K. Mumtaz, N. Hopkinson, Top surface and side roughness of Inconel 625 parts processed using selective laser melting, Rapid Prototyp. J. 15 (2009) 96–103. https://doi.org/10.1108/13552540910943397.

[106] Y. Lu, S. Wu, Y. Gan, T. Huang, C. Yang, L. Junjie, J. Lin, Study on the microstructure, mechanical property and residual stress of SLM Inconel-

718 alloy manufactured by differing island scanning strategy, Opt. Laser Technol. 75 (2015) 197–206. https://doi.org/10.1016/j.optlastec.2015.07.009.

[107] R. Casati, J. Lemke, M. Vedani, Microstructure and Fracture Behavior of 316L Austenitic Stainless Steel Produced by Selective Laser Melting, J. Mater. Sci. Technol. 32 (2016) 738–744. https://doi.org/10.1016/j.jmst.2016.06.016.

[108] D. Faidel, D. Jonas, G. Natour, W. Behr, Investigation of the selective laser melting process with molybdenum powder, Addit. Manuf. 8 (2015) 88–94. https://doi.org/10.1016/j.addma.2015.09.002.

[109] J. Beuth, N. Klingbeil, The Role of Process Variables in Laser-Based Direct Metal Solid Freeform Fabrication, (2001).

[110] Y. Pupo, J. Delgado, L. Serenó, J. Ciurana, Scanning space analysis in Selective Laser Melting for CoCrMo powder, Procedia Eng. 63 (2013) 370–378. https://doi.org/10.1016/j.proeng.2013.08.228.

[111] W. Schneller, M. Leitner, S. Pomberger, S. Springer, F. Beter, F. Grün, Effect of post treatment on the microstructure, surface roughness and residual stress regarding the fatigue strength of selectively laser melted AlSi10Mg structures, J. Manuf. Mater. Process. 3 (2019). https://doi.org/10.3390/jmmp3040089.

[112] Z. Tong, X. Ren, J. Jiao, W. Zhou, Y. Ren, Y. Ye, E.A. Larson, J. Gu, Laser additive manufacturing of FeCrCoMnNi high-entropy alloy: Effect of heat treatment on microstructure, residual stress and mechanical property, J. Alloys Compd. 785 (2019) 1144–1159. https://doi.org/10.1016/j.jallcom.2019.01.213.

[113] M. Shiomi, K. Osakada, K. Nakamura, T. Yamashita, F. Abe, Residual stress within metallic model made by selective laser melting process, CIRP Ann. - Manuf. Technol. 53 (2004) 195–198. https://doi.org/10.1016/S0007-8506(07)60677-5.

[114] A. Salmi, E. Atzeni, History of residual stresses during the production phases of AlSi10Mg parts processed by powder bed additive manufacturing technology, Virtual Phys. Prototyp. 12 (2017) 153–160. https://doi.org/10.1080/17452759.2017.1310439.

[115] K.N. Amato, S.M. Gaytan, L.E. Murr, E. Martinez, P.W. Shindo, J. Hernandez, S. Collins, F. Medina, Microstructures and mechanical behavior of Inconel 718 fabricated by selective laser melting, Acta Mater. 60 (2012) 2229–2239. https://doi.org/10.1016/j.actamat.2011.12.032.

[116] S. Das, M. Wohlert, J.J. Beaman, D.L. Bourell, Producing metal parts with selective laser sintering/hot isostatic pressing, Jom. 50 (1998) 17–20. https://doi.org/10.1007/s11837-998-0299-1.

[117] A. du Plessis, E. Macdonald, Hot isostatic pressing in metal additive manufacturing: X-ray tomography reveals details of pore closure, Addit. Manuf. 34 (2020) 101191. https://doi.org/10.1016/j.addma.2020.101191.

[118] H. V. Atkinson, S. Davies, Fundamental aspects of hot isostatic pressing:

An overview, Metall. Mater. Trans. A Phys. Metall. Mater. Sci. 31 (2000) 2981–3000. https://doi.org/10.1007/s11661-000-0078-2.

[119] M.H. Bocanegra-Bernal, Hot Isostatic Pressing (HIP) technology and its, J. Mater. Sci. 9 (2004) 6399–6420.

[120] A.H. Maamoun, M.A. Elbestawi, S.C. Veldhuis, Influence of shot peening on alsi10mg parts fabricated by additive manufacturing, J. Manuf. Mater. Process. 2 (2018). https://doi.org/10.3390/jmmp2030040.

[121] J. Damon, S. Dietrich, F. Vollert, J. Gibmeier, V. Schulze, Process dependent porosity and the influence of shot peening on porosity morphology regarding selective laser melted AlSi10Mg parts, Addit. Manuf. 20 (2018) 77–89. https://doi.org/10.1016/j.addma.2018.01.001.

[122] J.M. Torralba, U. Carlos, I.I.I. Madrid, 3 . 11 Improvement of Mechanical and Physical Properties in Powder Metallurgy, Elsevier, 2014. https://doi.org/10.1016/B978-0-08-096532-1.00316-2.

[123] P.A. Rometsch, Y. Zhu, X. Wu, A. Huang, Review of high-strength aluminium alloys for additive manufacturing by laser powder bed fusion, Mater. Des. 219 (2022) 110779. https://doi.org/10.1016/j.matdes.2022.110779.

[124] S. Dixit, S. Liu, Laser Additive Manufacturing of High-Strength Aluminum Alloys: Challenges and Strategies, J. Manuf. Mater. Process. 6 (2022). https://doi.org/10.3390/jmmp6060156.

[125] S. Kim, S.K. Moon, A part consolidation design method for additive manufacturing based on product disassembly complexity, Appl. Sci. 10 (2020). https://doi.org/10.3390/app10031100.

[126] S.C. Altıparmak, V.A. Yardley, Z. Shi, J. Lin, Challenges in additive manufacturing of high-strength aluminium alloys and current developments in hybrid additive manufacturing, Int. J. Light. Mater. Manuf. 4 (2021) 246–261. https://doi.org/10.1016/j.ijlmm.2020.12.004.

[127] J.C. Najmon, S. Raeisi, A. Tovar, Review of additive manufacturing technologies and applications in the aerospace industry, Elsevier Inc., 2019. https://doi.org/10.1016/B978-0-12-814062-8.00002-9.

[128] H.R. Kotadia, G. Gibbons, A. Das, P.D. Howes, A review of Laser Powder Bed Fusion Additive Manufacturing of aluminium alloys: Microstructure and properties, Addit. Manuf. 46 (2021) 102155. https://doi.org/10.1016/j.addma.2021.102155.

[129] J. Zhang, B. Song, Q. Wei, D. Bourell, Y. Shi, A review of selective laser melting of aluminum alloys: Processing, microstructure, property and developing trends, J. Mater. Sci. Technol. 35 (2019) 270–284. https://doi.org/10.1016/j.jmst.2018.09.004.

[130] AZom., https://www.azom.com/article.aspx?ArticleID=6588, (n.d.).

[131] B. Rahimi, H. Khosravi, M. Haddad-Sabzevar, Microstructural characteristics and mechanical properties of Al-2024 alloy processed via a rheocasting route, Int. J. Miner. Metall. Mater. 22 (2015) 59–67. https://doi.org/10.1007/s12613-015-1044-8.

[132] J. Weritz, Aluminum Alloy Nomenclature and Temper Designations[1], Alum. Sci. Technol. 2A (2018) 0. https://doi.org/10.31399/asm.hb.v02a.a0006482.

[133] A. Wang, H. Wang, Y. Wu, H. Wang, 3D printing of aluminum alloys using laser powder deposition: a review, Int. J. Adv. Manuf. Technol. 116 (2021) 1–37. https://doi.org/10.1007/s00170-021-07440-5.

[134] Lynch Metals, https://lynchmetals.com/work-aluminum-4047/, (n.d.).

[135] M.A. Wahid, A.N. Siddiquee, Z.A. Khan, Aluminum alloys in marine construction: characteristics, application, and problems from a fabrication viewpoint, Mar. Syst. Ocean Technol. 15 (2020) 70–80.

[136] J.A. Van Der Hoeven, L. Zhuang, B. Schepers, P. De Smet, J.P. Baekelandt, A new 5xxx series alloy developed for automotive applications, SAE Technical Paper, 2002.

[137] A.M. Abd El-Hameed, Y.A. Abdel-Aziz, Aluminium Alloys in Space Applications: A Short Report, J. Adv. Res. Appl. Sci. Eng. Technol. 22 (2021) 1–7.

[138] O. Engler, J. Hirsch, Texture control by thermomechanical processing of AA6xxx Al–Mg–Si sheet alloys for automotive applications—a review, Mater. Sci. Eng. A. 336 (2002) 249–262.

[139] J.R. Davis, Aluminum and aluminum alloys, ASM international, 1993.

[140] S. Lathabai, Additive Manufacturing of Aluminium-Based Alloys and Composites, Elsevier Ltd., 2018. https://doi.org/10.1016/B978-0-08-102063-0.00002-3.

[141] B.A. Fulcher, D.K. Leigh, T.J. Watt, Comparison of AlSi10Mg and Al6061 processed through DMLS, in: Int. Solid Free. Fabr. Symp., 2014: pp. 404–419.

[142] M. Tang, P.C. Pistorius, Version of Record: https://www.sciencedirect.com/science/article/pii/S0142112316301463, (n.d.) 1–22.

[143] E. Louvis, P. Fox, C.J. Sutcliffe, Journal of Materials Processing Technology Selective laser melting of aluminium components, J. Mater. Process. Tech. 211 (2011) 275–284. https://doi.org/10.1016/j.jmatprotec.2010.09.019.

[144] T.B. Sercombe, X. Li, Selective laser melting of aluminium and aluminium metal matrix composites: review, Mater. Technol. 7857 (2016). https://doi.org/10.1080/10667857.2016.1161147.

[145] C. Lun, A. Leung, S. Marussi, M. Towrie, R.C. Atwood, J. Philip, P.D. Lee, AC SC, Acta Mater. (2018). https://doi.org/10.1016/j.actamat.2018.12.027.

[146] K. Kempen, L. Thijs, J. Van Humbeeck, J. Kruth, Mechanical properties of AlSi10Mg produced by Selective Laser Melting, 39 (2012) 439–446. https://doi.org/10.1016/j.phpro.2012.10.059.

[147] X.P. Li, K.M.O. Donnell, T.B. Sercombe, Selective laser melting of Al-12Si alloy : Enhanced densification via powder drying, 10 (2016) 10–14.

https://doi.org/10.1016/j.addma.2016.01.003.

[148] S. Touzé, M. Rauch, J. Hascoët, Flowability characterization and enhancement of aluminium powders for Additive Manufacturing, (n.d.) 1–30.

[149] S. Ozbilen, Influence of oxygen on morphology and oxide content in gas atomised Al powders, (2018).

[150] L.J. Jallo, M. Schoenitz, E.L. Dreizin, R.N. Dave, C.E. Johnson, The effect of surface modification of aluminum powder on its flowability, combustion and reactivity ☆, Powder Technol. 204 (2010) 63–70. https://doi.org/10.1016/j.powtec.2010.07.017.

[151] R.C. Weast, CRC Handbook of Chemistry and Physics. A ready-reference book of chemical and physical data, Cleveland. (1975).

[152] J. Liu, P. Wen, Metal vaporization and its influence during laser powder bed fusion process, Mater. Des. 215 (2022) 110505. https://doi.org/10.1016/j.matdes.2022.110505.

[153] A. Ag, C. Au, S. Fe, J.K. Lasers, Laser processing of reflective materials, (2013) 18–20.

[154] H. Zhang, H. Zhu, T. Qi, Z. Hu, X. Zeng, Selective laser melting of high strength Al-Cu-Mg alloys: Processing, microstructure and mechanical properties, Mater. Sci. Eng. A. 656 (2016) 47–54. https://doi.org/10.1016/j.msea.2015.12.101.

[155] D. Buchbinder, H. Schleifenbaum, S. Heidrich, W. Meiners, J. Bültmann, High power Selective Laser Melting (HP SLM) of aluminum parts, Phys. Procedia. 12 (2011) 271–278. https://doi.org/10.1016/j.phpro.2011.03.035.

[156] K. Geng, Y. Yang, S. Li, R.D.K. Misra, Q. Zhu, Enabling high-performance 3D printing of Al powder by decorating with high laser absorbing Co phase, Addit. Manuf. 32 (2020) 101012. https://doi.org/10.1016/j.addma.2019.101012.

[157] A. Singh, A. Ramakrishnan, D. Baker, A. Biswas, G.P. Dinda, Laser metal deposition of nickel coated Al 7050 alloy, J. Alloys Compd. 719 (2017) 151–158. https://doi.org/10.1016/j.jallcom.2017.05.171.

[158] D. Gu, X. Rao, D. Dai, C. Ma, L. Xi, K. Lin, Laser additive manufacturing of carbon nanotubes (CNTs) reinforced aluminum matrix nanocomposites: Processing optimization, microstructure evolution and mechanical properties, Addit. Manuf. 29 (2019) 100801. https://doi.org/10.1016/j.addma.2019.100801.

[159] W.E. King, A.T. Anderson, R.M. Ferencz, N.E. Hodge, C. Kamath, S.A. Khairallah, A.M. Rubenchik, Laser powder bed fusion additive manufacturing of metals; physics, computational, and materials challenges, Appl. Phys. Rev. 2 (2015) 041304. https://doi.org/10.1063/1.4937809.

[160] N. Kaufmann, M. Imran, T.M. Wischeropp, C. Emmelmann, S. Siddique, F. Walther, Influence of process parameters on the quality of aluminium alloy en AW 7075 using Selective Laser Melting (SLM), Phys. Procedia. 83 (2016) 918–926. https://doi.org/10.1016/j.phpro.2016.08.096.

[161] E.O. Olakanmi, R.F. Cochrane, K.W. Dalgarno, A review on selective laser sintering/melting (SLS/SLM) of aluminium alloy powders: Processing, microstructure, and properties, Prog. Mater. Sci. 74 (2015) 401–477. https://doi.org/10.1016/j.pmatsci.2015.03.002.

[162] X. Cao, W. Wallace, J. Immarigeon, C. Poon, Research and Progress in Laser Welding of Wrought Aluminum Alloys . II . Metallurgical Microstructures , Defects , and Mechanical Properties, 6914 (2007). https://doi.org/10.1081/AMP-120017587.

[163] M. Kumar, G.J. Gibbons, A. Das, I. Manna, D. Tanner, H.R. Kotadia, Additive manufacturing of aluminium alloy 2024 by laser powder bed fusion: microstructural evolution, defects and mechanical properties, Rapid Prototyp. J. 27 (2021) 1388–1397. https://doi.org/10.1108/RPJ-10-2020-0241.

[164] Q. Tan, J. Zhang, Q. Sun, Z. Fan, G. Li, Y. Yin, Y. Liu, M.X. Zhang, Inoculation treatment of an additively manufactured 2024 aluminium alloy with titanium nanoparticles, Acta Mater. 196 (2020) 1–16. https://doi.org/10.1016/j.actamat.2020.06.026.

[165] J. Sha, M. Li, L. Yang, X. Rong, B. Pu, D. Zhao, S. Sui, X. Zhang, C. He, J. Lan, N. Zhao, Si-Assisted Solidification Path and Microstructure Control of 7075 Aluminum Alloy with Improved Mechanical Properties by Selective Laser Melting, Acta Metall. Sin. (English Lett. 35 (2022) 1424–1438. https://doi.org/10.1007/s40195-022-01419-1.

[166] L. Xinwei, S. Shi, H. Shuang, H. Xiaogang, Z. Qiang, L. Hongxing, L. Wenwu, S. Yusheng, D. Hui, Microstructure, solidification behavior and mechanical properties of Al-Si-Mg-Ti/TiC fabricated by selective laser melting, Addit. Manuf. 34 (2020) 101326. https://doi.org/10.1016/j.addma.2020.101326.

[167] T. Soysal, S. Kou, Acta Materialia A simple test for assessing solidification cracking susceptibility and checking validity of susceptibility prediction, Acta Mater. 143 (2018) 181–197. https://doi.org/10.1016/j.actamat.2017.09.065.

[168] D. Grange, J. Bartout, B. Macquaire, C. Colin, Processing a non-weldable Nickel-base superalloy by Selective Laser Melting : role of the shape and size of the melt pools on solidification cracking, (n.d.) 1–29.

[169] P. Mair, V.S. Goettgens, T. Rainer, N. Weinberger, I. Letofsky-papst, S. Mitsche, G. Leichtfried, Laser powder bed fusion of nano-CaB 6 decorated 2024 aluminum alloy, J. Alloys Compd. 863 (2024) 158714. https://doi.org/10.1016/j.jallcom.2021.158714.

[170] S. Wu, Z. Lei, B. Li, J. Liang, Y. Chen, Hot cracking evolution and formation mechanism in 2195 Al-Li alloy printed by laser powder bed fusion, Addit. Manuf. 54 (2022) 102762. https://doi.org/https://doi.org/10.1016/j.addma.2022.102762.

[171] W. Chen, T. Voisin, Y. Zhang, J.B. Florien, C.M. Spadaccini, D.L. McDowell, T. Zhu, Y.M. Wang, Microscale residual stresses in additively

manufactured stainless steel, Nat. Commun. 10 (2019) 1–12. https://doi.org/10.1038/s41467-019-12265-8.

[172] J.A. Glerum, C. Kenel, T. Sun, D.C. Dunand, Synthesis of precipitation-strengthened Al-Sc, Al-Zr and Al-Sc-Zr alloys via selective laser melting of elemental powder blends, Addit. Manuf. 36 (2020) 1–23. https://doi.org/10.1016/j.addma.2020.101461.

[173] J.H. Martin, B.D. Yahata, J.M. Hundley, J.A. Mayer, T.A. Schaedler, T.M. Pollock, 3D printing of high-strength aluminium alloys, Nature. 549 (2017) 365–369. https://doi.org/10.1038/nature23894.

[174] Z. Hu, X. Nie, Y. Qi, H. Zhang, H. Zhu, Cracking criterion for high strength Al–Cu alloys fabricated by selective laser melting, Addit. Manuf. 37 (2021) 101709. https://doi.org/10.1016/j.addma.2020.101709.

[175] S.R. Narasimharaju, W. Zeng, T.L. See, Z. Zhu, P. Scott, X. Jiang, S. Lou, A comprehensive review on laser powder bed fusion of steels: Processing, microstructure, defects and control methods, mechanical properties, current challenges and future trends, J. Manuf. Process. 75 (2022) 375–414. https://doi.org/10.1016/j.jmapro.2021.12.033.

[176] T. Qi, H. Zhu, H. Zhang, J. Yin, L. Ke, X. Zeng, Selective laser melting of Al7050 powder: Melting mode transition and comparison of the characteristics between the keyhole and conduction mode, Mater. Des. 135 (2017) 257–266. https://doi.org/10.1016/j.matdes.2017.09.014.

[177] Z. Wang, X. Lin, N. Kang, Y. Hu, J. Chen, W. Huang, Strength-ductility synergy of selective laser melted Al-Mg-Sc-Zr alloy with a heterogeneous grain structure, Addit. Manuf. 34 (2020) 101260. https://doi.org/10.1016/j.addma.2020.101260.

[178] W. Cheng, Y. Liu, X. Xiao, B. Huang, Z. Zhou, X. Liu, Microstructure and mechanical properties of a novel (TiB 2 + TiC)/ AlSi10Mg composite prepared by selective laser melting, (n.d.).

[179] P. Yuan, D. Gu, Molten pool behaviour and its physical mechanism during selective laser melting of TiC/AlSi10Mg nanocomposites: Simulation and experiments, J. Phys. D. Appl. Phys. 48 (2015). https://doi.org/10.1088/0022-3727/48/3/035303.

[180] Y.K. Xiao, Z.Y. Bian, Y. Wu, G. Ji, Y.Q. Li, M.J. Li, Q. Lian, Z. Chen, A. Addad, H.W. Wang, Effect of nano-TiB2 particles on the anisotropy in an AlSi10Mg alloy processed by selective laser melting, J. Alloys Compd. 798 (2019) 644–655. https://doi.org/10.1016/j.jallcom.2019.05.279.

[181] S.R. Sabuj, M. Hamamura, Random cognitive radio network performance in Rayleigh-lognormal environment, 2017 14th IEEE Annu. Consum. Commun. Netw. Conf. CCNC 2017. 6 (2017) 992–997. https://doi.org/10.1109/CCNC.2017.7983268.

[182] W. Wu, C. Gao, Z. Liu, K. Wong, Z. Xiao, Laser powder bed fusion of crack-free TiN / Al7075 composites with enhanced mechanical properties, Mater. Lett. 282 (2021) 128625. https://doi.org/10.1016/j.matlet.2020.128625.

[183] L.K. Ang, Y.Y. Lau, R.M. Gilgenbach, H.L. Spindler, Analysis of laser absorption on a rough metal surface, 696 (2008) 10–13. https://doi.org/10.1063/1.118242.

[184] C. Gao, Z. Xiao, Z. Liu, Q. Zhu, W. Zhang, Selective laser melting of nano-TiN modified AlSi10Mg composite powder with low laser reflectivity, Mater. Lett. 236 (2019) 362–365. https://doi.org/10.1016/j.matlet.2018.10.126.

[185] X.P. Li, G. Ji, Z. Chen, A. Addad, Y. Wu, H.W. Wang, J. Vleugels, J. Van Humbeeck, J.P. Kruth, Acta Materialia Selective laser melting of nano-TiB 2 decorated AlSi10Mg alloy with high fracture strength and ductility, 129 (2017) 183–193. https://doi.org/10.1016/j.actamat.2017.02.062.

[186] C. Gao, W. Wu, Z. Xiao, Simultaneous Enhancement of Strength, Ductility, and Hardness of TiN/AlSi10Mg Nanocomposites via Selective Laser Melting, (2020). https://doi.org/10.1016/j.addma.2020.101378.

[187] D. Gu, Y. Yang, L. Xi, J. Yang, M. Xia, Laser absorption behavior of randomly packed powder-bed during selective laser melting of SiC and TiB 2 reinforced Al matrix composites, Opt. Laser Technol. 119 (2019) 105600. https://doi.org/10.1016/j.optlastec.2019.105600.

[188] L. Xi, L. Feng, D. Gu, K.G. Prashanth, I. Kaban, R. Wang, K. Xiong, B. Sarac, J. Eckert, Microstructure formation and mechanical performance of micro-nanoscale ceramic reinforced aluminum matrix composites manufactured by laser powder bed fusion, J. Alloys Compd. 939 (2023) 168803. https://doi.org/10.1016/j.jallcom.2023.168803.

[189] L. Xi, D. Gu, S. Guo, R. Wang, K. Ding, K.G. Prashanth, Grain refinement in laser manufactured Al-based composites with TiB2 ceramic, J. Mater. Res. Technol. 9 (2020) 2611–2622. https://doi.org/10.1016/j.jmrt.2020.04.059.

[190] Q. Tan, J. Zhang, N. Mo, Z. Fan, Y. Yin, M. Bermingham, Y. Liu, H. Huang, M.X. Zhang, A novel method to 3D-print fine-grained AlSi10Mg alloy with isotropic properties via inoculation with LaB6 nanoparticles, Addit. Manuf. 32 (2020) 101034. https://doi.org/10.1016/j.addma.2019.101034.

[191] X. Liu, Y. Liu, Z. Zhou, Q. Zhan, Enhanced strength and ductility in Al-Zn-Mg-Cu alloys fabricated by laser powder bed fusion using a synergistic grain-refining strategy, J. Mater. Sci. Technol. 124 (2022) 41–52. https://doi.org/10.1016/j.jmst.2021.12.078.

[192] Z. Wang, L. Zhuo, E. Yin, Z. Zhao, Microstructure evolution and properties of nanoparticulate SiC modified AlSi10Mg alloys, Mater. Sci. Eng. A. 808 (2021) 140864. https://doi.org/10.1016/j.msea.2021.140864.

[193] Z. Du, H.C. Chen, M.J. Tan, G. Bi, C.K. Chua, Effect of nAl2O3 on the part density and microstructure during the laser-based powder bed fusion of AlSi10Mg composite, Rapid Prototyp. J. 26 (2020) 727–735. https://doi.org/10.1108/RPJ-05-2019-0136.

[194] X. Liu, Y. Liu, Z. Zhou, K. Wang, Q. Zhan, X. Xiao, Grain refinement and

crack inhibition of selective laser melted AA2024 aluminum alloy via inoculation with TiC–TiH2, Mater. Sci. Eng. A. 813 (2021) 141171. https://doi.org/10.1016/j.msea.2021.141171.

[195] T. Minasyan, I. Hussainova, Laser Powder-Bed Fusion of Ceramic Particulate Reinforced Aluminum Alloys: A Review, Materials (Basel). 15 (2022). https://doi.org/10.3390/ma15072467.

[196] Y.K. Xiao, H. Chen, Z.Y. Bian, T.T. Sun, H. Ding, Q. Yang, Y. Wu, Q. Lian, Z. Chen, H.W. Wang, Journal of Materials Science & Technology Enhancing strength and ductility of AlSi10Mg fabricated by selective laser melting by TiB 2 nanoparticles, 109 (2022) 254–266.

[197] I.J. Polmear, Aluminium alloys - A century of age hardening, Mater. Forum. 28 (2004) 1–14.

[198] J.T. Vietz, I.J. Polmear, The influence of small additions of silver on the ageing of aluminium alloys.. Observations on AL-CU-MG alloys, Inst Met. J. 94 (1966) 410–419.

[199] B.H. North, United States Patent (19), (1988) 0–5.

[200] S.R. Arumalla, I.J. Polmear, Fatigue and Creep Behaviour of Aged Alloys Based on Al-4%Cu-0.3%Mg, in: Strength Met. Alloy. (ICSMA 7), Pergamon, 1985: pp. 453–458. https://doi.org/https://doi.org/10.1016/B978-0-08-031642-0.50082-9.

[201] I.J. Polmear, M.J. Couper, Design and development of an experimental wrought aluminum alloy for use at elevated temperatures, Metall. Trans. A. 19 (1988) 1027–1035. https://doi.org/10.1007/BF02628387.

[202] R.J. Chester, I.J. Polmear, The metallurgy of light alloys', 75-81; 1983, London, Inst. Metall. (n.d.).

[203] M. Hillert, The mechanism of phase transformations in crystalline solids, Inst. Met. London. 231 (1969).

[204] J.H. Auld, Structure of metastable precipitate in some Al–Cu–Mg–Ag alloys, Mater. Sci. Technol. (United Kingdom). 2 (1986) 784–787. https://doi.org/10.1179/mst.1986.2.8.784.

[205] S. Kerry, V.D. Scott, Structure and orientation relationship of precipitates formed in Al–Cu–Mg–Ag alloys, Met. Sci. 18 (1984) 289–294. https://doi.org/10.1179/030634584790420069.

[206] B.C. Muddle, I.J. Polmear, The precipitate Ω phase in Al-Cu-Mg-Ag alloys, Acta Metall. 37 (1989) 777–789. https://doi.org/10.1016/0001-6160(89)90005-9.

[207] K.M. Knowles, W.M. Stobbs, The structure of {111} age-hardening precipitates in Al–Cu–Mg–Ag alloys, Acta Crystallogr. Sect. B. 44 (1988) 207–227. https://doi.org/10.1107/S0108768187012308.

[208] A. Garg, Y.C. Chang, J.M. Howe, Precipitation of the Ω phase in an Al-4.0Cu-0.5Mg alloy, Scr. Metall. Mater. 24 (1990) 677–680. https://doi.org/10.1016/0956-716X(90)90222-3.

[209] S. Abis, P. Mengucci, G. Riontino, A study of the high-temperature ageing of Al-Cu-Mg-Ag alloy 201, Philos. Mag. B Phys. Condens. Matter; Stat.

Mech. Electron. Opt. Magn. Prop. 67 (1993) 465–484. https://doi.org/10.1080/13642819308207686.

[210] J.A. Taylor, B.A. Parker, I.J. Polmear, Precipitation in Ai-Cu-Mg-Ag casting alloy, Met. Sci. 12 (1978) 478–482. https://doi.org/10.1179/030634578790433341.

[211] K. Hono, T. Sakurai, I.J. Polmear, Pre-precipitate clustering in an AlCuMgAg alloy, Scr. Metall. Mater. 30 (1994) 695–700. https://doi.org/10.1016/0956-716X(94)90184-8.

[212] K. Hono, N. Sano, S.S. Babu, R. Okano, T. Sakurai, Atom probe study of the precipitation process in AlCuMgAg alloys, Acta Metall. Mater. 41 (1993) 829–838. https://doi.org/10.1016/0956-7151(93)90016-L.

[213] S.P. Ringer, W. Yeung, B.C. Muddle, I.J. Polmear, Precipitate stability in AlCuMgAg alloys aged at high temperatures, Acta Metall. Mater. 42 (1994) 1715–1725. https://doi.org/10.1016/0956-7151(94)90381-6.

[214] L. Reich, M. Murayama, K. Hono, Evolution of Ω phase in an Al–Cu–Mg–Ag alloy—a three-dimensional atom probe study, 46 (1998) 6053–6062. https://doi.org/https://doi.org/10.1016/S1359-6454(98)00280-8.

[215] S.P. Ringer, K. Hono, I.J. Polmear, T. Sakurai, Nucleation of precipitates in aged AlCuMg (Ag) alloys with high Cu: Mg ratios, Acta Mater. 44 (1996) 1883–1898. https://doi.org/10.1016/1359-6454(95)00314-2.

[216] C.R. Hutchinson, X. Fan, S.J. Pennycook, G.J. Shiflet, On the origin of the high coarsening resistance of Ω plates in Al–Cu–Mg–Ag alloys, Acta Mater. 49 (2001) 2827–2841. https://doi.org/10.1016/S1359-6454(01)00155-0.

[217] Al-Cu phase diagram.pdf, (n.d.).

[218] S. Bai, X. Zhou, Z. Liu, P. Ying, M. Liu, S. Zeng, Materials Science & Engineering A Atom probe tomography study of Mg-dependent precipitation of Ω phase in initial aged Al-Cu – Mg – Ag alloys, Mater. Sci. Eng. A. 637 (2015) 183–188. https://doi.org/10.1016/j.msea.2015.04.052.

[219] S. Bai, Z. Liu, X. Zhou, P. Xia, S. Zeng, Mg-controlled formation of Mg – Ag co-clusters in initial aged Al – Cu – Mg – Ag alloys, J. Alloys Compd. 602 (2014) 193–198. https://doi.org/10.1016/j.jallcom.2014.03.008.

[220] B. Huang, Z. Zheng, Independent and combined roles of trace Mg and Ag additions in properties precipitation process and precipitation kinetics of Al–Cu–Li–(Mg)–(Ag)–Zr–Ti alloys, Acta Mater. 46 (1998) 4381–4393. https://doi.org/https://doi.org/10.1016/S1359-6454(98)00079-2.

[221] R. Ferragut, A. Dupasquier, C.E. Macchi, A. Somoza, R.N. Lumley, I.J. Polmear, Vacancy – solute interactions during multiple-step ageing of an Al – Cu – Mg – Ag alloy, Scr. Mater. 60 (2009) 13–16. https://doi.org/10.1016/j.scriptamat.2008.09.011.

[222] Y. Nagai, T. Honma, Z. Tang, K. Hono, M. Hasegawa, of the pre-precipitation stage of an, 8610 (2016). https://doi.org/10.1080/01418610208240037.

[223] S. Bai, X. Zhou, Z. Liu, P. Xia, M. Liu, S. Zeng, Materials Science &

Engineering A Effects of Ag variations on the microstructures and mechanical properties of Al – Cu – Mg alloys at elevated temperatures, Mater. Sci. Eng. A. 611 (2014) 69–76. https://doi.org/10.1016/j.msea.2014.05.065.

[224] A. Zhu, E.A.S. Jr, G.J. Shiflet, An FP-CVM calculation of pre-precipitation clustering in Al A Cu A Mg A Ag alloys, 53 (2005) 35–40. https://doi.org/10.1016/j.scriptamat.2005.03.023.

[225] S. Bai, P. Ying, Z. Liu, J. Wang, J. Li, Materials Science & Engineering A Quantitative transmission electron microscopy and atom probe tomography study of Ag-dependent precipitation of Ω phase in Al-Cu-Mg alloys, Mater. Sci. Eng. A. 687 (2017) 8–16. https://doi.org/10.1016/j.msea.2017.01.045.

[226] S.P. Ringer, I.J. Polmearb, T. Sakurai, Effect of additions of Si and Ag to ternary Al-Cu-Mg the a + S phase field alloys in, (1996).

[227] B.M. Gable, G.J. Shiflet, E.A.S. Jr, The effect of Si additions on X precipitation in Al – Cu – Mg –(Ag) alloys, 50 (2004) 149–153. https://doi.org/10.1016/j.scriptamat.2003.09.004.

[228] L. Wang, M. Makhlouf, D. Apelian, Aluminium die casting alloys : alloy composition , microstructure , and properties-performance relationships, 40 (1995).

[229] J.E. Hatch, Aluminium: Properties and Physical Metallurgy, by ASM, Met. Park. OH. 135 (1984).

[230] Butler-GB2334966A.pdf, (n.d.).

[231] I. Bureau, W o 2011/098813, (2011).

[232] M. Indriyati, Effect of TiB2 addition on the microstructure and mechanical properties of Al-Cu-Mg-Ag alloy, Doctoral dissertation, University of Warwick, 2016.

[233] P.S. Mohanty, J.E. Gruzleskit, Mechanism of grain refinement in Aluminium, Acta Mater. 43 (2012) 2001–2012. https://doi.org/https://doi.org/10.1016/0956-7151(94)00405-7.

[234] ECKART GmbH, A20X powder- Technical Information Sheet, (2020).

[235] Aeromet International LTD, Working for Aerospace and Defence Customers Worldwide ., (n.d.).

[236] J. Li, F.S. Hage, Q.M. Ramasse, P. Schumacher, The nucleation sequence of α -Al on TiB 2 particles in Al-Cu alloys, 206 (2021). https://doi.org/10.1016/j.actamat.2021.116652.

[237] Z. Fan, Y. Wang, Y. Zhang, T. Qin, X.R. Zhou, G.E. Thompson, T. Pennycook, ScienceDirect Grain refining mechanism in the Al / Al – Ti – B system, ACTA Mater. 84 (2015) 292–304. https://doi.org/10.1016/j.actamat.2014.10.055.

[238] AMS D Nonferrous Alloys Committee, ast Aluminum Alloy Composite 4.6 Cu – 3.4Ti – 1.4B – 0.75Ag – 0.27Mg (A205.0/TiB2/3p-T7P) Investment Cast, Solution and Precipitation Heat Treated AMS4471, SAE Int. (n.d.). https://doi.org/https://doi.org/10.4271/AMS4471.

[239] AMS D Nonferrous Alloys Committee, Cast Aluminum Alloy Composite

4.6Cu - 3.4Ti - 1.4B - 0.75Ag - 0.27Mg (205.0/TiB2/3p-T7P) Sand Cast, Solution, and Precipitation Heat Treated AMS4482A, SAE Int. (n.d.). https://doi.org/https://doi.org/10.4271/AMS4482A.

[240] AMS AM Additive Manufacturing Metals, Aluminum Alloy Powder 4.6Cu - 3.4Ti - 1.4B - 0.75Ag - 0.27Mg, SAE International, 2021. https://doi.org/10.4271/AMS7033.

[241] ASTM International, ASTM F3049-14 Standard Guide For Characterizing Properties Of Metal Powders Used For Additive Manufacturing Processes, n.d. https://doi.org/doi:https://doi.org/10.1520/ F3049-14.

[242] A. Kordijazi, D. Weiss, Effect of solidification time on microstructure , wettability , and corrosion properties of A205-T7 aluminum alloys, Int. J. Met. 15 (2021) 2–12. https://doi.org/10.1007/s40962-020-00457-8.

[243] S.I. Shakil, A.S. Zoeram, H. Pirgazi, B. Shalchi-Amirkhiz, B. Poorganji, M. Mohammadi, M. Haghshenas, Microstructural-micromechanical correlation in an Al–Cu–Mg–Ag–TiB2 (A205) alloy: additively manufactured and cast, Mater. Sci. Eng. A. 832 (2022) 142453. https://doi.org/10.1016/j.msea.2021.142453.

[244] J. Mayer, L.A. Giannuzzi, T. Kamino, J. Michael, TEM sample preparation and FIB-induced damage, MRS Bull. 32 (2007) 400–407. https://doi.org/10.1557/mrs2007.63.

[245] A. Kovács, R. Schierholz, K. Tillmann, FEI Titan G2 80-200 CREWLEY, J. Large-Scale Res. Facil. JLSRF. 2 (2016) A43–A43.

[246] G.K. Williamson, R.E. Smallman, III. Dislocation densities in some annealed and cold-worked metals from measurements on the X-ray Debye-Scherrer spectrum, Philos. Mag. 1 (1956) 34–46. https://doi.org/10.1080/14786435608238074.

[247] N. Naga Krishna, R. Tejas, K. Sivaprasad, K. Venkateswarlu, Study on cryorolled Al-Cu alloy using X-ray diffraction line profile analysis and evaluation of strengthening mechanisms, Mater. Des. 52 (2013) 785–790. https://doi.org/10.1016/j.matdes.2013.05.095.

[248] M.A. Kaleem, M.Z. Alam, M. Khan, S.H.I. Jaffery, B. Rashid, An experimental investigation on accuracy of Hausner Ratio and Carr Index of powders in additive manufacturing processes, Met. Powder Rep. 76 (2021) S50–S54. https://doi.org/10.1016/j.mprp.2020.06.061.

[249] J. Zegzulka, D. Gelnar, L. Jezerska, R. Prokes, J. Rozbroj, Characterization and flowability methods for metal powders, Sci. Rep. 10 (2020) 1–19. https://doi.org/10.1038/s41598-020-77974-3.

[250] L. Marchetti, C. Hulme-smith, Citation for the original published paper (version of record): Permanent link to this version : Flowability of steel and tool steel powders : A comparison between testing methods, Powder Technol. 384 (2021) 402–413. https://doi.org/10.1016/j.powtec.2021.01.074.

[251] ASTM International, ASTM B213 − 13 Standard Test Methods for Flow Rate of Metal Powders Using the Hall Flowmeter Funnel, (n.d.).

https://doi.org/10.1520/B0213-20.

[252] D.C. Zapisotski, Characterizing flowability of metal powders, (2019).

[253] ASTM International, ASTMB964−16. Standard test methods for flow rate of metal powders using the carney funnel, n.d. https://doi.org/https://doi.org/10.1520/b0964-16.

[254] ASTM International, ASTMB527−15 Standard test method for tap density of metal powders and compounds, n.d. https://doi.org/https://doi.org/10.1520/B0527-15.

[255] B.S. Murty, S.A. Kori, M. Chakraborty, Grain refinement of aluminium and its alloys by heterogeneous nucleation and alloying, Int. Mater. Rev. 47 (2002) 3–29. https://doi.org/10.1179/095066001225001049.

[256] A.L. Greer, P.S. Cooper, M.W. Meredith, W. Schneider, P. Schumacher, J.A. Spittle, A. Tronche, Grain refinement of aluminium alloys by inoculation, Adv. Eng. Mater. 5 (2003) 81–91. https://doi.org/10.1002/adem.200390013.

[257] T. Liu, J.D. Leazer, S.K. Menon, L.N. Brewer, Microstructural analysis of gas atomized Al-Cu alloy feedstock powders for cold spray deposition, Surf. Coatings Technol. 350 (2018) 621–632. https://doi.org/10.1016/j.surfcoat.2018.07.006.

[258] A. Aversa, M. Lorusso, F. Trevisan, D. Manfredi, F. Calignano, S. Biamino, E.P. Ambrosio, P. Fino, M. Pavese, Microstructural and Mechanical Properties of Al-Si-Ni alloy Produced by Direct Metal Laser Sintering, in: Eur. Congr. Exhib. Powder Metall. Eur. PM Conf. Proc., The European Powder Metallurgy Association, 2016: pp. 1–6.

[259] T. Mukherjee, J.S. Zuback, A. De, T. DebRoy, Printability of alloys for additive manufacturing, Sci. Rep. 6 (2016) 1–8. https://doi.org/10.1038/srep19717.

[260] F. Bosio, A. Aversa, M. Lorusso, S. Marola, D. Gianoglio, L. Battezzati, P. Fino, D. Manfredi, M. Lombardi, A time-saving and cost-effective method to process alloys by Laser Powder Bed Fusion, Mater. Des. 181 (2019) 107949. https://doi.org/10.1016/j.matdes.2019.107949.

[261] C.C. Ng, M.M. Savalani, M.L. Lau, H.C. Man, Microstructure and mechanical properties of selective laser melted magnesium, Appl. Surf. Sci. 257 (2011) 7447–7454. https://doi.org/10.1016/j.apsusc.2011.03.004.

[262] E.A. Jägle, Z. Sheng, L. Wu, L. Lu, J. Risse, A. Weisheit, D. Raabe, Precipitation reactions in age-hardenable alloys during laser additive manufacturing, JOM. 68 (2016) 943–949. https://doi.org/10.1007/s11837-015-1764-2.

[263] S. Tang, R. Ummethala, C. Suryanarayana, J. Eckert, K.G. Prashanth, Z. Wang, Additive Manufacturing of Aluminum-Based Metal Matrix Composites — A Review, 2100053 (2021) 1–17. https://doi.org/10.1002/adem.202100053.

[264] L. Wang, J. Jue, M. Xia, L. Guo, B. Yan, D. Gu, Effect of the thermodynamic behavior of selective laser melting on the formation of in

situ oxide dispersion-strengthened aluminum-based composites, Metals (Basel). 6 (2016) 286.

[265] A. Aversa, G. Marchese, M. Lorusso, F. Calignano, S. Biamino, E.P. Ambrosio, D. Manfredi, P. Fino, M. Lombardi, M. Pavese, Microstructural and Mechanical Characterization of Aluminum Matrix Composites Produced by Laser Powder Bed Fusion, Adv. Eng. Mater. 19 (2017). https://doi.org/10.1002/adem.201700180.

[266] Y. Karabulut, R. Ünal, Additive manufacturing of ceramic particle-reinforced aluminum-based metal matrix composites: a review, J. Mater. Sci. 57 (2022) 19212–19242. https://doi.org/10.1007/s10853-022-07850-0.

[267] M. Ghasri-Khouzani, H. Karimialavijeh, R. Tangestani, M. Pröbstle, Martin, Single-track study of A20X aluminum alloy fabricated by laser powder bed fusion: Modeling and experiments, Opt. Laser Technol. 162 (2023) 1–10. https://doi.org/10.1016/j.optlastec.2023.109276.

[268] M. Ghasri-Khouzani, H. Karimialavijeh, M. Pröbstle, R. Batmaz, W. Muhammad, A. Chakraborty, T.D. Sabiston, J.P. Harvey, Martin, Processability and characterization of A20X aluminum alloy fabricated by laser powder bed fusion, Mater. Today Commun. 35 (2023). https://doi.org/10.1016/j.mtcomm.2023.105555.

[269] P. WANG, J. ECKERT, K. gokuldoss PRASHANTH, M. wei WU, I. KABAN, L. xia XI, S. SCUDINO, A review of particulate-reinforced aluminum matrix composites fabricated by selective laser melting, 2020. https://doi.org/10.1016/S1003-6326(20)65357-2.

[270] P. Mair, L. Kaserer, J. Braun, N. Weinberger, I. Letofsky-Papst, G. Leichtfried, Microstructure and mechanical properties of a TiB2-modified Al–Cu alloy processed by laser powder-bed fusion, Mater. Sci. Eng. A. 799 (2021) 140209. https://doi.org/10.1016/j.msea.2020.140209.

[271] M.H. Ghoncheh, M. Sanjari, A.S. Zoeram, E. Cyr, B.S. Amirkhiz, A. Lloyd, M. Haghshenas, M. Mohammadi, On the microstructure and solidification behavior of new generation additively manufactured Al-Cu-Mg-Ag-Ti-B alloys, Addit. Manuf. 37 (2021) 101724. https://doi.org/10.1016/j.addma.2020.101724.

[272] A.B. Spierings, K. Dawson, K. Kern, F. Palm, K. Wegener, SLM-processed Sc- and Zr- modified Al-Mg alloy: Mechanical properties and microstructural effects of heat treatment, Mater. Sci. Eng. A. 701 (2017) 264–273. https://doi.org/10.1016/j.msea.2017.06.089.

[273] Z. Hu, Y. Qi, X. Nie, H. Zhang, H. Zhu, The Portevin-Le Chatelier (PLC) effect in an Al-Cu aluminum alloy fabricated by selective laser melting, Mater. Charact. 178 (2021) 111198. https://doi.org/10.1016/j.matchar.2021.111198.

[274] X.P. Li, G. Ji, Z. Chen, A. Addad, Y. Wu, H.W. Wang, J. Vleugels, J. Van Humbeeck, J.P. Kruth, Selective laser melting of nano-TiB2decorated AlSi10Mg alloy with high fracture strength and ductility, Acta Mater. 129 (2017) 183–193. https://doi.org/10.1016/j.actamat.2017.02.062.

[275] E.P. Masuku, G. Govender, L. Ivanchev, H. Möller, Rheocasting of Al-Cu alloy A201 with different silver contents, Solid State Phenom. 141–143 (2008) 151–156. https://doi.org/10.4028/www.scientific.net/ssp.141-143.151.

[276] H. Möller, G. Govender, The heat treatment of rheo-high pressure die cast Al-Cu-Mg-Ag alloy 2139, Solid State Phenom. 192–193 (2013) 173–178. https://doi.org/10.4028/www.scientific.net/SSP.192-193.173.

[277] P. Daswa, H. Möller, G. Govender, Optimization of the solution heat treatment of rheo-high pressure die cast Al-Cu-Mg-Ag 2139 alloy, Mater. Sci. Forum. 828–829 (2015) 226–231. https://doi.org/10.4028/www.scientific.net/MSF.828-829.226.

[278] M. Zamani, S. Toschi, A. Morri, L. Ceschini, S. Seifeddine, Optimisation of heat treatment of Al–Cu–(Mg–Ag) cast alloys, J. Therm. Anal. Calorim. 139 (2020) 3427–3440. https://doi.org/10.1007/s10973-019-08702-x.

[279] M. Avateffazeli, P.E. Carrion, B. Shachi-Amirkhiz, H. Pirgazi, M. Mohammadi, N. Shamsaei, M. Haghshenas, Correlation between tensile properties, microstructure, and processing routes of an Al–Cu–Mg–Ag–TiB2 (A205) alloy: Additive manufacturing and casting, Mater. Sci. Eng. A. 841 (2022) 142989. https://doi.org/10.1016/j.msea.2022.142989.

[280] S.K. Varma, D. Salas, E. Corral, E. Esquivel, K.K. Chawla, R. Mahapatra, Microstructural development during aging of 2014 aluminum alloy composite, J. Mater. Sci. 34 (1999) 1855–1863. https://doi.org/10.1023/A:1004527729424.

[281] C. Bartels, D. Raabe, G. Gottstein, U. Huber, Investigation of the precipitation kinetics in an A16061/TiB2 metal matrix composite, Mater. Sci. Eng. A. 237 (1997) 12–23. https://doi.org/10.1016/S0921-5093(97)00104-4.

[282] A. Mandal, R. Maiti, M. Chakraborty, B.S. Murty, Effect of TiB2 particles on aging response of Al–4Cu alloy, Mater. Sci. Eng. A. 386 (2004) 296–300. https://doi.org/10.1016/j.msea.2004.07.026.

[283] I. Dutta, D.L. Bourell, A theoretical and experimental study of aluminum alloy 6061-SiC metal matrix composite to identify the operative mechanism for accelerated aging, Mater. Sci. Eng. A. 112 (1989) 67–77. https://doi.org/10.1016/0921-5093(89)90345-6.

[284] T. Christman, A. Needleman, S. Nutt, S. Suresh, On microstructural evolution and micromechanical modelling of deformation of a whisker-reinforced metal-matrix composite, Mater. Sci. Eng. A. 107 (1989) 49–61. https://doi.org/10.1016/0921-5093(89)90374-2.

[285] M. PA, M. Ferry, T. Chandra, Five decades of the Zener equation, ISIJ Int. 38 (1998) 913–924. https://doi.org/10.2355/isijinternational.38.913.

[286] S. Marola, D. Gianoglio, F. Bosio, A. Aversa, M. Lorusso, D. Manfredi, M. Lombardi, L. Battezzati, Alloying AlSi10Mg and Cu powders in laser Single Scan Tracks, melt spinning, and Laser Powder Bed Fusion, J. Alloys Compd. 821 (2020) 153538. https://doi.org/10.1016/j.jallcom.2019.153538.

[287] N.T. Aboulkhair, M. Simonelli, L. Parry, I. Ashcroft, C. Tuck, R. Hague, 3D printing of Aluminium alloys: Additive Manufacturing of Aluminium alloys using selective laser melting, Prog. Mater. Sci. 106 (2019) 100578. https://doi.org/10.1016/j.pmatsci.2019.100578.

[288] J. Wang, Z. Liu, S. Bai, J. Cao, J. Zhao, L. Luo, J. Li, Microstructure evolution and mechanical properties of the electron-beam welded joints of cast Al–Cu–Mg–Ag alloy, Mater. Sci. Eng. A. 801 (2021) 140363. https://doi.org/10.1016/j.msea.2020.140363.

[289] I. Zuiko, R. Kaibyshev, Aging behavior of an Al–Cu–Mg alloy, J. Alloys Compd. 759 (2018) 108–119. https://doi.org/10.1016/j.jallcom.2018.05.053.

[290] X.J. Jiang, B. Noble, B. Holme, G. Waterloo, J. Tafto, Differential scanning calorimetry and electron diffraction investigation on low-temperature aging in Al-Zn-Mg alloys, Metall. Mater. Trans. A Phys. Metall. Mater. Sci. 31 (2000) 339–348. https://doi.org/10.1007/s11661-000-0269-x.

[291] L.D.E.L. Castillo, E.J. Lavernia, Microstructure and Mechanical Behavior of Spray-Deposited Al-Cu-Mg (-Ag-Mn) Alloys, 31 (2000) 2287–2298. https://doi.org/https://doi.org/10.1007/s11661-000-0145-8.

[292] X.Y. Liu, Q.L. Pan, L.Y. Zheng, Q.R. Fu, F. Gao, M.X. Li, Y.M. Bai, Effect of aging temper on the thermal stability of Al–Cu–Mg–Ag heat-resistant alloy, Mater. Des. 46 (2013) 360–365. https://doi.org/10.1016/j.matdes.2012.10.039.

[293] D. Bakavos, P.B. Prangnell, B. Bes, F. Eberl, The effect of silver on microstructural evolution in two 2xxx series Al-alloys with a high Cu: Mg ratio during ageing to a T8 temper, Mater. Sci. Eng. A. 491 (2008) 214–223. https://doi.org/10.1016/j.msea.2008.03.014.

[294] D.H. Xiao, J.N. Wang, D.Y. Ding, S.P. Chen, Effect of Cu content on the mechanical properties of an Al–Cu–Mg–Ag alloy, J. Alloys Compd. 343 (2002) 77–81. https://doi.org/10.1016/S0925-8388(02)00076-2.

[295] S. Bai, X. Zhou, Z. Liu, P. Xia, M. Liu, S. Zeng, Effects of Ag variations on the microstructures and mechanical properties of Al–Cu–Mg alloys at elevated temperatures, Mater. Sci. Eng. A. 611 (2014) 69–76. https://doi.org/10.1016/j.msea.2014.05.065.

[296] M. Gazizov, R. Kaibyshev, Precipitation structure and strengthening mechanisms in an Al-Cu-Mg-Ag alloy, Mater. Sci. Eng. A. 702 (2017) 29–40. https://doi.org/10.1016/j.msea.2017.06.110.

[297] Y. Gazizova, R.O. Kaibyshev, Materials Characterization Precipitate / matrix incompatibilities related to the { 111 } Al Ω plates in an Al-Cu-Mg-Ag alloy, 182 (2021). https://doi.org/https://doi.org/10.1016/j.matchar.2021.111586.

[298] S.J. Kang, Y.W. Kim, M. Kim, J.M. Zuo, Determination of interfacial atomic structure, misfits and energetics of Ω phase in Al-Cu-Mg-Ag alloy, Acta Mater. 81 (2014) 501–511.

https://doi.org/10.1016/j.actamat.2014.07.074.

[299] K. Kim, B.C. Zhou, C. Wolverton, Interfacial stability of θ′/Al in Al-Cu alloys, Scr. Mater. 159 (2019) 99–103. https://doi.org/10.1016/j.scriptamat.2018.09.018.

[300] V. Vaithyanathan, C. Wolverton, L.Q. Chen, Multiscale modeling of θ′ precipitation in Al-Cu binary alloys, Acta Mater. 52 (2004) 2973–2987. https://doi.org/10.1016/j.actamat.2004.03.001.

[301] J.E. Franklin, W.F. Savage, Stress Relaxation and Strain-Age Cracking in Rene 41 Weldments, Weld. J. 53 (1974) 380–387. http://aws.perusion.com/wj/supplement/WJ_1974_09_s380.pdf.

[302] F. Hanning, G. Singh, J. Andersson, The Effect of Grain Size on the Susceptibility towards Strain Age Cracking of Wrought Haynes® 282®, Adv. Transdiscipl. Eng. 13 (2020) 407–416. https://doi.org/10.3233/ATDE200178.

[303] A.W. Dix, W.F. Savage, Factors influencing strain-age cracking in Inconel X-750, Weld. J. 50 (1971) 247. http://files.aws.org/wj/supplement/WJ_1971_06_s247.pdf.

[304] G. Itoh, M. Kanno, T. Hagiwara, T. Sakamoto, Embrittlement in an age-hardened 2091 aluminum alloy by exposure at elevated temperatures below the aging temperature, Acta Mater. 47 (1999) 3799–3809. https://doi.org/10.1016/S1359-6454(99)00243-8.

[305] M. Fourmeau, C.D. Marioara, T. Børvik, A. Benallal, O.S. Hopperstad, A study of the influence of precipitate-free zones on the strain localization and failure of the aluminium alloy AA7075-T651, Philos. Mag. 95 (2015) 3278–3304. https://doi.org/10.1080/14786435.2015.1040099.

[306] G. Sharma, R. V. Ramanujan, G.P. Tiwari, Instability mechanisms in lamellar microstructures, Acta Mater. 48 (2000) 875–889. https://doi.org/10.1016/S1359-6454(99)00378-X.

[307] J.C.M. Kampe, T.H. Courtney, Y. Leng, Shape instabilities of plate-like structures-I. Experimental observations in heavily cold worked in situ composites, Acta Metall. 37 (1989) 1735–1745. https://doi.org/10.1016/0001-6160(89)90059-X.

[308] R.D. Vengrenovitch, On the ostwald ripening theory, Acta Metall. 30 (1982) 1079–1086. https://doi.org/10.1016/0001-6160(82)90004-9.

[309] M. Zamani, I. Belov, E. Sjölander, A. Bjurenstedt, E. Ghassemali, S. Seifeddine, Study on dissolution of Al2Cu in al-4.3 cu and a205 cast alloys, Metals (Basel). 10 (2020) 900. https://doi.org/10.3390/met10070900.

[310] A. Lombardi, D. Sediako, C. Ravindran, M. Barati, Analysis of precipitation, dissolution and incipient melting of Al2Cu in B206 Al alloy using in-situ neutron diffraction, J. Alloys Compd. 784 (2019) 1017–1025. https://doi.org/10.1016/j.jallcom.2019.01.104.

[311] J. Geng, T. Hong, Y. Ma, M. Wang, D. Chen, N. Ma, H. Wang, The solution treatment of in-situ sub-micron TiB2/2024 Al composite, Mater. Des. 98 (2016) 186–193. https://doi.org/10.1016/j.matdes.2016.03.024.

[312] Z. Asghar, G. Requena, H.P. Degischer, P. Cloetens, Three-dimensional study of Ni aluminides in an AlSi12 alloy by means of light optical and synchrotron microtomography, Acta Mater. 57 (2009) 4125–4132. https://doi.org/10.1016/j.actamat.2009.05.010.

[313] Q. Zhang, X. Luan, S. Dhawan, D.J. Politis, Q. Du, M.W. Fu, K. Wang, M.M. Gharbi, L. Wang, Development of the post-form strength prediction model for a highstrength 6xxx aluminium alloy with pre-existing precipitates and residual dislocations, Int. J. Plast. 119 (2019) 230–248. https://doi.org/10.1016/j.ijplas.2019.03.013.

[314] J. Buha, R.N. Lumley, A.G. Crosky, K. Hono, Secondary precipitation in an Al-Mg-Si-Cu alloy, Acta Mater. 55 (2007) 3015–3024. https://doi.org/10.1016/j.actamat.2007.01.006.

[315] P. Sepehrband, R. Mahmudi, F. Khomamizadeh, Effect of Zr addition on the aging behavior of A319 aluminum cast alloy, Scr. Mater. 52 (2005) 253–257. https://doi.org/10.1016/j.scriptamat.2004.10.025.

[316] M. de Haas, S.M. van Scherpenzeel, J.T.M. de Hosson, Grain Boundary Segregation and Precipitation in Aluminium Alloy AA6061, Mater. Sci. Forum. 519–521 (2006) 467–472. https://doi.org/10.4028/www.scientific.net/msf.519-521.467.

[317] T. Pardoen, D. Dumont, A. Deschamps, Y. Brechet, Grain boundary versus transgranular ductile failure, J. Mech. Phys. Solids. 51 (2003) 637–665. https://doi.org/10.1016/S0022-5096(02)00102-3.

[318] Y. Li, Z. Liu, S. Bai, X. Zhou, H. Wang, S. Zeng, Enhanced mechanical properties in an Al-Cu-Mg-Ag alloy by duplex aging, Mater. Sci. Eng. A. 528 (2011) 8060–8064. https://doi.org/10.1016/j.msea.2011.07.055.

[319] J. Wang, Z. Liu, S. Bai, J. Cao, J. Zhao, L. Luo, Microstructure evolution and mechanical properties of the electron-beam welded joints of cast Al – Cu – Mg – Ag alloy, Mater. Sci. Eng. A. 801 (2021) 140363. https://doi.org/10.1016/j.msea.2020.140363.

[320] J. Barode, A. Vayyala, E. Virgillito, A. Aversa, J. Mayer, P. Fino, Revisiting heat treatments for additive manufactured parts : A case study of A20X alloy, Mater. Des. 225 (2023) 111566. https://doi.org/10.1016/j.matdes.2022.111566.

[321] J. Wang, J. Xie, Z. Mao, T. Liang, A. Wang, W. Wang, S. Hao, Microstructure evolution and mechanical properties of the Al-Cu-Mg-Ag alloy during non-isothermal aging, J. Alloys Compd. 942 (2023) 169031. https://doi.org/10.1016/j.jallcom.2023.169031.

[322] M. Avateffazeli, P.E. Carrion, B. Shachi-Amirkhiz, H. Pirgazi, M. Mohammadi, N. Shamsaei, M. Haghshenas, Correlation between tensile properties, microstructure, and processing routes of an Al–Cu–Mg–Ag–TiB2 (A205) alloy: Additive manufacturing and casting, Mater. Sci. Eng. A. 841 (2022) 142989. https://doi.org/10.1016/j.msea.2022.142989.

[323] X.Y. Liu, Q.L. Pan, L.Y. Zheng, Q.R. Fu, F. Gao, M.X. Li, Y.M. Bai, Effect of aging temper on the thermal stability of Al-Cu-Mg-Ag heat-

resistant alloy, Mater. Des. 46 (2013) 360–365. https://doi.org/10.1016/j.matdes.2012.10.039.

[324] J.F. Nie, B.C. Muddle, Microstructural design of high-strength aluminum alloys, J. Phase Equilibria. 19 (1998) 543–551. https://doi.org/10.1361/105497198770341734.

[325] Z. Yu, H. Li, P. Cai, X. Fu, Z. Feng, L. Zhang, J. Wang, N. Xiao, Effect of aging route on the precipitation behavior and thermal stability of Al–Cu–Mg–Ag alloy, J. Mater. Res. Technol. 23 (2023) 2010–2019. https://doi.org/10.1016/j.jmrt.2023.01.140.

[326] C.-L. Tai, M.-C. Chen, T.-F. Chung, Y.-L. Yang, S.-L. Lee, T.-C. Tsao, Z. Shi, J. Lin, T.-C. Su, H.-R. Chen, J.-R. Yang, The nano-structural characterization of Ω and S phases in Al-5.1Cu-1.0 Mg-(0.4Ag) AA2024 aluminum alloys, Mater. Sci. Eng. A. (2023) 145361. https://doi.org/https://doi.org/10.1016/j.msea.2023.145361.

[327] Y. Te Chen, S.L. Lee, H.Y. Bor, J.C. Lin, Effect of natural aging and cold working on microstructures and mechanical properties of Al-4.6Cu-0.5Mg-0.5Ag alloy, Metall. Mater. Trans. A. 44 (2013) 2831–2838. https://doi.org/10.1007/s11661-013-1611-4.

[328] Y. Weng, Z. Jia, L. Ding, Y. Pan, Y. Liu, Q. Liu, Effect of Ag and Cu additions on natural aging and precipitation hardening behavior in Al-Mg-Si alloys, J. Alloys Compd. 695 (2017) 2444–2452. https://doi.org/10.1016/j.jallcom.2016.11.140.

[329] N. Ünlü, B.M. Gable, G.J. Shiflet, E.A. Starke, The Effect of Cold Work on the Precipitation of Omega and Theta prime in a Ternary Al-Cu-Mg Alloy, Metall. Mater. Trans. A. 34 (2003) 24–27. https://doi.org/https://doi.org/10.1007/s11661-003-0177-y.

[330] M.J. Starink, S.C. Wang, The thermodynamics of and strengthening due to co-clusters : General theory and application to the case of Al – Cu – Mg alloys, Acta Mater. 57 (2009) 2376–2389. https://doi.org/10.1016/j.actamat.2009.01.021.

[331] K.S. Ghosh, Calorimetric studies of 2024 Al–Cu–Mg and 2014 Al–Cu–Mg–Si alloys of various tempers, J. Therm. Anal. Calorim. 136 (2019) 447–459. https://doi.org/10.1007/s10973-018-7702-0.

[332] X.H. Zhu, Y.C. Lin, Q. Wu, Y.Q. Jiang, Effects of aging on precipitation behavior and mechanical properties of a tensile deformed Al–Cu alloy, J. Alloys Compd. 843 (2020) 155975. https://doi.org/10.1016/j.jallcom.2020.155975.

[333] Z. Chen, Y. Zhao, Z. Zhang, Theoretical and experimental study of precipitation and coarsening kinetics of θ′ phase in Al–Cu alloy, Vacuum. 189 (2021) 110263. https://doi.org/10.1016/j.vacuum.2021.110263.

[334] C. García Cordovilla, E. Louis, Characterization of the microstructure of a commercial Al-Cu alloy (2 0 1 1) by differential scanning calorimetry (DSC), J. Mater. Sci. 19 (1984) 279–290. https://doi.org/10.1007/BF02403136.

[335] Y. Nagai, T. Honma, Z. Tang, K. Hono, M. Hasegawa, Coincidence Doppler broadening study of the pre-precipitation stage of an Al-Cu-Mg-Ag alloy, Philos. Mag. A. 82 (2002) 1559–1572. https://doi.org/10.1080/01418610208240037.

[336] X. Xu, G. Wu, L. Zhang, X. Tong, F. Qi, Y. Guo, Materials Science & Engineering A Regulation of precipitation behavior among T 1 , S ’ , and θ ’ phases in Al – Cu – Li- (Mg – Ag) alloys by optimizing Ag / Mg ratios, Mater. Sci. Eng. A. 876 (2023) 145158. https://doi.org/10.1016/j.msea.2023.145158.

[337] P. Merle, J. Merlin, Coarsening of θ′ plates in Al-Cu alloys—II. influence of ledge mechanism, Acta Metall. 29 (1981) 1929–1938. https://doi.org/https://doi.org/10.1016/0001-6160(81)90030-4.

[338] R. Sankaran, L. C., Kinetics of growth of platelike precipitates, Acta Metall. 22 (1974) 957–969. https://doi.org/https://doi.org/10.1016/0001-6160(74)90021-2.

[339] F. Jiang, L. Tang, S. Li, H. Ye, M.M. Attallah, Z. Yang, Achieving strength-ductility balance in a laser powder bed fusion fabricated TiB2/Al–Cu-Mg-Ag alloy, J. Alloys Compd. 945 (2023) 169311. https://doi.org/10.1016/j.jallcom.2023.169311.

[340] C.S. Kim, I. Sohn, M. Nezafati, J.B. Ferguson, B.F. Schultz, Z. Bajestani-Gohari, P.K. Rohatgi, K. Cho, Prediction models for the yield strength of particle-reinforced unimodal pure magnesium (Mg) metal matrix nanocomposites (MMNCs), J. Mater. Sci. 48 (2013) 4191–4204. https://doi.org/10.1007/s10853-013-7232-x.

[341] M. Liu, S. Bai, Z. Liu, X. Zhou, P. Xia, S. Zeng, Analysis of modulus hardening in an artificial aged Al-Cu-Mg alloy by atom probe tomography, Mater. Sci. Eng. A. 629 (2015) 23–28. https://doi.org/10.1016/j.msea.2015.01.079.

[342] K. Ma, H. Wen, T. Hu, T.D. Topping, D. Isheim, D.N. Seidman, E.J. Lavernia, J.M. Schoenung, Mechanical behavior and strengthening mechanisms in ultrafine grain precipitation-strengthened aluminum alloy, Acta Mater. 62 (2014) 141–155. https://doi.org/10.1016/j.actamat.2013.09.042.

[343] T. Honma, S. Yanagita, K. Hono, Y. Nagai, M. Hasegawa, Coincidence Doppler broadening and 3DAP study of the pre-precipitation stage of an Al-Li-Cu-Mg-Ag alloy, Acta Mater. 52 (2004) 1997–2003. https://doi.org/10.1016/j.actamat.2003.12.043.

[344] M. Murayama, K. Hono, Three dimensional atom probe analysis of pre-precipitate clustering in an Al-Cu-Mg-Ag alloy, Scr. Mater. 38 (1998) 1315–1319. https://doi.org/10.1016/S1359-6462(98)00027-X.

[345] S. Bai, Z. Liu, X. Zhou, P. Xia, S. Zeng, Mg-controlled formation of Mg – Ag co-clusters in initial aged Al – Cu – Mg – Ag alloys, J. Alloy. Compd. J. 602 (2014) 193–198. https://doi.org/10.1016/j.jallcom.2014.03.008.

[346] S. Bai, X. Zhou, Z. Liu, P. Ying, M. Liu, S. Zeng, A Atom probe

tomography study of Mg-dependent precipitation of Ω phase in initial aged Al-Cu – Mg – Ag alloys, Mater. Sci. Eng. A. 637 (2015) 183–188. https://doi.org/10.1016/j.msea.2015.04.052.

[347] S. Bai, Z. Liu, P. Ying, J. Wang, J. Li, Investigation of modulus hardening of various co-clusters in aged Al-Cu-Mg-Ag alloy by atom probe tomography, Mater. Sci. Eng. A. 668 (2016) 234–242. https://doi.org/10.1016/j.msea.2016.05.016.

[348] S. Bai, Z. Liu, P. Ying, J. Wang, A. Wang, Quantitative study of the solute clustering and precipitation in a pre- stretched Al-Cu-Mg-Ag alloy, J. Alloys Compd. 725 (2017) 1288–1296. https://doi.org/10.1016/j.jallcom.2017.07.258.

[349] M.R. Gazizov, A.N. Belyakov, R. Holmestad, M.Y. Gazizova, V.S. Krasnikov, P.A. Bezborodova, R.O. Kaibyshev, The deformation behavior of the {111}Al plates in an Al-Cu-Mg-Ag alloy, Acta Mater. 243 (2023) 118534. https://doi.org/10.1016/j.actamat.2022.118534.

[350] S. Bai, H. Di, Z. Liu, Dislocation interaction with Ω phase in crept Al-Cu-Mg-Ag alloys, Mater. Sci. Eng. A. 651 (2016) 399–405. https://doi.org/10.1016/j.msea.2015.10.031.

[351] B.Q. Li, F.E. Wawner, Dislocation interaction with semicoherent precipitates (ω phase) in deformed Al-Cu-Mg-Ag alloy, Acta Mater. 46 (1998) 5483–5490. https://doi.org/10.1016/S1359-6454(98)00188-8.

[352] J. da Costa Teixeira, D.G. Cram, L. Bourgeois, T.J. Bastow, A.J. Hill, C.R. Hutchinson, On the strengthening response of aluminum alloys containing shear-resistant plate-shaped precipitates, Acta Mater. 56 (2008) 6109–6122. https://doi.org/10.1016/j.actamat.2008.08.023.

[353] J.F. Nie, B.C. Muddle, Strengthening of an Al-Cu-Sn alloy by deformation-resistant precipitate plates, Acta Mater. 56 (2008) 3490–3501. https://doi.org/10.1016/j.actamat.2008.03.028.

[354] N. Hansen, Hall-petch relation and boundary strengthening, Scr. Mater. 51 (2004) 801–806. https://doi.org/10.1016/j.scriptamat.2004.06.002.

[355] T. Shanmugasundaram, M. Heilmaier, B.S. Murty, V.S. Sarma, On the Hall-Petch relationship in a nanostructured Al-Cu alloy, Mater. Sci. Eng. A. 527 (2010) 7821–7825. https://doi.org/10.1016/j.msea.2010.08.070.

[356] S. Bai, X. Yi, Z. Liu, On the role of Ag additions on the initial solute hardening and competitive precipitation of Al-Cu-Mg alloys, J. Alloys Compd. 945 (2023) 169339. https://doi.org/10.1016/j.jallcom.2023.169339.

[357] V.A. Lubarda, On the effective lattice parameter of binary alloys, Mech. Mater. 35 (2003) 53–68. https://doi.org/10.1016/S0167-6636(02)00196-5.

[358] J.R. Davis, Aluminum and Aluminum Alloys, ASM International, 1993. https://doi.org/10.1361/autb2001p351.

[359] L.M. Cheng, W.J. Poole, J.D. Embury, D.J. Lloyd, The influence of precipitation on the work-hardening behavior of the aluminum alloys AA6111 and AA7030, Metall. Mater. Trans. A Phys. Metall. Mater. Sci. 34 A (2003) 2473–2481. https://doi.org/10.1007/s11661-003-0007-2.

[360] P. Zhang, K. Shi, J. Bian, J. Zhang, Y. Peng, G. Liu, A. Deschamps, J. Sun, Solute cluster evolution during deformation and high strain hardening capability in naturally aged Al–Zn–Mg alloy, Acta Mater. 207 (2021) 23–27. https://doi.org/10.1016/j.actamat.2021.116682.

[361] C. Zhang, D. Juul Jensen, T. Yu, Effects of initial 3D printed microstructures on subsequent microstructural evolution in 316L stainless steel, Acta Mater. 242 (2023) 118481. https://doi.org/10.1016/j.actamat.2022.118481.

[362] X. Wang, J.A. Muñiz-Lerma, M. Attarian Shandiz, O. Sanchez-Mata, M. Brochu, Crystallographic-orientation-dependent tensile behaviours of stainless steel 316L fabricated by laser powder bed fusion, Mater. Sci. Eng. A. 766 (2019) 138395. https://doi.org/10.1016/j.msea.2019.138395.

[363] Q. Jia, C. Lu, Y. Yan, Y. Zhuo, L. Wang, Z. Xia, C. Wang, X. Wu, Tensile deformation behaviors of laser powder bed fusion fabricated Al–Mn-Sc alloy with heterogeneous grain structure, Mater. Sci. Eng. A. 849 (2022) 143447. https://doi.org/10.1016/j.msea.2022.143447.

[364] L.S. Aota, I.R. Souza Filho, M. Roscher, D. Ponge, H.R. Zschommler Sandim, Strain hardening engineering via grain size control in laser powder-bed fusion, Mater. Sci. Eng. A. 838 (2022) 142773. https://doi.org/10.1016/j.msea.2022.142773.

[365] A. Taghipour, Y. Mazaheri, J. McDavid, S. Sheikhi, M. Braun, J. Shen, B. Klusemann, S. Ehlers, Strengthening Mechanisms and Strain Hardening Behavior of 316L Stainless Steel Manufactured by Laser-Based Powder Bed Fusion, Adv. Eng. Mater. 25 (2023). https://doi.org/10.1002/adem.202201230.

[366] S.S. Joshi, C. Keller, L. Mas, W. Lefebvre, E. Hug, J.P. Couzinie, On the origin of the strain hardening mechanisms of Ni20Cr alloy manufactured by laser powder bed fusion, Int. J. Plast. 165 (2023). https://doi.org/10.1016/j.ijplas.2023.103610.

[367] H. Eskandari Sabzi, X.H. Li, C. Zhang, H. Fu, P.E.J. Rivera-Díaz-del-Castillo, Strain hardening in twinning-induced plasticity stainless steel produced by laser powder bed fusion, Mater. Sci. Eng. A. 855 (2022) 143882. https://doi.org/10.1016/j.msea.2022.143882.

[368] A. Zafari, E.W.C. Lui, M. Li, K. Xia, Enhancing work hardening and ductility in additively manufactured β Ti: roles played by grain orientation, morphology and substructure, J. Mater. Sci. Technol. 105 (2022) 131–141. https://doi.org/10.1016/j.jmst.2021.08.006.

[369] G.E. Dieter, D. Bacon, Mechanical metallurgy, McGraw-hill New York, 1976.

[370] D.R. Askeland, P.P. Phulé, W.J. Wright, D.K. Bhattacharya, The science and engineering of materials, (2003).

[371] O.F. The, O.F.W. Hardening, LosA l amos, (n.d.).

[372] T.S. Byun, N. Hashimoto, K. Farrell, Temperature dependence of strain hardening and plastic instability behaviors in austenitic stainless steels,

Acta Mater. 52 (2004) 3889–3899. https://doi.org/10.1016/j.actamat.2004.05.003.

[373] A. Deschamps, B. Decreus, F. De Geuser, T. Dorin, M. Weyland, The influence of precipitation on plastic deformation of Al – Cu – Li alloys, Acta Mater. 61 (2013) 4010–4021. https://doi.org/10.1016/j.actamat.2013.03.015.

[374] P. Zhang, K. Shi, J. Bian, J. Zhang, Y. Peng, G. Liu, Acta Materialia Solute cluster evolution during deformation and high strain hardening capability in naturally aged Al – Zn – Mg alloy, 207 (2021) 23–27.

[375] D. Raabe, Multistage strain hardening through dislocation substructure and twinning in a high strength and ductile weight-reduced Fe – Mn – Al – C steel, Acta Mater. 60 (2012) 5791–5802. https://doi.org/10.1016/j.actamat.2012.07.018.

[376] L. Reich, M. Murayama, K. Hono, Evolution of Ω phase in an Al–Cu–Mg–Ag alloy—a three-dimensional atom probe study, Acta Mater. 46 (1998) 6053–6062. https://doi.org/https://doi.org/10.1016/S1359-6454(98)00280-8.

[377] M.R. Gazizov, A.N. Belyakov, R. Holmestad, M.Y. Gazizova, V.S. Krasnikov, P.A. Bezborodova, R.O. Kaibyshev, The deformation behavior of the {111}Al plates in an Al-Cu-Mg-Ag alloy -2, Acta Mater. 243 (2023) 118534. https://doi.org/10.1016/j.actamat.2022.118534.

[378] M. Khadyko, O.R. Myhr, O.S. Hopperstad, PT US CR, Mech. Mater. (2019) 103069. https://doi.org/10.1016/j.mechmat.2019.103069.

[379] G.M. Ludtka, D.E. Laughlin, The influence of microstructure and strength on the fracture mode and toughness of 7XXX series aluminum alloys, Metall. Trans. A. 13 (1982) 411–425. https://doi.org/10.1007/BF02643350.

[380] M.R. Ghomashchi, A. Vikhrov, Squeeze casting: An overview, J. Mater. Process. Technol. 101 (2000) 1–9. https://doi.org/10.1016/S0924-0136(99)00291-5.

[381] C. Morando, O. Fornaro, O. Garbellini, H. Palacio, Fluidity on Metallic Eutectic Alloys, Procedia Mater. Sci. 8 (2015) 959–967. https://doi.org/10.1016/j.mspro.2015.04.157.

[382] T.K. Akopyan, N.A. Belov, A.G. Padalko, N. V. Letyagin, N.N. Avksent'yeva, Analysis of the Effect of Hydrostatic Pressure on the Nonvariant Eutectic Transformation in Al–Si, Al–Cu, and Al–Cu–Si Systems, Phys. Met. Metallogr. 120 (2019) 593–599. https://doi.org/10.1134/S0031918X19060024.

[383] R. Ivanov, A. Deschamps, F. De Geuser, Clustering kinetics during natural ageing of Al-Cu based alloys with (Mg, Li) additions, Acta Mater. 157 (2018) 186–195. https://doi.org/10.1016/j.actamat.2018.07.035.

[384] S. Bai, Z. Liu, X. Zhou, Y. Gu, D. Yu, Strain-induced dissolution of Cu-Mg co-clusters and dynamic recrystallization near a fatigue crack tip of an underaged Al-Cu-Mg alloy during cyclic loading at ambient temperature, Scr. Mater. 64 (2011) 1133–1136.

https://doi.org/10.1016/j.scriptamat.2011.03.012.

[385] M. Liu, Z. Liu, S. Bai, P. Xia, P. Ying, A. Wang, Analysis on the dissolution behavior of various size Cu-Mg co-clusters near a fatigue crack tip of underaged Al-Cu-Mg alloy during cyclic loading, J. Alloys Compd. 699 (2017) 119–125. https://doi.org/10.1016/j.jallcom.2016.12.323.

[386] M. Liu, Z. Liu, S. Bai, P. Xia, P. Ying, S. Zeng, Solute cluster size effect on the fatigue crack propagation resistance of an underaged Al-Cu-Mg alloy, Int. J. Fatigue. 84 (2016) 104–112. https://doi.org/10.1016/j.ijfatigue.2015.11.023.

[387] P. Xu, H. Luo, Improving the ductility of nanostructured Al alloy using strongly textured nano-laminated structure combined with nano-precipitates, Mater. Sci. Eng. A. 675 (2016) 323–337. https://doi.org/10.1016/j.msea.2016.08.072.